



University  
of Glasgow

Cui, Li (1999) *Conducting polymer-based QCM-interdigitated electrode hybrid electronic nose system.*

PhD thesis

<http://theses.gla.ac.uk/3974/>

Copyright and moral rights for this thesis are retained by the author

A copy can be downloaded for personal non-commercial research or study, without prior permission or charge

This thesis cannot be reproduced or quoted extensively from without first obtaining permission in writing from the Author

The content must not be changed in any way or sold commercially in any format or medium without the formal permission of the Author

When referring to this work, full bibliographic details including the author, title, awarding institution and date of the thesis must be given



UNIVERSITY  
*of*  
GLASGOW

**CONDUCTING POLYMER-BASED  
QCM-INTERDIGITATED ELECTRODE HYBRID  
ELECTRONIC NOSE SYSTEM**

Li Cui

B.Sc. M.Sc.

A Thesis for the Degree of  
Doctor of Philosophy,  
Submitted to the Faculty of Engineering,  
University of Glasgow

May 1999

© Li Cui May 1999

**To my parents**



## Acknowledgements

I am extremely grateful to my supervisors Professor Jonathan Cooper and Professor John Barker for their invaluable supervision, encouragement and continual support throughout this research project. A great deal of what has been achieved is due to their useful suggestions and clear sense of direction.

I would like to thank Professor Steve Beaumont, my Head of the Department for a large proportion of the project, for providing me with excellent research facilities.

I would like to express my sincere gratitude to Dr. Marcus Swann for his considered advice, valuable suggestions and discussions, which have been proven to be very important to the success of this work. I would appreciate Dr. Andrew Glidle greatly for his help in this study on electronics and computing technique, and all other related areas.

Thanks are also due to the technicians Mr. Bill Monaghan, Mrs. Mary Robertson, Mr. Ian McNicholl, Mr. Robert Harkins and other technical staff in the cleanroom and mechanical workshop for their continual and efficient technical support in the use of microfabrication facilities, technical training, experimental materials supply, mask making and system hardware construction.

I am grateful to my colleagues Dr. Li Jiang, Dr. James Davis and Dr. Nick Green in the biogroup and friends Dr. Binsheng Zhang, Dr. Bocang Qiu, Dr. Yahong Qian, Dr. Haiping Zhou and Dr. Maolong Ke for their great concern and various helps.

Special thanks and appreciation are due to my parents and my husband Yinpeng for their solid and selfless support and tremendous understanding, love and patience through all these years.

I would also like to thank MAFF for the financial support of this project.

## Abstract

This research project was concerned with the establishment and characterisation of a quartz crystal microbalance (QCM) – conductimetric interdigitated electrode hybrid “second generation” *Electronic Nose* system. Research objectives covered a number of technical limitations and analytical difficulties existed in the “first generation” *Electronic Nose* system. A wide variety of work was carried out, including the design and fabrication of the electronic nose system, the optimisation of sensors response, the device modelling, the studies of vapour-polymer interaction mechanisms and the application of the electronic nose in multi-component analysis.

A QCM–interdigitated electrode hybrid sensor odour measurement system was established, and sensor fabrication techniques developed. Some important parameters corresponding to sensor characteristics were investigated such as the conditions for polymer film polymerisation. By studying 16 different coatings, “optimal” individual initial resistances were proposed, which minimise long-term baseline resistance drift, whilst maintaining good sensitivity. A set of sensors was made with low initial resistance variation. Sensor detection dynamic range was found to be depended on the type of the coating material and the film thickness. The response of a combined hybrid sensor pair remained stable during a test period of 45 days, which showed an improved stability.

The principle of the sensor’s response and device modelling were addressed. The vapour-polymer interactions and sensor pair’s response were linked by a sensitivity coefficient ( $S$ ), which was defined as the relative resistivity change by a single molecule absorbed into the polymer film. A pair of sensors showing concentration independence over a wide concentration range can be formed on separate QCM and interdigitated electrodes with the same polymer. The combined response ( $S_{ff}$ ) can be used to identify a particular vapour. Based on the concentration independence, the proposed “odour maps” showed the feasibility of distinguishing odourants using a significantly lower number of different types of sensor coatings. This demonstrated the improved selectivity of a hybrid system compared with the single property system.

The nature of vapour-polymer interactions was studied based on the hybrid system response multiplied by molecular weight. Linear solvation energy relationships (LSERs), determined by the multivariable regression of a set of experimental results with the five basic representative molecular interaction parameters, were employed to analyse particular interactions contributing to the overall sorption process. A number of the interaction mechanisms were assessed. Among the five possible interaction terms concerned, hydrogen bonding and dispersion interactions played more important roles.

In addition, a method of multi-component analysis for organic vapour mixtures was explored. Mixtures of two or three components can be analysed on an odour map composed of two pairs of sensors using different polymer coatings after calibration. The results showed the feasibility of distinguishing the mixing ratios of mixtures using a significantly simpler method and a lower number of polymer coatings.

# Contents

<b>Notations</b>	v
<b>List of Figures</b>	viii
<b>Chapter 1: Introduction</b>	1
1.1 Significance of an Electronic Nose	1
1.2 Electronic Nose Technology	2
1.2.1 Brief History of Electronic Nose	2
1.2.2 Technical Approaches	3
1.2.2.1 Metal Oxide Sensors and MOSFETs	3
1.2.2.2 Piezoelectric-Based Sensors Including the QCM and SAW	4
1.2.2.3 Conductivity-Based Sensors	5
1.2.2.4 Optical and Spectroscopic Sensors	6
1.2.2.5 Multi-Property Sensors	7
1.2.3 Available Electronic Nose Instruments	8
1.3 Conducting Polymer Technology	8
1.4 Research Objectives	13
1.5 Thesis Outline	14
<b>Chapter 2: Establishing A QCM - Interdigitated Electrode Odour Measurement System</b>	15
2.0 Introduction	15
2.1 Materials	16
2.2 Methods	17
2.2.1 Design of Resistive Measurement Instrumentation	17

2.2.2 Design of QCM Measurement Instrumentation	17
2.2.3 Configuration of Flow System and FT-iR Spectroscopy Measurement	19
2.2.4 Microfabrication of Interdigitated Electrodes and QCM Sensors	21
2.2.4.1 Protocol of Microfabrication	21
2.2.4.2 Design and Fabrication of Interdigitated Electrodes	24
2.2.4.3 QCM Electrodes	24
2.2.4.4 Polymerisation of Conducting Polymer Films on Interdigitated Electrodes	26
2.2.4.5 Polymerisation of Conducting Polymer Films on QCM Electrodes	28
2.2.4.6 Quality Control of Polymers	29
2.2.5 Measurement of Vapours at Interdigitated Electrode and QCM Sensors	31
2.2.5.1 Control of Flow Rate	31
2.2.5.2 Recovery of Sensors	31
2.2.5.3 Control of Humidity	32
2.2.5.4 Mixing of Gases	32
2.2.5.5 Determination of Sensors Dynamic Range	33
2.2.5.6 Sensors Response Stability with Respect to Time	33
2.3 Results and Discussion	34
2.3.1 Microfabrication and Quality Control of Sensors	34
2.3.1.1 Deposition of Polymer on Square Electrodes	34
2.3.1.2 Deposition of Polymer on Interdigitated Electrodes	42
2.3.1.3 Deposition of Polymer on QCM Electrodes	48
2.3.1.4 Baseline Resistance Stability with Time	51
2.3.2 Measurement of Vapours with Interdigitated Electrodes and QCMs	55
2.3.2.1 Effect of Flow Rate and Use of FT-iR	55
2.3.2.2 Optimisation of Recovery	55
2.3.2.3 Effect of Humidity	60
2.3.2.4 Mixing of Gases	61
2.3.2.5 Dynamic Range Measurement	65
2.3.2.6 Effect of Film Thickness on Sensitivity of Response	70
2.3.2.7 Fabrication Reproducibility	75
2.3.2.8 Response Stability with Time	75
2.4 Conclusions	79

<b>Chapter 3: Detection Mechanisms of Polymer-Based Sensors</b>	<b>81</b>
3.0 Introduction	81
3.1 Thermodynamics of Adsorption and Polymer Sorption	83
3.1.1 Thermodynamics of Adsorption: Adsorption Isotherms	83
3.1.2 Absorption and Gas Sorption in Polymer Films	85
3.1.3 Langmuir and Freundlich Adsorption Isotherms	87
3.2 Detection Mechanisms of Polymer-Based Sensors	90
3.2.1 Piezoelectric-Based Sensors	90
3.2.1 Resistive-Based Sensors	92
3.2.3 Hybrid Systems	93
3.3 Results and Discussion	95
3.3.1 Piezoelectric-Based Sensors	95
3.3.2 Resistive-Based Sensors	98
3.3.3 Hybrid Systems	100
3.4 Odour Mapping	109
3.5 Conclusions	114
<b>Chapter 4: Studies on the Mechanisms of Vapour-Polymer Interaction</b>	<b>115</b>
4.0 Introduction	115
4.1 Charge Transport in PPy and Possible Effects Contributing to the Gas Sensitivity	117
4.2 Relevant Solubility Interactions to the Sorption of Vapours by Organic Materials	119
4.3 Linear Solvation Energy Relationships (LSERs)	122
4.3.1 Linear Solvation Energy Relationships (LSERs)	122
4.3.2 Sample Set Chosen	124
4.4 $S_{rf}MW$ — An Introduced Solubility Property	125
4.5 Results and Discussion	126
4.5.1 Experimental Strategy	126
4.5.2 Effect of Vapour Characters on Vapour-Polymer Interactions	127

4.5.3 Effect of Incorporated Counterions on Vapour-Polymer Interactions	131
4.5.4 Effect of Backbone Monomers on Vapour-Polymer Interactions	142
4.6 Conclusions	147
<b>Chapter 5: Multi-Component Analysis Using QCM-Interdigitated Electrode Hybrid Sensor Pairs</b>	<b>149</b>
5.0 Introduction	149
5.1 QCM-Interdigitated Electrode Hybrid System in Multi-Component Analysis	150
5.2 Results and Discussion	157
5.2.1 Sample Sets Chosen	157
5.2.2 Concentration Independence of Sensor Pair to Vapour Mixtures	156
5.2.3 Two-Component Vapour Mixtures	159
5.2.4 Three-Component Vapour Mixtures	166
5.2.5 Odour Mapping in Multi-Component Vapour Analysis	168
5.3 Conclusions	174
<b>Chapter 6: Conclusions and Future Work</b>	<b>175</b>
6.1 Conclusions	175
6.2 Future Work	178
<b>References</b>	<b>xiv</b>
<b>Appendix: Interdigitated Electrode Sensor Baseline Resistance Stability with Time</b>	<b>xxvii</b>

## Notations

A	Combined output of a sensor pair for the first component of a mixture
a	Solvent property constant
$a_a$	Chemical activity of the adsorbed analyte
$a\alpha_2^H$	Vapour-polymer interaction hydrogen-bond acidity term
B	Combined output of a sensor pair for the second component of a mixture
b	Solvent property constant
$b\beta_2^H$	Vapour-polymer interaction hydrogen-bond base term
C, $C_a$	Vapour concentration
$C_s$	Vapour concentration in the sorbate coatings at equilibrium
$C_1$	Vapour concentration of first vapour component
$C_2$	Vapour concentration of second vapour component
$f_c$	Frequency change due to a mass of a polymer coating (Hz)
$\Delta f$	Frequency change due to absorption of a mass of vapour (Hz)
$\Delta f_1$	Frequency change due to absorption of a mass of first component of a mixture (Hz)
$\Delta f_2$	Frequency change due to absorption of a mass of second component of a mixture (Hz)
$\Delta G_a$	Gibb's free energy associated with adsorption
K	Partition coefficient
$K_a$	Equilibrium coefficient for adsorption
$K_1$	Partition coefficient of first component
$K_2$	Partition coefficient of second component
$k_1, k_2$	Constants
$k_F$	Constant
$k', k''$	Geometric constants for the polymer coated interdigitated electrode
l	Solvent property constant
$l \log L^{16}$	Vapour-polymer interaction dispersion term
$\log L^{16}$	Solute parameter representing dispersion

MW	Vapour molecular weight
$\Delta m$	Absorption mass of vapour
$\Delta m'$	Mass change of coating on interdigitated electrode by absorption of vapour
$m_{ML}$	Mass of adsorbate per unit area at monolayer coverage
$m_a$	Mass of adsorbate per unit area
$m_c$	Mass of polymer coating
$m_c'$	Mass of coating material on interdigitated electrode
$m_s$	Mass of analyte sorbed into the polymer
$N_{abs}$	Number of absorbed molecules
$n'$	Constant
$n_F$	Constant
$n_1, n_2$	Constants
$p$	Partial pressure
$R$	Ideal gas constant
$\Delta R$	Change of resistance of an interdigitated electrode
$R_0$	Initial resistance of an interdigitated electrode
$\Delta R_1$	Change of resistance of an interdigitated electrode by first component of a mixture
$R_2$	Solute parameter representing polarizability
$\Delta R_2$	Change of resistance of an interdigitated electrode caused by second component of a mixture
$r$	Solvent property constant
$rR_2$	Vapour-polymer interaction polarizability term
$S$	Gas-polymer interaction sensitivity coefficient
SP	Solubility property under investigation
$SP_0$	Constant
$S_f$	Relative frequency change
$S_r$	Relative resistance change
$S_{rf}$	Ratio of $S_r$ and $S_f$ , combined sensor's response
$s$	Solvent property constant
$s\pi_2^H$	Vapour-polymer interaction polarity term
$u$	Atomic mass unit
$V_s$	Polymer coating volume

$\alpha$	Ratio of $k_1$ to $k_2$
$\alpha_2^H$	Solute parameter representing solute hydrogen-bond basicity
$\beta_2^H$	Solute parameter representing solute hydrogen-bond acidity
$\pi_2^H$	Solute parameter representing dipolarity-polarizability
$\rho$	Density of the polymer coating
$\Delta\rho$	Conducting polymer resistivity change
$\rho_0$	Initial resistivity

### Electrolytes & Polymers

SDSO <sub>4</sub> Na	Dodecyl sulfate sodium salt
DecSO <sub>3</sub> Na	1-decanesulphonic acid sodium salt
HexSO <sub>3</sub> Na	1-hexanesulphonic acid sodium salt
ButSO <sub>3</sub> Na	1-butanesulphonic acid sodium salt
EtSO <sub>3</sub> Na	1-ethanesulphonic acid sodium salt
CF <sub>3</sub> SO <sub>3</sub> Li	Lithium trifluoromethanesulphonate
TEAC <sub>8</sub> F <sub>17</sub> SO <sub>3</sub>	Perfluoro-1-octanesulphonic acid tetraethylammonium salt
KCl	Potassium chloride
TEAT <sub>08</sub>	Tetraethylammonium p-toluenesulphonate
TEAClO <sub>4</sub>	Tetraethylammonium perchlorate
TEAPF <sub>6</sub>	Tetraethylammonium hexafluorophosphate
TEABF <sub>4</sub>	Tetraethylammonium tetrafluoroborate
PPy	Polypyrrole
Py	Pyrrole
$\phi$ Py	N-phenyl pyrrole

## List of Figures

- Figure 1.1 The structure of doped polypyrrole.
- Figure 2.1 A block schematic of the hybrid nose electronic system.
- Figure 2.2 Configuration of a flow system which generates simple or mixed samples.
- Figure 2.3 Complete schematic diagram of the hybrid electronic nose system.
- Figure 2.4 Protocol for microelectrode fabrication.
- Figure 2.5 Plan view and cross section of an interdigitated electrode.
- Figure 2.6 Plan view of a square electrode (4mm×4mm) for polymerisation study.
- Figure 2.7 Diagram of QCM electrode used in this study.
- Figure 2.8 Electrochemical cell configuration and electrodes used for polymerisation in this study.
- Figure 2.9 Shows a typical polymerisation process of DecSO<sub>3</sub><sup>-</sup>/PPy film using a square electrode (area = 16 mm<sup>2</sup>), demonstrating the relationship between polymerisation current (mA) and the time (seconds) during the application of a step potential (0.8 V).
- Figure 2.10 Demonstrates the method for electric charge (Q) calculation by integrating the current passed during the electrochemical polymerisation with time.
- Figure 2.11 Shows the relationship between polymerisation charge (Q) passed at the electrode and the polymerisation time for a DecSO<sub>3</sub><sup>-</sup>/PPy film on a square electrode with an active area of 16 mm<sup>2</sup>.
- Figure 2.12 Plot of DecSO<sub>3</sub><sup>-</sup>/PPy polymer film thickness on a square electrode (area = 16 mm<sup>2</sup>) as measured by Dektak.
- Figure 2.13 DecSO<sub>3</sub><sup>-</sup>/PPy polymer film thickness on separate square electrodes (area = 16 mm<sup>2</sup>) versus polymerisation time.
- Figure 2.14 Scanning electron micrographs of polypyrrole films of DecSO<sub>3</sub><sup>-</sup>/PPy at different thicknesses at 10 kV electron beam.
- Figure 2.15 Shows a typical polymerisation process of C<sub>8</sub>F<sub>17</sub>SO<sub>3</sub><sup>-</sup>/PPy film using an interdigitated electrode, demonstrating the relationship between

polymerisation current ( $\mu\text{A}$ ) and the time (seconds) during the application of a step potential (0.8 V). The gap was bridged after about 40 s.

- Figure 2.16 Electric charge (Q) passed versus polymerisation time of  $\text{DecSO}_3^-/\text{PPy}$  film on interdigitated electrodes (gap = 10  $\mu\text{m}$ ).
- Figure 2.17 Plot of initial resistance value (as the natural logarithm) versus electric charge (Q) passed during the polymerisation of  $\text{DecSO}_3^-/\text{PPy}$  film on interdigitated electrodes (gap = 10  $\mu\text{m}$ ). Inserted picture shows a linear relationship between  $\text{Ln } R$  and  $Q^{-1}$ .
- Figure 2.18  $\text{DecSO}_3^-/\text{PPy}$  polymer film thickness on interdigitated electrode.
- Figure 2.19 Shows the result of the fabrication consistency of a small batch of ten interdigitated electrode sensors by showing the initial resistance values versus number of sensors successively made.
- Figure 2.20 Shows a typical polymerisation process of  $\text{C}_8\text{F}_{17}\text{SO}_3^-/\text{PPy}$  film on a QCM electrode, indicating the relationship between polymerisation current and the time a step potential applied.
- Figure 2.21 Interdigitated electrode sensor baseline resistance stability with time. Sensors were coated with polypyrrole films containing different types of counterions.
- Figure 2.22 FT-iR absorption spectra of methanol vapour diluted at different levels by pure nitrogen.
- Figure 2.23 Plot of FT-iR absorption peak intensity versus relative methanol concentration, calculated by the flow rates of the corresponding flow meters.
- Figure 2.24 Shows the relative vapour concentration calibration curve for the flow system, obtained using FT-iR calibrated concentration versus calculated concentration by flow rates.
- Figure 2.25 A typical measurement cycle to 50% methanol vapour and effect of water vapour purging on the recovery of sensor baseline resistance.
- Figure 2.26 FT-iR spectra for a methanol and ethanol mixture at wave number from 3500 to 4000  $\text{cm}^{-1}$  showing the absorption by  $-\text{OH}$  stretch.
- Figure 2.27 FT-iR absorption spectra for methanol and ethanol mixtures at different vibrations.

- Figure 2.28 A plot of vapour pressure (mm Hg) versus temperature (°C) for methanol and ethanol.
- Figure 2.29 A plot of vapour pressure (mm Hg) versus temperature (°C) for decyl alcohol.
- Figure 2.30 QCM sensors dynamic range of low concentration detection limit to 3 ppm decanol and high concentration detection limit to  $10^5$  ppm methanol.
- Figure 2.31 Interdigitated electrode sensors dynamic range of low concentration detection limit to 3 ppm decanol and high concentration detection limit to  $10^5$  ppm methanol.
- Figure 2.32 Interdigitated electrode sensors showing the lower concentration detection limit of 1.5 ppm decanol. Sensors were coated with  $\text{DecSO}_3^-/\text{PPy}$  films and varied in initial resistance from  $36\Omega$  to  $440\Omega$ .
- Figure 2.33 A typical measurement cycle for 50% methanol on a set of interdigitated electrode sensors with  $\text{DecSO}_3^-/\text{PPy}$  films, varying in thickness.
- Figure 2.34 Sensitivities to methanol at different relative concentrations from a set of interdigitated electrode sensors covered by  $\text{SDSO}_4^-/\text{PPy}$  films and varied in thickness.
- Figure 2.35 Sensitivities to a series of alcohols from a set of interdigitated electrode sensors covered with  $\text{Cl}^-/\text{PPy}$  film and varied in film thickness.
- Figure 2.36 Shows the result of a typical measurement cycle for 50% methanol from a set of interdigitated electrode sensors with  $\text{DecSO}_3^-/\text{PPy}$  films and with similar initial resistances. Inserted plot shows normalised response curves demonstrating the consistency in response speed.
- Figure 2.37 Figures (a) to (c) shows the baseline resistance value, the values of relative frequency change  $S_f$ , relative resistance change  $S_r$  and combined sensors response  $S_{rf}$  to 50% methanol during a period of 45 days on three sensor pairs.
- Figure 2.38 Comparison of the baseline resistance drift during a period of time from a set of interdigitated electrode sensors.
- Figure 3.1 A selection of typical sorption isotherms representing different polymer sorption models.

- Figure 3.2 Illustration of the distribution of analyte between ambient phase and the absorbed phase (in polymer coating) on the QCM electrode.  $C_a$  is ambient phase concentration and  $C_s$  is absorbed phase concentration.
- Figure 3.3 Illustration of the distribution of analyte between ambient phase and the absorbed phase into polymer coating on interdigitated electrode.
- Figure 3.4 A plot of the QCM resonant frequency change in Hz versus normalised methanol concentration for a HexSO<sub>3</sub><sup>-</sup>/PPy polymer coating. The solid line represents the best fit line to Freundlich isotherm equation, determined using linear regression.
- Figure 3.5 A plot of the QCM resonant frequency change in Hz versus normalised methanol concentration for a HexSO<sub>3</sub><sup>-</sup>/PPy polymer coating of different film thicknesses. (a) the best fit to the Freundlich isotherm equation, determined using linear regression; and (b) the best fit to the Langmuir isotherm equation, determined using linear regression.
- Figure 3.6 A plot of the relative resistance change,  $S_r$ , versus normalised methanol concentration for a SDSO<sub>4</sub><sup>-</sup>/PPy polymer coating at different initial resistance ( $R_0$ ) values measured using interdigitated electrodes. The solid lines are the best fit line to the Freundlich isotherm equation, determined using linear regression.
- Figure 3.7 Plots of  $S_f$  (□),  $S_r$  (◆) and  $S_{rf}$  (▲) versus methanol concentration for a DecSO<sub>3</sub><sup>-</sup>/PPy polymer sensor pair. The curved lines represent the best fit to the Freundlich isotherm equation. The straight line through the points representing  $S_{rf}$  is the average of the  $S_{rf}$  values.
- Figure 3.8 A plot showing the long term stability of  $S_f$  (□),  $S_r$  (◆) and  $S_{rf}$  (▲) for methanol for a DecSO<sub>3</sub><sup>-</sup>/PPy sensor pair over a period of 45 days.
- Figure 3.9 A plot of  $S_{rf}$  versus molecular weight for a series of vapours for (a) a DecSO<sub>3</sub><sup>-</sup>/PPy sensor pair; (b) a SDSO<sub>4</sub><sup>-</sup>/PPy sensor pair; (c) a CF<sub>3</sub>SO<sub>3</sub><sup>-</sup>/PPy sensor pair; and (d) a Tos<sup>-</sup>/PPy sensor pair. The error-bars represent the variation of  $S_{rf}$  in three measurements, at three different vapour concentrations (9%, 25% and 60% of the S.V.P.).
- Figure 3.10 A plot of curve demonstrating an inverse proportionality.
- Figure 3.11  $S_{rf}$  value multiplied by molecular weight ( $S_{rf}MW$ ) versus molecular weight (MW) for a series of vapours for (a) a DecSO<sub>3</sub><sup>-</sup>/PPy sensor pair; (b) a

SDSO<sub>4</sub><sup>-</sup>/PPy sensor pair; (c) a CF<sub>3</sub>SO<sub>3</sub><sup>-</sup>/PPy sensor pair; and (d) a Tos<sup>-</sup>/PPy sensor pair.

Figure 3.12 A two-dimensional odour map for a series of vapours using S<sub>rf</sub> values from (a) DecSO<sub>3</sub><sup>-</sup>/PPy and Tos<sup>-</sup>/PPy sensor pairs; (b) CF<sub>3</sub>SO<sub>3</sub><sup>-</sup>/PPy and SDSO<sub>4</sub><sup>-</sup>/PPy sensor pairs; (c) CF<sub>3</sub>SO<sub>3</sub><sup>-</sup>/PPy and DecSO<sub>3</sub><sup>-</sup>/PPy sensor pairs; and (d) DecSO<sub>3</sub><sup>-</sup>/PPy and SDSO<sub>4</sub><sup>-</sup>/PPy sensor pairs.

Figure 3.13 A group of polar odour maps showing a series odorants: (a) normalised S<sub>rf</sub> value for PPy decanesulphonate film; (b) normalised S<sub>rf</sub> value for PPy dodecylsulphate film; (c) normalised S<sub>rf</sub> value for PPy trifluoromethane sulphonate film; and (d) normalised S<sub>rf</sub> value for PPy toluenesulphonate film.

Figure 4.1 Illustration of possible mechanisms of the gas sensitivity of conducting polymer microresistors.

Figure 4.2 Graphic illustration of the possible physisorption intermolecular interactions.

Figure 4.3 Plots showing (a) S<sub>rf</sub>MW; and (b) relative changes in responses of S<sub>rf</sub>MW as a consequence of methanol and deuterated methanols for DecSO<sub>3</sub><sup>-</sup>/PPy sensor pairs.

Figure 4.4 Plots showing (a) S<sub>rf</sub>MW; and (b) relative changes in responses of S<sub>rf</sub>MW as a consequence of methanol and deuterated methanols for SDSO<sub>4</sub><sup>-</sup>/PPy sensor pairs.

Figure 4.5 Experimental and LSERs (linear solvation energy relationships) regression results for different polypyrrole films.

Figure 4.6 LSERs (linear solvation energy relationships) regression results versus experimental S<sub>rf</sub>MW values for different polypyrrole films.

Figure 4.7 Interaction of contributing terms to the S<sub>rf</sub>MW response for a family of alcohols for different polypyrrole films.

Figure 4.8 S<sub>r</sub> against time of measurement for different polymer coatings for: (a) triethylamine (20% svp); and (b) n-hexane (50% svp).

Figure 4.9 Experimental and LSERs (linear solvation energy relationships) regression results for polypyrrole and copolymer films.

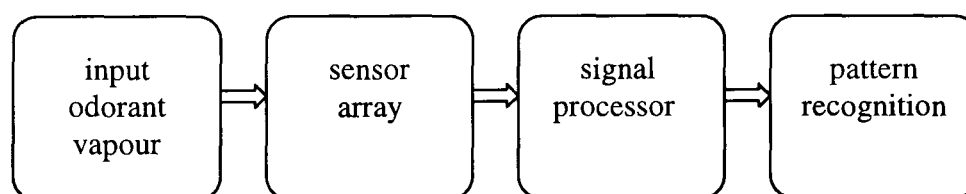
- Figure 4.10 LSERs (linear solvation energy relationships) regression results versus experimental  $S_{rf}MW$  values for polypyrrole and copolymer films.
- Figure 4.11 Polymer hydrogen-bonding acidity contribution to the overall response for  $S_{rf}MW$  against a set of vapour molecules for polypyrrole and copolymer films.
- Figure 5.1 Illustration of normalized  $S_{rf}$  as a function of mixing ratio of two gaseous components, varying with different values of  $\alpha$ .
- Figure 5.2 Plot of  $S_{rf}$  versus concentration ratio of iso-propanol in iso-propanol/water mixtures for a DecSO<sub>3</sub><sup>-</sup>/PPy sensor pair.
- Figure 5.3 Plot of  $S_{rf}$  versus concentration ratio of methanol in methanol/ethanol mixtures for: (a) a DecSO<sub>3</sub><sup>-</sup>/PPy sensor pair; (b) a CF<sub>3</sub>SO<sub>3</sub><sup>-</sup>/PPy sensor pair; and (c) a Tos<sup>-</sup>/PPy sensor pair.
- Figure 5.4 Plot of  $S_{rf}$  versus concentration ratio of methanol in methanol/water mixtures for: (a) a DecSO<sub>3</sub><sup>-</sup>/PPy sensor pair; (b) a CF<sub>3</sub>SO<sub>3</sub><sup>-</sup>/PPy sensor pair; and (c) a Tos<sup>-</sup>/PPy sensor pair.
- Figure 5.5 Plot of  $S_{rf}$  versus concentration ratio of ethanol in ethanol/water mixtures for: (a) a DecSO<sub>3</sub><sup>-</sup>/PPy sensor pair; (b) a CF<sub>3</sub>SO<sub>3</sub><sup>-</sup>/PPy sensor pair; and (c) a Tos<sup>-</sup>/PPy sensor pair.
- Figure 5.6 Plot of  $S_{rf}$  versus ratio of methanol (in volume) in ethanol/water (1:1 v/v) mixtures for: (a) a DecSO<sub>3</sub><sup>-</sup>/PPy sensor pair; (b) a CF<sub>3</sub>SO<sub>3</sub><sup>-</sup>/PPy sensor pair; and (c) a Tos<sup>-</sup>/PPy sensor pair.
- Figure 5.7 Plot showing a two-dimensional odour maps for a series of vapour mixtures based on  $S_{rf}$  values from a CF<sub>3</sub>SO<sub>3</sub><sup>-</sup>/PPy sensor pair and a Tos<sup>-</sup>/PPy sensor pair: (a) methanol/ethanol mixtures; (b) methanol/water mixtures; (c) ethanol/water mixtures; and (d) methanol/ethanol/water mixtures.
- Figure 5.8 Plot showing a two-dimensional odour map for vapour mixtures of two and three components based on  $S_{rf}$  values from a CF<sub>3</sub>SO<sub>3</sub><sup>-</sup>/PPy sensor pair and a Tos<sup>-</sup>/PPy sensor pair.

## Introduction

### 1.1 SIGNIFICANCE OF AN ELECTRONIC NOSE

For many decades, scientists have recognised the power of incorporating biological principles into the design of sensors or sensory systems. One example of this approach is the development of the *Electronic Nose*.

An *Electronic Nose* is an instrument, which comprises an array of electronic chemical sensors with partial specificity and an appropriate pattern-recognition system, capable of recognising simple or complex odours [1]. The four main functional components consisting the *Electronic Nose* system are as follows: (i) a sample handler for odour vapour input; (ii) an array of sensors; (iii) a signal processing system; and (iv) a system for pattern recognition. Generally these operate serially on an odourant sample, and can be represented by a schematic diagram as follows:



The output of the *Electronic Nose* may be the identity of the odourant, an estimate of the concentration of the odourant, or indeed some measure of the characteristic properties of the odour, as might be perceived by a human.

The potential applications for *Electronic Nose* instruments span a wide range of areas, from industrial process monitoring to medical diagnosis via breath analysis [2-4], and are likely to extend beyond the gas phase to liquid phase measurements [5]. For

example, this technology can undertake continuous real-time monitoring in the food industry, including tasks such as detecting product freshness, or controlling the brewing process of whisky (wine or beer, where products and processes critically depend on their smell). Such an electronic device may also circumvent many other problems associated with the use of human panels to overcome the individual variability, fatigue, infections and mental state. The *Electronic Nose* can also be used to monitor odour at specific sites, such as long-term pollution in hazardous environments. The ever increasing potential applications have made the *Electronic Nose* technology a fast growing field for research, and commercial exploitation.

## **1.2 ELECTRONIC NOSE TECHNOLOGY**

### **1.2.1 Brief History of Electronic Nose**

The earliest work on the development of an instrument which could detect odours dated back to the 1960's, when pioneering works in the chromatography enabled the detection of odourants [6-8]. Such instruments for smell measurement generally involved an adsorption process of the odorant material on a sensitive sensor surface. For example, Moncrieff demonstrated an instrument for measuring and classifying odours using a polymer film coated thermistor in 1960 [6].

However, it was not until the 1980's, that the concept of an *Electronic Nose* as an "intelligent" chemical array sensor system for odour classification emerged [9]. In 1982, Persaud and Dodd suggested that to make sensitive discriminations between complex odorant mixtures containing varying ratios of odorants, without the need for highly specialized peripheral receptors, the olfactory system made use of "feature detection" using broadly tuned receptor cells organized in a neuron pathways. Based on this principle, a simple electronic model was constructed based upon chemo-resistive conductimetric sensors, which could reproducibly discriminate between a wide variety of odours. Since then, increasing amount of research using different technologies has been published on *Electronic Noses* based on the idea of using arrays of cross-reactive (non-

specific) chemical sensors coupled to various pattern-recognition programs, analogous to the biological olfactory system, in which semi-selective olfactory receptors are combined with high-order neural processing [10-17]. Dodd, Shurmer and Barker got the first UK grant in 1983 (known as *Warwick Nose*). A first generation *Electronic Nose* was launched commercially by Neotronics in London in 1994 [18], using an array of 12 conducting polymer coated microresistors. So far, there are at least three different types of commercial noses using different technologies, including the use of conducting polymer sensor arrays [19, 20], metal oxide sensor arrays [21] and acoustic wave sensor arrays [3]. There are several hundred commercial *Electronic Nose* instruments currently in use throughout the world and, although nearly all of these are bench-top, laboratory-scale instruments, a number of second-generation instruments that are smaller, faster and more sensitive are beginning to evolve.

## 1.2.2 Technical Approaches

Various physical and chemical phenomena have been employed to generate so called “cross-reactive” sensors for use in array-based odour sensing [10]. In all cases, the goal has been to create an array of differentially-sensitive sensing elements. Each of which responds in a different manner to an odour or a mixture of odours. The technical approaches, including sensors and sensing materials are summarised below.

### 1.2.2.1 Metal oxide sensors and MOSFETs

Metal oxide semiconductors can be used as sensors by observing the electrical-resistance changes that occur when vapours are absorbed onto a semiconductor surface [22-29]. Sensors, such as the Figaro, Taguchi and Nemoto gas sensors, are typically prepared by depositing a thin porous film of a metal oxide material such as tin oxide onto an electrically-heated ceramic pellet and annealing at high temperatures. The advantage of these devices are their good sensitivity, particularly for polar analytes, as well as their “manufacturability”. They are typically run at elevated temperatures up to 400°C and hence relatively high power levels are needed (which is considered to be one of the primary drawbacks of these sensor systems). The metal oxide sensor array is one of the

commonly used type of sensors in the commercial *Electronic Nose* instruments, such as that made by Alpha-Fox.

Metal oxide silicon field effect transistor (MOSFET) sensors are based on the principle that organic vapours in contact with a catalytic metal, such as platinum, palladium, iridium, or some organic materials can produce a reaction [30-32]. The products from the reactions can diffuse through the gate of a MOSFET to change the electrical properties, such as gate potential or source-drain current of the device. The advantage of MOSFETs is that they can be made with integrated circuit fabrication process, so that batch-to-batch variations can be minimised. The disadvantages are baseline drift and encapsulation of the electrical connections.

#### *1.2.2.2 Piezoelectric-based sensors including the QCM and SAW*

The use of piezoelectric-based sensor quartz-crystal microbalance (QCM) as transducers for chemical analysis was first suggested by Sauerbrey in 1959 [33] and demonstrated by King in 1964 [34]. This approach utilises the frequency resonance of a piezoelectric material, such as single crystal quartz, when an acoustic waves passes through it. A sensing film coating is applied to the crystal's surface, to enable the absorption of gas molecules, which in turn, induces a shift in the oscillation frequency that is directly related to the mass of the adsorbed compounds [35-38].

Alternatively, the surface acoustic wave (SAW) device utilises waves produced along the surface of a crystal by the electric field of surface deposited metal electrodes. Each SAW sensor incorporates four interdigitated electrodes to serve as input and output transducers for a sensing and reference pair. There is also an active membrane in between the working electrodes on the same piezoelectric substrate. An ac signal applied across the input electrode creates an acoustic Raleigh wave that “surfs” over the substrate (analogous to a shock wave during an earth-quake). When the wave reaches the output electrode, the ac voltage is shifted in phase as a result of the distance travelled as well as the mass and the absorption properties of a sensing layer deposited between the electrodes [39, 40].

These MOSFETs and piezoelectric sensors are two main devices used in the commercial *Electronic Nose* at present. The low detection limit (to ppb) and the large number of available coatings (including those developed for gas chromatograph (GC) column materials [41-45] as well as conducting polymers [46-48] ) provide the main advantages of *Electronic Noses* made using piezoelectric sensors. Indeed, coating materials can be synthesised or tailored for different sensing purposes. The drawbacks to this methods are batch-to-batch reproducibility and the difficulty of replacing sensors.

QCMs coated with conducting polymer sensing materials are one of the types of sensors used in this study, as they can provide information about both the mass and number of molecules absorbed (which is important in vapour detection and in understanding mechanisms of vapour-polymer interactions).

### 1.2.2.3 Conductivity-based sensors

A third type of sensor uses conducting polymers such as polypyrrole and its derivatives as a resistive devices. The transducer is usually a microfabricated interdigitated electrode with an electrochemically polymerised conducting polymer sensing film deposited over it. Such a sensor array is also commonly used in a number of commercial *Electronic Nose* systems [49-57]. The use of conducting polymers started in 1979, when Diaz and co-workers first successfully made a free-standing thin film of polypyrrole electrochemically from aqueous solution [58]. Since then, much attention has been given to the study of these materials and their unique properties. Importantly, the polymers can be modified by incorporating different counterions during film deposition or by attaching functional groups to the polymer backbone.

Polypyrrole was first used as a vapour detector based on resistance change property by Persaud and Travers in 1985 [59]. The authors observed that a reversible adsorption of molecules to the film induced a reversible, rapid change in the electrical resistance. The sensors show a number of important properties, including good mechanical strength and electrical stability over a period of several months, an absence of poisoning by any gases or odorants tested, and reproducible responses to a broad but

overlapping range of compounds. Since then, there have been an increasing interest in using this material for electronic nose fabrication because of its versatility in composition and broad sensitivity towards organic vapours. There is also the additional advantage of being able to operate at room temperature [21, 22, 60-64]. The device (usually an interdigitated electrode) can be miniaturised using photolithography technology. The main shortcomings of the technology are both the time and temperature dependent drift, the batch-to-batch reproducibility, and the sensitivity to changes in humidity.

Besides polypyrrole and its derivatives, there are many other types of materials which can be used in conductivity sensing, e.g., lipid materials [65-69]. Recently, another new approach has been developed which is referred to as polymer conductive composites. Lewis et al. have used a single conducting material carbon-black powder incorporated into various polymers and printed across the interdigitated electrode [70, 71]. Upon exposure to a particular vapour, each polymer layer undergoes a characteristic swelling, drawing the conducting particles away from one another and thus increasing the measured resistance. Low cost and ease of fabrication are the main advantages of this method. Importantly, a wide range of different polymers can be used in this application.

#### *1.2.2.4 Optical and spectroscopic sensors*

Previously, sensors have also been developed which utilise optical fibres [72] with a thin chemically active material coating, either on their sides or ends, comprising a fluorescent dye immobilised in different organic polymers. A light source, at a single frequency is used to interrogate the active material, which in turn responds to the presence of the vapour to be detected with a change in wavelength. Such sensors give a fast response and can be miniaturised. However, their lifetime is presently limited by photo-bleaching of the fluorescent dye. Optical measurement also require the use of relatively sophisticated instruments, including lasers, photo-multiple-tubes, and filters, although these are becoming cheaper.

Other approaches based on impedance spectroscopy [73], surface plasmon resonance [74], and ellipsometry [75] have also been developed for organic vapour

detection. However, like optical measurement system, these methods need the use of specialised instrumentation (which is both expensive and difficult to miniaturise), and these are largely considered as “research” devices at present.

#### *1.2.2.5 Multi-property sensors*

Recently the approach of combining different sensor types has been shown characteristics that differ from those of the commonly used single property measurement system. This method combines different sensor technologies into hybrid systems which can provide multi property information after exposure to odorants. These methods have shown particular characteristics other than the commonly used single-property measurement system, including, for example concentration independence [76, 77]. Multi-property measurement systems can be formed using the same type of sensors with different geometries [78-80] and properties [81, 82] or two different types of devices. For example, a SAW device combined with a chemoresistor [39, 40], or a QCM device with an interdigitated electrode [83-87]. Slater and co-workers examined the vapour-polypyrrole interaction by the combination of piezoelectric and conductivity measurements and found analogies in the two sensing mechanisms which can be interpreted in terms of the gas adsorption by the polymer coating. They also studied the swelling of polymers and concluded that the response mechanism of polypyrrole sensing of different gases and vapours is due to a mixed response involving both electronic effects and physical effects [83, 84]. Combined sensors can either be made separately or can be integrated [85, 86]. Yamashita et al. observed that molecular species such as acetone, methanol and ethanol can be recognised by the ratio of resistance change to frequency change on a polypyrrole film and used this combined sensor to clarify the interactions between polymer and vapour molecules by corresponding work function studies of each film.

In the study presented in this thesis, the basic concept of a hybrid measurement system is further developed and optimised based upon detailed studies of the response mechanisms of each of the two types of sensors. The nature and condition of the sensor pairs' concentration independence is explored and hybrid system device modelling is

established. In addition, the application of a hybrid system to vapour identification is achieved where the use of multiple sensor pairs coated with different types of coatings is proven necessary. It is demonstrated that the combination of different types of devices can be realised on a QCM and a separate interdigitated electrode, both coated with the same conducting polymer film without the necessity of device integration. Importantly, such sensor pairs can be used to study the vapour-conducting polymer response mechanisms for different polymer coatings and detailed molecular interaction contribution terms can be evaluated. This hybrid system shows characteristics not available in single property measurement systems, e.g. concentration independence, an increased discrimination ability towards odorants, and a usefulness in the study of vapour-polymer interaction mechanisms.

### **1.2.3 Available Electronic Nose Instruments**

There are several hundred commercial *Electronic Nose* instruments currently in use throughout the world produced by about a dozen different companies. For example, Neutronic nose (UK) uses 12 conducting polymer resistors, AromaScan Nose (UK, Crewe) and Bloodhound nose (UK, Leeds) use 32 conducting polymer resistors, Fox 4000 (France, Alpha MOS) uses 18 MOS sensors, Olfactometer (Germany, Lennartz) uses 6 QCM sensors, and Cyrano Nose (USA, California) uses 32 carbon-black polymer composites sensors. This list is not all-inclusive, as this is such an important area of technology that new companies are “starting-up” at a high rate.

## **1.3 CONDUCTING POLYMER TECHNOLOGY**

The conducting polymers used in this work are polypyrrole and its N-functional derivatives incorporated with different counterions. Polypyrrole is a conducting polymer with conductivity between  $10^{-3}$  to  $100 \text{ S cm}^{-1}$  [88] (depending upon its polymerisation and measurement conditions). It can be prepared by either chemical or electrochemical oxidation in a suitable electrolytic solution onto gold, carbon or platinum electrodes. One

of the advantages of the electrochemical method of deposition is that the growth rate and film thickness are easily controlled by the polymerisation current over the growth period. The polymerisation reaction is initiated by the electrochemical generation of monomer radicals which combine with other units in solution to form the polymer chains [89]. The oxidation potential of polypyrrole is lower than that of the monomer, and thus the polymer is simultaneously oxidised during the polymerisation. Consequently, counterions from the electrolyte are incorporated into the growing polymer in order to maintain electrical neutrality, such that the level of the counterions incorporation reflects the extent of oxidation of pyrrole units. Typically, polypyrrole contains between 20 to 40 mol% of counterions, which means ca. 3 to 5 pyrrole rings carry a positive charge delocalised over the pyrrole units. The structure of doped polypyrrole is shown in Figure 1.1. The films have an amorphous and insoluble nature with a flotation density value between 1.37 to 1.58  $\text{gcm}^{-3}$  depending on the counterions present [90].

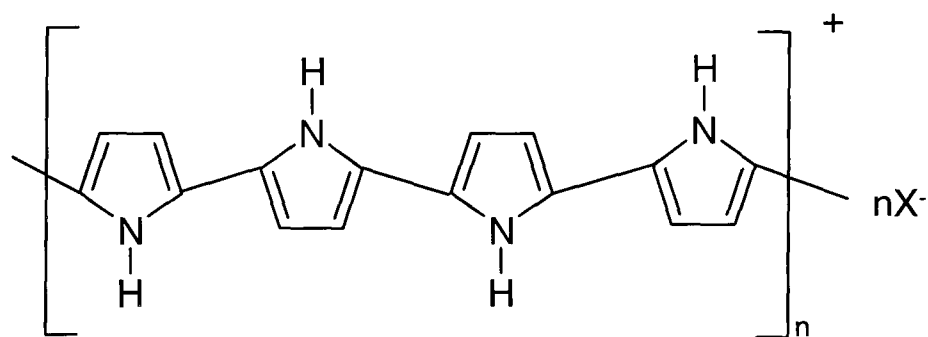


Figure 1.1 The structure of doped polypyrrole ( $X^-$ : counterion).

Polypyrrole is one of the most stable of the known conducting polymers and also one of the easiest to synthesise. The properties of polypyrrole can be modified by a number of variables and, as stated, the conductivity of the polypyrrole film can be controlled by the preparation conditions. For example, the materials electrical properties differ with respect to the extent of polymer oxidation, which is related with the amount of counterion doped in each film, and the doping level is controlled by the total electric charge passed during the polymerisation [91]. The type and concentration of doping counterion will change the morphology of the polymer as well as the oxidation state and the number of chemical defects [92-96]. Finally, other conditions such as solvent composition, the nature of the substrate material, deposition method (either cyclic potential or step potential method or galvanostatically) and preparation temperature will

also affect the properties of the film. To obtain polymers with reproducible properties, it is vital that considerable care and attention to detail are paid to the preparation of the film.

Polymer films can be characterised in many ways. For example, the current flowing during the polymerisation can be recorded by the potentiostat, and the total amount of charge passed can be calculated by the integration of the current with respect to the corresponding polymerisation time. Likewise, the thickness of films can be measured using a surface profile measuring system or an atomic force microscope. Alternatively, the morphological analysis of the film can be performed by X-ray diffraction (XRD), transmission electron microscopy (TEM) [92, 94], and scanning electron microscopy (SEM) [97-99]. Finally, the chemical composition analysis of the film can be obtained using X-ray photoelectron spectra (XPS) [100]. Bloor and Cheung used SEM to study the structure-property relationships for conductive conjugated polymers incorporated a series of different counterions and the impact of morphological details on chemical and physical properties [97-99]. Warren and Wernet used X-ray diffraction to study the structure of the polypyrrole containing counterions of alkyl sulfonates and alkyl sulfates and suggested a structure consisting of stacked polypyrrole chains separated by counterion aggregates [92, 93]. The stacked layer spacing for these counterions obeys a linear relationship with the length of the alkyl chain of counterions. The length increases by 0.125 nm if one CH<sub>2</sub> unit is added.

Like other materials, the electrical conductivity of polypyrrole is proportional to the concentration of charge carriers and their mobilities. The nature of the charge carriers within polypyrrole has been identified as “polarons” and “bipolarons” [91]. The concentration of charge carriers in polypyrrole may be altered by changing the extent of oxidation, i.e. electrochemically reduced polypyrrole contains few charge carriers. The carrier mobility may be regarded as a measure of the ease with which the charge carriers move through the material, and it is sensitive to the level of structural order present, i.e. defects decrease the conductivity through a decrease in mobility [91].

Charge transport in polypyrrole is made up of two components: intrachain charge transport and interchain charge transport [101]. Intrachain charge transport occurs along the polymer chains and requires little energy. Interchain charge transport involves the

hopping of the charge to neighboring chains, a process which requires considerable energy. The total resistivity of the film is therefore usually dominated by the interchain component. A number of experimental variables will influence the conductivity of polypyrrole, i.e. large counterions increase the separation of the polypyrrole chains, thereby presenting a greater obstacle to interchain charge transport [102] and increasing the resistivity.

When a vapour molecule is absorbed into the polypyrrole film, in general, it will change the conductivity of the film. Bartlett and Gardner have presented various mechanisms to describe the possible interactions between gases and conducting polymer coatings [103]. They identified five possible effects which might contribute to the overall observed gas sensitivity of a conducting polymer microresistor: first, the direct generation or removal of charge carriers within the film corresponding to oxidation or reduction of the polymer by the gas; secondly, the change in intrachain carrier mobility along the polymer chains due to the presence of gas molecules; thirdly, the interaction of the vapour with counterions held within the film (if the counterion motion is coupled to charge transfer along the polymer chains or if the interaction of the counterion with the vapour leads to a change in the structure of the polymer); fourthly, the change in interchain hopping if the vapour absorption into the polymer alters the interchain contacts; and finally, the effect of the gas molecules on the rate of interfacial charge transfer between the metal contact and the polymer film. In addition to the above possible electronic effects, there is evidence that the response of the polymer film is also influenced by some physical effects such as polymer swelling for a given solvent analyte, e.g. methanol at high concentration [54, 84, 104].

At present, the mechanism of the gas sensitivity is still poorly understood and it is difficult to distinguish between these various mechanisms. One of the tasks of this study is therefore a detailed fundamental study of the vapour-polymer interaction mechanism based on the investigation of molecular solubility interactions (all of the possible mechanisms proposed above are related with the corresponding molecular interactions between vapours molecules and polymer matrix). For example, one reason of the direct generation or removal of charge carriers within the conducting film could be related to the interaction between vapour molecule and polymer chain via hydrogen bonding.

There are some published works devoted to the study of the sorption process during the vapour-polymer interaction [54, 84, 104] using various methods. For example, a combination of mass, optical spectroscopy and work function measurements have been used [105, 106] to examine the electronic structure in the bandgap and charge that moves into/out of the polymer backbone by monitoring the changes of charge concentration. Other methods such as an optical Fourier transform infrared spectroscopy (FT-iR) [107, 108], cyclic voltammetry [107], Raman spectroscopy [109], electron spin resonance (ESR) [107, 110], atomic force microscopy (AFM) [108] and ultraviolet UV-vis spectrometer [111] have also been used to study the anion substitution of the dopant counterions, hydrogen bonding interaction and other related properties of polypyrrole films such as the role of the counterions in the transport and magnetic properties, substrate surface effect and the effect of oxygen.

The FT-iR measurements by Zotti et al. [107] confirmed that the hydroxide anion can substitute for the counterion reversibly in polypyrrole toluenesulphonate ( $\text{Tos}^-/\text{PPy}$ ) films. The interactions between vapour acidity and polymer basicity have been confirmed by Josowicz, Blackwood and Topart [105, 106] using a combination of mass and optical spectroscopy, as well as work function measurements. They observed a charge transfer from the polymer to the dopant molecule and the removal of electrons by the methanol dopant from a polypyrrole tetraethylammonium tetrafluoroborate ( $\text{BF}_4^-/\text{PPy}$ ) polymer film. The interactions between vapour basicity and polymer acidity have been confirmed by Zotti et al. [107] using cyclic voltammetry measurement, showing that there is an interaction between oxidised polypyrrole with  $\text{OH}^-$  which is likely provided by the proton on the amine group via hydrogen bonding. Other approaches using molecular orbital computations have been adapted to study hydrogen-bonding mechanisms [112, 113]. In addition, a more comprehensive solubility model (linear solvation energy relationships, LSERs) has also been used successfully to characterise solubility properties in a number of diverse systems. Comparisons have been made with the experimental results of SAW sensors [41,42,44,115,116]. This method uses representative molecular parameters to analyse particular interactions contributing to the overall sorption process, such as hydrogen bonding interactions and other interactions like polarity, polarizability and dispersion interactions.

In the context of modelling of conducting polymer-based sensors, there are papers concerning the sorption process of polar vapours by polar polymers for both QCM and interdigitated electrode sensors [54,62,83,104,117,118] and device modelling based on a semi-infinite co-planar electrodes, when the electrode gap is less than the electrode width and where the lateral film thickness of the gap is larger than the gap width [119-122] (although this is not the real case where the lateral film thickness in the gap is less than the gap width). To my knowledge, there has been little systematic research work linking hybrid system's characteristic with the nature of the interaction between the analyte and the sensor coating for an interdigitated electrode and a QCM-interdigitated electrode sensor pair. Such a fundamental understanding is necessary to interpret sensor responses and to establish a theoretical basis to optimise the configuration of sensors (or pairs) with improved selectivity so as to enable the improvement in electronic nose technology. This is another important task of this study and is to be carried out based upon the thermodynamics of adsorption and polymer sorption, signal-transduction mechanisms and device modelling for both piezoelectric-based QCM sensors and resistive-based interdigitated electrode sensors coated with conducting polymers. Here, the nature of sensor's responses will be linked with the nature of analyte-polymer interaction. Other relative fundamental studies are also to be carried out systematically for a clearer understanding of the properties of a hybrid sensor system (see below).

## 1.4 RESEARCH OBJECTIVES

Despite the growing number of applications and commercial *Electronic Nose* instruments based on conducting polymers, much development and research work is still required before “artificial noses” can reach their full potential. For the “first generation” *Electronic Nose*, there still exist a number of technical limitations that need to be overcome. For example, poor sensor batch-to-batch reproducibility, relatively low selectivity, long term drift related instability, long recovery periods, history dependence of the response and humidity problems. There are also a number of analytical difficulties which need to be solved, e.g., difficulties in interpreting sensors' and sensor pairs' responses, understanding the nature of vapour-polymer interactions, designing useful

coatings for analytical application and quantitatively distinguishing mixtures. These existing problems provide the objectives of research to be carried out and opportunities for contribution in the “second generation” *Electronic Nose* development.

## 1.5 THESIS OUTLINE

This research is concerned with the establishment and characterisation of a QCM-interdigitated electrode hybrid “second generation” electronic nose system. To this end, much work, including the design and fabrication of the electronic nose system, the optimisation of sensors response property, the device modelling, the study of vapour-polymer interaction mechanisms, and the application of the nose in multi-component analysis, needs to be carried out.

In Chapter 2, a QCM–interdigitated electrode hybrid odour measurement system is established. Sensor fabrication techniques are developed. Some important parameters corresponding to the sensor characteristics are investigated. Chapter 3 is concerned with the sensor’s response principle and device modelling, in which the sensor response models for QCM, interdigitated electrodes and hybrid system, as well as the odour mapping technique are addressed. Chapter 4 is concerned with the vapour-polymer interaction mechanism, in which an analytical method based on an introduced solubility property and linear solvation energy relationships is proposed. Some of the interaction mechanisms are also assessed. In Chapter 5, a simple and novel method of multi-component analysis for organic vapour mixtures is presented.

## **Establishing A QCM - Interdigitated Electrode Odour Measurement System**

### **2.0 INTRODUCTION**

This chapter describes the methodology for establishing an integrated quartz-crystal microbalance (QCM) – interdigitated conductimetric electrode hybrid sensor measurement system which includes the following corresponding results:

An eight-way resistance measurement and a two-way resonant frequency measurement instrument has been designed in-house to collect the signals from a QCM-interdigitated electrode hybrid electronic nose; the configuration of a flow system has been constructed in-house to generate single or mixed vapour samples; more detailed calibration of vapour concentration and humidity control have been implemented using an in-line FT-IR spectrophotometer with an incorporated humidity sensor.

Microfabrication techniques for the design and fabrication of interdigitated microelectrodes have been achieved using state-of-the-art semiconductor photolithographic facilities, used in conjunction with substrate surface chemical modification techniques. Electrochemical polymerisation and quality control have been used to make conducting polymer films of polypyrrole (and its derivatives) as sensitive and selective coatings for both interdigitated electrode and QCM electrode sensors using a specially in-house designed electrochemical cell to achieve the maximum fabrication consistency. Subsequently, the electrochemical conditions have been optimised for polymerisation of different monomers with various counterions and initial resistance and film thickness control techniques have been applied to make sensors with the best

characteristics, e.g., low baseline resistance drift with time, good sensitivity and wide concentration detection range.

## 2.1 MATERIALS

### **Solvent reagents and test odorants:**

Methanol (MeOH), methyl alcohol-d<sub>1</sub> (CH<sub>3</sub>OD), methyl-d<sub>3</sub> alcohol-d<sub>1</sub> (CD<sub>3</sub>OD), ethanol (EtOH), i-propanol (IPA), 1-propanol (PrOH), 1-butanol (1-BuOH), 2-butanol (2-BuOH), t-butanol (t-BuOH), hexanol (HexOH), octanol (OctOH), decanol (DecOH), n-hexane, triethylamine, diethyl ether, trichloromethane, toluene, acetic acid, ethylacetate, dichloroethane, acetaldehyde, acetone (AcO), acetonitrile (AN) and dimethylformamide were all AR grade and used, as supplied, from Aldrich.

### **Pyrrole monomers and their derivatives:**

Pyrrole (Aldrich) was purified by charcoal chromatography before use. 1-methyl pyrrole 99% and N-phenyl pyrrole 99% were AR grade, also from Aldrich and were used as received.

### **Electrolyte salts:**

Dodecylsulfate sodium salt (SDSO<sub>4</sub>Na) 98%, 1-decanesulphonic acid sodium salt (DecSO<sub>3</sub>Na) 99%, 1-hexanesulphonic acid sodium salt (HexSO<sub>3</sub>Na) 99%, 1-butanedisulphonic acid sodium salt (ButSO<sub>3</sub>Na) 99%, 1-ethanesulphonic acid sodium salt (EtSO<sub>3</sub>Na) 98%, lithium trifluoromethanesulphonate (CF<sub>3</sub>SO<sub>3</sub>Li) 96%, perfluoro-1-octanesulphonic acid tetraethylammonium salt (TEAC<sub>8</sub>F<sub>17</sub>SO<sub>3</sub>) 98%, potassium chloride (KCl), tetraethylammonium p-toluenesulphonate (TEATos), tetraethyl ammonium perchlorate (TEAClO<sub>4</sub>), tetraethylammonium hexafluorophosphate (TEAPF<sub>6</sub>) and tetraethyl ammonium tetrafluoroborate (TEABF<sub>4</sub>) were AR grade (Aldrich) and used as received.

### **Thiolation reagents:**

3-mercaptopropyl trimethoxy silane and iso-propyl alcohol were from Aldrich and used as provided.

**Sensors:**

Single quartz crystal microbalance (QCM) electrodes (10 MHz, unpolished AT-cut) were from ICM (Oklahoma city, USA). Gold (Au) wire for evaporation, purity 99.99%, was from Goodfellow Limited (Cambridge).

**2.2 METHODS****2.2.1 Design of Resistive Measurement Instrumentation**

An eight-way resistance measurement module was designed and constructed in-house and used in this study. The design philosophy was to develop a fully programmable precision circuit, using a combination of analogue and digital components. It comprises a detachable interface with an eight element “nose” head (eight chemoresistive interdigitated sensors), a back-off amplifier, independent power supplies and cabling for connection and control with a personal computer I/O card. Figure 2.1 shows a simplified block schematic diagram of the NOSE electronic system.

A voltage of 10 mV was applied across each sensor and the resulting current was measured to determine the sensor resistance. The sensor resistance signal undergoes automatic amplification in the sensor head, followed by manual back-off and subsequent amplification. This combination provides maximum flexibility for sensors of widely varying electrical characteristics. The signals from the array of eight amplifiers were multiplexed on the data acquisition card, with the common output of the multiplexer being passed to an analogue-to-digital converter. The data was collected by software control from the host personal computer.

**2.2.2 Design of QCM Measurement Instrumentation**

A two-way (single crystal) quartz crystal microbalance (QCM) resonant measurement module was also designed and constructed in-house. This approach exploits

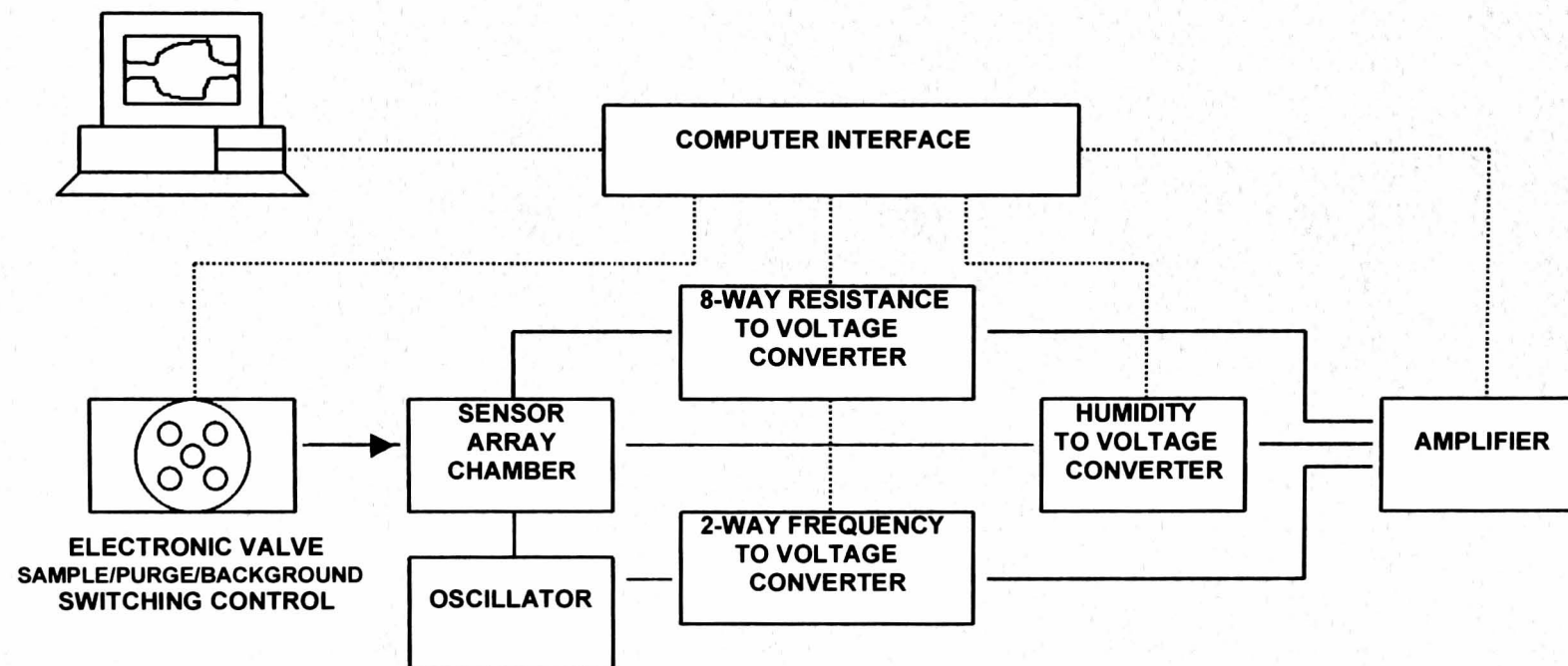


Figure 2.1 A block schematic of the hybrid nose electronic system.  
 (—: electrical or “sensing” connects, .....: computer connects, →: odour flow connect)

the stable frequency resonance of piezoelectric materials such as quartz when an alternating voltage is applied across the crystal. The diagram for QCM measurement is also shown in Figure 2.1. It comprises a sensor head connector with detachable set up to interface two piezoelectric sensors. The frequency difference between crystal-oscillator circuit (oscillating at 10 MHz) and reference crystal-oscillator circuit is passed to a frequency to voltage converter, then back-off amplifier. The data was also collected by software control from the host personal computer. In this study, a combination measurement of conductimetric and QCM sensors was established. The two-way frequency measurement module was coupled with the eight-way resistance measurement module, providing a dual resistance-mass measurement system, which permits simultaneous measurements on the same type of polymer film and for the same vapour samples.

In addition, a Vaisala (Suffolk, UK) humidity sensor was incorporated to the sensor array chamber which measured the humidity of the sensor head chamber. A five port Omnifit (Omnifit Limited, Cambridge, UK) electronic rotary valve was also used to control the switching between sampling and purging operations. Flow manipulations can be controlled either automatically by computer or manually. The detailed function of the electronic rotary valve will be introduced in the following section.

### **2.2.3 Configuration of Flow System and FT-iR Spectroscopy Measurement**

A flow system was designed and constructed to generate and control the concentration of the test sample vapours, as shown in Figure 2.2. This system employed bubblers to generate a simple vapour (or mixtures from the corresponding liquid sample(s)) which could subsequently be diluted by pure nitrogen to different levels, ranging from 100% to 2.5% relative to the saturated vapour. A humidity background/washing function was also developed which not only enabled the control of water vapour, but also was used to "re-generate" the sensors (see later). All gas flow rates were controlled by Platon (LT Platon Ltd, Basingstoke, UK) flow meters. The function changes were switched by an integrated five port Omnifit electronic rotary valve which could be controlled either automatically by computer or manually. This five port valve

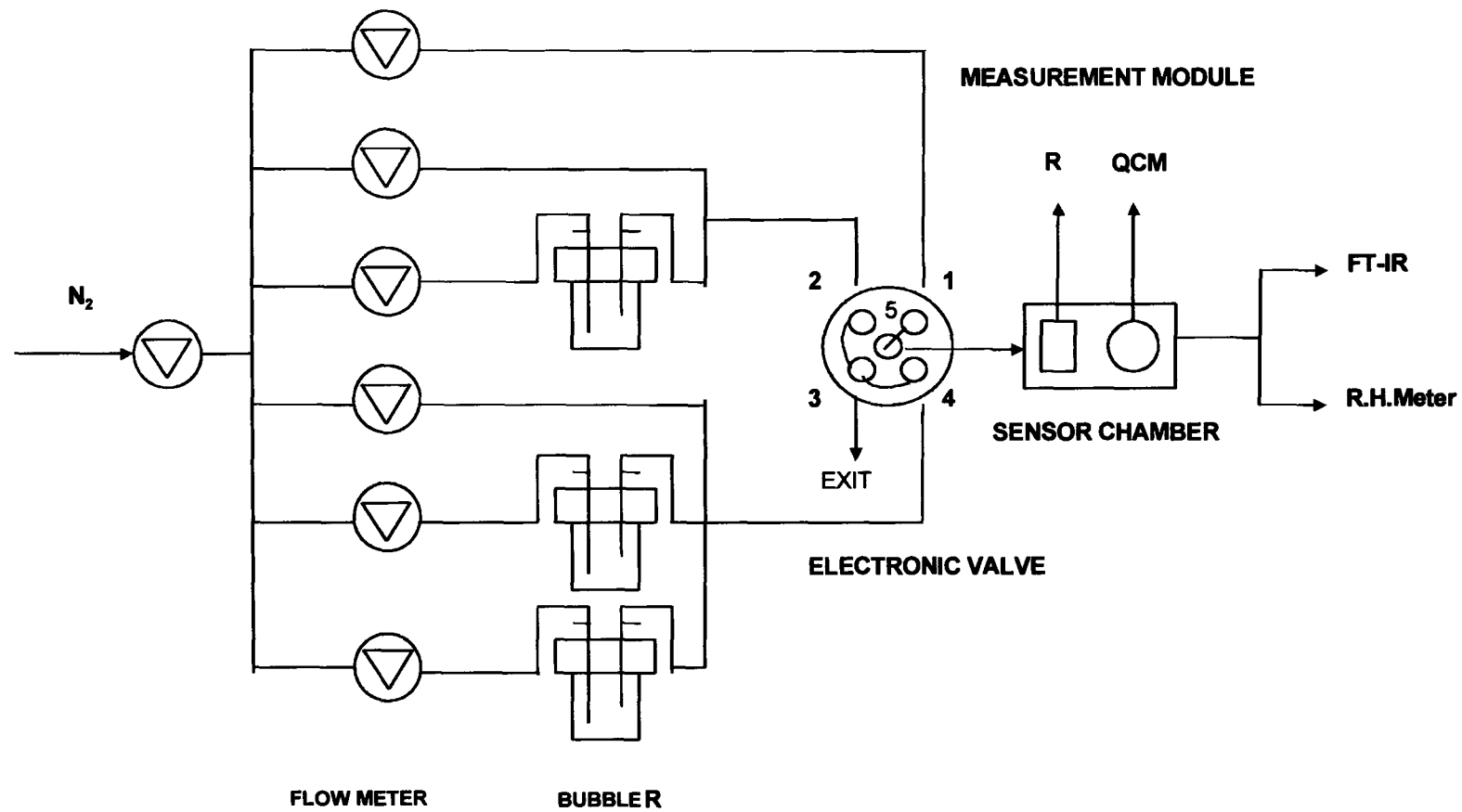


Figure 2.2 Configuration of a flow system which generates simple or mixed samples.  
 (1, 2, 3 and 4 represent electronic rotary valve port 1 to 4, 5 represents centre port)

connected two valves at 180° with one port at 90°, and the centre port (numbered as 5) to one other port. In this configuration, the centre port was connected to the sensor array chamber (the volume of which is 9 ml). This is shown in Figure 2.2.

In position one (as in figure 2.2), the five port rotary valve connects port 1 with centre port 5, and the other three ports (2, 3 and 4) are connected. In this position, background of pure nitrogen flows to the sensor array chamber. The other ports exit to the exhaust. In the second position, when the centre port and port 2 are connected, (and 1, 3 and 4 are joined), background humidity vapour flows to the cell. In the third position, while the centre port and 4 are connected, (1, 2 and 3 are connected), background air flows to the exhaust and the gas samples of either single or mixture components flow to the chamber. The flow rate through the chamber containing sensors was maintained at  $200 \text{ cm}^3 \text{ min}^{-1}$  which was controlled by a flow meter. A humidity sensor was connected with the sensor array chamber to monitor its humidity.

Concentrations of the tested vapours were calibrated by in-line Fourier transform infrared (FT-iR) spectroscopy, with the photometer connected to the sensors chamber cell, parallel with the humidity measurement. Figure 2.3 shows the complete schematic diagram of the hybrid multi-property measurement electronic nose system used in this project.

## **2.2.4 Microfabrication of Interdigitated Electrodes and QCM Sensors**

### *2.2.4.1 Protocol of microfabrication*

The protocol of microelectrode fabrication is shown in Figure 2.4 from (A) to (F). There are three main steps for the fabrication of microelectrodes. First, the glass microscopic slides were chemically modified by thiolation (using a thiol solution of 3-mercaptopropyl trimethoxy silane), which promotes good adhesion between the glass surface and gold electrode deposited onto it. Clean slides were refluxed in a 20 mM solution of the silane for 1 hour providing an even molecular layer with sulphur

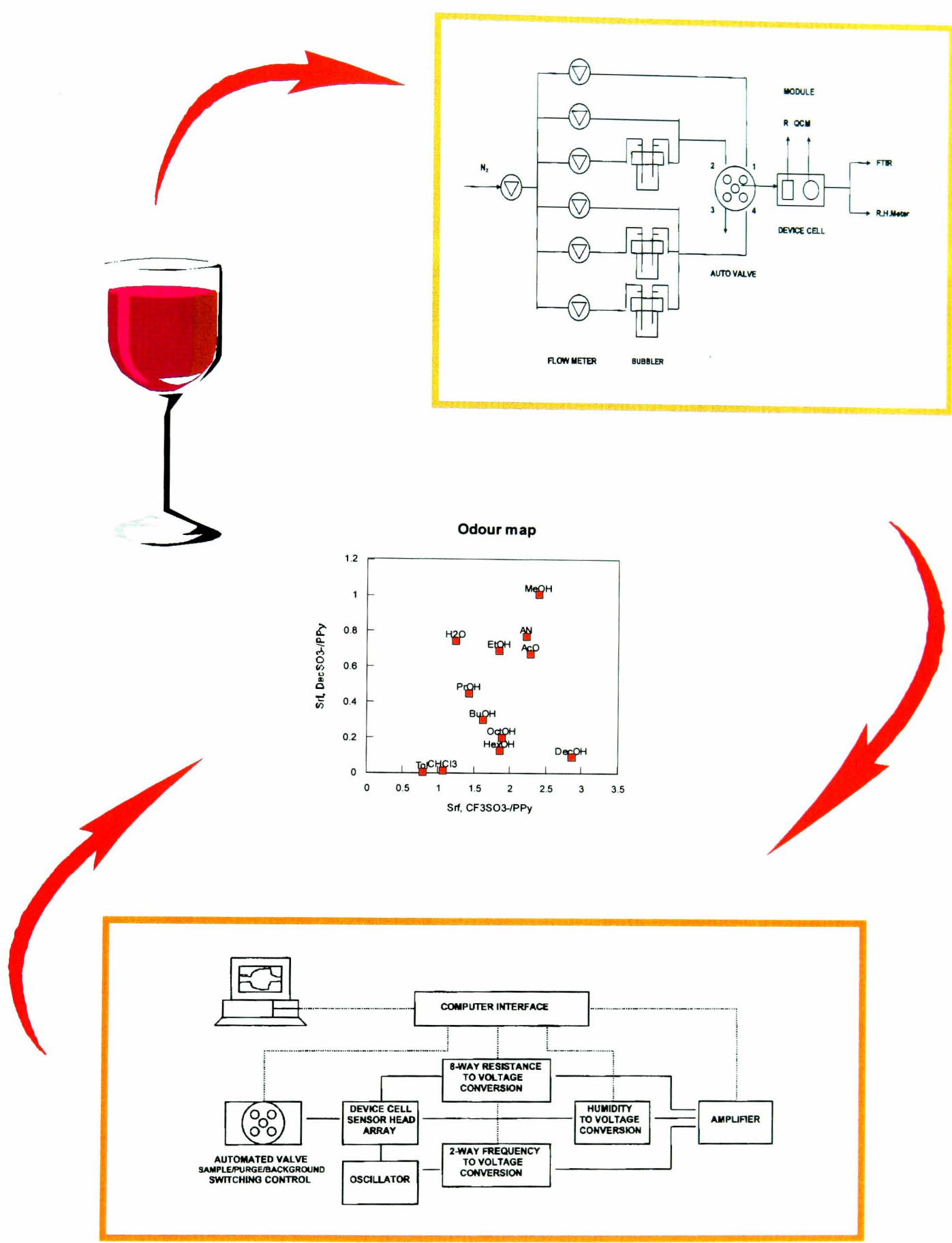
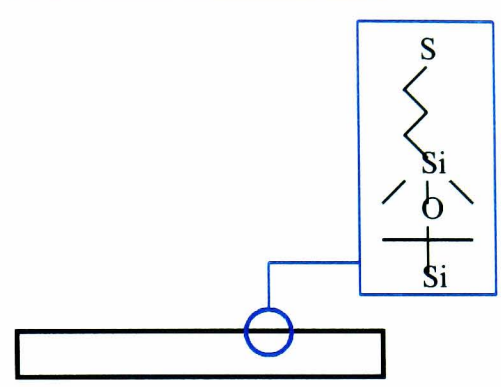


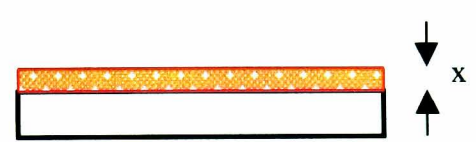
Figure 2.3 Complete schematic diagram of the hybrid electronic nose system.



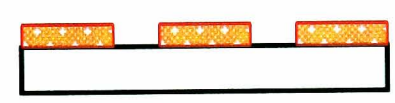
(A) clean glass slide



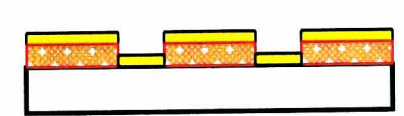
(B) chemical modification of the slide surface



(C) coat with S1818 photoresist  
( $x = 1.8 \mu\text{m}$ )



(D) expose and develop the electrode pattern



(E) evaporate 100nm gold



(F) "lift-off" in acetone

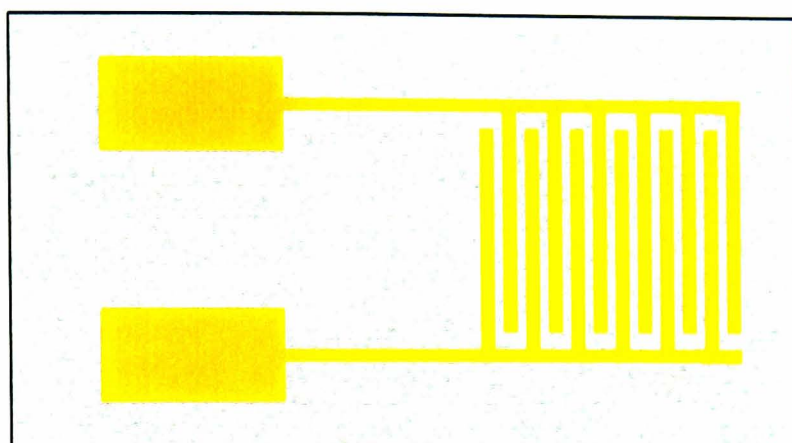
Figure 2.4 (A) to (F) show the protocol for microelectrode fabrication.

functionalities (which bind gold via a strong thiol bond). The slides were then coated with S1818 photoresist (Shipley Ltd, UK) by spinning at 4000 rpm for 30 seconds and baking at 90 °C for 30 mins, giving a resist thickness of 1.8  $\mu\text{m}$ . The polymer coated slides were exposed to UV light through a chrome mask (see 2.2.4.2) for 12 seconds on a mask aligner, and developed with AZ developer (Shipley Ltd, UK) for 90 seconds. The patterned slides were then loaded into the Balzers PKR 250 thin film deposition system, which was controlled by a Intellemetrics IL 150 programmable peripheral interface (this instrument controls the thickness of deposited metal using a QCM). Once a pressure of  $10^{-6}$  Torr. had been reached in the evaporation chamber, gold deposition was carried out until the thickness of gold reached 100 nm. Finally, the pattern of electrode was developed by “lift-off” in acetone and checked under a microscope.

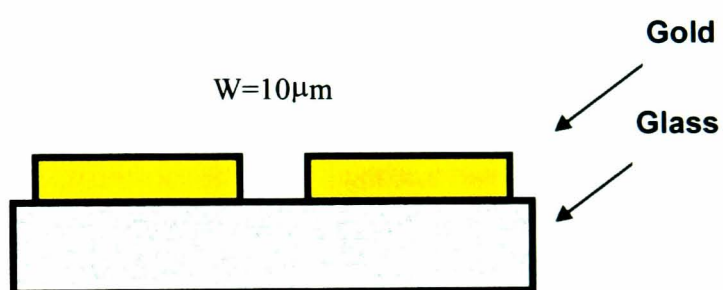
#### *2.2.4.2 Design and fabrication of interdigitated electrodes*

In microfabrication, the pattern of interdigitated electrode was formed using a chrome-on-quartz mask with electron beam lithography. The masks for the photolithographic technique were designed using the mask software Wavemaker (WAM). At an early stage of this study, interdigitated electrodes with various gap sizes (from 5  $\mu\text{m}$  to 40  $\mu\text{m}$ ), active areas, device densities on a single slide and shapes of bonding pads were designed. The design was optimised iteratively (by trial and error). For example, the gap size was chosen as 10  $\mu\text{m}$  for improved sensor sensitivity; the device density on one slide was increased from 6 to 20 for fabrication efficiency and the shape of bonding pads was changed for compatible electronic connection. The most commonly used design throughout this work comprises a 10  $\mu\text{m}$  gap with 20 pairs of interdigitated fingers (the width of each process being 65  $\mu\text{m}$ ). The active area of this electrode is 7.5  $\text{mm}^2$  (2.5 mm  $\times$  3 mm), shown in Figure 2.5.

A second “square” electrode design was also used to study the electrochemical polymerisation process, e.g., current-time relationship, thickness of the polymer film–polymerisation time relationships. Figure 2.6 shows the design of a square electrode. The active electrode area was 16  $\text{mm}^2$  (4 mm  $\times$  4 mm).



(a)



(b)

Figure 2.5 Plan view (a) and transverse section (b) of an interdigitated electrode, where the gap ( $w$ ) = 10  $\mu\text{m}$ .

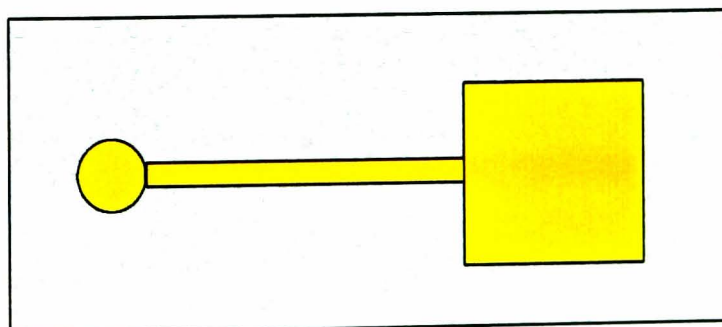


Figure 2.6 Plan view of a square electrode (4mm  $\times$  4mm) used for the polymerisation study.

#### *2.2.4.3 QCM electrodes*

The quartz crystal microbalance (QCM) electrodes used in this study were 10 MHz, unpolished AT-cut piezoelectric crystals with gold electrodes, which were purchased from ICM (Oklahoma city, USA). The diameter of the gold electrode is 5 mm. Figure 2.7 shows a diagram of a QCM electrode. The connectors from the two electrodes were modified to fit the electronic measurement system.

#### *2.2.4.4 Polymerisation of conducting polymer films on interdigitated electrodes*

Electrochemical polymerisation of polypyrrole and its derivatives was carried out in an “in-house” designed three electrode cell which is shown in Figure 2.8, where the luggin capillary was designed close to the working electrode for setting a stable potential. Fabricated microelectrodes were used as working electrodes. A large coiled platinum wire grid was used as a counter electrode and a Ag /AgCl electrode functioned as the reference electrode. All polymer films were deposited onto the working electrode from freshly prepared solution of 0.1M pyrrole monomer and 0.1M counterion in either R.O. (Reverse Osmosis) water or acetonitrile (AN), as shown in Table 2.1.

Step potential (from initial zero to a constant potential) deposition was performed using a potentiostat (Potentiostat, Model 273A, EG&G). A step potential of 0.75 V to 1.15 V against Ag/AgCl reference electrode was applied to the interdigitated electrode for a length of time until the polymer had bridged the gap of two electrodes and baseline resistance reached a fixed value. Table 2.1 gives details of the preparation conditions and electrode step potentials of the different polypyrrole films studied in this work (see notations for details of abbreviations).

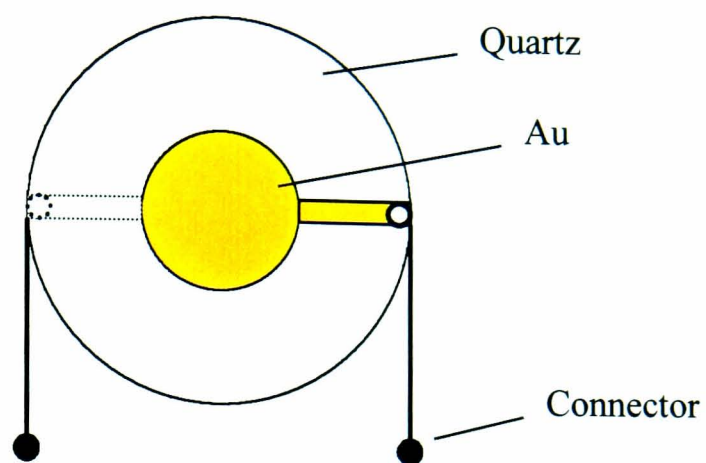


Figure 2.7 Diagram of QCM electrode (Au electrode diameter = 5mm) used in this study.

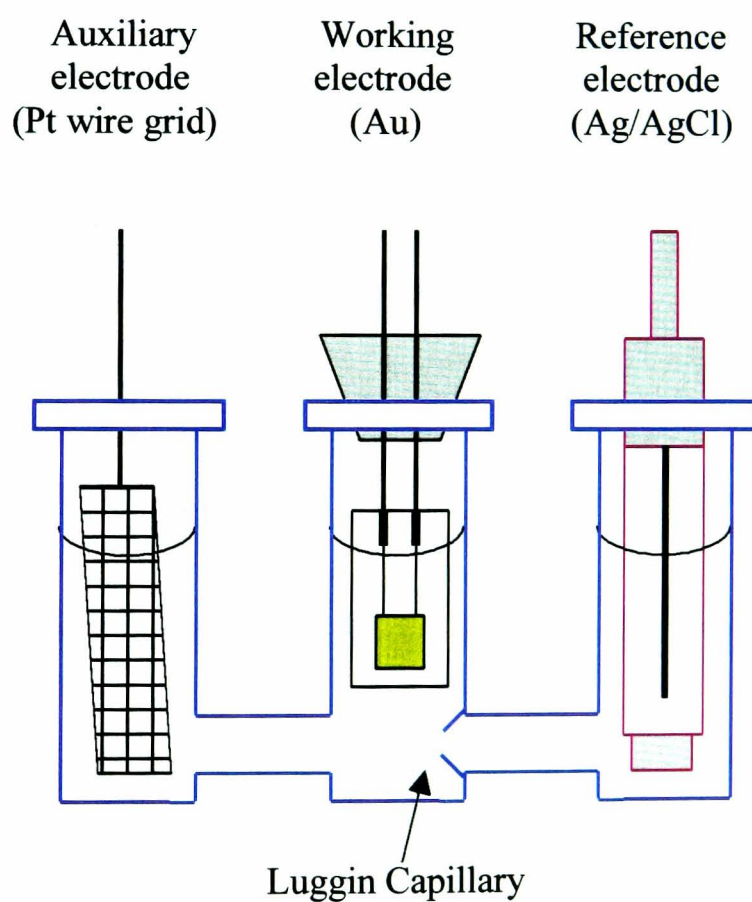


Figure 2.8 Electrochemical cell configuration and electrodes used for the polymerisation in this study.

Counterions	Monomer	Solute	PH value	Potential (V)
SDSO <sub>4</sub> <sup>-</sup>	Py	H <sub>2</sub> O	4.8	0.8
DecSO <sub>3</sub> <sup>-</sup>	Py	H <sub>2</sub> O	4.8	0.8
HexSO <sub>3</sub> <sup>-</sup>	Py	H <sub>2</sub> O	4.8	0.8
ButSO <sub>3</sub> <sup>-</sup>	Py	H <sub>2</sub> O	4.8	0.8
EtSO <sub>3</sub> <sup>-</sup>	Py	H <sub>2</sub> O	4.8	0.9
Tos <sup>-</sup>	Py	AN	-	1.0
ClO <sub>4</sub> <sup>-</sup>	Py	AN	-	1.10
ClO <sub>4</sub> <sup>-</sup>	φ*Py+10μlPy	AN	-	1.10
ClO <sub>4</sub> <sup>-</sup>	CH <sub>3</sub> Py+10μlPy	AN	-	1.10
PF <sub>6</sub> <sup>-</sup>	Py	AN	-	1.05
PF <sub>6</sub> <sup>-</sup>	φ*Py+20μlPy	AN	-	1.15
PF <sub>6</sub> <sup>-</sup>	CH <sub>3</sub> Py+5μlPy	AN	-	1.15
BF <sub>4</sub> <sup>-</sup>	Py	AN	-	1.05
Cl <sup>-</sup>	Py	H <sub>2</sub> O	4.5	0.75
CF <sub>3</sub> SO <sub>3</sub> <sup>-</sup>	Py	H <sub>2</sub> O	4.5	0.8
C <sub>8</sub> F <sub>17</sub> SO <sub>3</sub> <sup>-</sup>	Py	H <sub>2</sub> O	4.5	0.8

Table 2.1 Preparation conditions and electrode step potentials of the different polypyrrole films studied in this work ( φ : N-phenyl pyrrole).

#### 2.2.4.5 Polymerisation of conducting polymer films on QCM electrodes

Electrochemical polymerisation of polypyrrole onto the gold electrodes of QCM was also performed in a three-electrode cell from a solution of 0.1M pyrrole monomer containing 0.1M counterion. A constant potential vs. Ag/AgCl reference electrode was applied to each side of the QCM electrodes for 20-30 seconds, to yield a frequency change of about 10 KHz in total, representing ca. 10 μg polymer growth on the electrode (1 Hz in frequency change represents a change in mass of 1 ng).

#### *2.2.4.6 Quality control of polymers*

During the polymerisation process, the conductivity of the polypyrrole film can be controlled by the preparation conditions. For example, the polymer density differs with respect to the extent of polymer oxidation, which itself is related with the amount of counterion doped in each film. In general, conductivities increase with doping level, and the doping level is controlled by the potential applied during the polymerisation. The type and concentration of doping counterion will play an important part in the initiation and propagation of polypyrrole formation, changing the morphology of the polymer as well as the oxidation state and chemical defects. The length of the polypyrrole chain will also modify the properties of the film. Finally, other conditions such as solvent, substrate material, deposition method (either cyclic potential or step potential method) and temperature will also affect the properties of the film such as the surface roughness (e.g. films grown in AN have a rough surface) and adhesion of the film to the substrate [89].

Polymer films can be characterised in many ways. For example, the current,  $i$ , passed during the polymerisation can be recorded by a potentiostat, and the total amount of electric charge passed can be calculated by the integration of  $i(t)$  with respect to the corresponding polymerisation time; The thickness of films can be measured using a Dektak surface profile measuring system (Dektak 3ST, Sloan Technology, California, USA); Alternatively, the morphological analysis of the film can be performed by a scanning electron microscopy (S800 SEM, Hitachi, Japan); Finally, the chemical composition analysis of the film can be obtained using X-ray photoelectron spectra (XPS), otherwise known as ESCA (electron spectroscopy for chemical analysis).

In general, once the monomer and type of counterion have been chosen and the electrode geometry, solvent (AN or R.O.water) and deposition method have been selected, the key method of optimising the film quality is controlling the counterion doping level and the thickness of the film. This can be achieved by means of choosing an appropriate potential value to which the electrode is stepped at the end of polymerisation. As the result, conducting polymers of appropriate conductivity can be made.

One initial aim was to make interdigitated electrode resistive sensors of optimum characteristics with regards an appropriate conductivity, reflected by a defined initial resistance value  $R_0$ , a low resistance drift with time and a high sensitivity to the sensing odourant, with good consistency in batch to batch fabrication.

To achieve these objectives, step by step, the following experiments have been carried out:

Firstly, to study the polymerisation process, the relationship between  $i(t)$  and time was studied using both a square electrode and an interdigitated electrode. Here the electric charge,  $Q$ , was calculated by integrating the current with the time during which a step potential was applied. Also, the relationship between the polymerisation time  $t$ , initial resistance  $R_0$  and  $Q$  were studied. To determine the film thickness dependence, the relationship between polymer thickness and polymerisation time for both square and interdigitated electrodes was studied.

Secondly, to study the counterion effects, 16 different types of polymers were polymerised on interdigitated electrodes with various counterions and backbone monomer compositions, covering a range of initial resistance values from relatively low ( $\Omega$ ) to high ( $k\Omega$ ). Resistance drift over a long period of time was measured and an initial resistance value for each type of polymer was suggested.

Similarly, polymerisation on QCM electrode and study of the relationship between the frequency shift ( $f_c$ ) due to the coating with current passed and time was also carried out. Finally, sensor's fabrication consistency was studied, and a physico-chemical analysis of film properties was carried out.

## 2.2.5 Measurement of Vapours at Interdigitated Electrode and QCM Sensors

### 2.2.5.1 Control of flow rate

The amount of saturated vapour carried out by a stream of pure nitrogen was controlled by the flow rate of the Platon TM flow meter connected with the sample bubbler and port 4 of the electronic rotary valve, generating a flow rate from 5 to 200  $\text{cm}^3\text{min}^{-1}$ . However, the amount of saturated organic vapour carried in the flow system was not linear with the flow rate of the bubbling nitrogen stream through the bottle, especially when the flow rate was high. Thus, it was necessary to calibrate the system, which was performed using an in-line FT-iR measurement, employing methanol as the model sample vapour. The flow rate of carrying nitrogen gas was set at different levels and methanol concentrations relative to its saturated vapour were measured spectrophotometrically. A calibration curve of relative vapour concentration against flow rate of bubbling nitrogen was constructed.

The process of sample measurement was controlled either automatically or manually. Generally, before a sample vapour was introduced into the sensor chamber, a stream of dry nitrogen was flowed across the sensors at 200  $\text{cm}^3\text{min}^{-1}$  to obtain baseline values for both the resistance and frequency responses. Sample vapour was then switched to the chamber with a flow rate of 200  $\text{cm}^3\text{min}^{-1}$  and measurements were made for 120 seconds. Thereafter, the valve was switched back to nitrogen again to allow sensors to recover before the next measurement. Analysis of data involved studying the dependent responses for both the ON and OFF sample measurement.

### 2.2.5.2 Recovery of sensors

The recovery of sensors requires that either (or both) resistances or frequencies return to the original baseline value after sample measurement. This can usually be achieved by purging with either nitrogen or water vapour (or both). This process can be repeated for 1 to 3 times for a complete recovery. In general, there is a need to

“regenerate” sensors as quickly as possible, in order to speed up the throughput of samples.

### *2.2.5.3 Control of humidity*

The sensitivity to water is one of the main concerns in characterising responses in a particular field application of the sensor array. Usually water vapour or “humidity” is the main background “odour” in a sample mixture, and this can be generated by mixing water with the testing target sample. To test the sensor array’s sensitivity to mixtures of water vapour and other odour vapour, it is essential to supply the correct mixture, which can be achieved using a flow system. In our experimental set up, see Figure 2.2, there are two bubbler bottles which contain water, positioned in both the background/purging path and the sample path. The relative humidity can then be adjusted by changing the flow rate of the corresponding flow meters controlling water sample and nitrogen. The amount of water vapour is monitored by a humidity sensor. Thus, humid air with a desired relative humidity can pass through the sensor chamber as either a reference or purging gas. In a second position, humid air with the same relative humidity value is generated by the other bubbler, which is mixed with a dry odourant vapour to make a mixture. Usually the relative humidity was set to 50%, which is “ambient” in the local environment.

### *2.2.5.4 Mixing of gases*

Similar to making mixtures of water and other odour vapour, mixtures of two odorants can be made by using two bubblers, each containing one component of sample liquid. Each bubbler was controlled by an independent flow meter, see Figure 2.2. The mixing ratio of the two gases can be adjusted by changing the flow rate. Partial composition of one component can be changed from 0% to 100%, with 30%, 50%, 70%, 90% values as pre-defined intervals required. The accurate composition of the mixtures can be corroborated by the use of an in-line FT-iR measurement. By an alternative and easier method, the ratio compositions of the mixtures can be calculated by using the

saturated vapour pressure data [123] and calibrated flow meters readings. Detailed calculation will be introduced in a later Section 2.3.2.4.

#### *2.2.5.5 Determination of sensors dynamic range*

The sensor's dynamic range is the concentration interval over which a sensor provides a continuous changing response. Dynamic range is bounded by the limit of detection at the low end and by saturation effects at the upper end. Usually, the main concern is at the low concentrations because the needs to sense trace odour samples, e.g. in indoor air quality control, the sensors are expected to detect chemicals at and below ppm level [4, 124]. At high concentrations, it is also important to know if the sensor array still works well, giving quantitative data.

To test the sensors dynamic range, it was necessary to choose the right vapour samples. The 50% diluted methanol was selected as upper detection limit sample, which is about  $10^5$  ppm in concentration at 25 °C. Low concentration limits can be tested by diluting samples to ppm level in nitrogen. Although there is a dilution limitation for the flow system and it is difficult to dilute some gases (e.g. MeOH) to a concentration of less than 10 ppm level because of their high saturated vapour pressure, other samples like decyl alcohol (DecOH) can provide very "dilute" gases (e.g. 2.5% DecOH gives a concentration of 1.5 ppm).

#### *2.2.5.6 Sensors response stability with respect to time*

In addition to the stability of the baseline resistance with time, both QCM and interdigitated electrode sensor's (repeat) measurement stability was determined by exposure to 50% methanol vapour. Responses were measured during a period of 45 days, each time after an interval of at least two days. Sensors were stored (covered) in air, at room temperature. Baseline resistance change, individual responses from the interdigitated electrode and QCM sensors as well as the combined sensors response were recorded and the data were analysed accordingly.

## 2.3 RESULTS AND DISCUSSION

### 2.3.1 Microfabrication and Quality Control of Sensors

#### 2.3.1.1 Deposition of polymer on square electrodes

DecSO<sub>3</sub><sup>-</sup>/PPy coatings were prepared on square electrodes from a solution of 0.1M pyrrole and 0.1M DecSO<sub>3</sub>Na electrolyte in R.O. water. A step potential was applied at 0.8V, with a polymerisation time between 2 to 80 seconds, at the end of which, the electrodes were switched to open circuit. Figure 2.9 shows a typical polymerisation process using a square electrode, showing the stability of the polymerisation current (mA) with polymerisation time (seconds). The polymerisation currents for this set of electrodes were all around 0.45 mA.

The electric charge (Q) passed can be calculated by integration of the current with the time (from 0 to t<sub>0</sub>) according to the following Equation 2-1:

$$Q = \int_0^{t_0} i(t) dt \quad (2-1)$$

Figure 2.10 demonstrates the calculation of Q by integration, whilst Figure 2.11 shows the relationship between the polymerisation charge passed and the polymerisation time on a square electrode with an active area of 16 mm<sup>2</sup>. It can be seen that the relationship between unit area of Q and time was linear with a gradient of 3.01 mCcm<sup>-2</sup>sec<sup>-1</sup>. The r<sup>2</sup> coefficient of linear regression was 0.99. This demonstrated that the polymerisation cell gave a consistent polymerisation, since the distance between the reference, counter and working electrode were all fixed with the relative positions and electrode depths in the solution all remaining unchanged. This geometric stability is important for the fabrication consistency. Also, the design of the luggin capillary provided a stable reference potential.

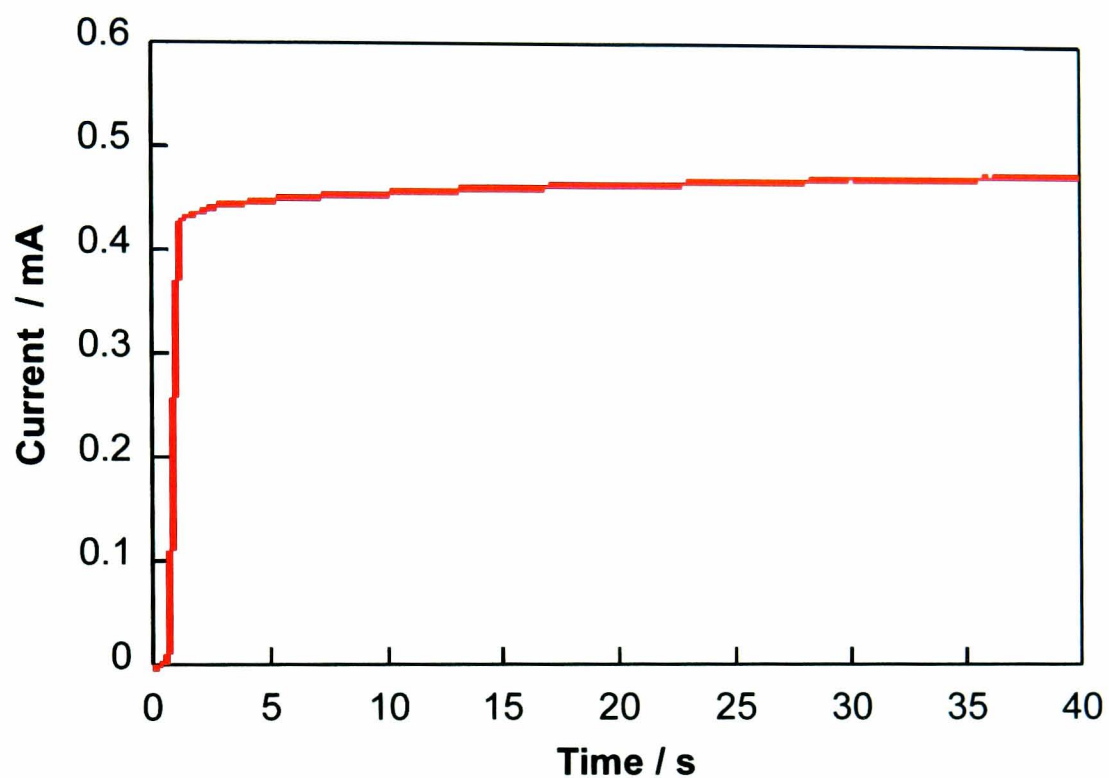


Figure 2.9 shows a typical polymerisation process of DecSO<sub>3</sub><sup>-</sup>/PPy film using a square electrode with an active area of 16 mm<sup>2</sup>, demonstrating the relationship between polymerisation current (mA) and the time (seconds) during the application of a step potential (0.8 V).

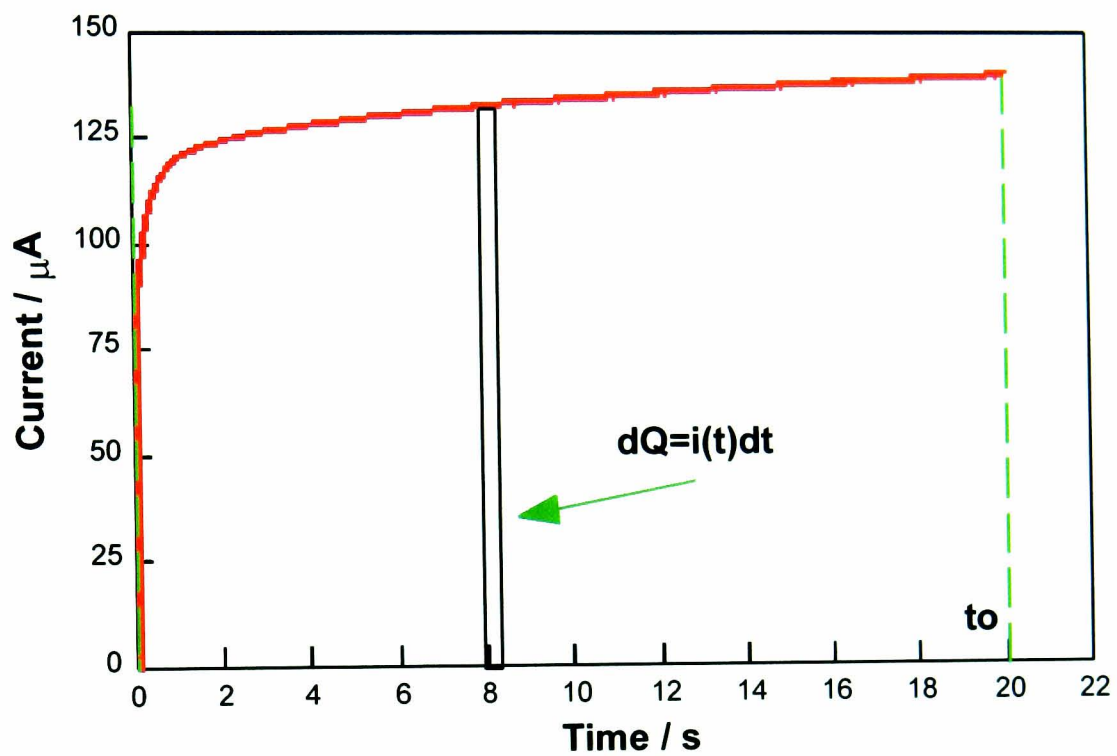


Figure 2.10 demonstrates the method for electric charge (Q) calculation by integrating the current passed during the electrochemical polymerisation with time.

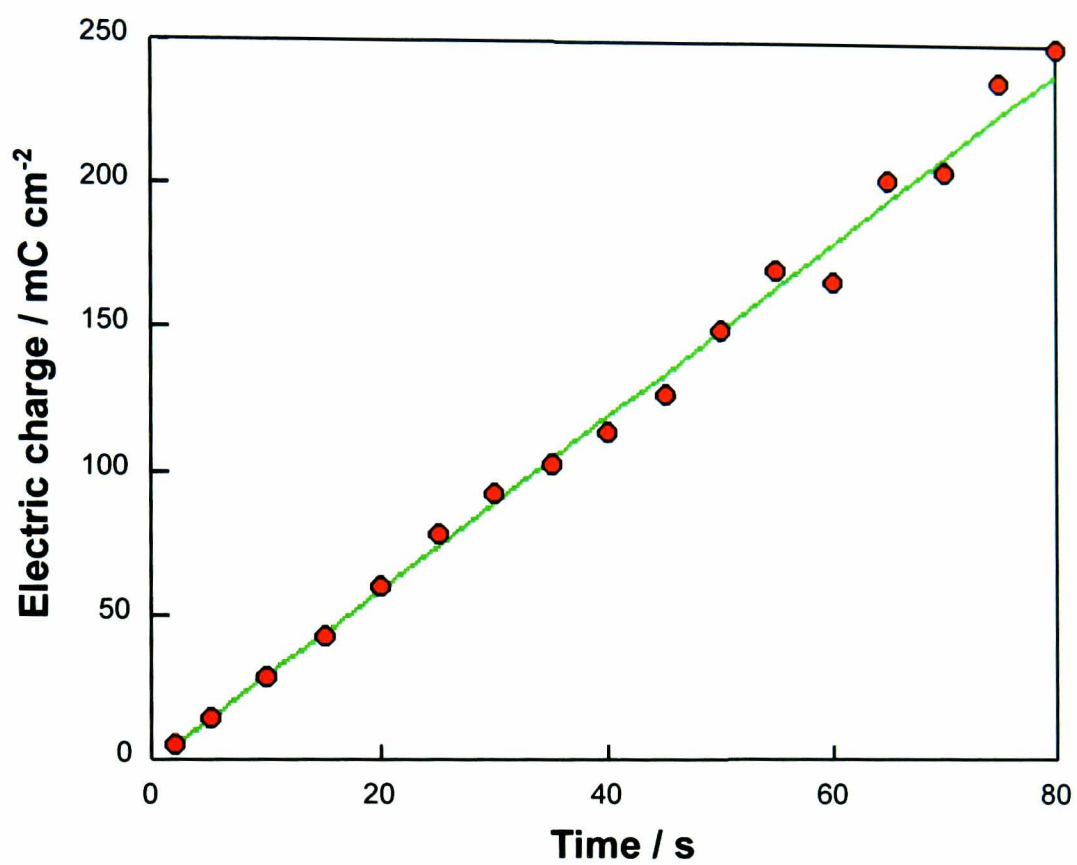
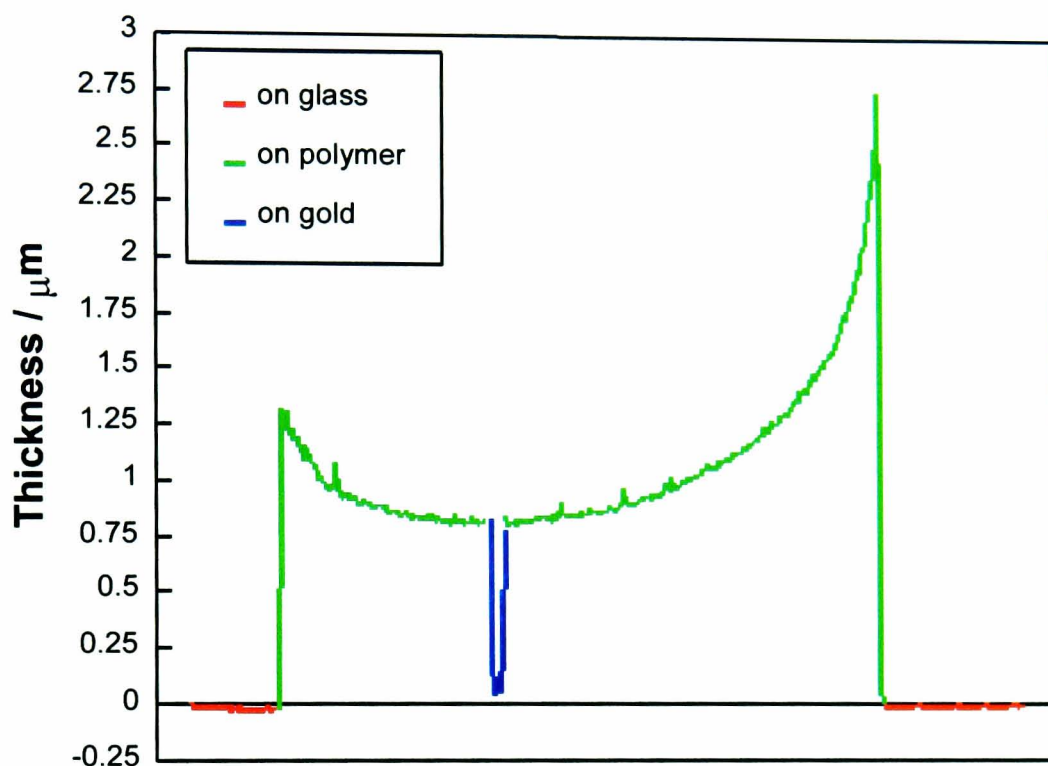


Figure 2.11 shows the relationship between polymerisation charge  $Q$  ( $\text{mC cm}^{-2}$ ) passed at the electrode and the polymerisation time ( $t$ ) applied for a  $\text{DecSO}_3^-/\text{PPy}$  film on a square electrode with an active area of  $16 \text{ mm}^2$ . The green line through the points represents the best fit to the equation  $Q = 3.01 t$ .

Figure 2.12 shows the polymer thickness on a square electrode measured using the Dektak surface profile system. The polymerisation was carried out at 0.8 V (current 0.5 mA) for 75 seconds. The detecting needle scanned across the electrode from top to bottom for 4 mm. The mass on the Dektak needle was set to a minimum (5 mg). It can be seen that the film thickness at the top and bottom were 1.25  $\mu\text{m}$  and 2.75  $\mu\text{m}$  respectively. In the middle, it was 1  $\mu\text{m}$ . The blue line indicated a measurement of gold electrode thickness, which was managed by scratching a strip of polymer off the electrode. The thickness of gold electrode was 0.08  $\mu\text{m}$  in this case. Figure 2.12 shows that the polymer on the electrode surface is not uniform in thickness. It is thicker at the edge than in the middle due to the non homogeneous diffusion of monomers to the centre with respect to the edge area of the electrode. Polymer is also thicker at the bottom (2.75  $\mu\text{m}$ ) than top (1.25  $\mu\text{m}$ ) due to the effect of denser oligomers in solution increasing polymerisation at bottom of electrode. The average value in thickness is 1.1  $\mu\text{m}$  for this electrode. Figure 2.13 shows the thickness of polymer film on square electrodes against the polymerisation electric charge ( $\text{mCcm}^{-2}$ ). The thickness readings were all taken at the junction of the square electrode and connecting strip to the bonding pad (which is about the average value for the film thickness across the whole electrode). It can be seen that the film thickness increased linearly with the increasing of unit area of polymerisation charge within the length of time used in this experiment (2s to 80s). The gradient was 0.0056  $\mu\text{m mC}^{-1}\text{cm}^2$  and the  $r^2$  coefficient of linear regression was 0.99.

The morphology of the polymer as electrochemically formed on the square electrodes was examined by SEM with 10 kV electron beam. Figure 2.14 (a) to (d) show the SEM photomicrograph for films deposited with a length of time of 5, 20, 45 and 80 seconds. The scanning electron micrographs show that the thin polymer is fine and uniform. As the amount of polymer deposited increases, the size of the spherical particles of polymer increases and the film is less uniform than the thin one. This has implications for rates of gas diffusion into the polymer film.



**Scan 4mm across an electrode from top to bottom**

Figure 2.12 Plot of DecSO<sub>3</sub><sup>-</sup>/PPy polymer film thickness on a square electrode in μm as measured by Dektak. Polymerisation was carried out at 0.8 V (0.5 mA) for 75 s. The length scanned along the electrode is 4 mm in the direction from “top” to “bottom”. Here “top” and “bottom” represent the relative position of the polymer film on the electrode during polymerisation in the solution.

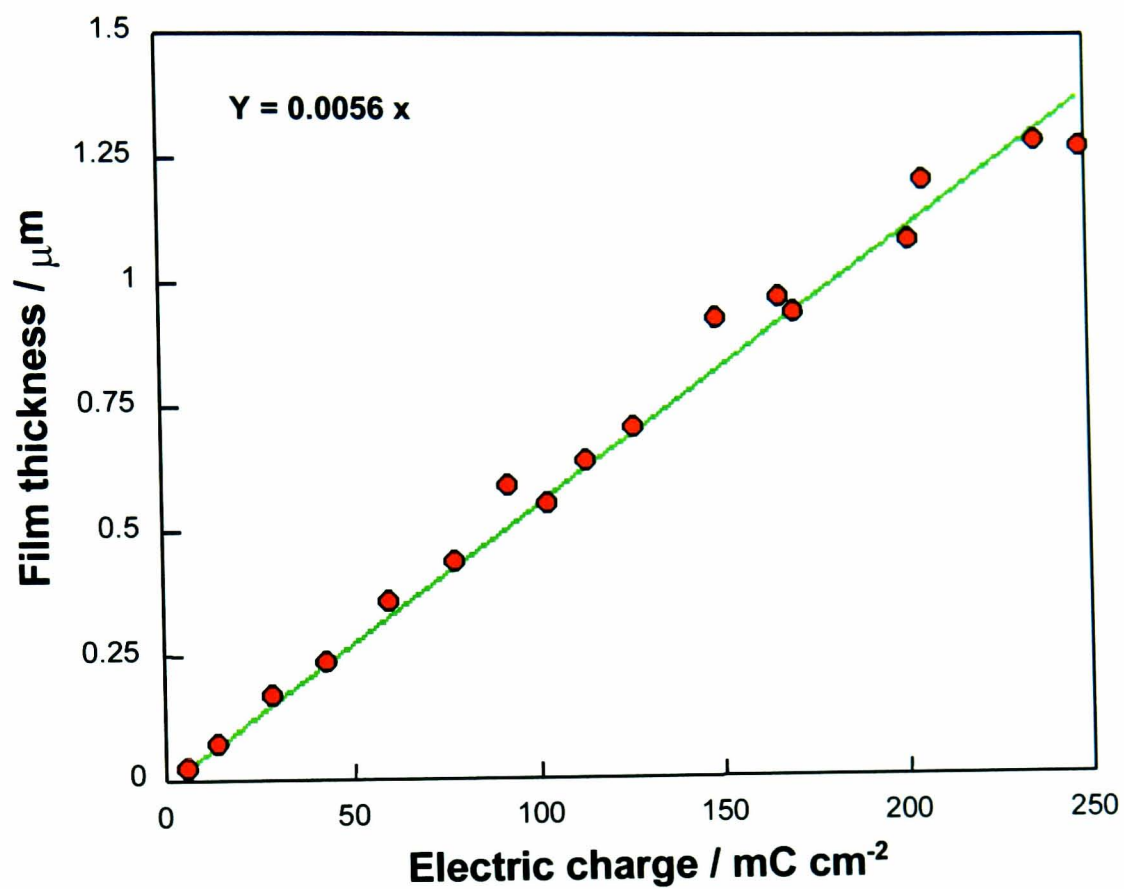
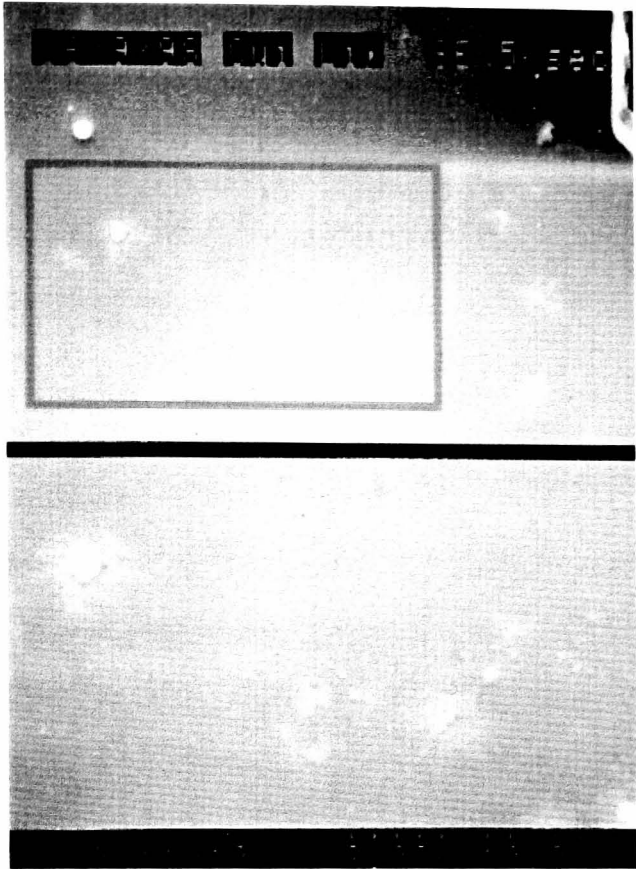
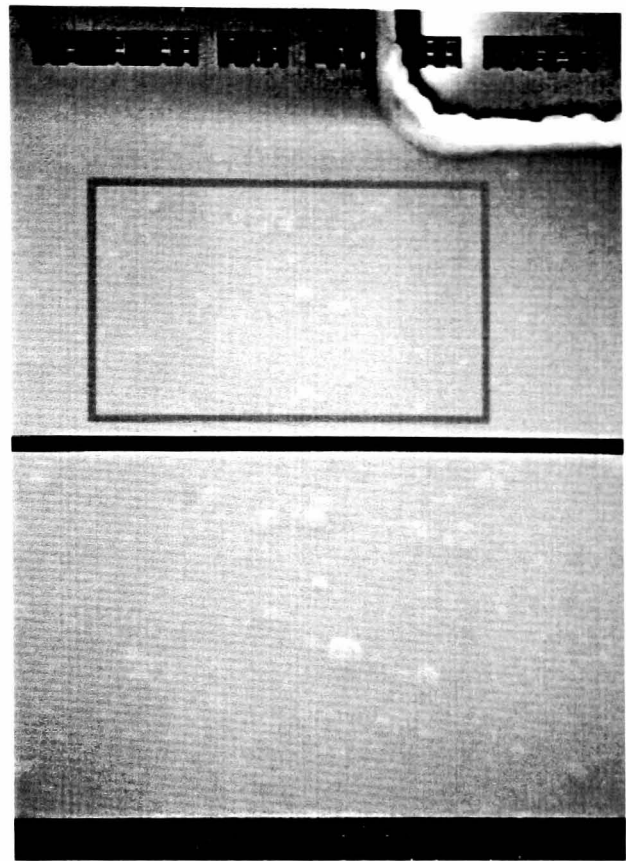


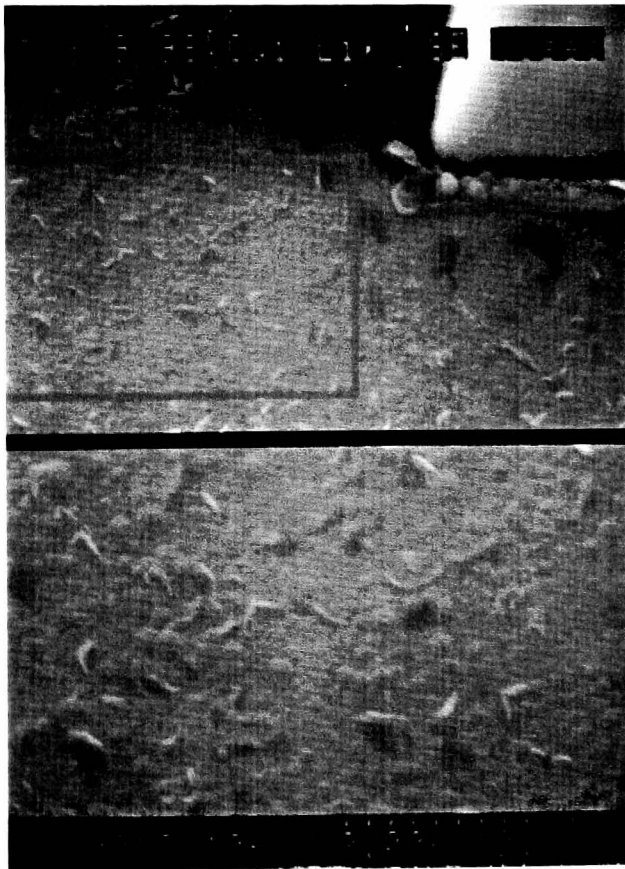
Figure 2.13 DecSO<sub>3</sub><sup>-</sup>/PPy polymer film thickness on separate square electrodes (active area = 16 mm<sup>2</sup>) versus polymerisation charge. The green line through the points represents the best linear fit with a slope of 0.0056.



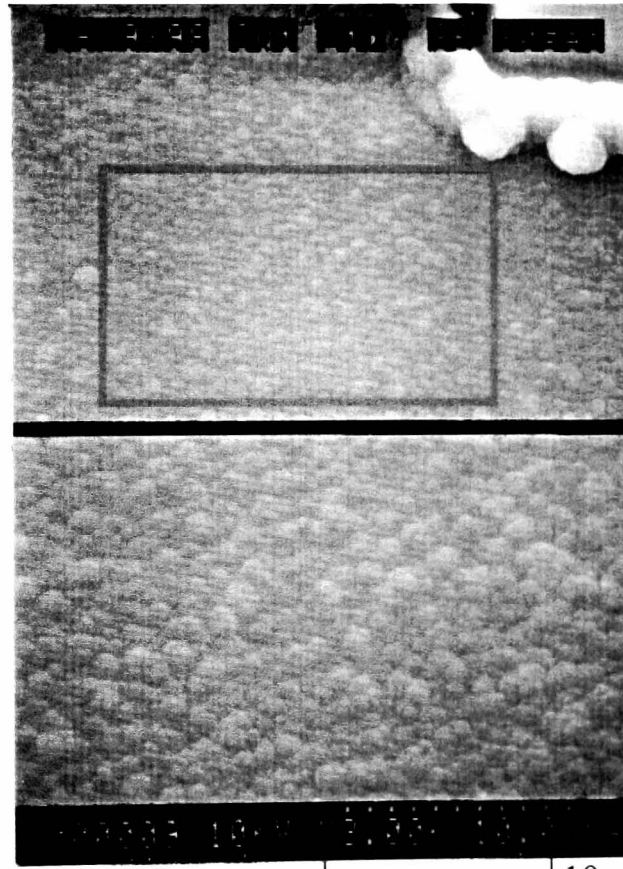
(a)



(b)



(c)



..... | 10 μm

(d)

Figure 2.14 Scanning electron micrographs for polypyrrole films of DecSO<sub>3</sub><sup>-</sup>/PPy at different thicknesses: (a) 5s; (b) 20s; (c) 45s; and (d) 80s. Images recorded with a 10kV electron beam.

### 2.3.1.2 Deposition of polymer on interdigitated electrodes

Polypyrrole films were also deposited on interdigitated electrodes, using a step potential of 0.8V applied to the two interdigitated electrodes alternatively, switching between each of the two electrodes at 1 Hz (controlled by a switch circuit made in-house). The circuit was designed to improve the uniformity of the polymer film by reducing the active area of the electrode and hence, the polymerisation speed, to meet the limitation of monomer diffusion rate in the solution. Figure 2.15 demonstrates a typical polymerisation process at a interdigitated electrode for a  $C_8F_{17}SO_3^-/PPy$  film. It can be seen that the current passed through the electrode was low during the first 40 seconds, which indicates that the two “digits” had not been bridged by the polymer. After 40 seconds, the current started to increase, as a result of the formation of a bridge between the two electrodes. The increase in current was due to a change in the active area of the electrode after the two electrodes were joined by the conducting polymer bridging the gap. The spikes were non-Faradaic currents which were caused by the capacitive effects within the electrodes’ double layers as the potential was switched. It is noted that there was not a sharp step, and the current was not “doubled” after the polymer had joined within the polymerisation time of 50 seconds. This can result from several factors, such as the potential drop across the thin polymers in the gap as well as monomer diffusion limitation.

$DecSO_3^-/PPy$  coatings were prepared on interdigitated electrodes from a solution containing 0.1M pyrrole and 0.1M  $DecSO_3Na$  electrolyte. A step potential of 0.8V was applied to the two interdigitated electrodes alternatively. The electric charge (Q) passed can be calculated in the same way as in Figure 2.11 by integration of the current with time. Figure 2.16 shows the result of charge passed versus the polymerisation time for an interdigitated electrode with total active area of  $7.5 \text{ mm}^2$  (after “polymer bridging”, c.f. Fig 2.17). It can be seen that the relationship between Q and time was also linear with a gradient of  $3.148 \text{ mCcm}^{-2}\text{sec}^{-1}$ . It was noticed that the electric charge passed per unit area was similar although the shape of the electrodes were different. Figure 2.17 is a plot of initial resistance value in natural logarithm (Ln) versus the electric charge passed. Alternatively, the insert shows a linear relationship between  $\text{Ln}(R_0)$  and  $Q^{-1}$ . Since  $R_0$  is inversely proportional to the film thickness in the gap (according to the general relation-

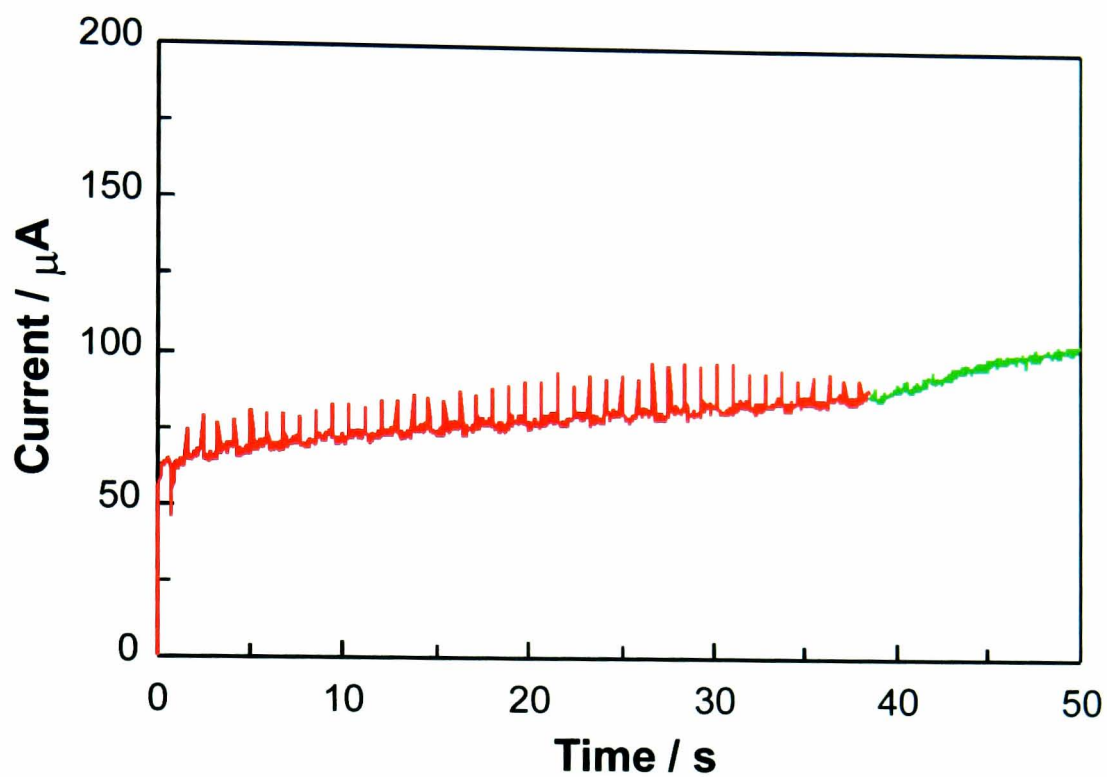


Figure 2.15 shows a typical polymerisation process of  $C_8F_{17}SO_3^-/PPy$  film using an interdigitated electrode, demonstrating the relationship between polymerisation current ( $\mu A$ ) and the time (seconds) during the application of a step potential (0.8 V for 50 s). The gap ( $10 \mu m$ ) was bridged after about 40 s which represented by the green curve. The non-Faradaic currents were caused by the switching between each of the two electrodes.

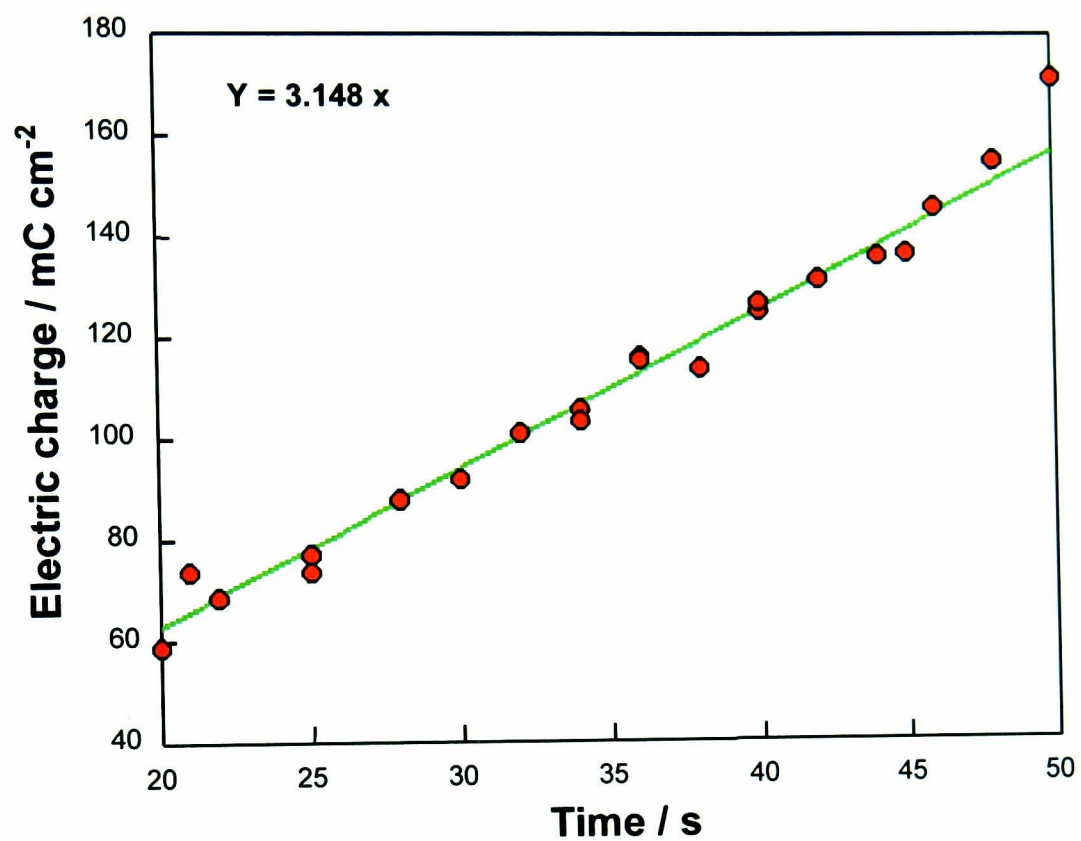


Figure 2.16 Electric charge  $Q$  ( $\text{mC cm}^{-2}$ ) passed versus polymerisation time for a  $\text{DecSO}_3^-$  /PPy film on interdigitated electrodes with  $10 \mu\text{m}$  gap. The green line through the points represents the best linear fit with a slope of 3.148.

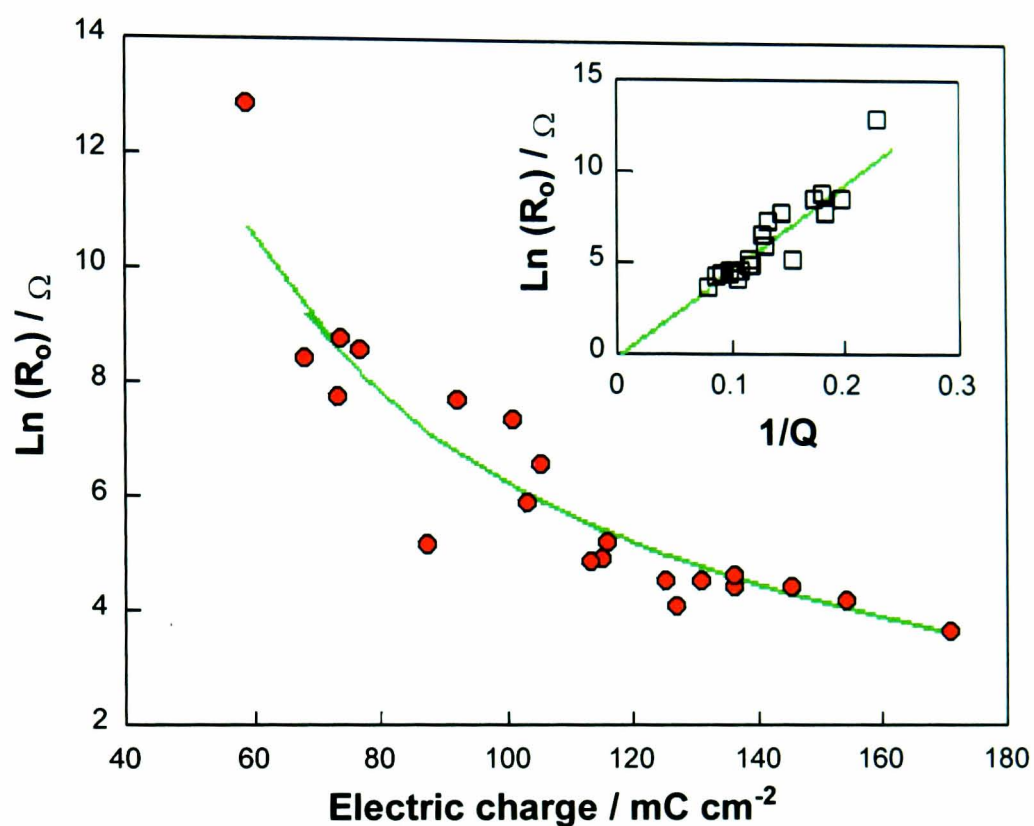
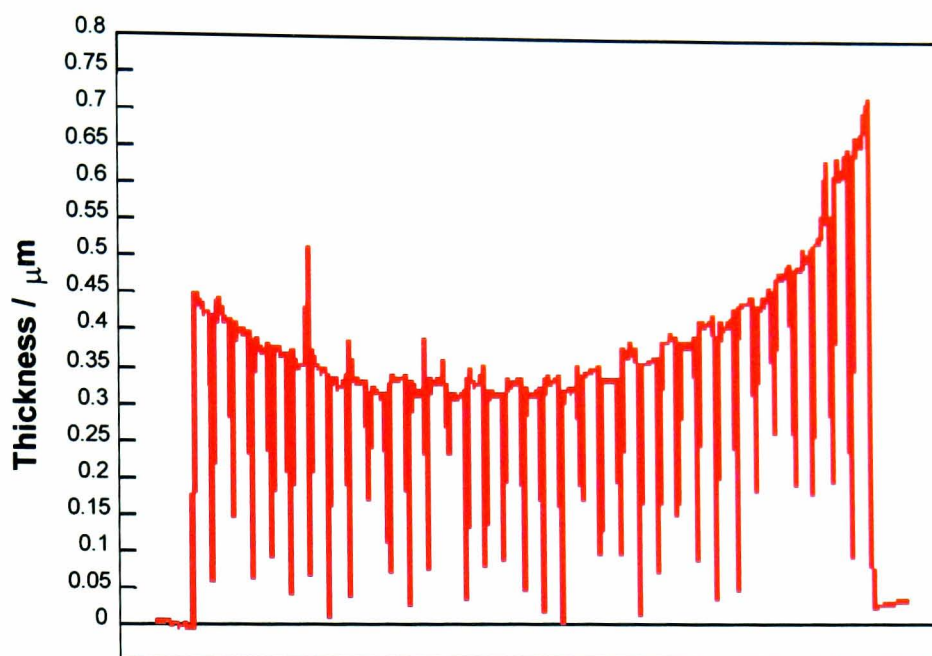


Figure 2.17 Plot of initial resistance value (as natural logarithm) versus electric charge  $Q$  ( $\text{mC cm}^{-2}$ ) passed during the polymerisation of  $\text{DecSO}_3^-/\text{PPy}$  film on interdigitated electrodes (gap =  $10 \mu\text{m}$ ). The green curve through the red points represents the best fit to the equation  $\text{Ln}(R_0) = 630.2 / Q$ . Inserted picture shows a linear relationship between  $\text{Ln} R$  and  $Q^{-1}$ .

ship between resistance and material geometry), the linear relationship between  $Q$  and thickness shown in Figure 2.13 indicates that lateral growth does not follow the same linear relationship between film thickness and polymerisation time. The data suggests an exponential relationship between the average thickness in the gap and the polymerisation time.

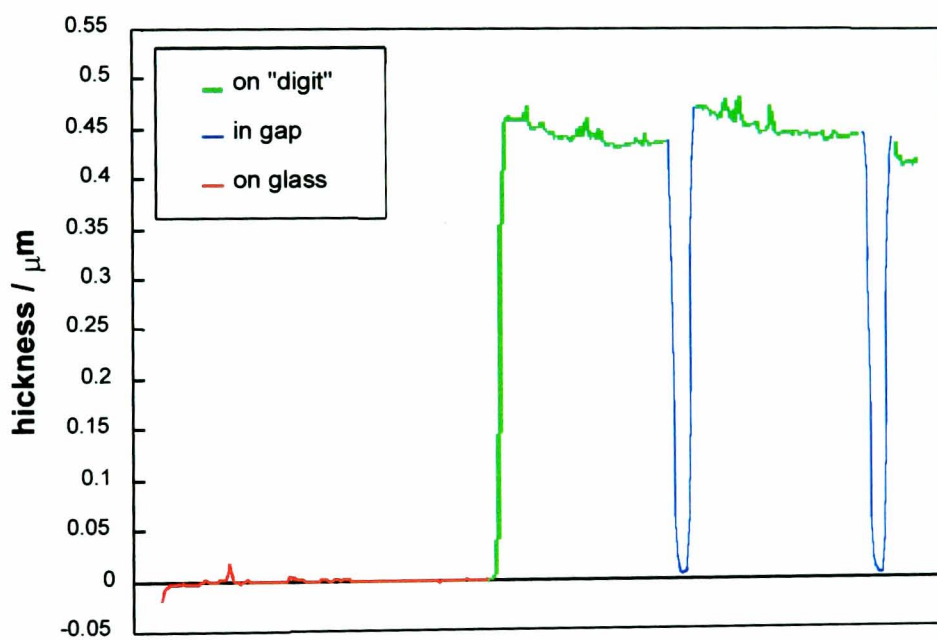
From Figures 2.16 and 2.17 it can be seen that initially, during a polymerisation time between 20 to 25 seconds, the electric charge passed was below 6 mC, and the sensor initial resistance values were between 7 to 400 k $\Omega$ , indicating that there were only few places which were bridged by the polymer. Subsequently, between the time period 25 to 40 seconds, the electric charge increased from 6 mC to 9 mC, and the resistance value became lower with a greater scatter of the values. This could be explained by the increased bridging between the gap due to the poor uniformity of polymer growth. The final phase of polymer growth related to the time after 40 seconds, when electric charge passed was more than 9 mC. With the increase of  $Q$  passed, the resistance became lower with a more controllable film growth process. At this stage, most of the gap was joined by the polymer. With increasing polymerisation time, the thickness of the film increased and the resistance decreased. As will be seen in a later Section 2.3.1.4, for each different polymer film coated on interdigitated electrode, there are a particular range of initial baseline resistances. For the DecSO<sub>3</sub><sup>-</sup>/PPy coating, the “best” initial resistance range is 120 to 150  $\Omega$ , which is at the polymerisation stage that the gap was completely joined.

The polymer film thickness of three electrodes, with representative resistance values, were measured as 400 k $\Omega$  (less joined), 100  $\Omega$  (ca. “optimal”) and 39  $\Omega$  (overgrown) respectively. For the 400 k $\Omega$  electrode, as shown in Figure 2.18 (a) and (b), the thicknesses were 0.45  $\mu\text{m}$  and 0.7  $\mu\text{m}$  at the top and bottom of the electrode and 0.35  $\mu\text{m}$  in the middle area, the polymer thickness in the gap was 0.006  $\mu\text{m}$ , the width of gap remained was 9.51  $\mu\text{m}$  (This is for the first gap at the top end). For the 100  $\Omega$  electrode, the thicknesses were 0.9  $\mu\text{m}$  and 1.3  $\mu\text{m}$  at the top and bottom of the electrode and 0.8  $\mu\text{m}$  in the middle, the polymer in the gap was 0.037  $\mu\text{m}$ , the width of gap remained was 5.38  $\mu\text{m}$ . For the 39  $\Omega$  electrode, the thicknesses were 1.2  $\mu\text{m}$  and 1.7  $\mu\text{m}$  at the top and bottom of the electrode and 1.1  $\mu\text{m}$  in the middle, the polymer in the gap was 0.31  $\mu\text{m}$ , the width of gap remained as 4.18  $\mu\text{m}$ . The thickness of gold electrode was 0.09  $\mu\text{m}$ .



Scan across electrode from top to bottom

(a)



Scan across electrode from top to bottom

(b)

Figure 2.18 DecSO<sub>3</sub><sup>-</sup>/PPy polymer film thickness on interdigitated electrode. (a) scan across electrode from top to bottom for 3 mm and; (b) scan across two gaps for 150 μm.

From these measurements, it can be seen that the polymer geometry for electrode with the “best” initial resistance is ca. 0.04  $\mu\text{m}$  in gap which is less than a half of gold electrode thickness (0.09  $\mu\text{m}$ ) and about 1  $\mu\text{m}$  on “digit” which is more than ten times of the thickness of gold electrode. It is also noted that the polymer growth laterally across the gap (10  $\mu\text{m}$  in width) is faster than the increase in thickness on the “digit” (between 0.45 to 1.7  $\mu\text{m}$ ).

The conductivity of the polypyrrole film can be roughly estimated using the Ohm’s Law and measured geometric parameters. For example, given the resistance value as 100  $\Omega$  and the pyrrole film geometry parameter as 10  $\mu\text{m}$  in length, 10 cm in width (20 pairs of “fingers”) and 0.037  $\mu\text{m}$  in thickness, the conductivity can be calculated as 0.27 S  $\text{cm}^{-1}$ .

Two different types of polymers, DecSO<sub>3</sub><sup>-</sup>/PPy and PF<sub>6</sub><sup>-</sup>/PPy, were chosen as examples to test the fabrication consistency for a batch production. Referring to the result in Section 2.3.1.4, the initial resistance for DecSO<sub>3</sub><sup>-</sup>/PPy was 120  $\Omega$  to 150  $\Omega$ , and 60  $\Omega$  to 100  $\Omega$  for PF<sub>6</sub><sup>-</sup>/PPy. A set of 10 sensors were made successively. After a step potential had been applied for a certain length of time, 50 seconds for DecSO<sub>3</sub><sup>-</sup>/PPy polymer coating and 25 seconds for PF<sub>6</sub><sup>-</sup>/PPy polymer coating, the resistance was measured in solution, and if necessary, an additional 1 to 3 seconds step potential was applied to adjust the resistance to its desired value.

Figure 2.19 shows the results of the consistency of a small batch fabrication. The standard derivation value were 8.4  $\Omega$  for DecSO<sub>3</sub><sup>-</sup>/PPy polymer coating and 9.6  $\Omega$  for PF<sub>6</sub><sup>-</sup>/PPy polymer coating. The response sensitivity consistency to odorant will be shown in a later Section 2.3.2.7.

### *2.3.1.3 Deposition of polymer on QCM electrodes*

The electrochemical polymerisation method used to prepare polypyrrole films on QCM electrode was similar to that used for interdigitated electrode, although the two gold electrodes on both sides of the QCM electrode need be coated separately. Figure 2.20

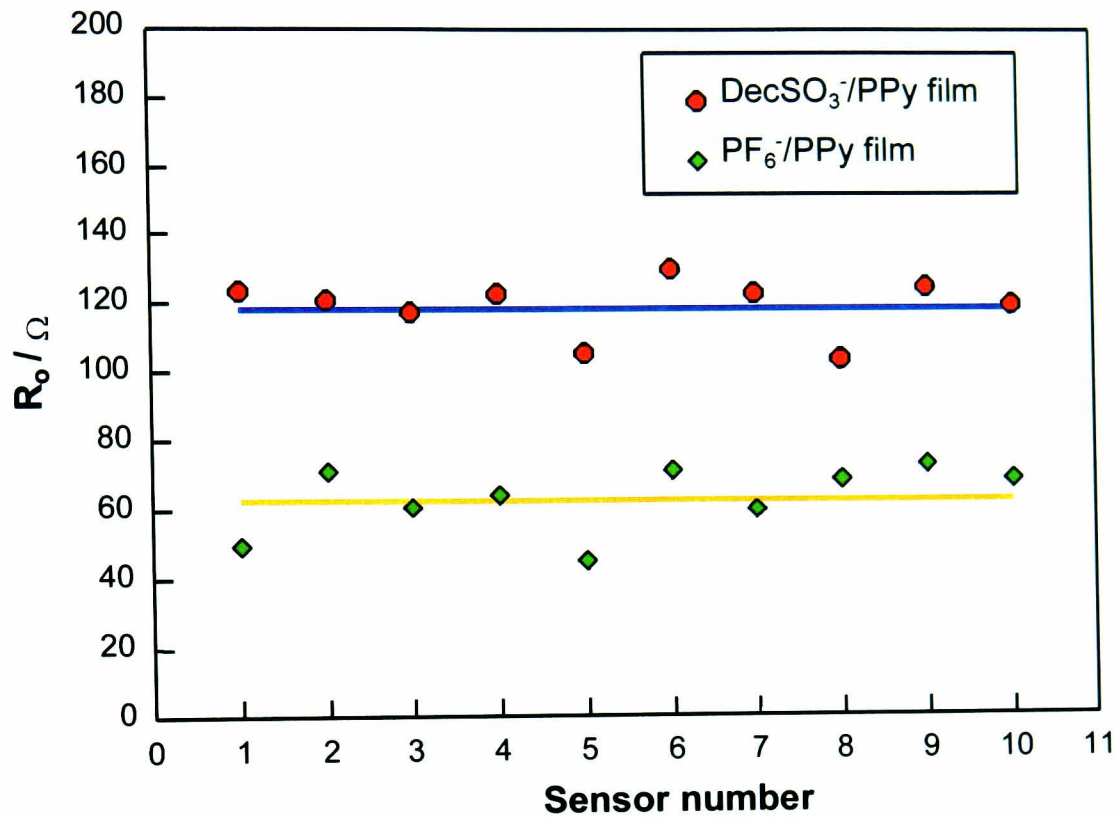


Figure 2.19 shows the result of the fabrication consistency of a small batch of ten interdigitated electrode sensors by showing the initial resistance values  $R_0$  versus number of sensors successively made of DecSO<sub>3</sub><sup>-</sup>/PPy film (●) and PF<sub>6</sub><sup>-</sup>/PPy film (◆). The straight lines through the points represent the average values of two initial resistances. For DecSO<sub>3</sub><sup>-</sup>/PPy film, average  $R_0 = 119.2\Omega$ ; and for PF<sub>6</sub><sup>-</sup>/PPy film, average  $R_0 = 63.2\Omega$ .

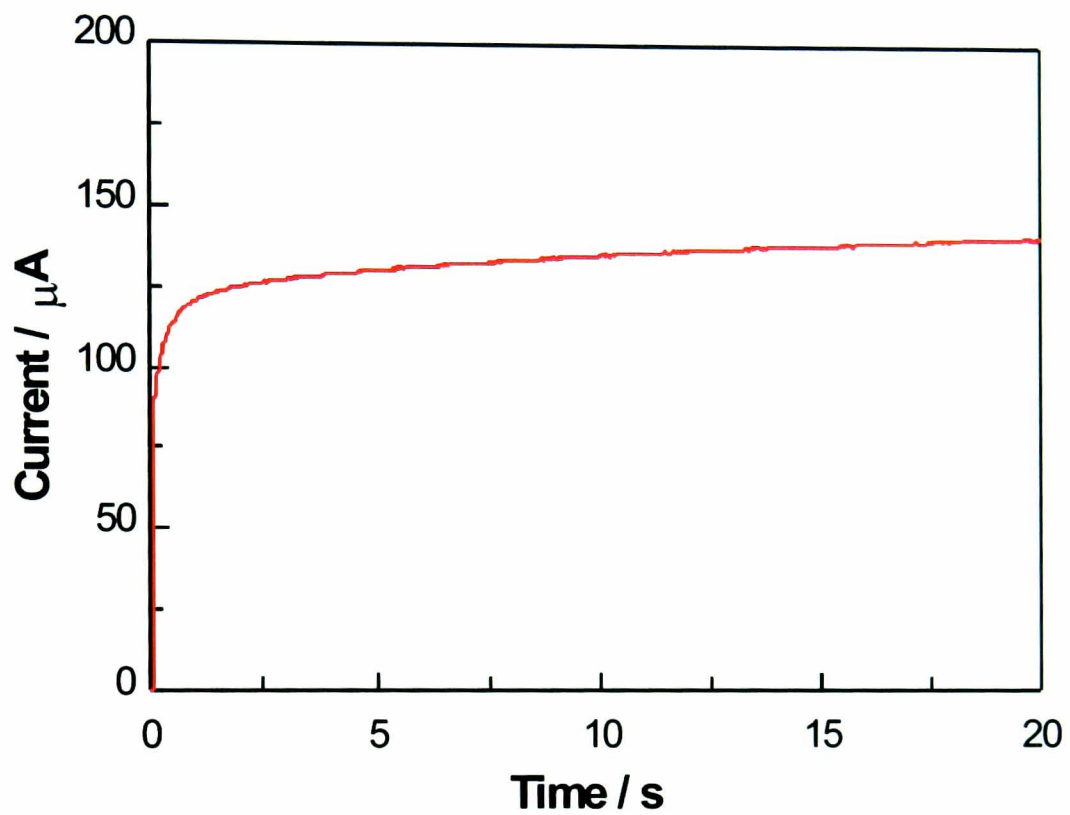


Figure 2.20 shows a typical polymerisation process of C<sub>8</sub>F<sub>17</sub>SO<sub>3</sub><sup>-</sup>/PPy film on a QCM electrode, indicating the relationship between polymerisation current and the time a step potential (0.8 V) applied.

shows a plot of polymerisation current versus time on one side of a QCM electrode using a step potential of 0 to 0.8V. Again, the electric charge passed can be calculated by integration.

The surface of the gold coated QCM is rough and hence the thickness of the film can not be easily measured by the Dektak. However it can be evaluated according to the Sauerbrey equation [33] by the frequency shift caused by the coating (3.6 kHz for this coating), the geometric area of the electrode ( $19.63 \text{ mm}^2$  for this QCM electrode), and the general density of the coating material which is  $1.48 \text{ g/cm}^3$  according to the literature [89]. The average film thickness shown in Figure 2.20 is calculated as about  $0.1 \text{ }\mu\text{m}$ . For a 10 kHz coating, the average film thickness is about  $0.3 \text{ }\mu\text{m}$ .

#### *2.3.1.4 Baseline resistance stability with time*

To examine the baseline resistance stability across interdigitated electrodes with time for each of the 16 polymers, described earlier in Section 2.2.4.4, interdigitated electrodes were covered by different types of polymers, with initial resistance values ranging from  $20 \text{ }\Omega$  to  $21 \text{ k}\Omega$ . Resistance changes were measured as a function of time during a period of up to 270 days. By analysing these changes, a range of “optimal” individual initial resistance could be determined, maintaining the resistance value below  $500 \text{ }\Omega$  after 6 months. Data are listed in Appendix.

Figure 2.21 (a) to (j) show histograms for (1) to (10) coatings. It can be seen that the drift in resistance is faster when the initial resistance value is higher, which corresponds with the case when the film thickness is thinner. This suggests that although a thinner film can give higher sensitivity to sample vapours (see later), it is also less stable with time. As a consequence, there is an “optimal” initial resistance value for each individual polymer, providing a resistive sensor with optimised characteristic, with both good sensitivity and stability. These resistances are evaluated as  $100\text{-}150 \text{ }\Omega$  for film (a)  $\text{SDSO}_4^-/\text{PPy}$ , (b)  $\text{DecSO}_3^-/\text{PPy}$ , (c)  $\text{HexSO}_3^-/\text{PPy}$ , (f)  $\text{Tos}^-/\text{PPy}$ , (g)  $\text{PF}_6^-/\text{PPy}$ , and (j)  $\text{C}_8\text{F}_{17}\text{SO}_3^-/\text{PPy}$ ;  $50\text{-}70 \text{ }\Omega$  for film (d)  $\text{ButSO}_3^-/\text{PPy}$ , (e)  $\text{EtSO}_3^-/\text{PPy}$ , and (h)  $\text{PF}_6^-/\phi\text{Ppy}$ ; and  $30\text{-}40 \text{ }\Omega$  for film (i)  $\text{CF}_3\text{SO}_3^-/\text{PPy}$ .

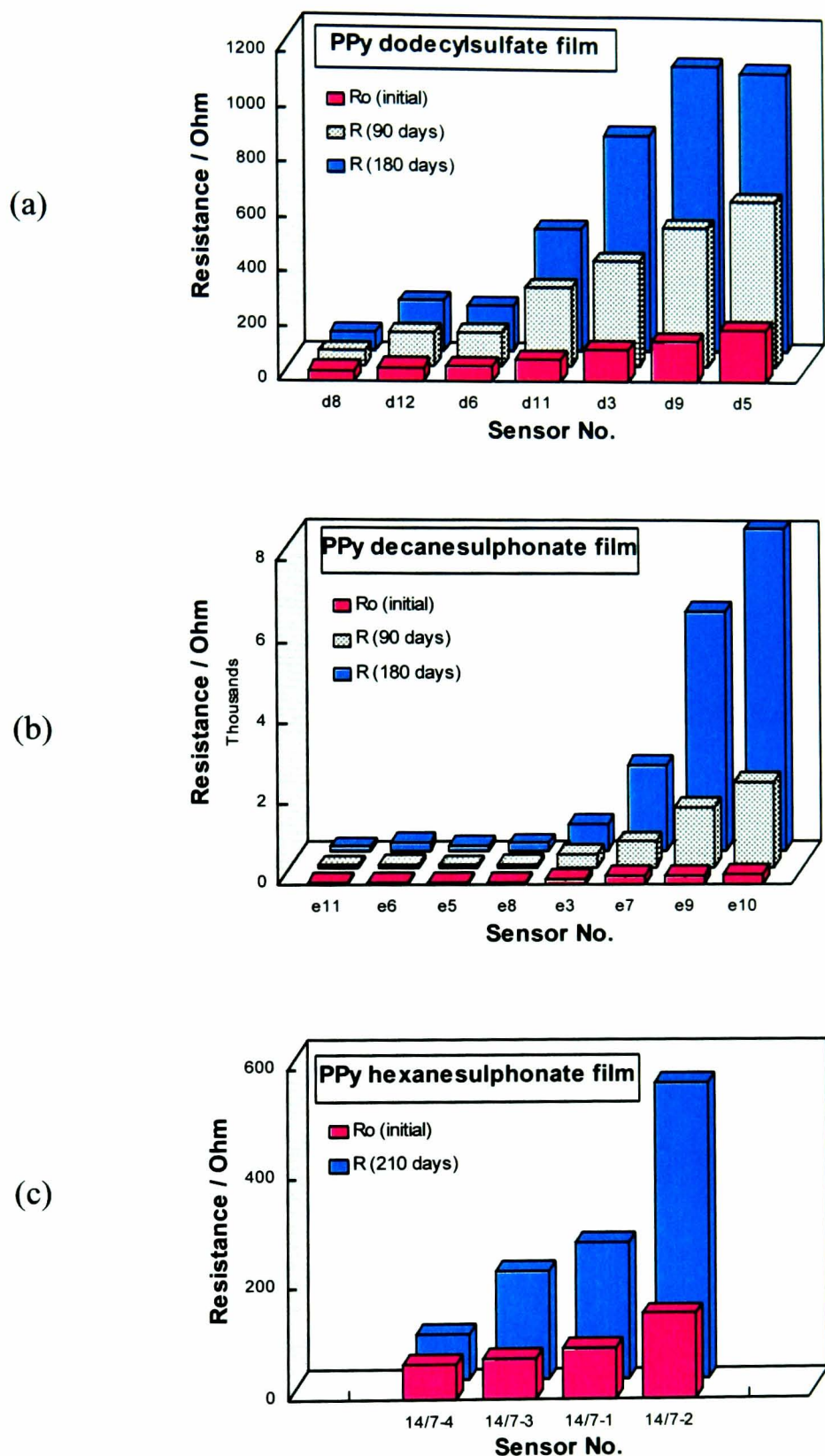
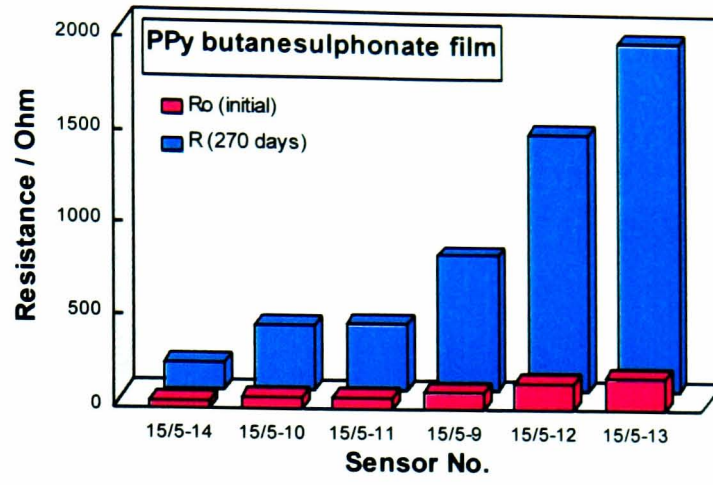
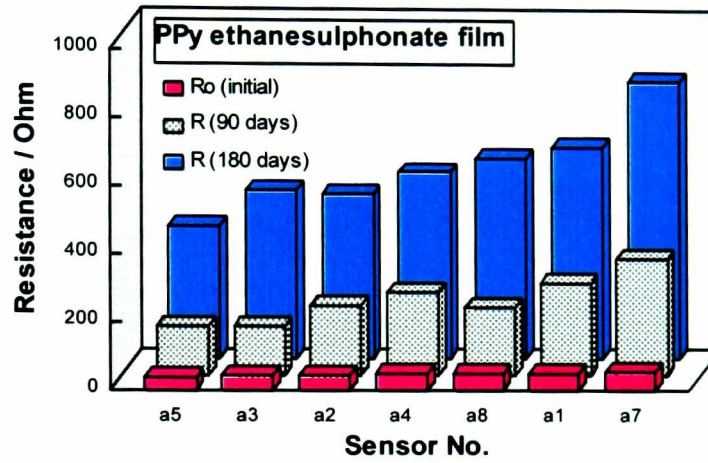


Figure 2.21 Interdigitated electrode sensor baseline resistance stability with time. Sensors were coated with polypyrrole films containing different types of counterions. (a)  $\text{SDSO}_4^- / \text{PPy}$ ; (b)  $\text{DecSO}_3^- / \text{PPy}$ ; (c)  $\text{HexSO}_3^- / \text{PPy}$ ; (d)  $\text{ButSO}_3^- / \text{PPy}$ ; (e)  $\text{EtSO}_3^- / \text{PPy}$ ; (f)  $\text{Tos}^- / \text{PPy}$ ; (g)  $\text{PF}_6^- / \text{PPy}$ ; (h)  $\text{PF}_6^- / \phi\text{PPy}$ ; (i)  $\text{CF}_3\text{SO}_3^- / \text{PPy}$ ; and (j)  $\text{C}_8\text{F}_{17}\text{SO}_3^- / \text{PPy}$ .

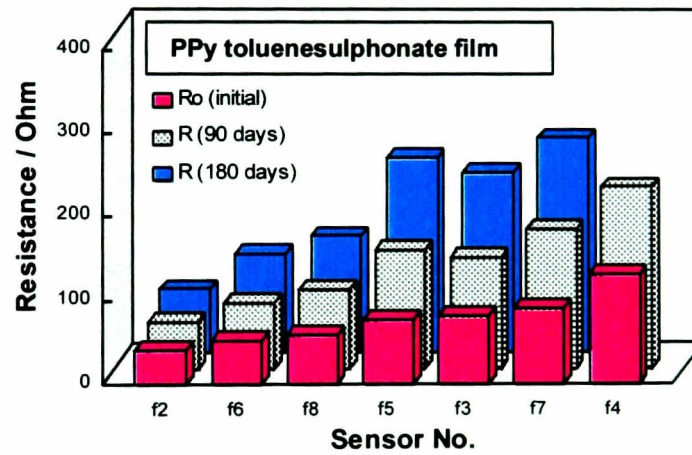
(d)



(e)



(f)



(g)

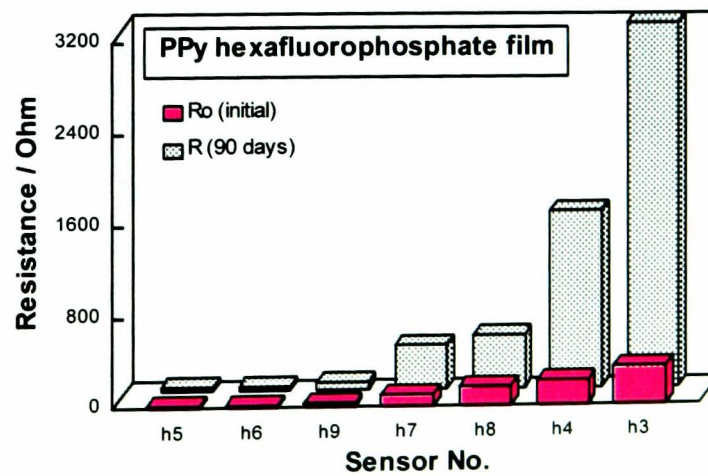
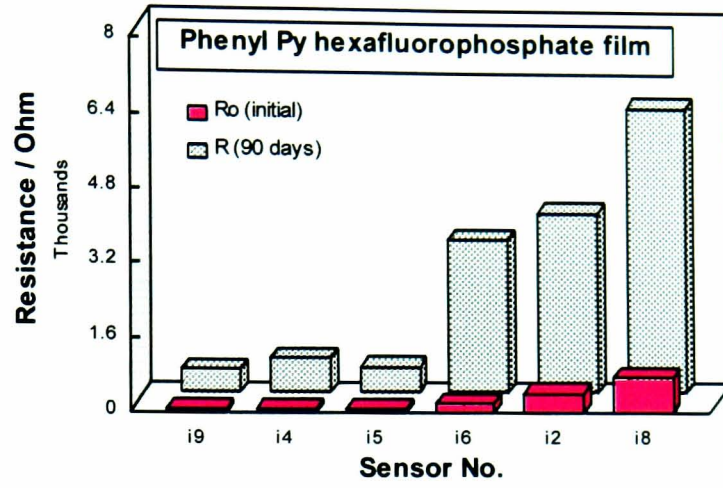
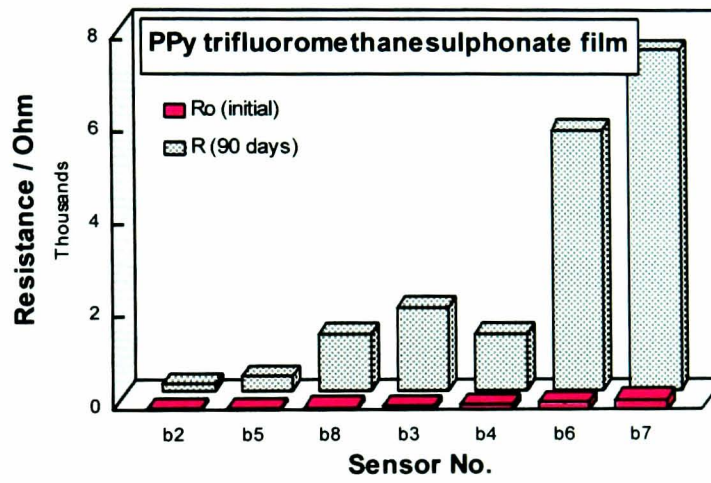


Figure 2.21 Continued.

(h)



(i)



(j)

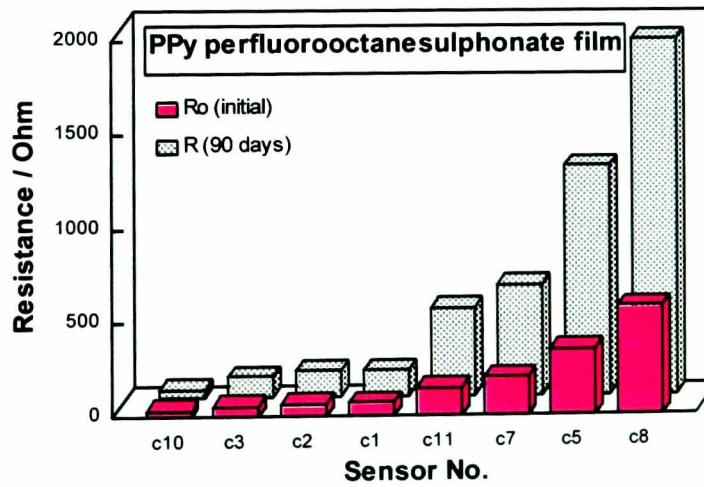


Figure 2.21 Continued.

## 2.3.2 Measurement of Vapours with Interdigitated Electrodes and QCMs

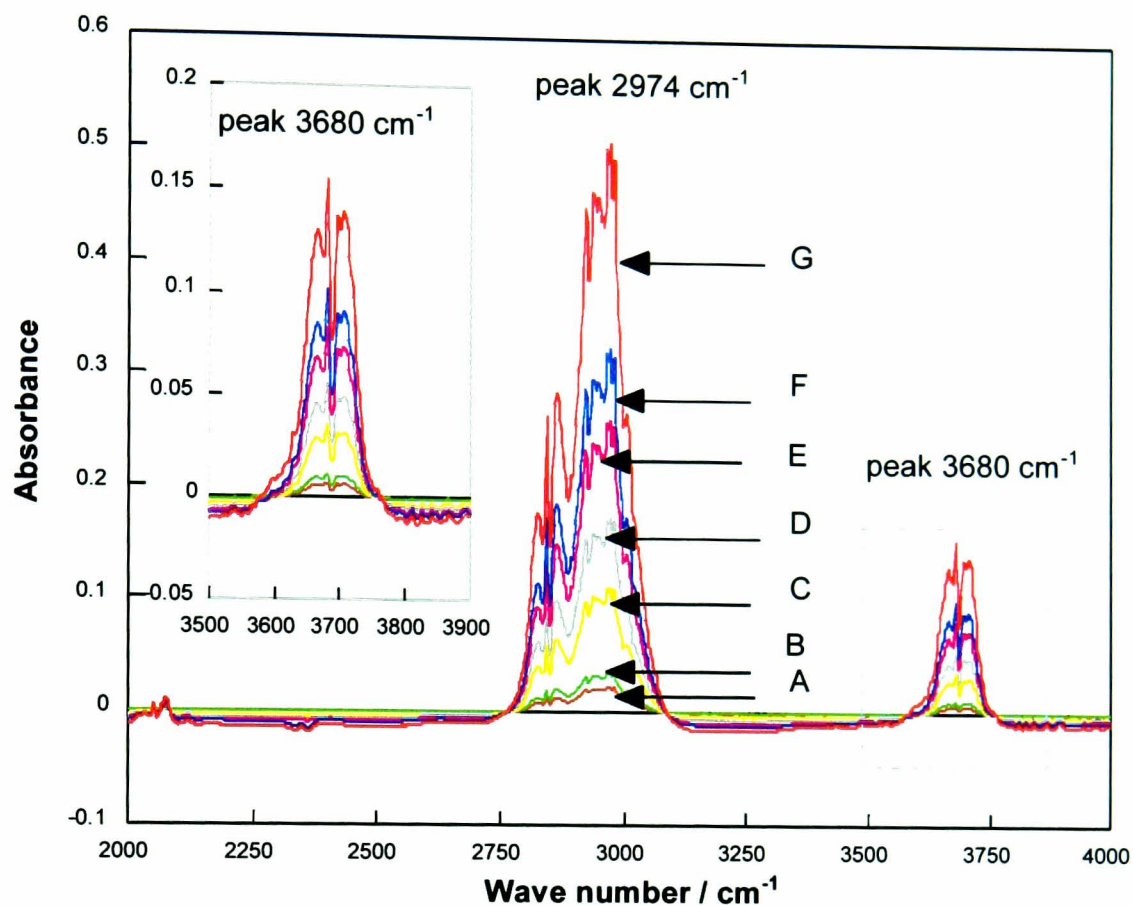
### 2.3.2.1 Effect of flow rate and use of FT-iR

Flow meters were calibrated by the use of an in line FT-iR measurement using methanol as sample vapour. To achieve this, methanol was diluted by pure nitrogen to different extents and the FT-iR absorption peak at  $3680\text{ cm}^{-1}$  characteristic of the –OH stretch or  $2974\text{ cm}^{-1}$  for C-H vibration [125] were used to calibrate the concentrations relative to saturated methanol vapour. Figure 2.22 shows the FT-iR absorption spectra for methanol vapours at different concentrations. Figure 2.23 is a plot of absorption peak intensities for each of the concentration versus relative methanol concentrations determined by ratios of flow. Each concentration was measured 6 times and mean results are presented. Figure 2.24 shows the calibration curve for the flow system by comparing the FT-iR calibrated relative vapour concentration with those from the flow meters reading. It can be seen that the calibrated line approximates to a straight line. The shape of the calibration curve shows that dilutions were not linear at increased flow rates.

### 2.3.2.2 Optimisation of recovery

It was found in the experiments that water vapour could improve the recovery of QCM and interdigitated electrode sensors to their original baseline after they measured odorant samples by “washing” the sensor. Figure 2.25 shows a typical cycle of measurements to methanol. Both the sensing and recovering process is shown in this figure and the role of water vapour can be clearly seen. The blue line in Figure 2.25 labelled by “recovery without wash” is an extra-plotted line which demonstrates an usual recovery observed in a process without the water vapour “washing”.

At  $25\text{ }^{\circ}\text{C}$ , the vapour pressure of water is  $3.1690\text{ kPa}$ , which is equivalent to  $23.77\text{ mm Hg}$  [123]. The water vapour concentration used was 50% diluted of saturated vapour. Since a pressure value of 1 atmosphere is equal to  $760\text{ mm Hg}$  and the unit ppm refers to



	$N_2$ (MeOH) $cm^3 min^{-1}$	$N_2$ $cm^3 min^{-1}$
A	5	200
B	10	190
C	25	180
D	50	140
E	75	130
F	100	100
G	50	0

Figure 2.22 FT-iR absorption spectra of methanol vapour diluted at different levels by pure nitrogen. Table below shows the nitrogen flow rates of bubbling the methanol solution and diluting methanol to different concentrations. The total flow rates were kept at  $200 cm^3 min^{-1}$ .

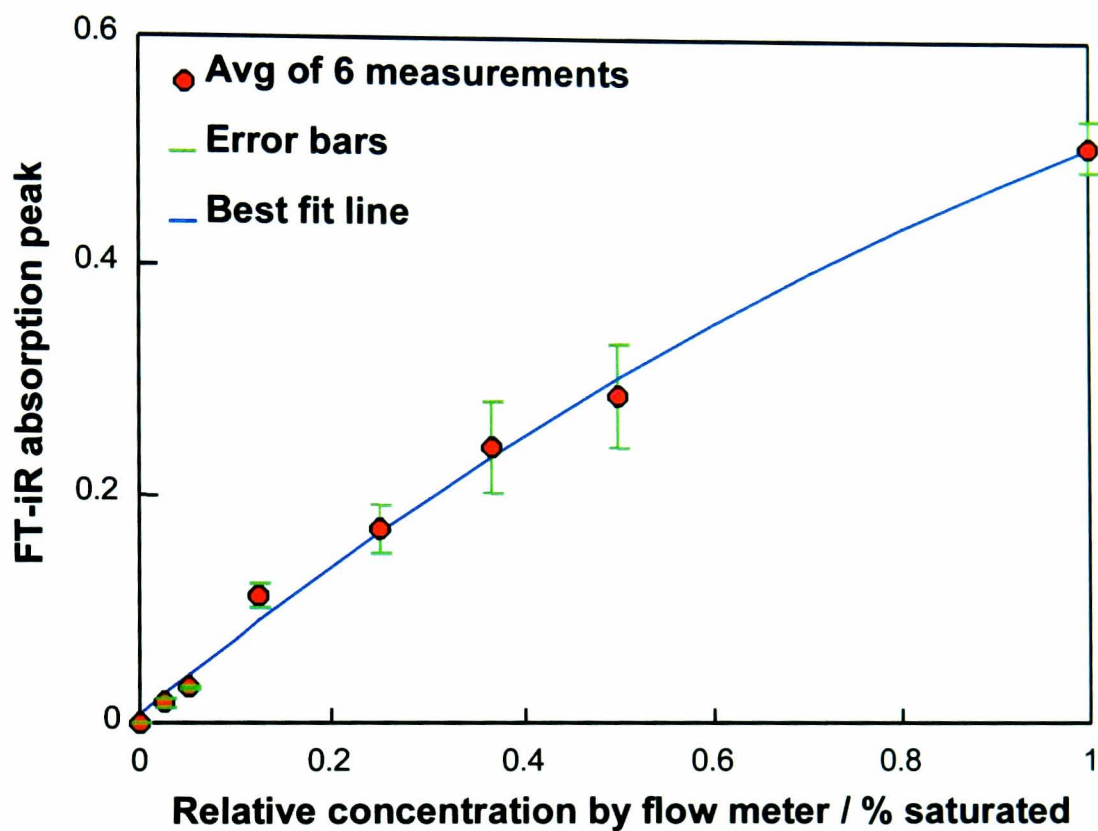


Figure 2.23 Plot of FT-iR absorption peak intensity versus relative methanol concentration, calculated by the flow rates of the corresponding flow meters. The blue curve is the calibration result represented by the equation  $y = 0.1817x^2 + 0.6766x + 0.0103$  with the R-squared value 0.994.

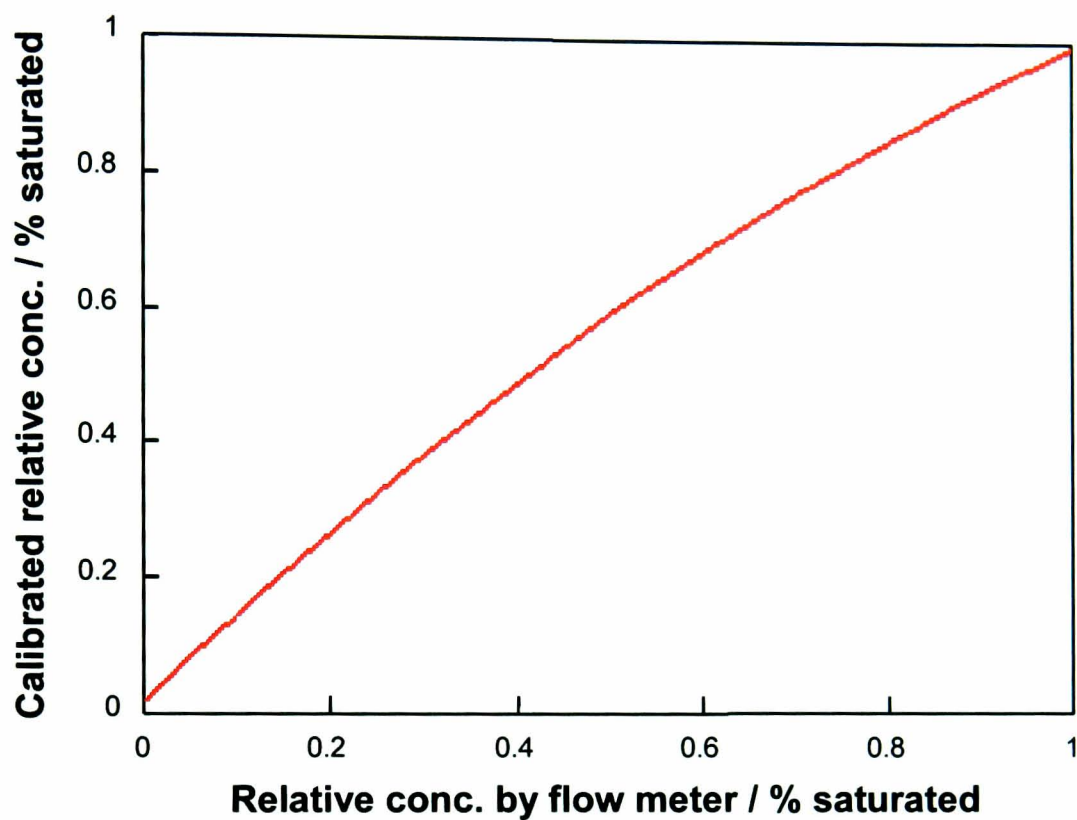


Figure 2.24 shows the relative vapour concentration calibration curve for the flow system, obtained using FT-iR calibrated concentration versus calculated concentration by flow rates. The equation describing the curve is:  $y = -0.3579x^2 + 1.3327x + 0.0203$ . The R-squared value is 0.994.

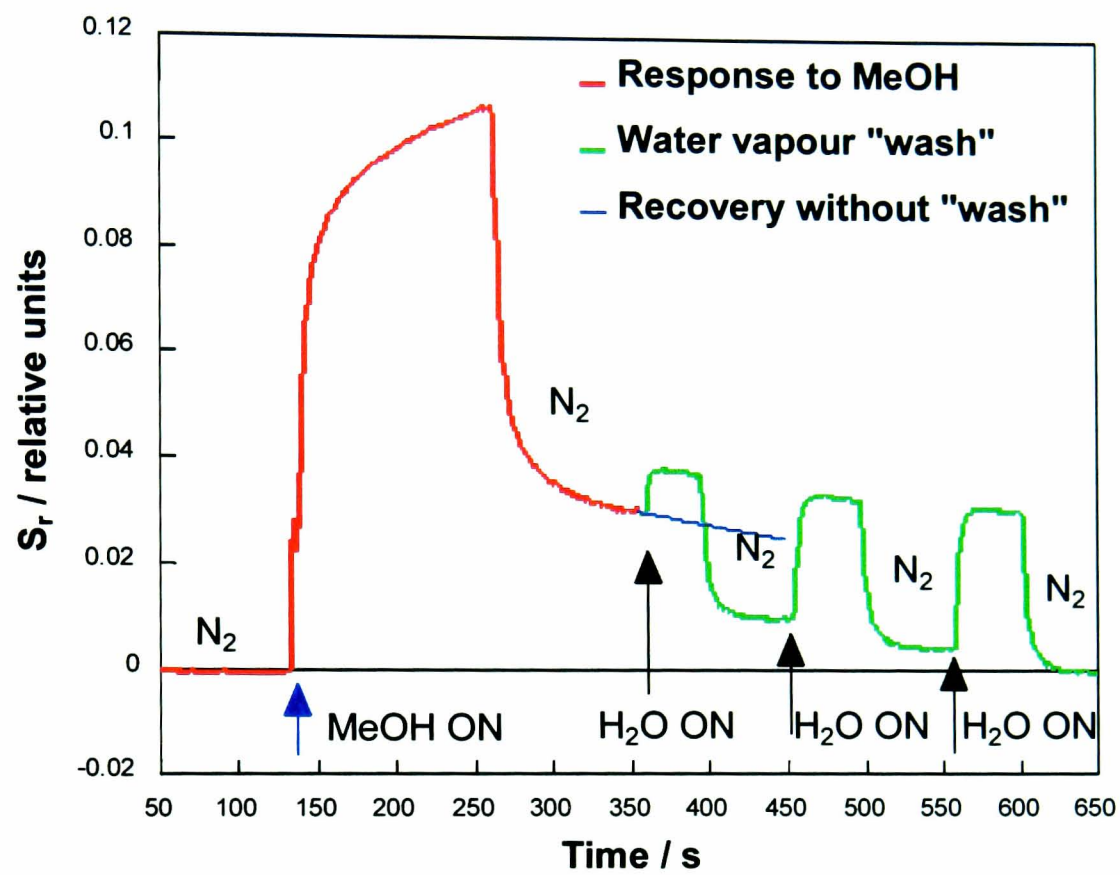


Figure 2.25 A typical measurement cycle to 50% methanol vapour and effect of water vapour purging on the recovery of sensor baseline resistance.

a fraction of  $10^{-6}$ , then, to estimate a vapour concentration in ppm at atmosphere pressure (which is 1 atoms), the following Equation (2-2) was used:

$$C(ppm) = \frac{V.P.(mm\ Hg)}{760(mm\ Hg)} \times 10^6 \quad (2-2)$$

where  $C(ppm)$  is the vapour concentration in ppm and  $V.P. (mm\ Hg)$  is the corresponding vapour pressure (in mm Hg).

For a 50% diluted saturated water vapour, the concentration was estimated using Equation 2-2 as ca.  $1.5 \times 10^4$  ppm.

### 2.3.2.3 Effect of humidity

All of the examined polymer coatings show responses to water vapour to various extents. Responses of eight different polymers to 50% saturated water vapour and 50% methanol vapours were compared. Table 2.2 summarises the results of  $S_r$  (which is the relative resistance change of microresistor when exposed to the tested vapour) from which the effect of water vapour can be evaluated for each polymer coating.  $R_0$  is the baseline resistance value.

Counterions	Monomer	$R_0$ ( $\Omega$ )	$S_r$ to H <sub>2</sub> O	$S_r$ to MeOH
SDSO <sub>4</sub> <sup>-</sup>	Py	199	0.026	0.029
DecSO <sub>3</sub> <sup>-</sup>	Py	186	0.032	0.032
EtSO <sub>3</sub> <sup>-</sup>	Py	449	0.024	0.035
Tos <sup>-</sup>	Py	251	0.071	0.059
PF <sub>6</sub> <sup>-</sup>	Py	101	-0.018	0.037
PF <sub>6</sub> <sup>-</sup>	$\phi^*$ Py+20 $\mu$ lPy	7200	0.063	0.073
CF <sub>3</sub> SO <sub>3</sub> <sup>-</sup>	Py	537	0.074	0.072
C <sub>8</sub> F <sub>17</sub> SO <sub>3</sub> <sup>-</sup>	Py	561	0.049	0.069

Table 2.2 Effect of water vapour ( $\phi$  : N-phenyl pyrrole)

### 2.3.2.4 Mixing of gases

Mixtures of methanol and ethanol were prepared for multi-component analysis. FT-iR measurements were carried out to analyse the mixing ratio of the two vapours. The FT-iR absorption peak at  $3680\text{ cm}^{-1}$  represent the total alcohol concentration (due to the –OH stretch). Figure 2.26 show the result of FT-iR absorption spectra over this range. The absorption band in the range  $1150\text{-}1450\text{ cm}^{-1}$  represents the difference of methanol and ethanol [125], which is shown by Figure 2.27 and can be used to calculate the ratio of the two alcohols.

A second method of calibrating the vapour mixture was also used which involved the calibrated flow meter's reading and vapour pressure data [123], providing that the saturated vapour pressure for both methanol and ethanol are known. Figure 2.28 (a) and (b) show a plot of vapour pressure (in mm Hg) versus temperature ( $^{\circ}\text{C}$ ) using data from the CRC handbook [123]. Given that the saturated vapour pressure of methanol at  $25^{\circ}\text{C}$  is 117.5 mm Hg and ethanol 57.5 mm Hg, a calibration can be done using the following Equation 2-3 according to the fraction of molecule numbers carried out by the stream of carrying nitrogen:

$$\frac{C_{MeOH} (ppm)}{C_{Total} (ppm)} = \frac{(F.R.)_{MeOH} (s.v.p.)_{MeOH}}{(F.R.)_{MeOH} (s.v.p.)_{MeOH} + (F.R.)_{EtOH} (s.v.p.)_{EtOH}} \quad (2-3)$$

where *F.R.* represents the calculated reading of the flow meter monitoring the bubblers, and *s.v.p.* the saturated vapour pressure.

Table 2.3 compares the results for these two calibrating methods, showing the excellent correlation between the different approaches. Clearly, the calibration using calibrated flow meter's reading and saturated vapour pressure data is more convenient than the use of the FT-iR spectrophotometer.

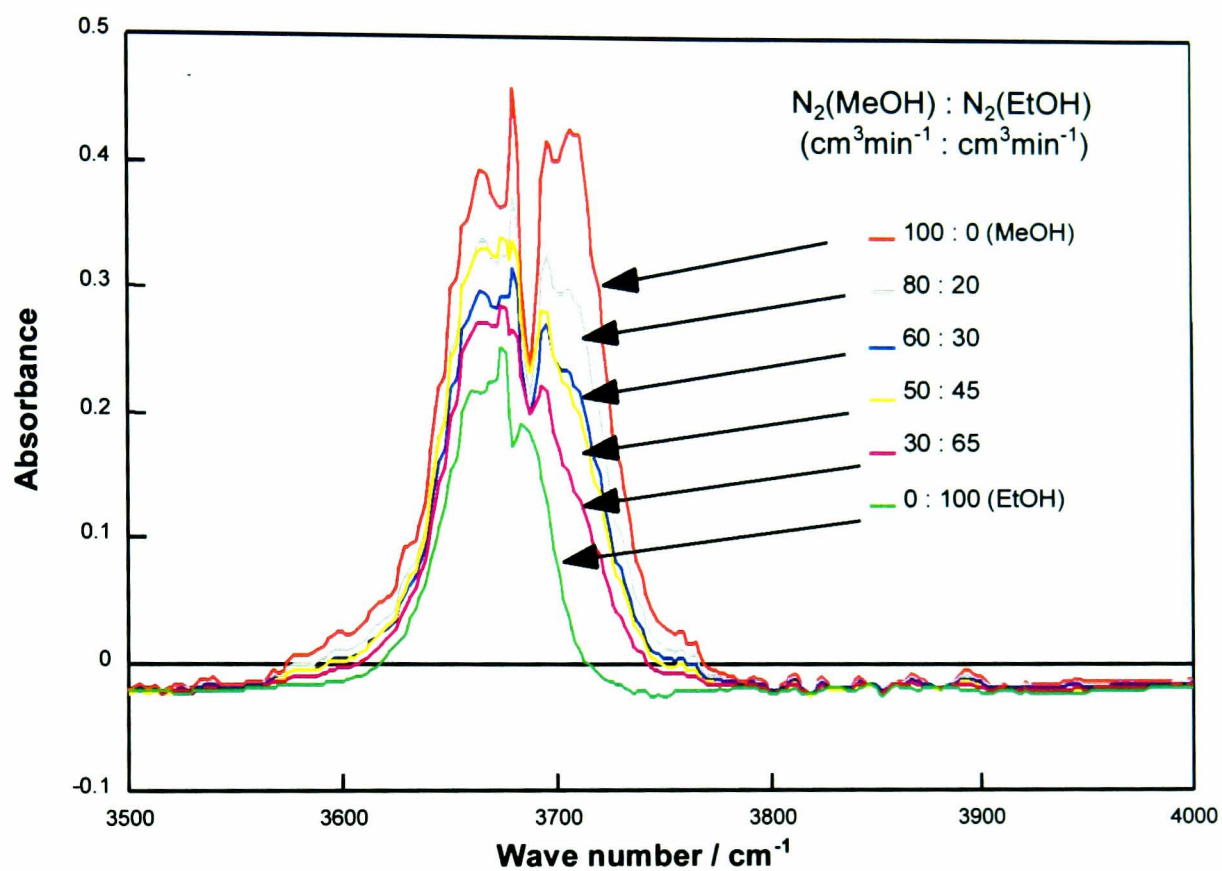


Figure 2.26 FT-iR spectra for a methanol and ethanol mixture at wave number from 3500 to  $4000 \text{ cm}^{-1}$  representing the absorption by  $-\text{OH}$  stretch. The position of the peak is at  $3680 \text{ cm}^{-1}$ .

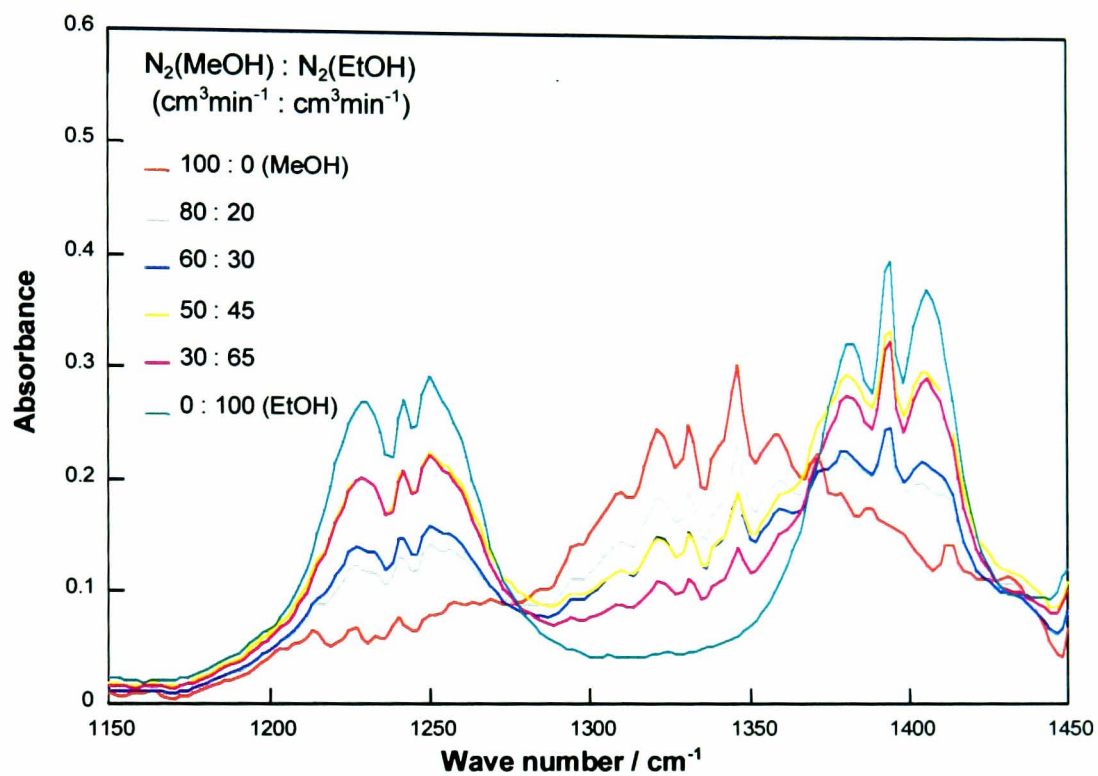
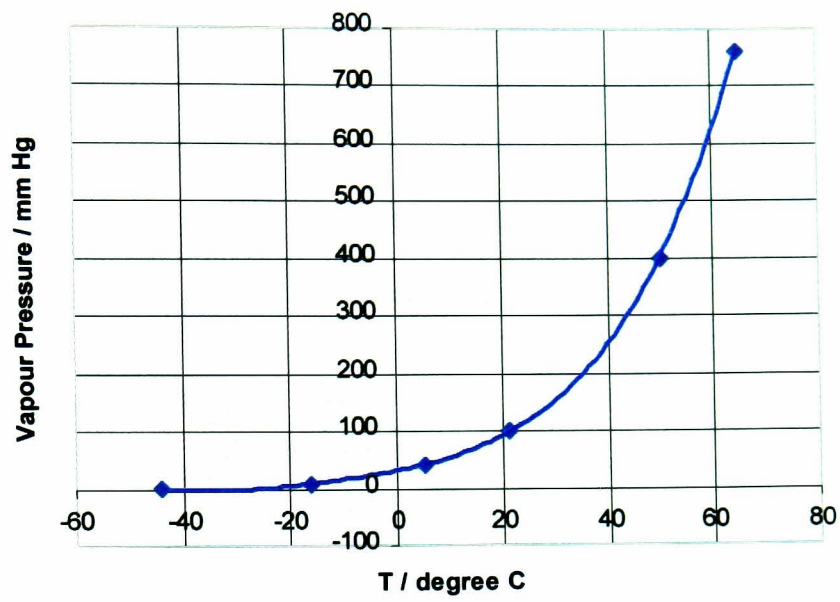
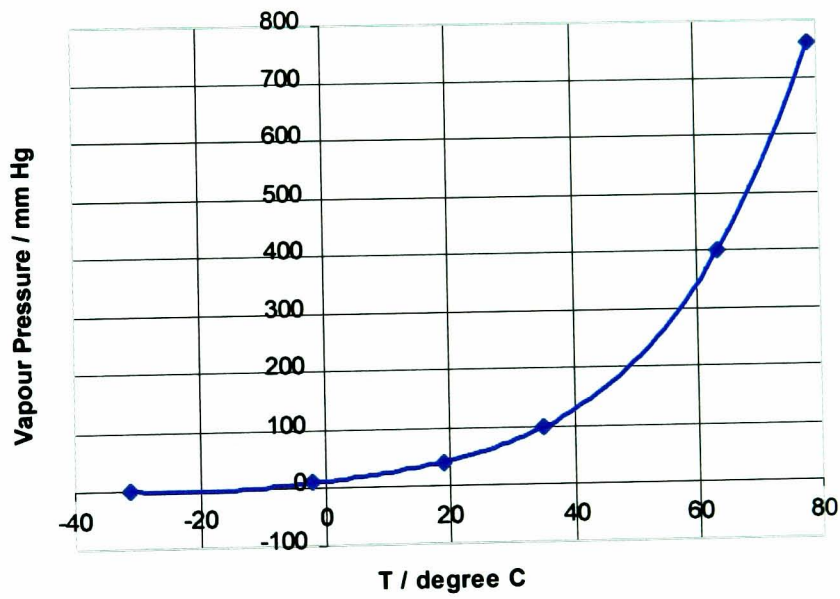


Figure 2.27 FT-iR absorption spectra for methanol and ethanol mixtures at different vibrations from 1150 to 1450 cm<sup>-1</sup>.



(a)



(b)

Figure 2.28 A plot of vapour pressure (mm Hg) versus temperature ( $^{\circ}\text{C}$ ) for (a) methanol and; (b) ethanol.

MeOH flow rate (cm <sup>3</sup> min <sup>-1</sup> )	EtOH flow rate (cm <sup>3</sup> min <sup>-1</sup> )	C <sub>MeOH</sub> /C <sub>total</sub> Cal. by FT-iR	C <sub>MeOH</sub> /C <sub>total</sub> Cal. by s.v.p.
100	0	1.00	1.00
80	20	0.86	0.88
60	30	0.78	0.80
50	45	0.61	0.69
30	65	0.48	0.50
20	80	0.36	0.36
0	100	0.00	0.00

Table 2.3. Comparison of the two concentration calibration methods. In the first and second columns, the flow meters' readings for alcohol carrying nitrogen are listed. The third column lists the calibration result using the FT-iR spectrophotometer. The fourth column lists the result using calibrated flow meter's reading and saturated vapour pressure data obtained from the CRC Handbook.

### 2.3.2.5 Dynamic range measurement

As stated, the sensors dynamic range represents the concentration range over which a sensor provides a continuously changing response [126]. It is bounded by the limit of detection at the low concentration end and by saturation effects at the upper end. Commonly, the limit of detection at the low end is defined as signal-to-noise ratios of two or three, standard deviations around the respective means, corresponding to situations where the signal exceeds the noise at statistical confidence levels of 95% and 99%, respectively.

As already introduced in Section 2.2.5.5, methanol (MeOH) was used as high concentration vapour sample with saturated vapour pressure of 117.5 mm Hg at 25 °C, and decyl alcohol (DecOH) was used as low concentration vapour sample. Figure 2.29 shows a plot of vapour pressure (in mm Hg) against temperature (in °C) for DecOH [123]. An approximate value of saturated vapour pressure for DecOH over an extended range of temperature can be estimated using Clapeyron-Clausius Equation (2-4) [127].

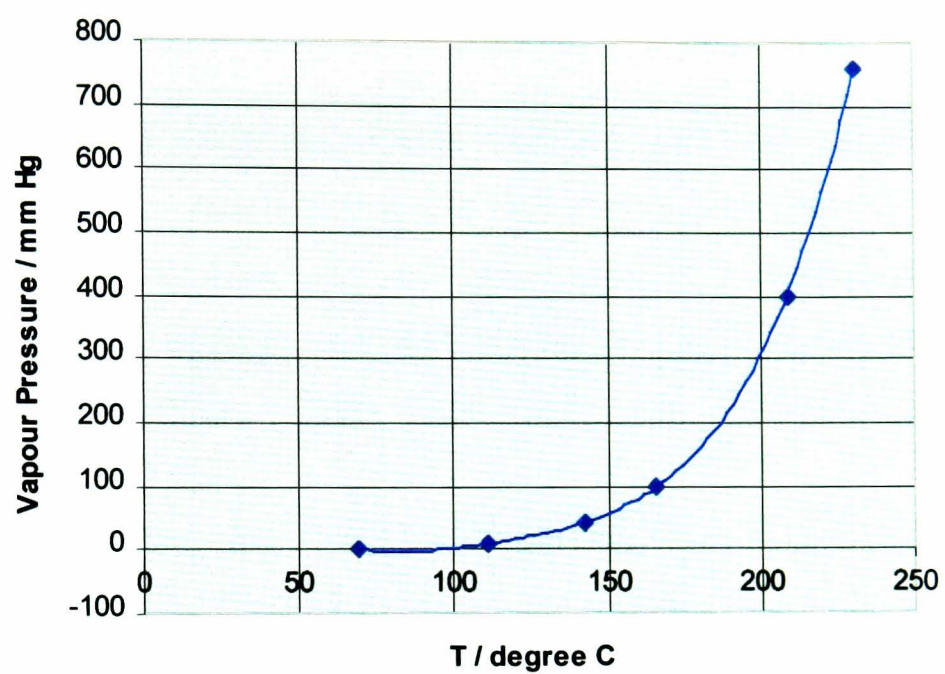


Figure 2.29 A plot of vapour pressure (mm Hg) versus temperature ( $^{\circ}\text{C}$ ) for decyl alcohol.

$$\ln \frac{P_2}{P_1} = \frac{\Delta H_v}{nR} \left( \frac{1}{T_1} - \frac{1}{T_2} \right) \quad (2-4)$$

where  $T_1$  and  $T_2$  are two temperatures,  $P_1$  and  $P_2$  are corresponding vapour pressures. The saturated vapour pressure of DecOH at 25 °C is calculated as 0.042 mm Hg, which corresponds ca. 56 ppm as shown by the inserted plot in Figure 2.29.

Hence, for a saturated methanol vapour, the vapour concentration can be calculated as  $1.54 \times 10^5$  ppm, whilst for DecOH it is 56 ppm. Dilution of MeOH by 50% gives a vapour concentration of ca.  $10^5$  ppm; whilst for DecOH, dilution to 5% give a concentration of ca. 3 ppm. Sensors covered with different polymer coatings were tested using these two gaseous samples. Both QCM and interdigitated electrode sensor responses were measured, with Figure 2.30 showing QCM sensors responses at both lower and upper range for DecSO<sub>3</sub><sup>-</sup>/PPy, SDSO<sub>4</sub><sup>-</sup>/PPy, Tos<sup>-</sup>/PPy and CF<sub>3</sub>SO<sub>3</sub><sup>-</sup>/PPy sensors. The figures show a frequency shift for 3 ppm decanol and  $10^5$  ppm methanol samples. Figure 2.31 show interdigitated electrode sensors relative resistance change for 3 ppm decanol and  $10^5$  ppm methanol samples for DecSO<sub>3</sub><sup>-</sup>/PPy, SDSO<sub>4</sub><sup>-</sup>/PPy, Tos<sup>-</sup>/PPy and CF<sub>3</sub>SO<sub>3</sub><sup>-</sup>/PPy sensors.

From the QCM results (see Figure 2.30 above), it can be seen that the “noise” on the QCM sensors was about 4 Hz. Then for the QCM sensors, the low detection limit is 8 or 12 Hz, respectively. From Figure 2.30, it can be seen that the frequency changes were ca. 20 Hz for 3 ppm vapour. According to the linear relationship between frequency change at the QCM sensor with the amount of mass absorbed within the polymer when the vapour concentration is low, the low detection limit for QCM can be evaluated as ca. 1.5 ppm for those coatings. For high concentration sample, the QCM showed stable responses as high as 400 Hz. A continuous changing response over the tested range was observed (c.f. Section 3.3.3), which means the QCM upper detection limit can be evaluated as  $10^5$  ppm and higher.

From the interdigitated electrode sensors results shown by Figure 2.31, it can be seen that different coatings showed different response sensitivities. Among the four

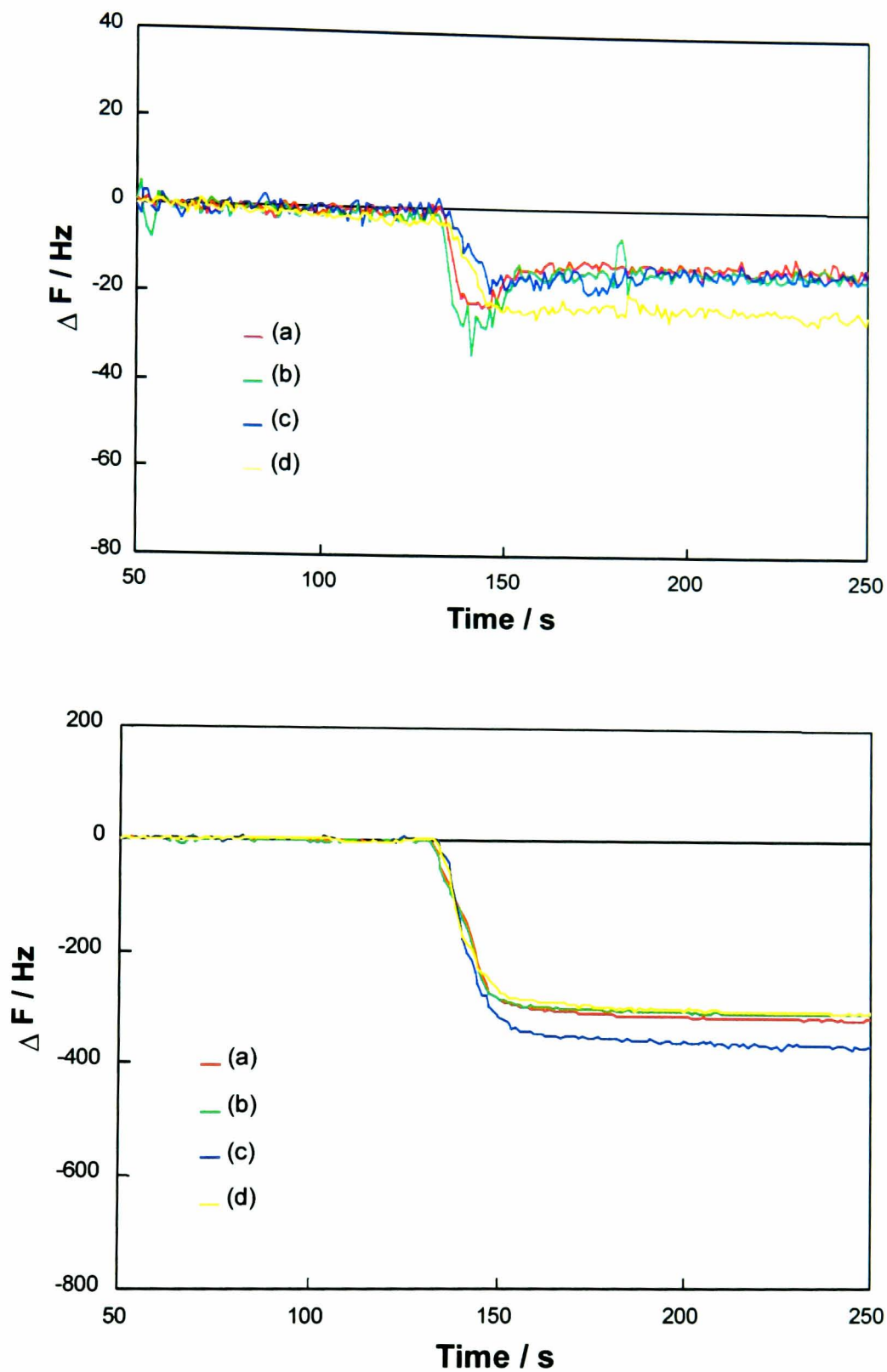


Figure 2.30 QCM sensors dynamic range of low concentration detection limit to 3 ppm decanol (above) and high concentration detection limit to  $10^5$  ppm methanol (below). The film coatings are as following: (a)  $\text{DecSO}_3^-/\text{PPy}$  coating of 12.7 kHz; (b)  $\text{SDSO}_4^-/\text{PPy}$  coating of 17 kHz; (c)  $\text{Tos}^-/\text{PPy}$  coating of 6.8 kHz; and (d)  $\text{CF}_3\text{SO}_3^-/\text{PPy}$  coating of 8.6 kHz.

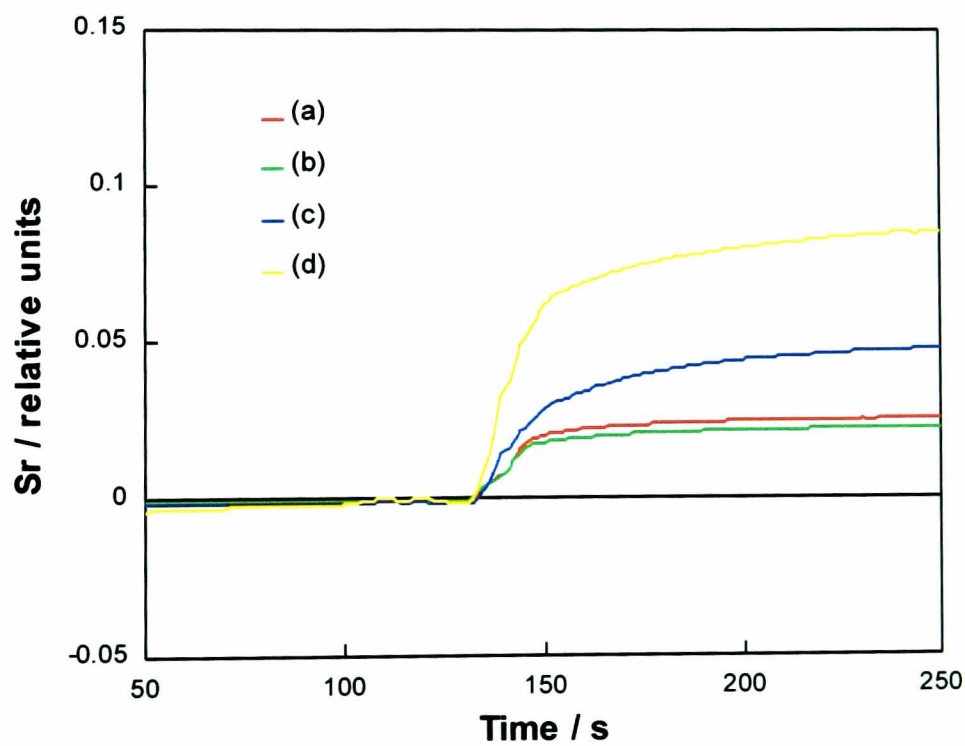
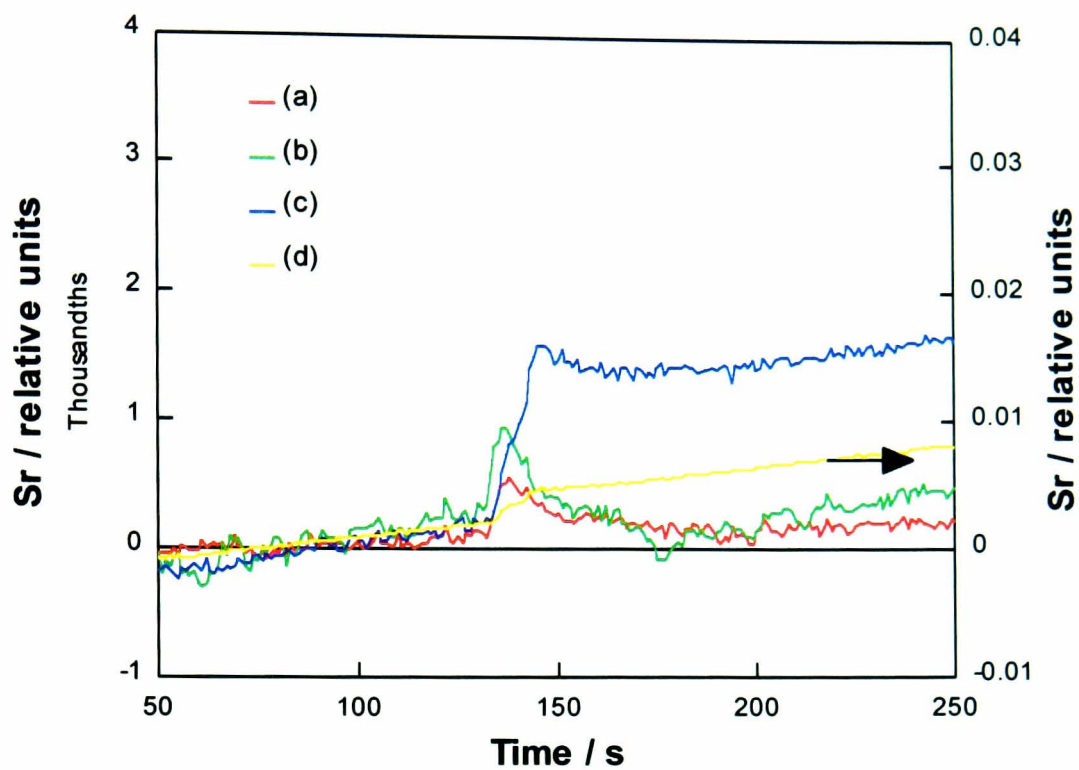


Figure 2.31 Interdigitated electrode sensors dynamic range of low concentration detection limit to 3 ppm decanol (above) and high concentration detection limit to  $10^5$  ppm methanol (below). The polymer films are as following: (a)  $\text{DecSO}_3^-/\text{PPy}$  coating of  $R_0$  57 $\Omega$ ; (b)  $\text{SDSO}_4^-/\text{PPy}$  coating of  $R_0$  70 $\Omega$ ; (c)  $\text{Tos}^-/\text{PPy}$  coating of  $R_0$  55 $\Omega$ ; and (d)  $\text{CF}_3\text{SO}_3^-/\text{PPy}$  coating of  $R_0$  70 $\Omega$ .

coatings with similar baseline resistance values,  $\text{CF}_3\text{SO}_4^-/\text{PPy}$  and  $\text{Tos}^-/\text{PPy}$  showed lower detection limits than the other two coatings, indicating that the detection limit will depend on the type of polymers employed. Figure 2.32 shows responses of a set of sensors with the same coating of  $\text{DecSO}_3^-/\text{PPy}$  but varying in thickness, and hence resistance, from 36 to 440  $\Omega$ , when exposed to 1.5 ppm DecOH. It can be seen that the detection limit at low concentrations is also dependent on the sensitivity of the sensor determined by the film thickness. Sensors covered with thinner polymeric films have a lower detection limit which can be evaluated as low as 1 ppm and below for this polymer. The upper detection limit of interdigitated electrode can be evaluated as  $10^5$  ppm and higher.

#### *2.3.2.6 Effect of film thickness on sensitivity of response*

A set of interdigitated electrode sensors, coated with same  $\text{DecSO}_3^-/\text{PPy}$  polymer material, but varying in film thickness were tested against 50% methanol. Figure 2.33 shows a typical cycle of measurements. The plot shows the relative resistance change to methanol versus measuring time. After 160 seconds, methanol was switched on for 120 seconds to allow the sensor to respond. Sensors with a thinner film, and higher resistance, showed a higher sensitivity to methanol. Figure 2.34 shows another set of sensors coated with  $\text{SDSO}_4^-/\text{PPy}$  films, which were exposed to methanol at different concentrations. It can be seen that thinner film always gave higher sensitivities. Likewise Figure 2.35 is a sensor set with  $\text{Cl}^-/\text{PPy}$  coatings, polymerised for 70s, 80s and 100s, respectively. Series of alcohol samples from methanol to butanol were tested, and again, the thinner film coating always showed higher response to all the four alcohol samples.

From the results of the above three sets of sensors, it can be demonstrated that thin film coatings on interdigitated electrode sensors, irrespective of the counterion used in these cases, showed high sensitivity to vapours varying both in type and concentration. A more detailed study concerning the effect of the film thickness on sensors characteristic will be introduced in Chapter 3.

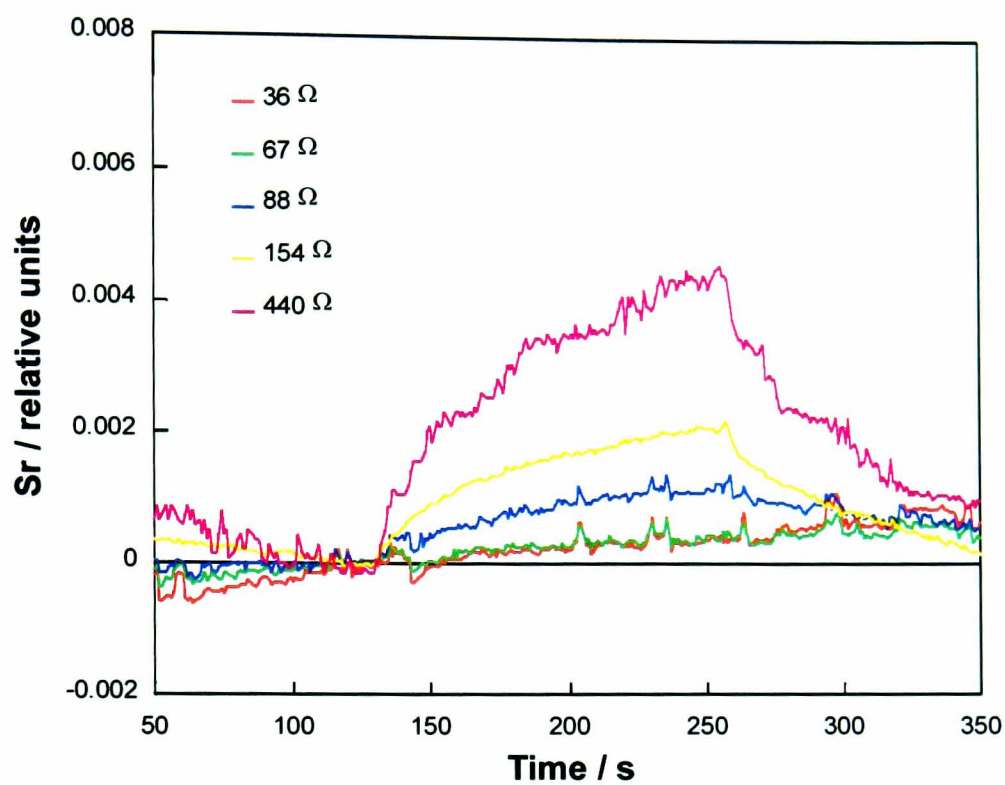


Figure 2.32 Interdigitated electrode sensors lower concentration detection limit of 1.5 ppm decanol. Sensors were coated with DecSO<sub>3</sub><sup>-</sup>/PPy films and varied in initial resistance from 36 Ω to 440 Ω.

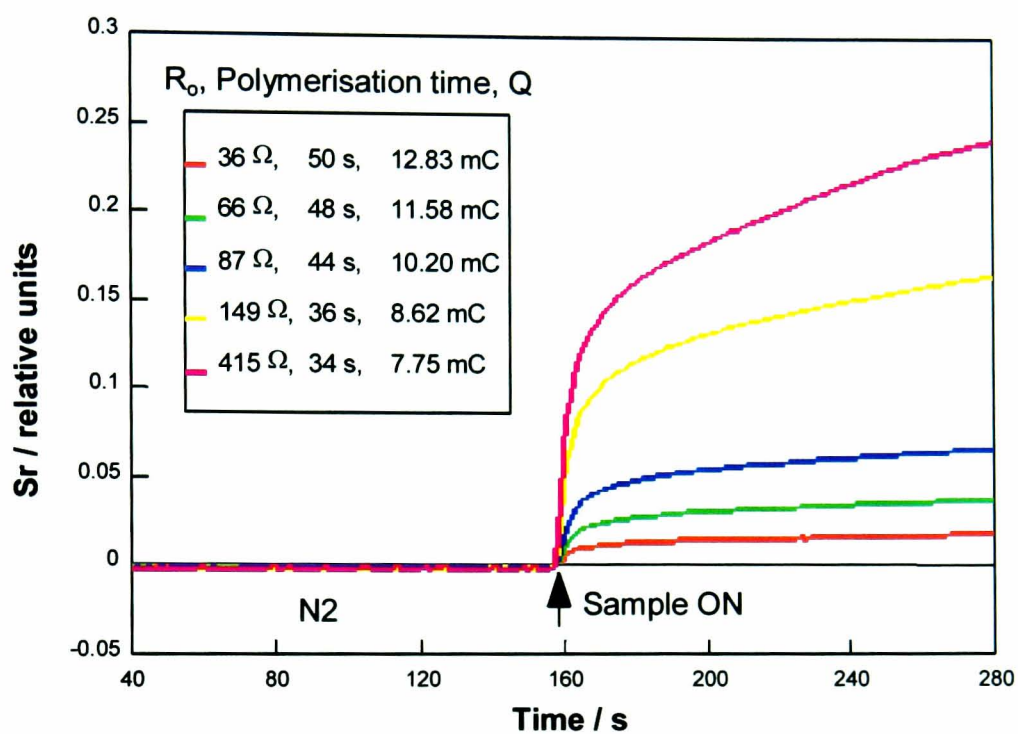


Figure 2.33 A typical measurement cycle on a set of interdigitated electrode sensors with DecSO<sub>3</sub><sup>-</sup>/PPy films of varying thickness, when measuring a sample which was 50% methanol in N<sub>2</sub>. The films were labelled by its initial resistance ( $\Omega$ ), polymerisation time (s) and the total charge passed (mC).

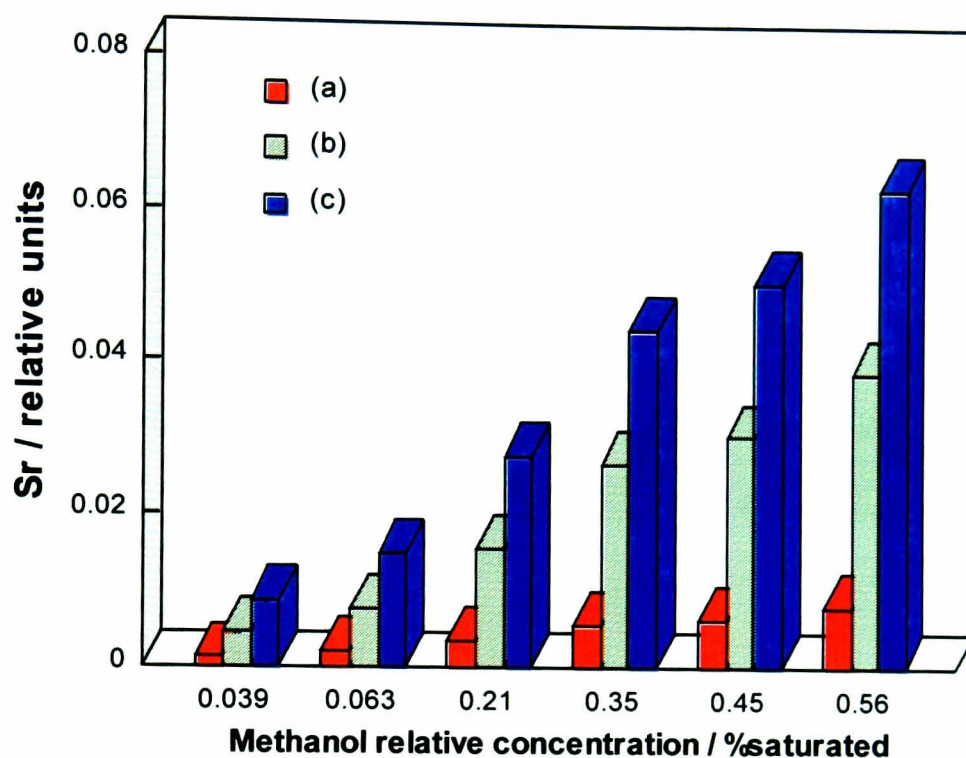


Figure 2.34 Sensitivities to methanol at different relative concentrations from a set of interdigitated electrode sensors covered by  $\text{SDSO}_4^-/\text{PPy}$  films and varied in thickness. The films were as follows: (a) polymerisation charge  $Q$  was 10.46 mC, initial resistance  $R_0$  was 40  $\Omega$ ; (b) polymerisation charge  $Q$  was 9.88 mC, initial resistance  $R_0$  was 70  $\Omega$ ; and (c) polymerisation charge  $Q$  was 8.14 mC, initial resistance  $R_0$  was 140  $\Omega$ .

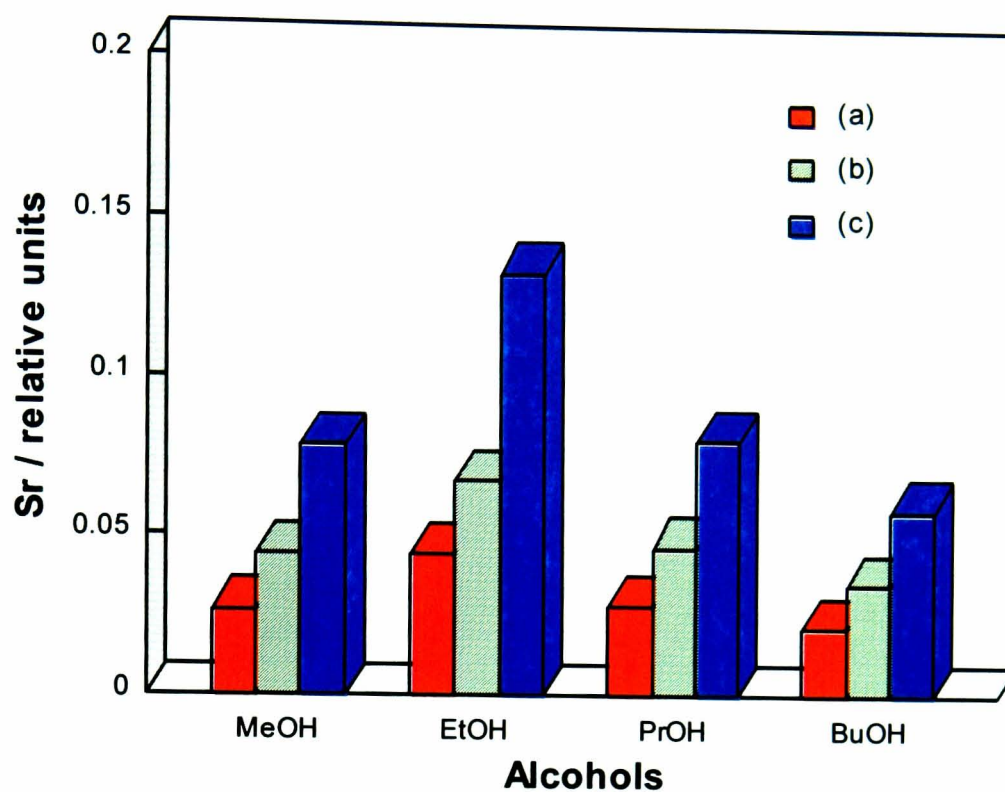


Figure 2.35 Sensitivities to a series of alcohols from a set of interdigitated electrode sensors covered with Cl<sup>-</sup>/PPy film and varied in film thickness. Films were labelled by the polymerisation time (s) and initial resistance ( $\Omega$ ). The films were as follows: (a) polymerisation time was 100 s, initial resistance  $R_0$  was 50  $\Omega$ ; (b) polymerisation time was 80 s, initial resistance  $R_0$  was 56  $\Omega$ ; and (c) polymerisation time was 70 s, initial resistance  $R_0$  was 146  $\Omega$ .

### 2.3.2.7 Fabrication reproducibility

As shown in Section 2.3.1.2, sets of interdigitated electrodes polymer sensors can be made with baseline resistance variation less than 10  $\Omega$ . Four sensors from the set, with similar resistance values (i.e. 125.3  $\Omega$ , 126.4  $\Omega$ , 127.1  $\Omega$  and 127.7  $\Omega$ ) were chosen to test their sensitivity consistency. Figure 2.36 shows the result of a typical measurement cycle to 50% methanol. The curves represent relative resistance changes with respect to time. The four sensors showed a similar trend in their response, including a similar sensitivity with a maximum difference of ca. 12% from each other. The same speed of response can be seen from the insert plot, which represents a normalised response versus time.

### 2.3.2.8 Response stability with time

Sensor pairs of interdigitated electrodes and QCM sensors coated with DecSO<sub>3</sub><sup>-</sup>/PPy were made and the stability of baseline resistance and response sensitivity with time were tested by measuring 50% methanol over a period of 45 days. Figure 2.37 (a), (b) and (c) show the values of relative frequency change  $S_f$ , relative resistance change  $S_r$  and combined sensors response  $S_{rf}$ , which is the ratio of  $S_r$  and  $S_f$ , against the time period in days on three DecSO<sub>3</sub><sup>-</sup>/PPy sensor pairs. There are also plots showing the baseline resistance change with time.

It can be seen from these figures that there were persistent monotonic increases in the baseline resistance values. The relative changes were 22.9%, 21.2% and 51.2% for the three sensors respectively. However,  $S_r$ ,  $S_f$  and  $S_{rf}$  (which is the ratio of  $S_r$  and  $S_f$ ) did not show such an increase in value during this period. At the start of the experiment, both QCM and interdigitated electrode were covered with fresh coatings and gave the highest response to methanol. Thereafter, the responses decreased with a non-monotonic variation, which was caused by either the ageing effect of polymer coatings or the sample vapour concentration changes with temperature. Statistical calculation showed that the coefficients of variation ( $C_v$ ) for  $S_r$  were 0.120, 0.159 and 0.106 and,  $C_v$  for  $S_f$  was 0.117. It can also be seen that the values of  $S_{rf}$  remained constant during the testing period, despite variations in the responses of both QCM and interdigitated electrode, as well as

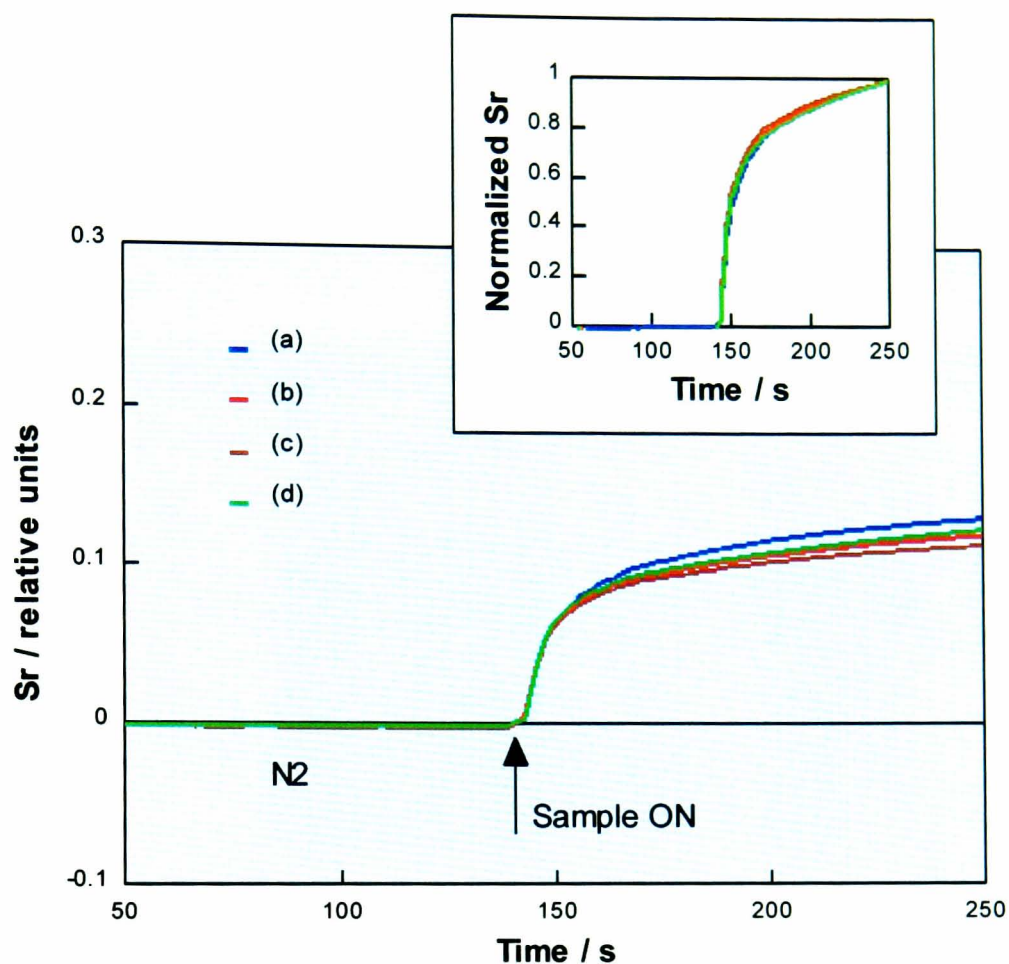
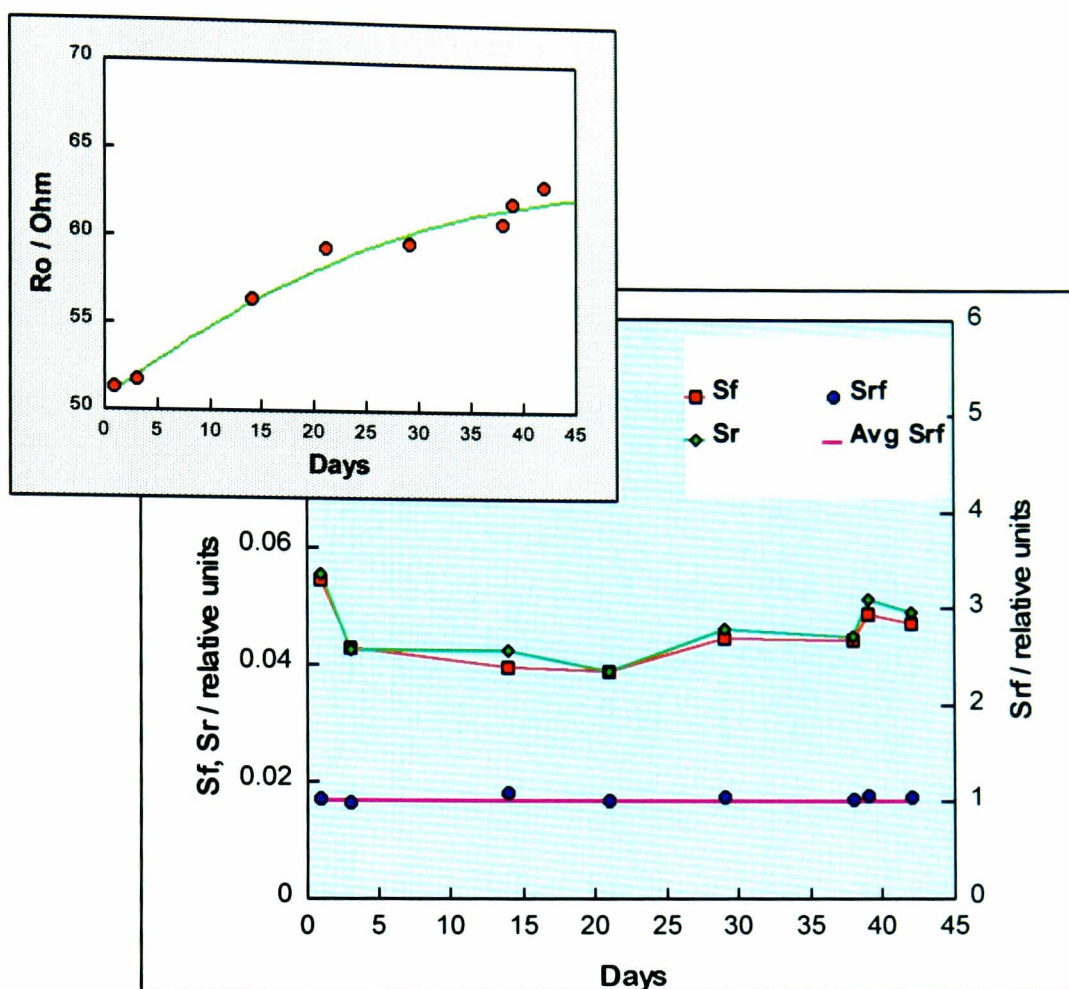
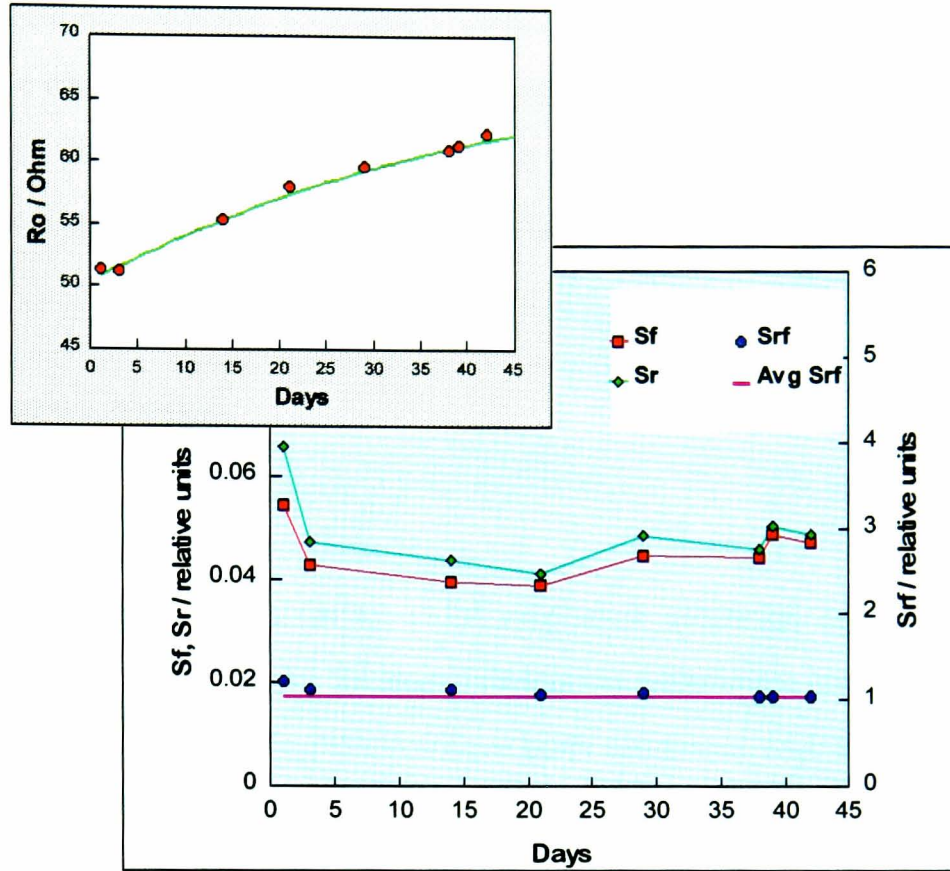


Figure 2.36 shows the result of a typical measurement cycle for 50% methanol from a set of interdigitated electrode sensors with  $\text{DecSO}_3^-/\text{PPy}$  films and with similar initial resistances as following: (a)  $127.1 \Omega$ ; (b)  $125.3 \Omega$ ; (c)  $127.7 \Omega$ ; and (d)  $126.4 \Omega$ . Inserted plot shows normalised response curves demonstrating the consistency in response speed.

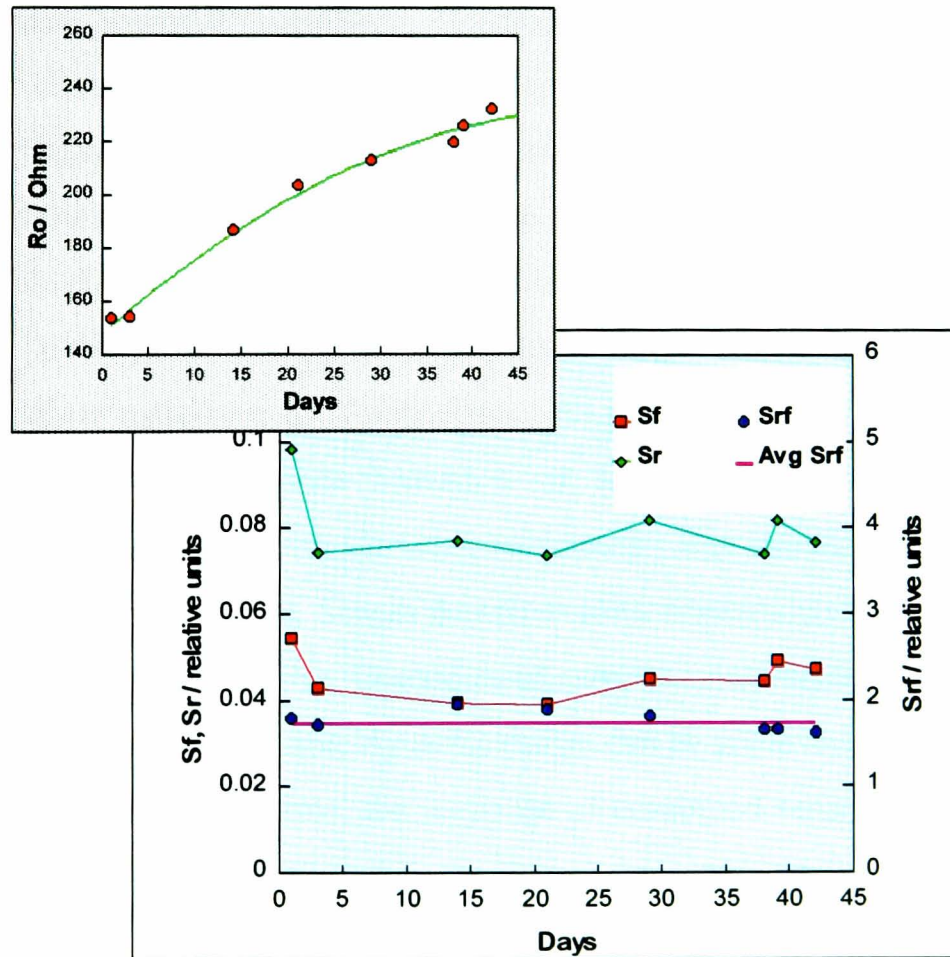


(a)

Figure 2.37 (a) to (c) show the baseline resistance value  $R_0$ , the values of relative frequency change  $S_f$ , relative resistance change  $S_r$  and combined sensors response  $S_{rf}$  to 50% methanol during a period of 45 days from three sensor pairs covered with  $\text{DecSO}_3^-$  /PPy films. The initial resistance of the films were: (a)  $R_0$  51.2 $\Omega$ ; (b)  $R_0$  51.4 $\Omega$ ; and (c)  $R_0$  153.8 $\Omega$ .



(b)



(c)

Figure 2.37 Continued.

differences in the baseline resistance.  $C_v$  for  $S_{rf}$  were 0.030, 0.031 and 0.071, respectively which demonstrated the response stability of the combined sensor pairs. Figure 2.38 shows the change in baseline resistance with time of the three interdigitated electrodes. It was noted from Figure 2.38 that for the same initial value of resistance (51.4 $\Omega$  and 51.2 $\Omega$ ), sensors drifted with time at a similar rate.

## 2.4 CONCLUSIONS

In this chapter, a QCM – interdigitated electrode hybrid odour measurement system has been established. Sensors fabrication techniques have been developed and the corresponding sensor characteristics have been discussed with the following conclusions:

During the sensor fabrication, the thickness of sensing film coatings can be controlled by the electrical charge passed during the polymerisation (i.e. by the length of time the step potential is applied). Electrical charge and polymer film thickness on gold electrode increase linearly with the increasing of polymerisation time, with the polymer growing faster laterally in the gap. Thinner films give a higher sensitivity but also show faster baseline resistance drift with time. There exists a balance between these two factors, which has to be resolved experimentally. By testing the properties of 16 different coatings, “optimal” individual initial resistance ranges have been suggested, which enable lower baseline resistance drift with time with good sensitivity. A set of sensors can be made with initial resistance variation of less than 10  $\Omega$  for batch fabrication. Interdigitated electrodes with the same resistance value showed a similar sensitivity and the same speed of response. Sensor detection limit depends on the type of coating and the thickness of the sensing film. Detection of sample concentrations between 1.5 ppm and 10<sup>5</sup> ppm, which is a reasonable dynamic range, can be achieved. Even though the baseline resistance increases with time, the response of combined sensors  $S_{rf}$  remains very stable during a test period of 45 days.

In the next chapter, a more detailed theoretical and experimental investigation on sensors modelling and properties will be introduced.

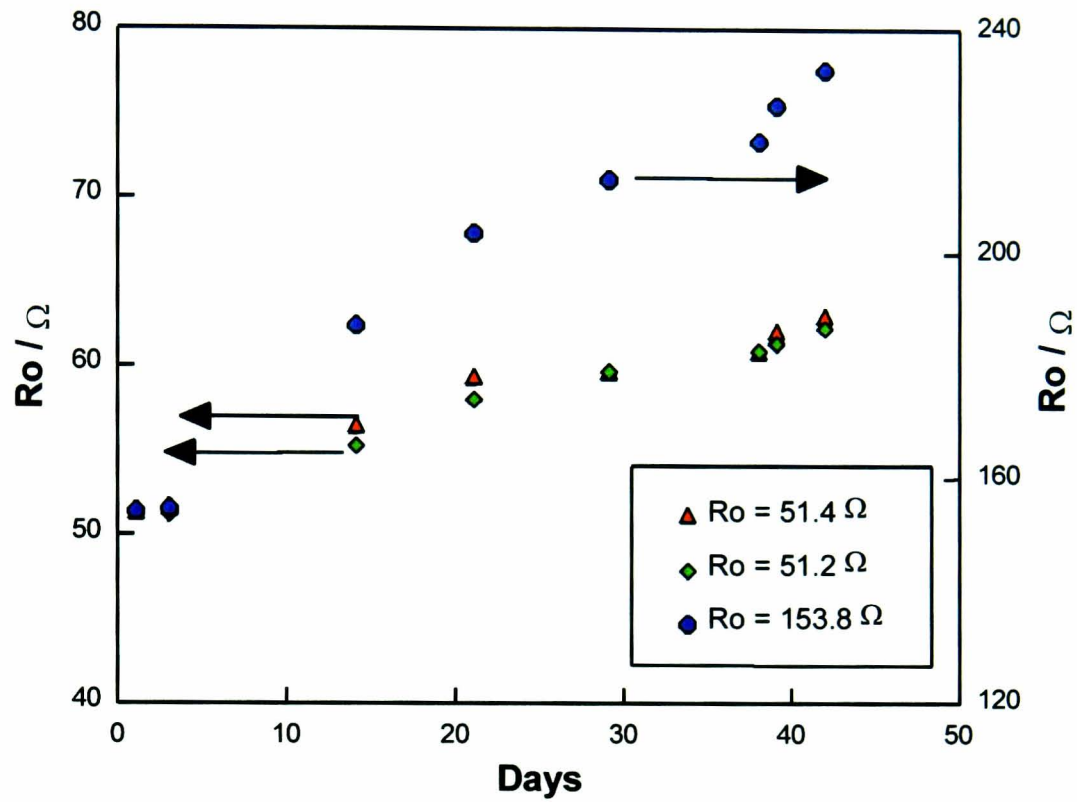


Figure 2.38 Comparison of the baseline resistance drift during a period of time from a set of interdigitated electrode sensors with initial resistance values as 51.4  $\Omega$ , 51.2  $\Omega$  and 153.8  $\Omega$ , respectively. The arrows refer to the Y-axis used by the data (Red and green points use the first Y-axis, and blue points use the second Y-axis).

## **Detection Mechanisms of Polymer-Based Sensors**

### **3.0 INTRODUCTION**

Within the context of a polymer based artificial olfactory system, chemical analytes can be detected based on changes in one or more of the physical and chemical characteristics of a thin film or layer in contact with the sensor surface. The intrinsic film properties which can be utilised for detection include mass, electrical conductivity, capacitance, permittivity, viscoelasticity and optical property. These various physical and chemical phenomena have been employed to generate sensors for use in array-based odour sensing. The types of the devices include metal-oxide sensors [23], metal-oxide-silicon field-effect transistors [32], conducting polymer microresistors [62], surface-acoustic-wave devices [39], quartz crystal resonators [46] and fibre-optic chemical sensors [72]. In all cases, the goal has become the creation of an array of sensing elements with different sensitivities. In this work, piezoelectric-based bulk acoustic wave devices — quartz crystal microbalance (QCM) and conducting polymer-based microresistor devices have been used, which are two of the main types of sensors which have previously dominated the development of electronic nose technologies [3, 128].

The use of piezoelectric crystals as transducers for chemical analysis was first proposed by Sauerbrey in 1959 [33] and demonstrated by King in 1964 [34] as mass sensitive absorption detector. The approach exploits the stable frequency resonance of piezoelectric materials such as single crystal quartz when acoustic waves are passed through the material. The selectivity of these sensors is dictated by the different coatings that are applied to the crystal surface. The absorption of gaseous species into the coating surface induces a shift in the resonant oscillation frequency, which is directly related to

the mass of the absorbed compound. To date, much of the research on QCM odour sensors has been performed with a variety of organic polymer coatings, including both conducting and non-conducting films [35, 47, 84].

The use of conducting polymers as a sensing material can be dated back to 20 years ago. In 1979, polypyrrole was first successfully electropolymerised from aqueous solution to form a free-standing thin film by Diaz and co-workers [58]. Since then, much attention has been paid to the study of these materials and their unique properties. The material was later used as a vapour detector based on the resistance change property in 1985 by Persaud [59]. The reversible absorption of vapour molecules into the film induced a reversible, rapid change in the electrical resistance. The sensors showed good mechanical strength and electrical stability over a period of several months, not poisoned by any of the gases or odorants tested, and gave reproducible responses to a broad but overlapping range of compounds. As a consequence, there have been increasing interests in using this material for electronic nose fabrication because of its versatility in composition and broad sensitivity towards organic vapours [19, 21, 22, 60]. All of this has resulted in a number of commercial resistivity-based devices [18, 20].

With the great diversity of polymer-based sensor systems, large numbers of different polymers (conducting or non-conducting) can be placed on various types of sensors. Alternatively, combining different sensor technologies into “hybrid” systems has recently been developed by employing two or more of the same or different types of sensors, to form, for example, a sensor pair capable of measuring multiple properties. This development is aimed at the improvement of sensing properties such as selectivity and the removal of interference signal [40, 79, 80, 83-87]. The different measurement mechanisms of QCM and interdigitated electrode have also been used to study the vapour-polymer interactions and have shown the potential usefulness of the method in improving the selectivity of polymers towards odorants [83-86]. In this work, a combination of QCM and interdigitated electrode sensor pairs has been established, aiming at improving the selectivity of the sensors, as well as their long term stability. The combination is also used to study the response characteristics of polymers.

To date, there has been little systematic research work linking sensor's (or a pair's) response characteristic with the nature of the interaction between the analyte and the sensor coating at an interdigitated electrode and a QCM-interdigitated electrode sensor pair. Such a fundamental understanding is necessary to interpret sensor responses and to design sensor coatings for specific analytical applications. Such an investigation is also important to establish a theoretical basis to optimise the configuration of sensors with improved selectivity so as to enable the improvement in electronic nose technology.

In this chapter, the thermodynamics of gas sorption, signal-transduction mechanisms and device modelling for both the piezoelectric-based QCM sensors and resistive-based interdigitated electrode sensors (coated with conducting polymers) will be discussed, either as single devices or in combination as a hybrid system. The nature of sensor's responses will be linked with the nature of analyte-polymer interaction, using the new concept of a sensor sensitivity coefficient ( $S$ ), which will be defined as the relative resistivity change by one molecule absorbed into the polymer film. This coefficient will be demonstrated as a useful concept in interpreting the gas-polymer interaction mechanisms. Effects of film thickness will also be studied, together with conditions of vapour concentration independence. Finally, long term stability and sensing selectivity of QCM, interdigitated electrode and QCM-interdigitated electrode sensor pairs will be studied theoretically and verified experimentally. Based upon these studies, an "odour map" will be constructed for two or more pairs of sensors, which facilitates the identification of a vapour's character and composition (in either single or mixed type). Thus, the enormous potential for improvements in selectivity and long term response stability of polymer-based systems will be shown and discussed.

## **3.1 THERMODYNAMICS OF ADSORPTION AND POLYMER SORPTION**

### **3.1.1 Thermodynamics of Adsorption: Adsorption Isotherms**

In the context of gas sensing, an equilibrium process can be defined as the one in which there is rapid (on the time scale of the sensor measurement) exchange of analyte

between the ambient and sorbed phases. The amount of analyte that is adsorbed depends upon the change in Gibb's free energy ( $\Delta G_a$ ) associated with adsorption. This relationship can be expressed as Equation 3-1:

$$K_a = \frac{a_a}{a} = e^{-G_a/RT} \quad (3-1)$$

where  $K_a$  is the equilibrium coefficient for adsorption,  $R$  is the ideal gas constant,  $a_a$  is the *chemical activity* of the adsorbed analyte, and  $a$  is the analyte chemical activity in the ambient phase. At low gas concentrations (or partial pressures), analyte activity is often approximated by either concentrations or partial pressures, terms which are related and can be used interchangeably.

The value of the equilibrium coefficient of adsorption ( $K_a$ ) is often evaluated as a function of ambient-phase activity at a constant temperature by acquiring an adsorption isotherm. The ambient-phase analyte concentration varies typically from zero, through the concentration range of interest, to its saturated value. It is not often the case that  $K_a$  remains constant over a broad range of analyte concentration, which implies a non-linear relationship between  $a_a$  and  $a$ . This phenomenon is observed in the experiments and will be shown later. In general, nonlinearity in an adsorption isotherm is a consequence of the activity-dependent thermodynamic relationship between surface-adsorbed coverage (expressed as a number/area or a "density") of an analyte and its concentration in the ambient phase. This is due to a number of factors, including the finite number of adsorption sites available, physical inhomogeneities (e.g. pores and capillaries) in/on the substrate, and adsorbate-adsorbate interactions [126].

Thus, the isotherm reflects the concentration-dependent  $K_a$  value, and is indicative of the relative strength of the polymer-gas interactions, the specific surface area of the sensor, the distribution of interaction energies, the polymeric pore sizes, the nature of adsorption (e.g. monolayer or multilayer), and the possible process of condensation in pores [126]. In the context of the detection of analytes, the shape of the isotherm characterises the sensitivity and dynamic range of sensors, as will be discussed in Section 3.2.1.

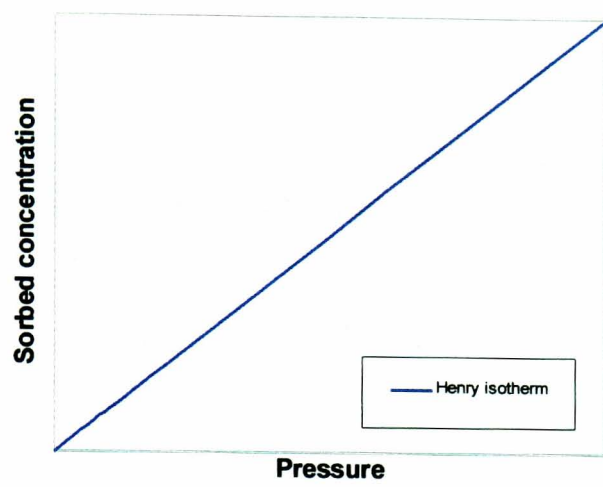
### 3.1.2 Absorption and Gas Sorption in Polymer Films

Polymers, especially elastic, amorphous polymers, have several inherent advantages as chemical sensitive sensor coatings: they can be deposited as thin, adherent, continuous films; they are nonvolatile and of homogeneous composition; and their chemical and physical properties can be modified to some extent by judicious choice of monomers and synthetic procedures.

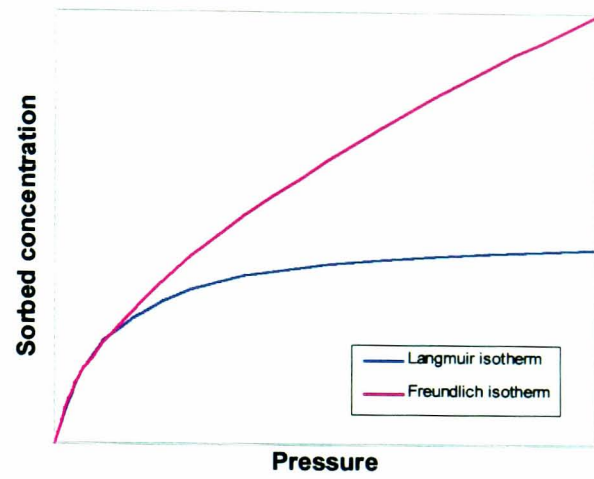
The general term used to describe the penetration and dispersal of gases and vapours into polymers is *sorption*. Sorption encompasses the processes of *absorption* (which implies intimate mixing at the molecular level of two substances where the absorbed species literally dissolved in the absorbent material, e.g. a coating and a vapour), *adsorption* (which is restricted to interfacial surfaces or fixed sites), filling of microvoids, and other mixing phenomena. The co-existence of these processes, coupled with the lack of well-defined internal surface in polymers, requires the use of this general term [129]. The quantity of an analyte that is sorbed by a polymer at equilibrium is referred to as the *solubility* of the analyte. The distribution of a species between a sorption phase and an ambient medium can be described by a *partition coefficient*  $K$ .

There are several typical sorption isotherms for polymers [126], as demonstrated in Figure 3.1(a) to (d). The ideal case of Henry's behaviour represented by Figure 3.1(a) occurs when the penetrant is dispersed randomly throughout the polymer and penetrant-penetrant interactions are energetically similar to, or much less than, penetrant-polymer interactions. This behaviour is usually found for gases below about one atmosphere pressure. For systems following this behaviour, the sorbed molecules and polymer chains are highly mobile.

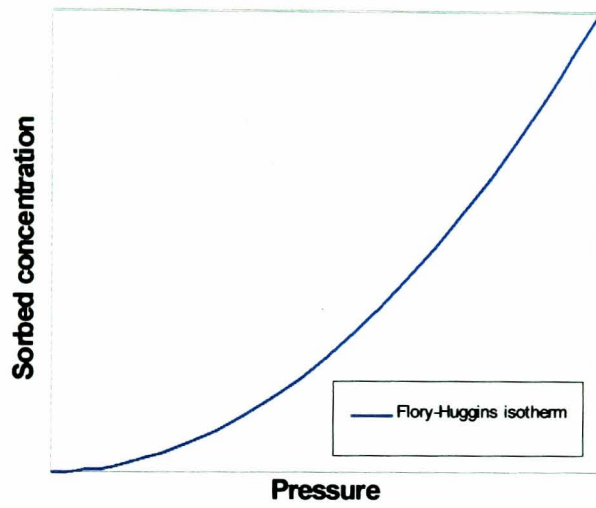
For polymer/penetrant combinations where strong interactions between specific functional groups occur and binding to specific sites predominates, a localised sorption model is more appropriate, which is shown in Figure 3.1(b) as either the Langmuir or the Freundlich isotherm model. This type of behaviour has been observed for the sorption of polar vapours by polar polymers (i.e. polypyrrole) for both QCM and interdigitated



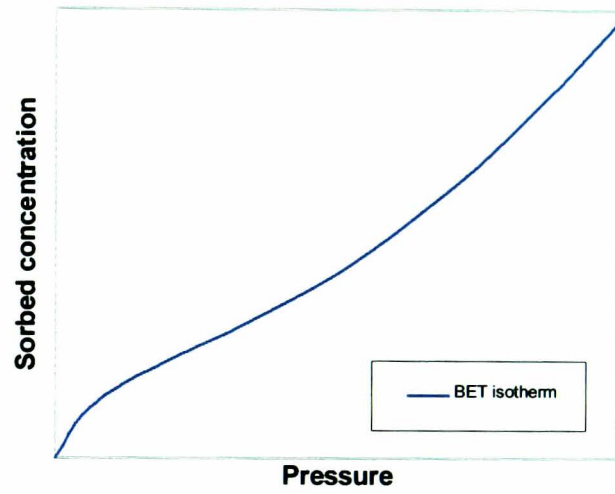
(a)



(b)



(c)



(d)

Figure 3.1 A selection of sorption isotherms representing different polymer sorption models.

electrode sensors [54,62,76,83,104,117,118]. Details about this model will be introduced in the next Section 3.1.3.

Figure 3.1(c) represents the case of Flory-Huggins behaviour, where there is a preference for penetrant-penetrant pairs to be formed, such that solubility increases with the concentration of penetrant in the polymer. This type of behaviour is observed in systems where the polymer is strongly plasticized by the penetrant molecules and they preferentially accumulate [126].

Figure 3.1(d) represents a BET (or Brunauer-Emmett-Teller) absorption isotherm. There is specific localised sorption at low concentrations, followed by clustering or aggregate formation at high concentrations. Sorption of water by hydrophobic polymers such as cellulosic materials follows this behaviour [126].

### 3.1.3 Langmuir and Freundlich Adsorption Isotherms

As indicated in the previous section, there are typical sorption isotherms representing different polymer sorption models, which describe the majority of the thermodynamics of absorptions. Research work has shown that the Langmuir/Freundlich type absorption can describe the sorption of polar vapours by polar polymers for both QCM and interdigitated electrode sensors [61, 62, 83, 84, 117].

The Langmuir adsorption theory, which was proposed in 1916, was the first quantitative theory of the adsorption of gases based on the following assumptions [127]: The solid surface contains a fixed number of adsorption sites. At equilibrium at any temperature and gas pressure, a fraction  $\theta$  of the sites are occupied by adsorbed molecules, and a fraction  $1-\theta$  is not occupied. Each site can hold one adsorbed molecule. The heat of adsorption is the same for all the sites and does not depend on the fraction covered  $\theta$ . There is no interaction between molecules on different sites. The chance that a molecule condenses at an unoccupied site or leaves an occupied site does not depend on whether or not neighboring sites are occupied. The Langmuir expression for the mass/area of adsorbate  $m_A$  as a function of partial pressure  $p$  is [126]:

$$m_A = \frac{m_{ML} K_a p}{(1 + K_a p)} \quad (3-2)$$

where  $m_{ML}$  is the adsorbed mass/area at monolayer coverage,  $K_a$  is the equilibrium coefficient for adsorption,  $p$  is the partial pressure of gas-phase analyte which is proportional to the gas concentration. A plot representing a Langmuir isotherm is illustrated by the blue line in Figure 3.1(b).

There are two limiting cases for the Langmuir isotherm. Where  $K_a p \ll 1$ , i.e., when the pressure is low or the adsorption coefficient is very small, there is a linear dependence of  $m_A$  on  $p$ . Such a relationship is always found in the low pressure region of the adsorption curve. Where  $K_a p \gg 1$ , i.e., when the pressure is high or, with particular strong adsorption, at lower pressures, the isotherm reduces in the flat upper region of the isotherm.

This model, though proven for many ultra-clean, well-ordered surfaces interacting with small molecule adsorbates, is over-simplified for many practical systems. The “pure” Langmuir type behaviour, in which there is no detectable adsorption beyond the first monolayer, is most often observed for species that strongly chemisorb onto a substrate, for example, thiol based self assembled monolayers on gold. Nevertheless, this model is the foundation upon which much of adsorption theory is built and provides a useful conceptual basis for understanding the processes involved.

Most practical surfaces are non-uniform, possessing surface sites that have a range of potential energies for a given adsorbate. Even when all sites (on an empty surface) are energetically equal, filling of the sites may lead to a progressive decrease in adsorption energy due to repulsive interactions between adjacent adsorbates. The consequence is that the heat of adsorption often declines markedly with increasing surface coverage.

The inability of the Langmuir model to account for a reduction in the heat of adsorption with increasing coverage led to the empirical derivation of the Freundlich

model, which assumes an exponential decline in the heat of adsorption with increasing coverage, then

$$m_A = k_F p^{1/n_F} \quad (3-3)$$

where  $k_F$  and  $n_F$  are empirical constants.  $n_F$  is a number greater than 1. The plot representing a Freundlich isotherm is also shown in Figure 3.1(b) by the pink line.

There is qualitative similarity between the Freundlich and Langmuir models. At very low pressures, the Langmuir model indicates a more linear variation in  $m_A$  with  $p$  than does the Freundlich model. At intermediate pressure, both models predict a dependence on a fractional power of  $p$ . Variation of partial pressure over several orders of magnitude or examination of a wide variety of adsorbates, often reveals non-Langmuirian behaviour. In these cases, the Freundlich model works better when the decline in the heat of adsorption with increasing coverage is non-negligible.

Besides the Langmuir and Freundlich models, there is another empirical isotherm called Temkin isotherm [127], which assumes a linear decline in the heat of adsorption with increasing coverage, then:

$$m_A = \frac{RT}{q_0^a \alpha} \ln(A_0 p) \quad (3-4)$$

where  $\alpha$ , and  $A_0$  are constants for the given system at temperature  $T$ .

Clearly, in the low pressure region of Temkin isotherm, when  $A_0 p \leq 1$ , Equation 3-4 gives a large negative increase with the decrease of  $p$ , which does not fit the practical case. In this study, hence, Langmuir and Freundlich isotherms will be adapted to analyse the experimental data. It will be shown experimentally in Section 3.3.1 that the Freundlich model will provide a better fit for the films produced in this study.

Thus, under atmospheric pressure, Equation 3-5 can be used to analyse the adsorption data for a Freundlich type absorption [126, 130]:

$$\frac{\Delta m}{m_c} = kC^n \quad (3-5)$$

where  $\Delta m$  is the change in the mass of substance absorbed (in grams) and the mass of odour vapour molecules here,  $m_c$  is the mass of polymer coating in gram,  $C$  is the concentration of analyte gas, and  $k$  and  $n$  are empirical constants.

## 3.2 DETECTION MECHANISMS OF POLYMER-BASED SENSORS

### 3.2.1 Piezoelectric-Based Sensors

The distribution of analyte between ambient phase and the sensor coating is illustrated in Figure 3.2 for both a gold coated QCM and a microresistive sensor. As stated before, the relationship between the change in resonant frequency and a given added mass, which was first proposed by Sauerbrey in 1959 [33], can be described as follows:

$$\Delta f = -k'f_o^2 \frac{\Delta m}{A} \quad (3-6)$$

where  $\Delta f$  is the change in frequency,  $\Delta m$  is the change in mass,  $f_o$  is the fundamental resonant frequency of the crystal in Hz and is 10 MHz in this study,  $A$  is the electrode area,  $k'$  is the mass sensitivity constant related with the density and thickness of crystal material ( $k' = 2.26 \times 10^{-10} \text{ m}^2 \text{sg}^{-1}$  for AT cut crystal in thickness shear mode). If we define the relative frequency change, i.e. the frequency change caused by mass absorption normalised by the frequency change resulting from the polymer coating, as a parameter  $S_f$ , Equation 3-5 can be expressed as:

$$S_f = \frac{\Delta f}{f_c} = \frac{\Delta m}{m_c} = kC^n \quad (3-7)$$

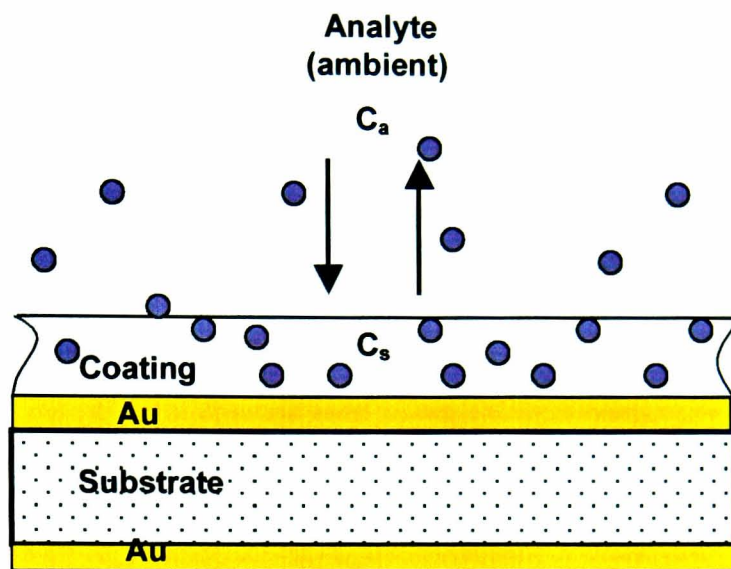


Figure 3.2 Illustration of the distribution of analyte between ambient phase and the absorbed phase (in polymer coating) on the QCM electrode.  $C_a$  is ambient phase concentration and  $C_s$  is absorbed phase concentration.

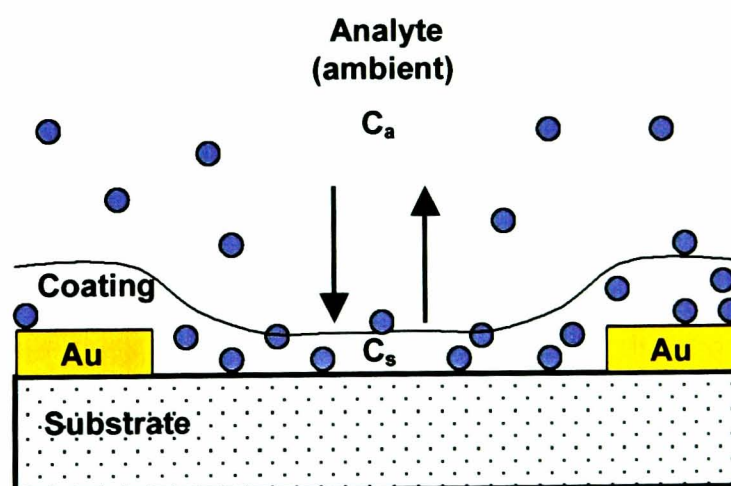


Figure 3.3 Illustration of the distribution of analyte between ambient phase and the absorbed phase into polymer coating on interdigitated electrode.  $C_a$  is ambient phase concentration and  $C_s$  is absorbed phase concentration.

or it can be expressed as:

$$\Delta f = k f_c C^n \quad (3-8)$$

where  $\Delta f$  is the steady state change in frequency produced by a vapour,  $f_c$  is the frequency change caused by the polymer coating,  $\Delta m$  is the change in mass,  $m_c$  is the mass of the coating material,  $C$  is the concentration of ambient phase vapour, and  $k$  and  $n$  are empirical constants.

Further, if we define the QCM sensor sensitivity as the relative frequency change obtained for an incremental change in the concentration of the analyte, i.e., the slope of the response-concentration curve, then for an isotherm shown in Figure 3.1(b), the slope decreases with increasing analyte concentration. Sensitivity to the analyte declines as the ambient-phase concentration increases, which means the greatest sensitivity is obtained at the lowest concentrations. This is not a shortcoming since the greatest sensitivity is often desired at the lower concentrations.

### 3.2.1 Resistive-Based Sensors

An illustration of the distribution of analyte between an ambient phase and the sensor coating on an interdigitated electrode is shown in Figure 3.3. It is known that the number of absorbed molecules is:

$$N_{abs} = \Delta m' / (MW)u \quad (3-9)$$

where  $\Delta m'$  is the absorbed mass change of the coating on the interdigitated electrode,  $MW$  is the vapour molecular weight, and  $u$  is atomic mass unit ( $1u = (1/12) m (^{12}\text{C})$ ) which is  $1.66 \times 10^{-27}$  kg) [123].

For an interdigitated electrode microresistor, a gas-polymer interaction sensitivity coefficient,  $S$ , can be defined as the relative equilibrium resistivity change caused by each absorbed molecule, i.e.

$$S = \left( \frac{\Delta\rho}{\rho_0} \right) / N_{abs} \quad (3-10)$$

where  $\Delta\rho$  is the equilibrium resistivity change, and  $\rho_0$  is the initial resistivity. Thus,  $S$  will be dependent on properties of both polymer film and analyte. For example,  $S$  will be dependent on the polymer morphology, its particular characteristics (such as composition, and charge carrier population), and geometric properties. It may also be independent of absorbate concentration.

Hence, the relative resistance change  $S_r$  can be written using a Freundlich isotherm expression, by combining Equations 3-5, 3-9 and 3-10, as:

$$S_r = \frac{\Delta R}{R_0} = S \frac{\Delta m'}{(MW)u} = \frac{S}{(MW)u} k' C^{n'} \quad (3-11)$$

where  $\Delta R$  is the resistance change caused by the vapour absorption,  $R_0$  is the baseline resistance, and  $k'$  and  $n'$  are material constants for the interdigitated electrode.

Similarly, if we define the interdigitated electrode sensor sensitivity as the relative resistance change obtained for an incremental change in the concentration of the analyte, then the greatest sensitivity is obtained at the lowest concentrations.

### 3.2.3 Hybrid Systems

For a QCM-interdigitated electrode sensor pair, coated with the same polymer material, we can introduce the parameter  $S_{rf} = S_r / S_f$ , which represents the response of the combined sensor pair. Combining into Equations 3-7 and 3-11, we get:

$$S_{rf} = \frac{S}{(MW)u} \frac{k' C^{n'}}{k C^n} \quad (3-12)$$

If we assume that the polymer coatings on the sensor pair are completely the same so that:

$$\Delta m/m_c = \Delta m'/m_c' \quad (3-13)$$

where  $m_c'$  is the mass of coating material on the interdigitated electrode.

Then,  $S_{rf}$  can be expressed as:

$$S_{rf} = \frac{S}{(MW)_u} m_c' = \frac{S}{(MW)_u} k'' \rho \quad (3-14)$$

where  $\rho$  is the density of the polymer, and  $k''$  is a geometric constant for the polymer coated on the interdigitated electrode.

From Equations 3-12 and 3-14, it can be seen that  $S_{rf}$  is related to the vapour-polymer interaction sensitivity coefficient  $S$ , the vapour molecular weight  $MW$ , and sensor pair characteristic  $k''\rho$  (or alternatively coating material constants  $k$ ,  $k'$ ,  $n$ , and  $n'$ ). With the assumption that the coating on QCM and interdigitated electrode are completely the same and have the same absorption property (see Equation 3-13), then if  $S$  is independent of the analyte concentration,  $S_{rf}$  will also be independent of the amount of the vapour absorbed. Hence it should be independent of the vapour concentration and can be used to identify that vapour. As will be shown in the later Section 3.3.3, when the sensor pairs were constructed from coatings with very similar properties and hence very close concentration dependency, then  $S_{rf}$ , and hence  $S$ , is independent of the concentration of the various vapours across the limits of concentration tested.

It is also noticed from Equation 3-12 that if the polymer material constants  $n$  and  $n'$  are different for the two coatings,  $S_{rf}$  is somewhat dependent on the vapour concentration  $C$ . Therefore Equation 3-12 can be used to test the similarity of the two coatings.

Finally, if  $S_{rf}$  is multiplied by the molecular weight  $MW$ , then:

$$S_{rf}MW = Su^{-1}k'' \rho \quad (3-15)$$

From Equations 3-14 and 3-15, it can be seen that for an unknown vapour,  $S_{rf}$  represents a characteristic value, which can be used to identify that vapour. For a series of known vapours,  $S_{rf}MW$  is proportional to  $S$ , and hence will represent the magnitude of response caused by one molecule of a vapour, and can be used to compare with that of other vapours.

In summary, this approach attempts to describe the sensing mechanisms of the conducting polymer-based hybrid system and to introduce methods for vapour-polymer interaction investigation. It will be shown experimentally in the following sections that whilst  $S_{rf}$  is used to improve the long term response stability and selectivity of sensors by a greatly enhanced specificity towards various vapours,  $S_{rf}MW$  can be introduced as a new parameter to study the nature of vapour-polymer interactions and response mechanism.

### 3.3 RESULTS AND DISCUSSION

#### 3.3.1 Piezoelectric-Based Sensors

Figure 3.4 is a plot of typical data showing how the QCM resonant frequency changes as a function of methanol concentration for a HexSO<sub>3</sub><sup>-</sup>/PPy polymer coating. The frequency change caused by the coating was 11.0 kHz, the concentration of methanol being calibrated by in-line FT-iR measurement. It can be seen that the frequency changes against concentration increased nonlinearly with the increase in concentration of methanol. Data were fitted using a Freundlich isotherm (Equation 3-3). Figure 3.5 shows resonant frequency changes of three QCMs, made of the same coating material as above, but with different coating film thickness versus concentration of methanol. The frequency shifts by the coating were from 4 kHz to 11 kHz (which is equivalent to ca. 4 to 11 µg of polymer films). Here data were fitted using both a Freundlich isotherm equation shown in Figure 3.5(a) and a Langmuir isotherm (Equation 3-2) shown in Figure 3.5(b).

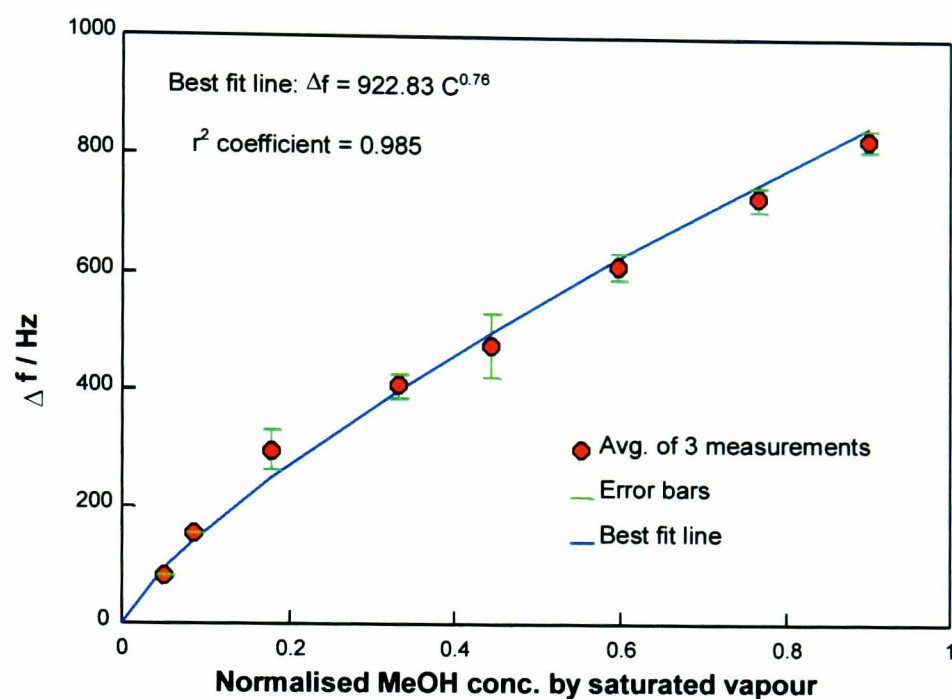
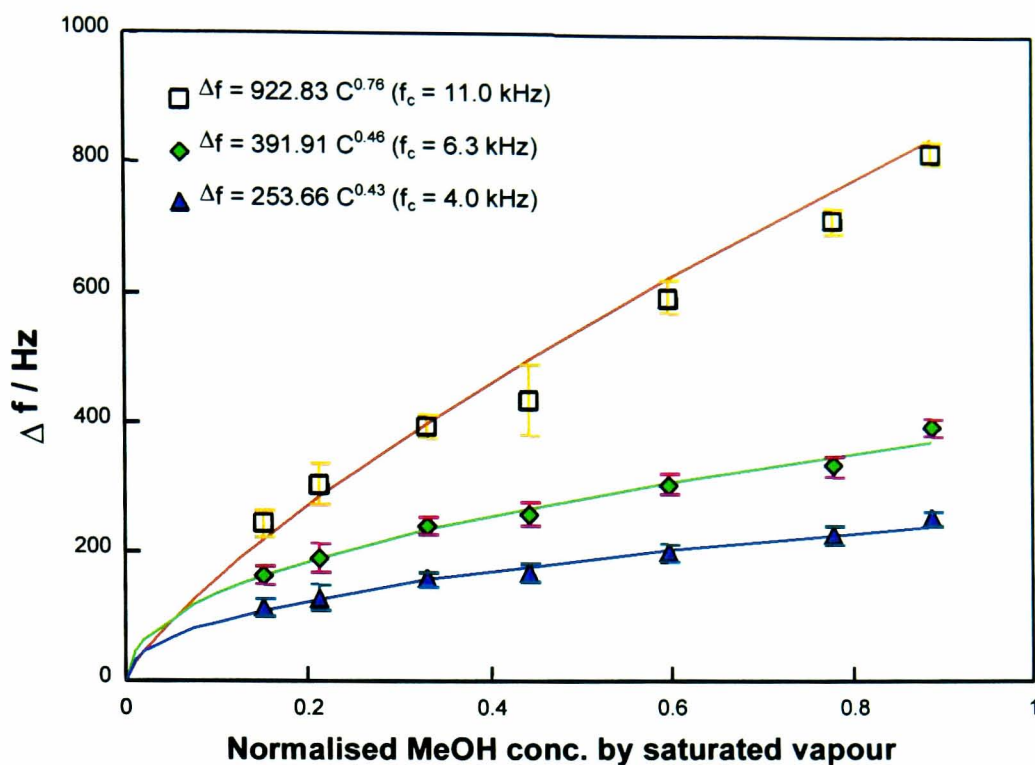
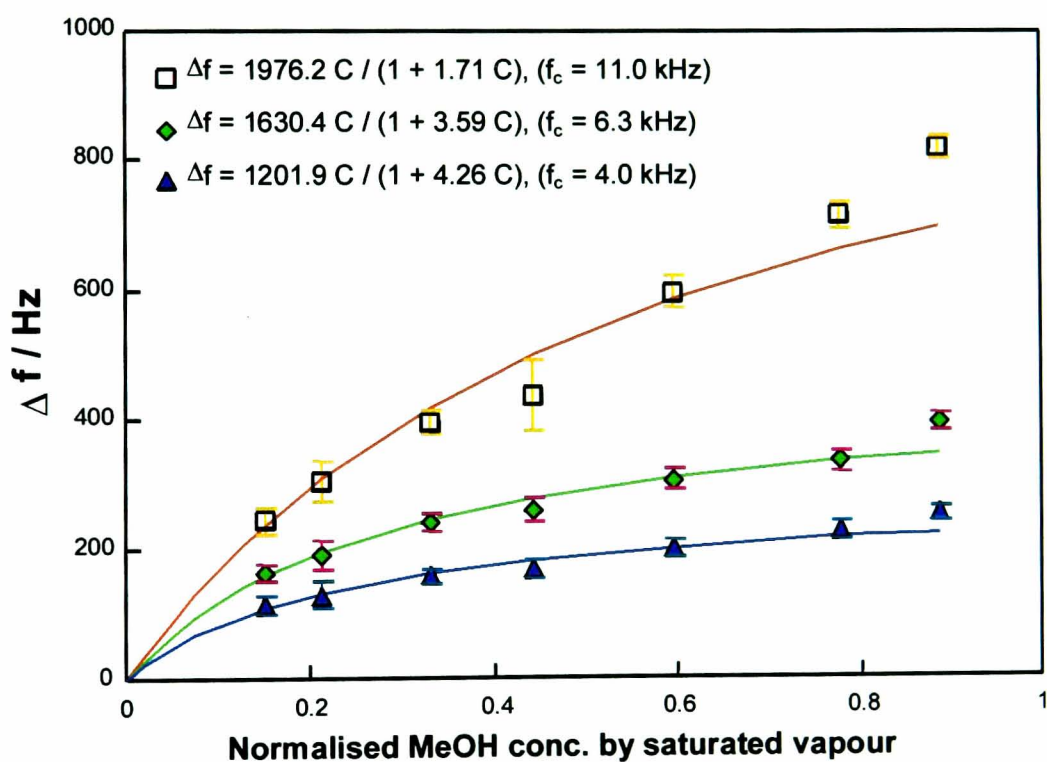


Figure 3.4 A plot of the QCM resonant frequency change in Hz versus normalised methanol concentration measured using FT-iR for a HexSO<sub>3</sub><sup>-</sup>/PPy polymer coating. All results are the mean of 3 readings. The solid line represents the best fit line to Freundlich isotherm equation, determined using linear regression.



(a)



(b)

Figure 3.5 A plot of the QCM resonant frequency change in Hz versus normalised methanol concentration for a HexSO<sub>3</sub><sup>-</sup>/PPy polymer coating of different film thicknesses. (a) the best fit to the Freundlich isotherm equation, determined using linear regression. (b) the best fit to the Langmuir isotherm equation, determined using linear regression.

It can be seen that the Freundlich model provides a better fit for thicker films, but the Langmuir isotherm more accurately describes the absorption isotherm for thinner films especially at the lower concentration end. Thus, the QCM response can be controlled by the character of the polymer film such as the thickness of film, although other parameters including doping level/oxidisation level or density can also be varied. These characters can be varied with the film deposition conditions such as growth speed, growth time, solute, and electrolyte. Experimental results presented here also suggest that the resonant frequency change can be as large as 850 Hz for an 11 kHz coating, which is a change of ca. 8% relatively.

### 3.3.2 Resistive-Based Sensors

Figure 3.6 shows  $S_r$  for three interdigitated electrodes with different initial baseline resistances (namely, 40  $\Omega$ , 70  $\Omega$  and 140  $\Omega$ ) as a function of concentration of methanol. The polymers were SDSO<sub>4</sub><sup>-</sup>/PPy polymerised at the same potential but for different lengths of time. The initial resistance was controlled by the polymerisation time and the polymerisation current, described by a total electric charge passed (corresponding to 10.46 mC, 9.88 mC and 8.14 mC for the three sensors, respectively). As shown in Chapter 2, thicker films have a lower baseline resistance. It can be seen that  $S_r$  also increased nonlinearly with the concentration of methanol, as was the case for the QCM. All the curves were found to have good fits to the Freundlich isotherm. It can be noted though that the linearity coefficient  $n'$  did not vary with film thickness.

For the interdigitated electrode, the experimental results have shown the great effect of the film thickness on the magnitudes of responses expressed by the relative resistance change  $S_r$ . In general, the response increases significantly with the decrease in film thickness. From Equation 3-11, it can be seen that for a given vapour,  $S_r$  is proportional to the mass change,  $\Delta m'$ , of absorbed vapour. For two polymer films of the same composition, a thinner film absorbs a smaller amount of vapour molecules than a thicker film, i.e.  $\Delta m'$  for thinner film is smaller. Thus, a greater  $S_r$  value for a thinner film coating comes from the contribution of a greater value of  $S$ . Since  $S$  is defined as the relative resistivity change caused by one absorbed molecule, the film thickness effect can

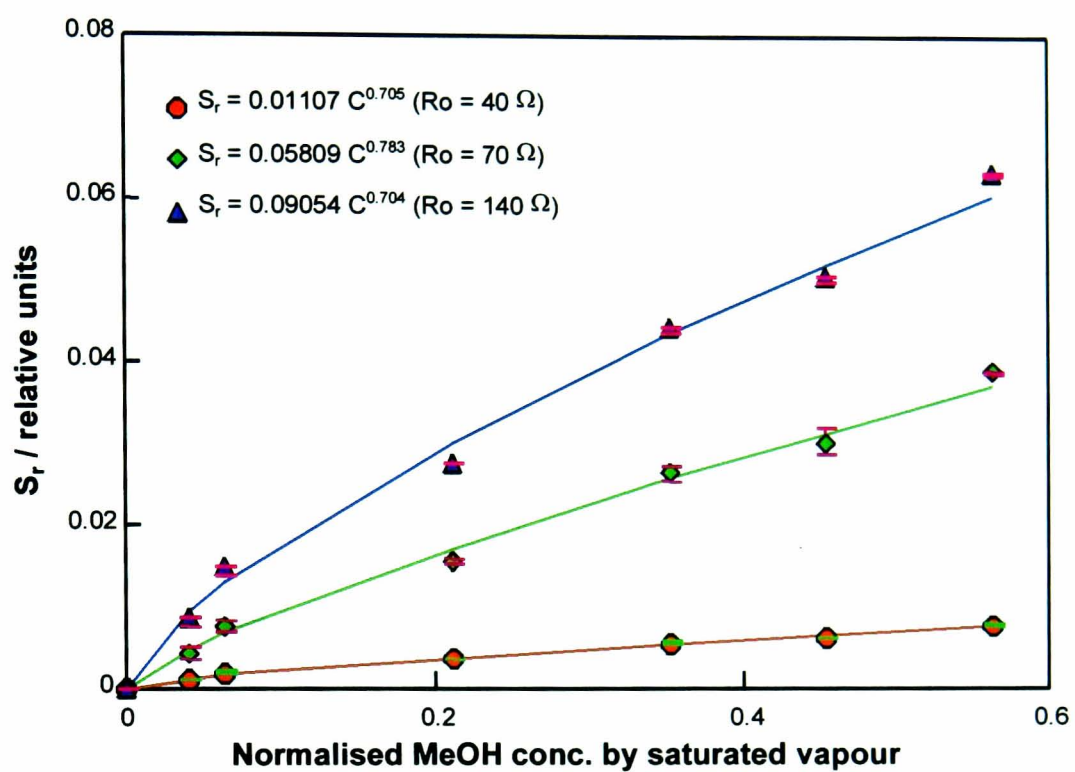


Figure 3.6 A plot of the relative resistance change,  $S_r$ , versus normalised methanol concentration for a SDSO<sub>4</sub><sup>-</sup>/PPy polymer coating at different initial resistance ( $R_0$ ) values measured using interdigitated electrodes. The solid lines are the best fit line to the Freundlich isotherm equation, determined using linear regression.

be interpreted as a greater relative effect of the absorption of one molecule on a thinner film than that on a thicker one. Conduction in a thinner film is more like a percolation process. As a simplistic example, a large molecule may block or break the whole electric flux in a thinner film but may still leave space for electric flow to pass in a thicker film. For interdigitated electrodes, the results showed that coating film thickness does not affect the response linearity with vapour concentration very much, but does affect the response magnitude, with the fact that thinner films give a higher response to a given concentration of methanol. In considering fabrication issues, the stability of sensors has to be taken into consideration with thinner films being less stable. Thus, for each polymer, there will be an optimum range of film thickness (and initial resistance), as was shown in Chapter 2.

### 3.3.3 Hybrid Systems

Figure 3.7 shows the values of  $S_f$ ,  $S_r$  and  $S_{rf}$  versus the concentration of methanol on a DecSO<sub>3</sub><sup>-</sup>/PPy polymer sensor pair, the concentration of methanol being calibrated by in-line FT-IR measurement. It can be seen that  $S_f$  and  $S_r$  increased nonlinearly with concentration with the best fit for Freundlich isotherm. However, the ratio  $S_{rf}$  remains constant for all the values of concentration tested, verifying that  $S$  is independent of concentration, over the tested range for methanol.

The conditions under which a concentration independent sensor pair could be formed is that the QCM and interdigitated electrode should have the same concentration linearity. Thus, a “good” pair of sensors with a concentration independence can be formed on a QCM and interdigitated electrode pair, if the films are polymerised under the same conditions to a thickness which yields the same concentration relationship.

Figure 3.8 shows the values of  $S_f$ ,  $S_r$  and  $S_{rf}$  for a DecSO<sub>3</sub><sup>-</sup>/PPy sensor pair for pure methanol diluted by 50% in N<sub>2</sub>, as a function of the time period (in days). As already shown in Chapter 2, the baseline resistance  $R_o$  increased monotonically due to the effect of degradation or ageing of the polymer coatings. It varied by 22.9% for this microresistor over 45 days. However, the ageing effect was not mirrored by the fluctuations of  $S_r$  and

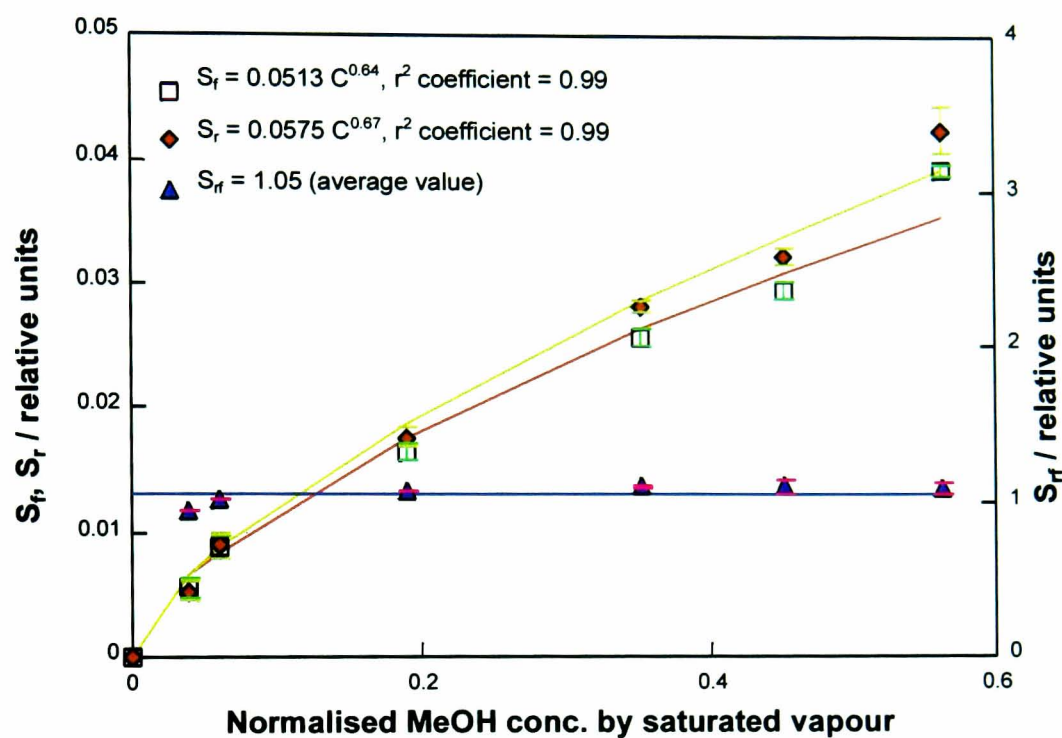


Figure 3.7 Plots of  $S_f$  ( $\square$ ),  $S_r$  ( $\blacklozenge$ ) and  $S_{rf}$  ( $\blacktriangle$ ) versus methanol concentration for a DecSO<sub>3</sub><sup>-</sup>/PPy polymer sensor pair. The curved lines represent the best fit to the Freundlich isotherm equation. The straight line through the points representing  $S_{rf}$  is the average of the  $S_{rf}$  values.

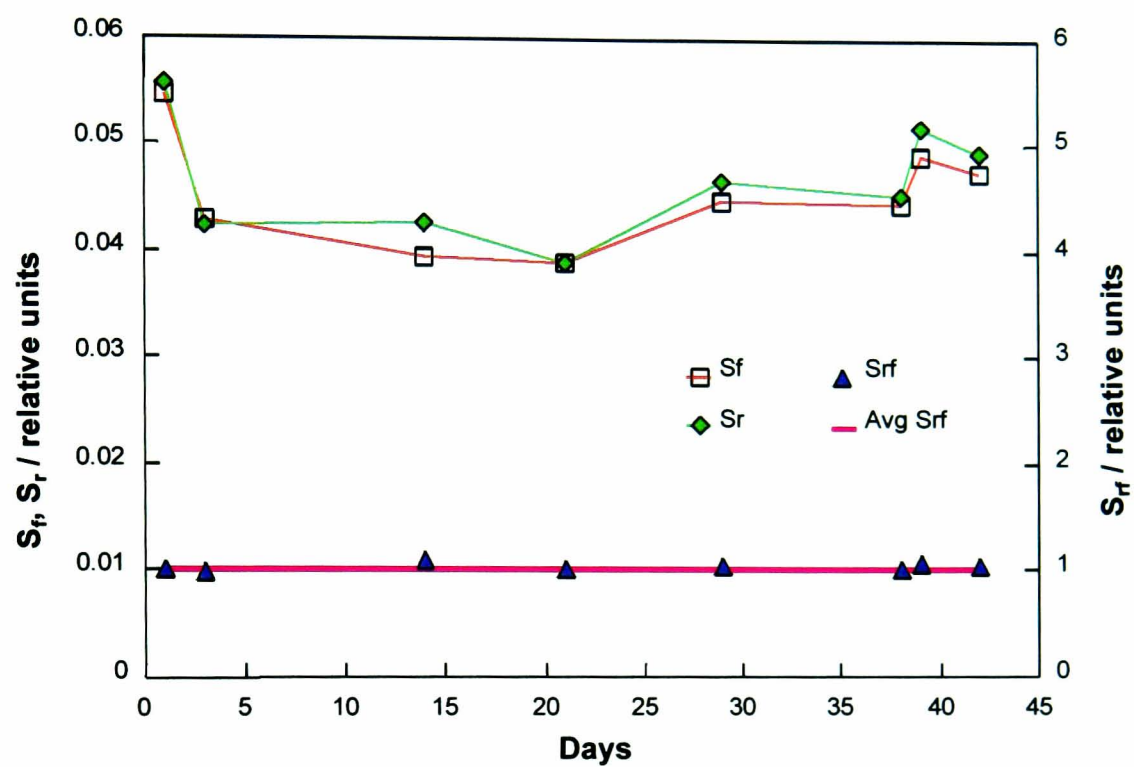


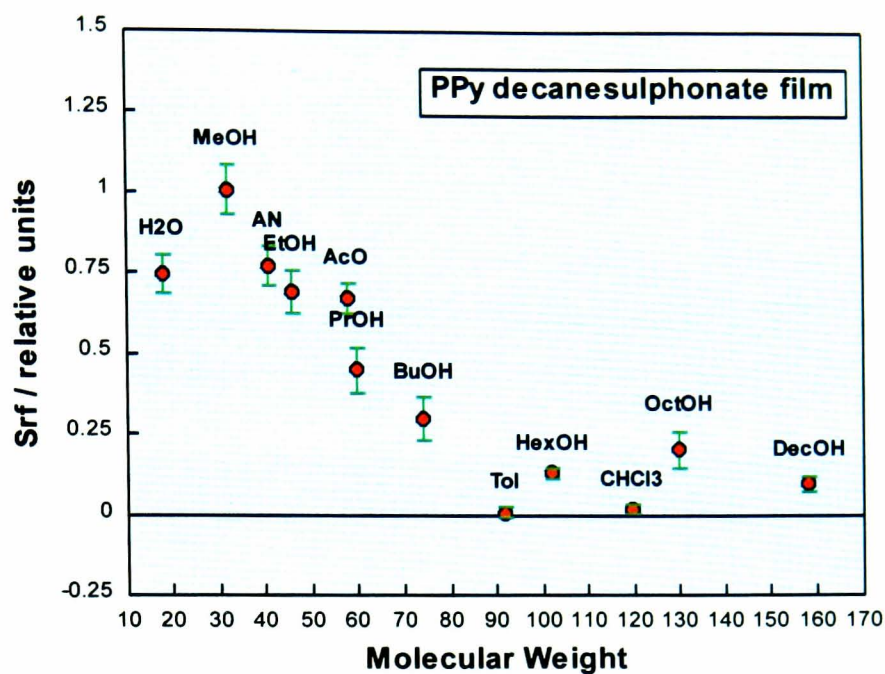
Figure 3.8 A plot showing the long term stability of  $S_f$  ( $\square$ ),  $S_r$  ( $\blacklozenge$ ) and  $S_{rf}$  ( $\blacktriangle$ ) for methanol for a  $\text{DecSO}_3^-/\text{PPy}$  sensor pair over a period of 45 days.

$S_f$ . Neither  $S_f$  nor  $S_r$  were stable over the period of study, with variation coefficients of 0.12 and 0.12, respectively, mainly due to variations in the sampling conditions (such as temperature). Meanwhile, the values of  $S_{rf}$  remained stable during the testing period, with a variation coefficient of 0.03, demonstrating an improved response stability by using a hybrid measurement system. These results also demonstrated the stability of  $S$  over the period of measurement so it can be used to represent particular interactions between methanol and polymer.

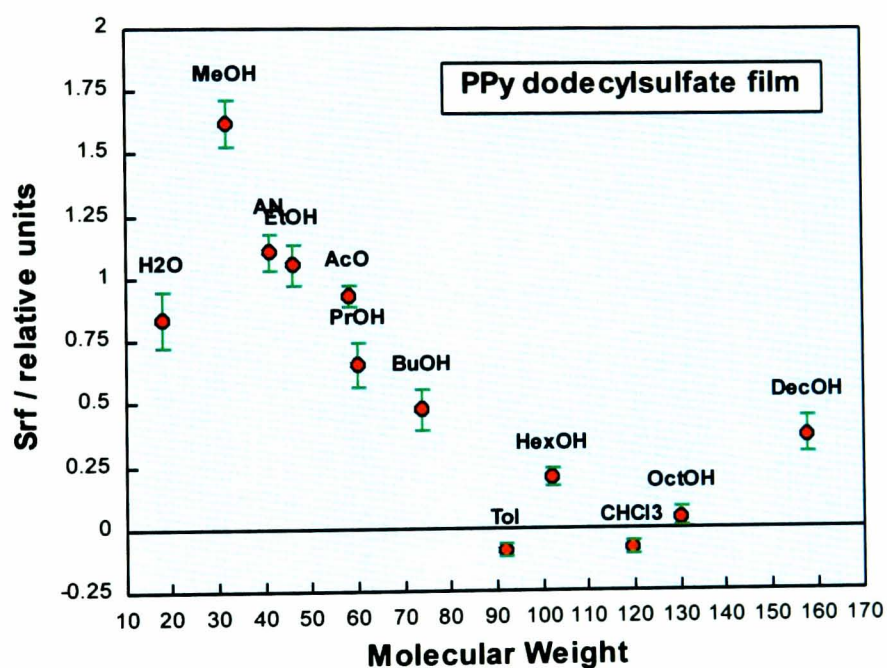
To test a broader applicability of the developed sensor response, in this study, a total of 12 odourants, of various molecular weights, were selected and measured at three concentrations (9%, 25% and 60% of the saturated vapour pressure, svp) using four sensor pairs, with the films composed of polypyrrole incorporating DecSO<sub>3</sub><sup>-</sup>, DodSO<sub>4</sub><sup>-</sup>, CF<sub>3</sub>SO<sub>3</sub><sup>-</sup>, and Tos<sup>-</sup> counterions. Figures 3.9(a) to (d) show the values of  $S_{rf}$  for DecSO<sub>3</sub><sup>-</sup>/PPy and SDSO<sub>4</sub><sup>-</sup>/PPy, CF<sub>3</sub>SO<sub>3</sub><sup>-</sup>/PPy and Tos<sup>-</sup>/PPy pairs, respectively, with each odourant yielding a particular  $S_{rf}$  value on each sensor pair. All the data from the different concentrations were closely grouped.

As indicated above, Equation 3-14 clearly shows that for a given sensor pair,  $S_{rf}$  is inversely proportional to the molecular weight of detected vapour but proportional to the vapour-polymer interaction sensitivity coefficient  $S$ . Figure 3.10 was plotted, to show an inversely proportional relationship, for comparison with Figures 3.9(a) to (d). It is found that the four sensor pairs showed different trends with increasing molecular weight. DecSO<sub>3</sub><sup>-</sup>/PPy and SDSO<sub>4</sub><sup>-</sup>/PPy have similar trends, i.e.  $S_{rf}$  decreased with an increase in molecular weight, while CF<sub>3</sub>SO<sub>3</sub><sup>-</sup>/PPy and Tos<sup>-</sup>/PPy pairs showed different trends with increasing molecular weight. For molecular weights over 90 daltons,  $S_{rf}$  for the DecSO<sub>3</sub><sup>-</sup>/PPy and SDSO<sub>4</sub><sup>-</sup>/PPy pair remained low, following the trend in Figure 3.10. For the CF<sub>3</sub>SO<sub>3</sub><sup>-</sup>/PPy and Tos<sup>-</sup>/PPy pair, however,  $S_{rf}$  increased, which is in complete contrast to the trend in Figure 3.10. This clearly indicates that  $S_{rf}$  is not solely determined by the molecular weight, the function of  $S$  is also important.

To show the effect of  $S$  on  $S_{rf}$  on each sensor pair, Figures 3.11(a) to (d) were plotted, as a bar graph of  $S_{rf}/MW$  for a series of vapours. These figures show not only how  $S$  represents different vapour-polymer interaction strengths for different odourants, but

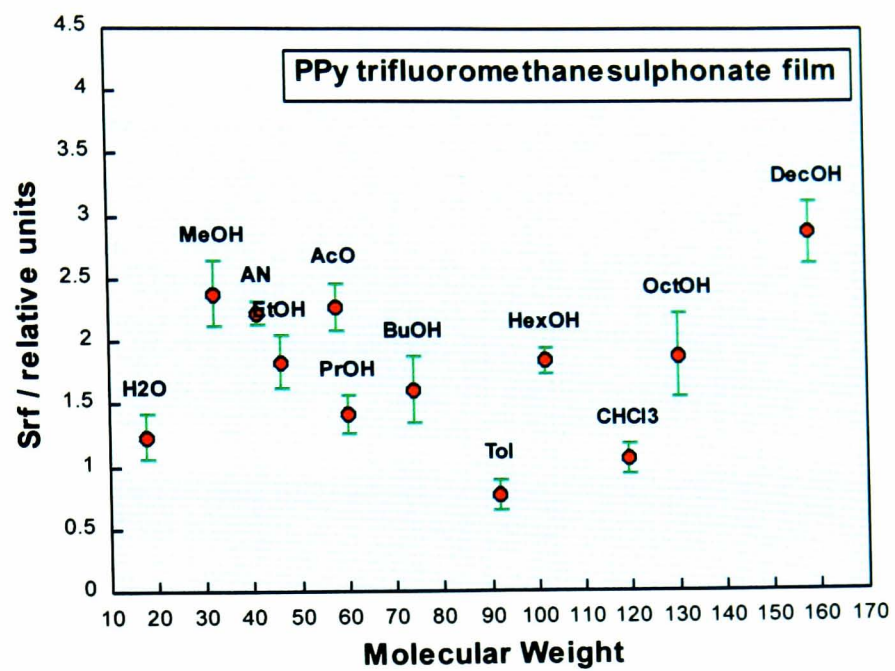


(a)

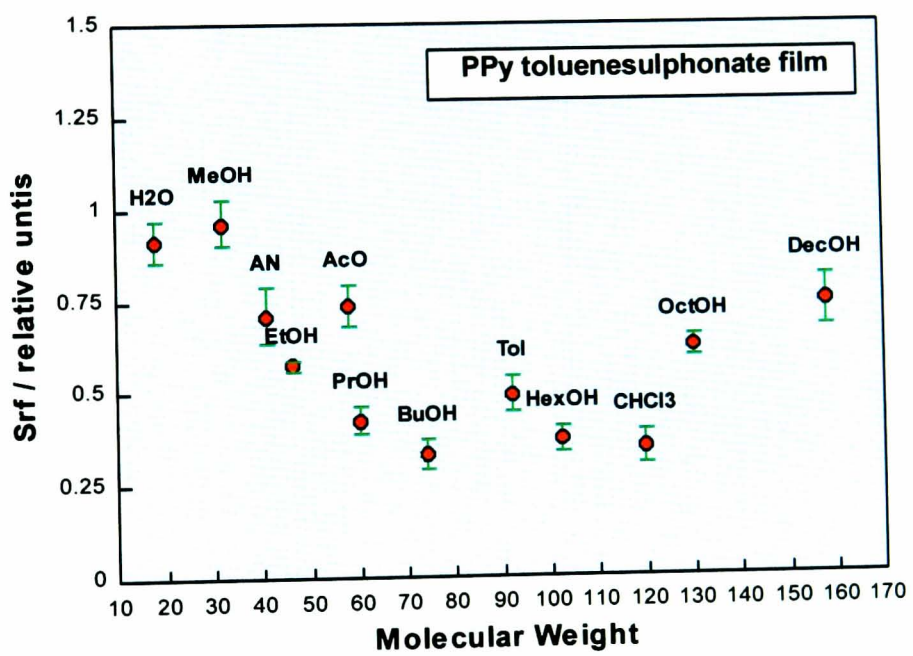


(b)

Figure 3.9  $S_{rf}$  versus molecular weight for a series of vapours for (a) a  $\text{DecSO}_3^-/\text{PPy}$  sensor pair; (b) a  $\text{SDSO}_4^-/\text{PPy}$  sensor pair; (c) a  $\text{CF}_3\text{SO}_3^-/\text{PPy}$  sensor pair; and (d) a  $\text{Tos}^-/\text{PPy}$  sensor pair. The error-bars represent the variation of  $S_{rf}$  in three measurements, at three different vapour concentrations (9%, 25% and 60% of the S.V.P.).



(c)



(d)

Figure 3.9 Continued.

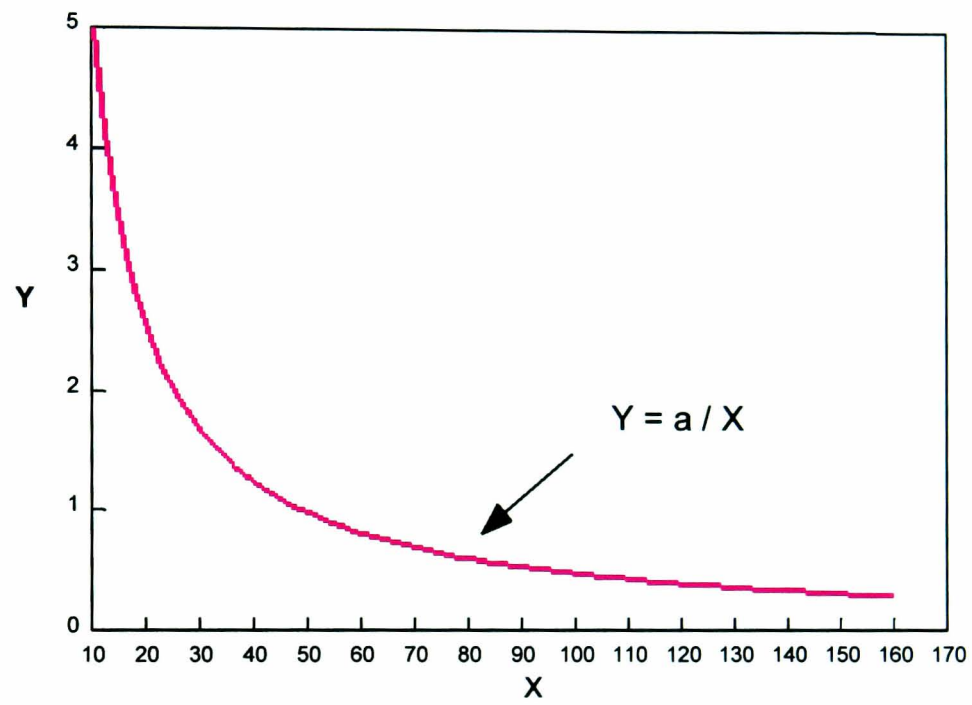
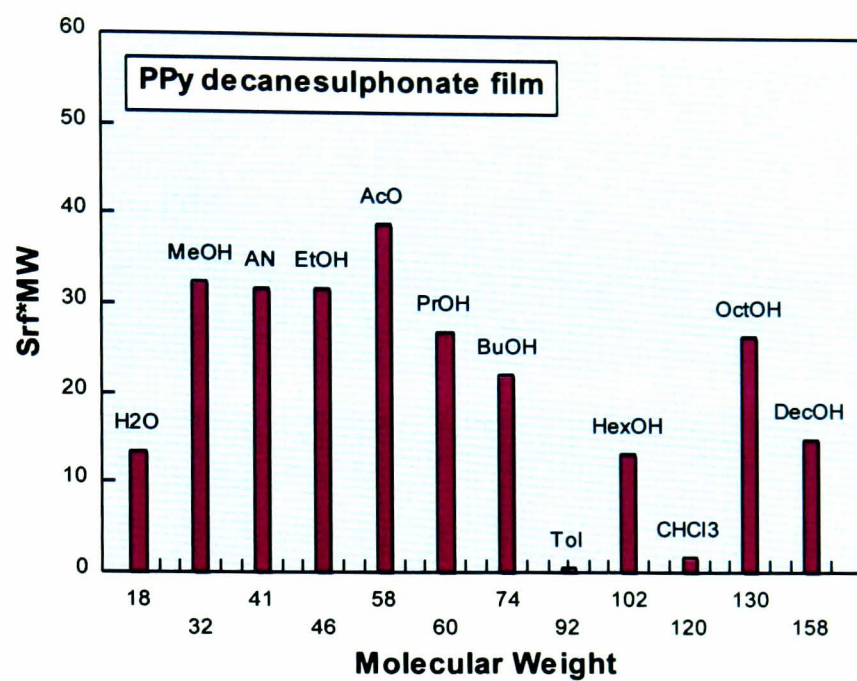
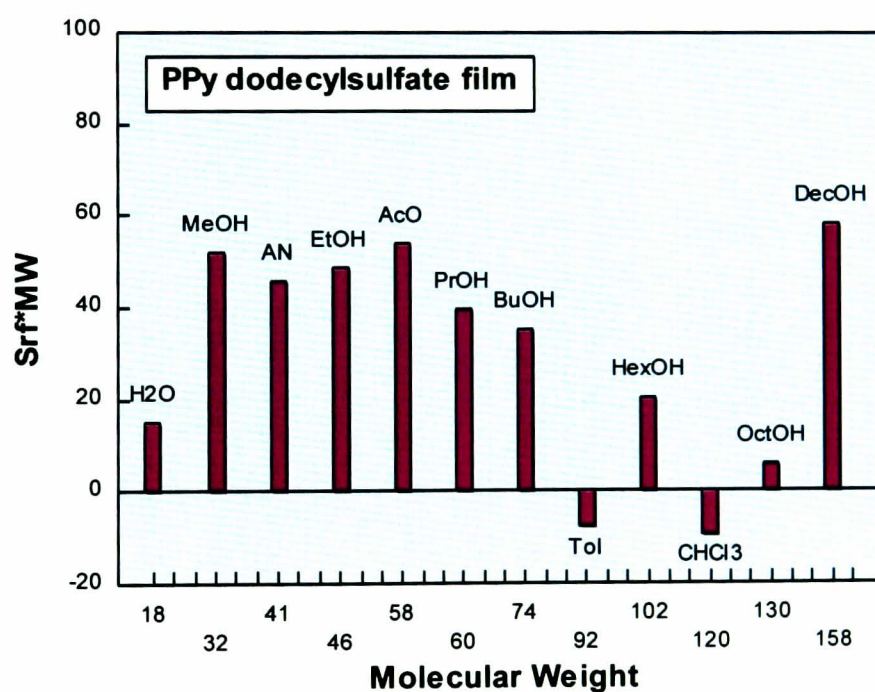


Figure 3.10 A curve demonstrating an inverse proportionality.

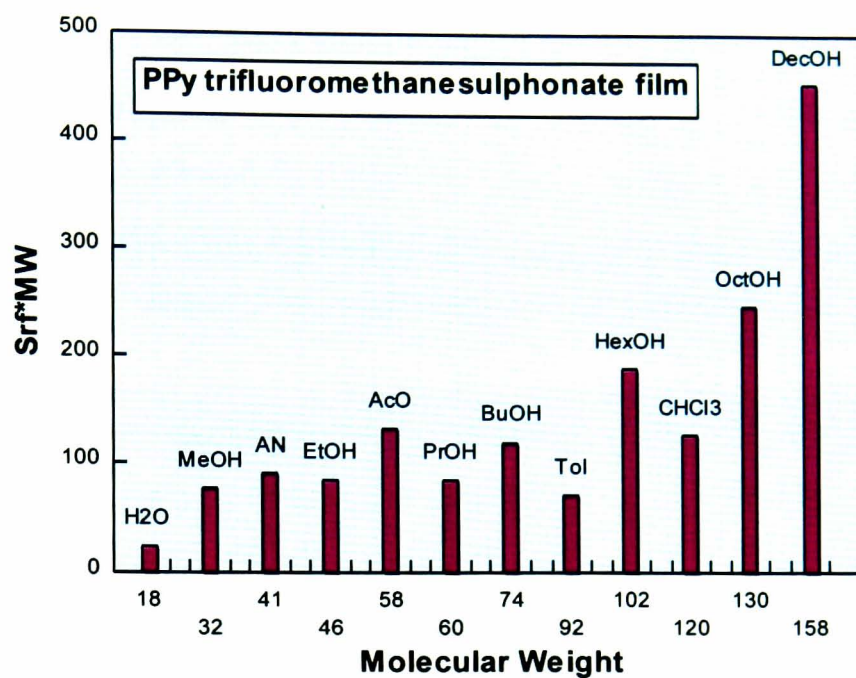


(a)

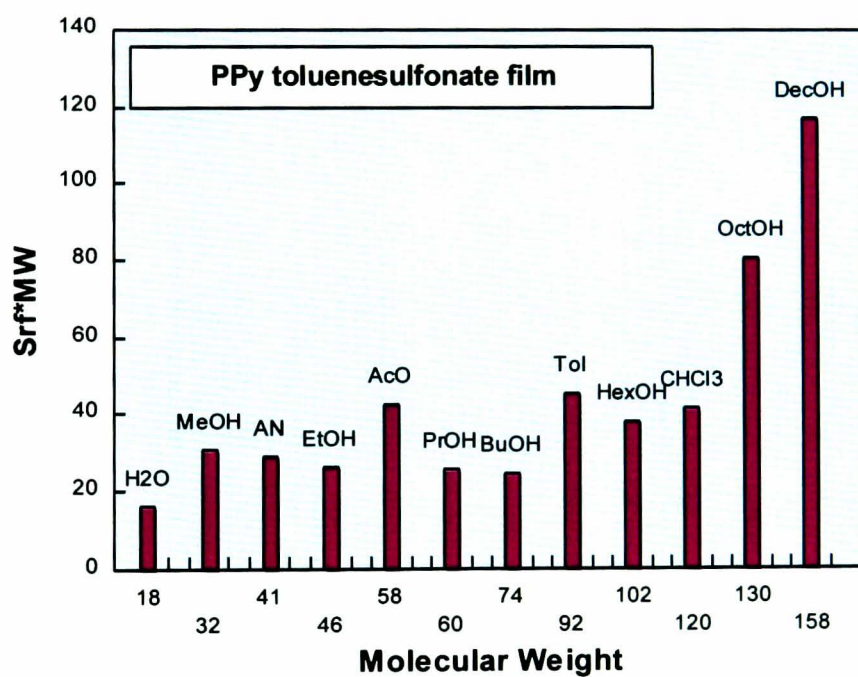


(b)

Figure 3.11  $S_{rf}$  value multiplied by molecular weight ( $S_{rf} \cdot MW$ ) versus molecular weight (MW) for a series of vapours for (a) a  $\text{DecSO}_3^-/\text{PPy}$  sensor pair; (b) a  $\text{SDSO}_4^-/\text{PPy}$  sensor pair; (c) a  $\text{CF}_3\text{SO}_3^-/\text{PPy}$  sensor pair; and (d) a  $\text{Tos}^-/\text{PPy}$  sensor pair.



(c)



(d)

Figure 3.11 Continued.

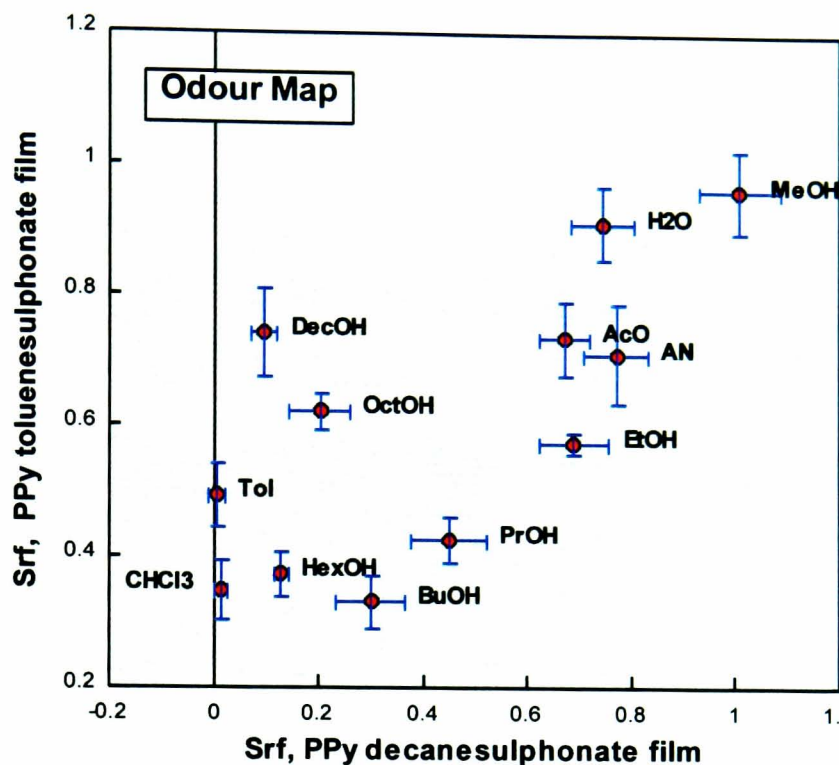
also the potential usefulness of normalising  $S_{rf}$  by the molecular weight in the investigation of vapour-polymer interactions (c.f. Chapter 4).

In summary, it has been shown in the above study that, within the concentration range tested, the gas sensitivity coefficient  $S$  was a constant for each of the 12 vapours on four polymer coatings. Also it has been shown that  $S_{rf}$  remained stable over a period of 45 days for methanol. Hence, the concentration independence of  $S_{rf}$  will be more widely applicable.  $S_{rf}$  was affected by both vapour type ( $S$ ) and vapour molecular weight. It can therefore be assumed that the selectivity of a conducting polymer to organic vapours will be determined by both the interaction between organic molecule and the polymer ( $S$ ) as well as the molecular weight of the vapour under detection. In other words, the properties of polymer backbone monomer, incorporated counterions and absorbed vapour molecules will all influence on the overall sensor pair's selectivity. In this way, the  $S_{rf}$  value can then be used to identify the characteristics of a vapour.

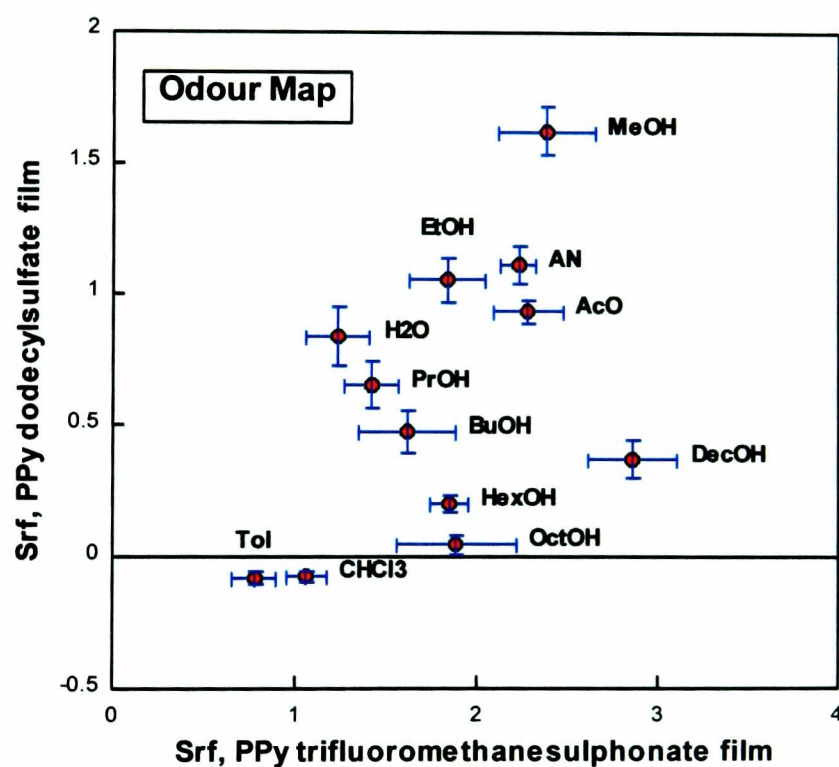
### 3.4 ODOUR MAPPING

Whilst one sensor pair has the ability to distinguish between a variety of different odourants as shown in Figures 3.9(a) to (d), an extension of using multiple pairs (of different specificities) is required to distinguish odours with similar  $S_{rf}$  values, for one particular polymer coated pair. Hence, a two-dimensional odour map can be produced in order to provide better discrimination between more than one odourant.

A two-dimensional odour map is shown in Figures 3.12(a) to (d) using the  $S_{rf}$  values from different sensor pairs. Figure 3.12(a) is a map for DecSO<sub>3</sub><sup>-</sup>/PPy and Tos<sup>-</sup>/PPy sensor pairs, Figure 3.12(b) is for CF<sub>3</sub>SO<sub>3</sub><sup>-</sup>/PPy and SDSO<sub>4</sub><sup>-</sup>/PPy sensor pairs, Figure 3.12(c) is for CF<sub>3</sub>SO<sub>3</sub><sup>-</sup>/PPy and DecSO<sub>3</sub><sup>-</sup>/PPy sensor pairs, and Figure 3.12(d) is for DecSO<sub>3</sub><sup>-</sup>/PPy and SDSO<sub>4</sub><sup>-</sup>/PPy sensor pairs. The locations of the tested vapours on these maps have changed according to the  $S_{rf}$  values of the chosen sensor pairs. Figures 3.12(a) to (c) show that those odourants could be clearly distinguished by their particular locations on the map. As to varying vapour concentrations,  $S_{rf}$  values were all closely

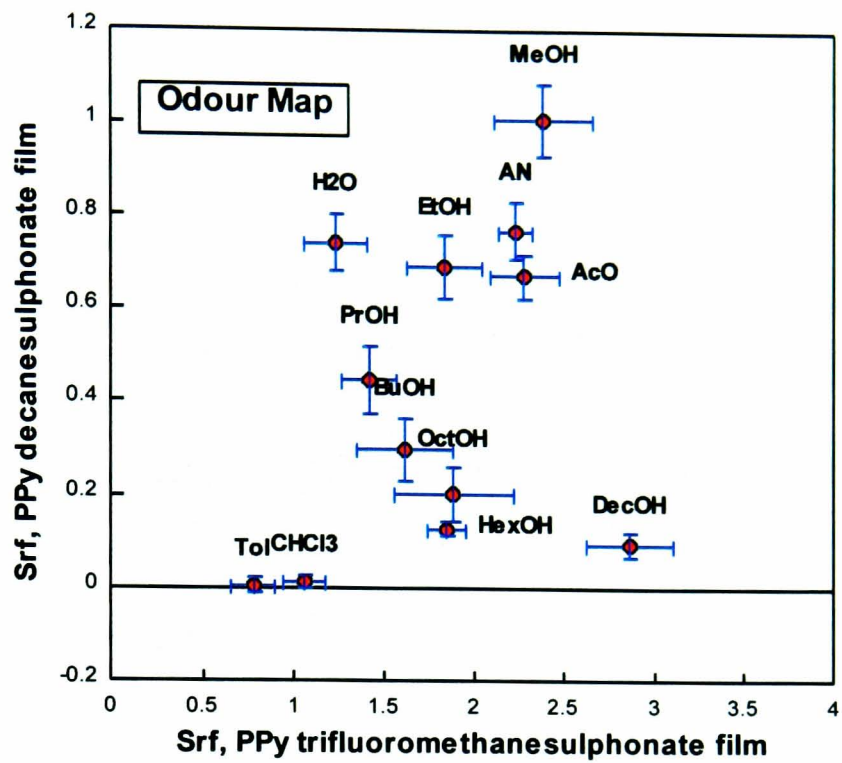


(a)

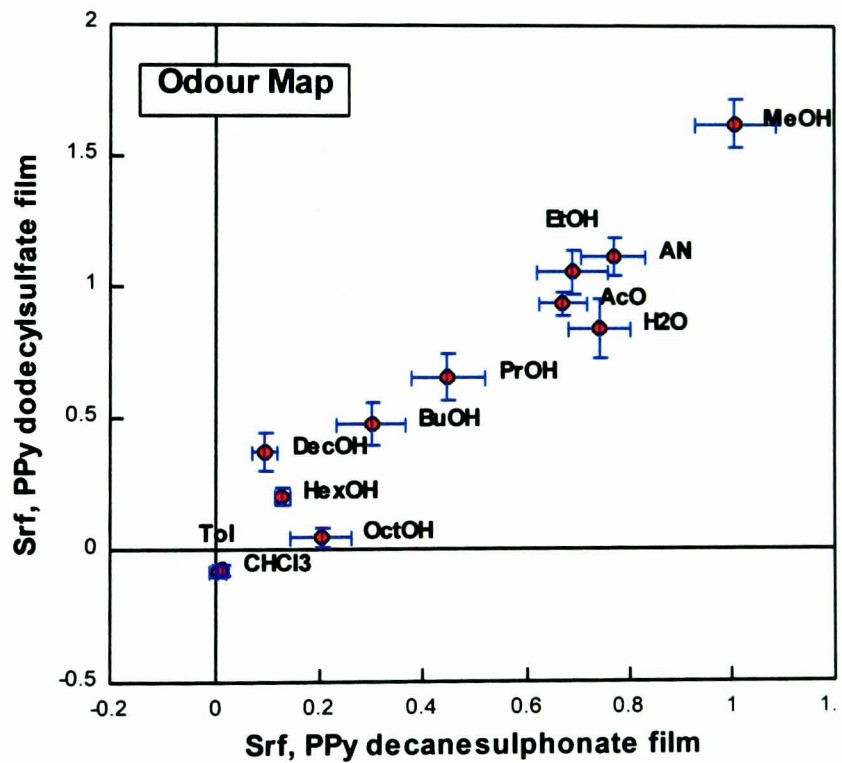


(b)

Figure 3.12 A two-dimensional odour map for a series of vapours using  $S_{rf}$  values from (a) DecSO<sub>3</sub><sup>-</sup>/PPy and Tos<sup>-</sup>/PPy sensor pairs; (b) CF<sub>3</sub>SO<sub>3</sub><sup>-</sup>/PPy and SDSO<sub>4</sub><sup>-</sup>/PPy sensor pairs; (c) CF<sub>3</sub>SO<sub>3</sub><sup>-</sup>/PPy and DecSO<sub>3</sub><sup>-</sup>/PPy sensor pairs; and (d) DecSO<sub>3</sub><sup>-</sup>/PPy and SDSO<sub>4</sub><sup>-</sup>/PPy sensor pairs. The error-bars represent the variation of  $S_{rf}$  in three measurements, at three different vapour concentrations (9%, 25% and 60% of the S.V.P.).



(c)



(d)

Figure 3.12 Continued.

grouped, which means that the location of one vapour on the map is relatively fixed. From the location on the odour map, the type of vapour can be identified. This demonstrates an increased discriminatory ability of a hybrid sensor pair in a multi-property measurement system from the lower number of different sensitive coatings employed compared with the single property measurement system.

Whilst  $S_{rf}$  can be used to discriminate types of vapours without influence from the vapour concentration, either individual  $S_f$  or  $S_r$  values can still be used to determine the vapour concentration when necessary, because they contain vapour concentration information.

The choice of the correct sensor pairs to construct an odour map is important. In this study, it was found that  $\text{DecSO}_3^-/\text{PPy}$  and  $\text{SDSO}_4^-/\text{PPy}$  sensor pairs gave similar selectivities to odourants. An odour map plotted using  $S_{rf}$  values from these two sensor pairs is shown in Figure 3.12(d). Here, all odourants were located close to a straight line, showing that this map is less discriminative than the other maps. The reason is that these two sensor pairs covered by polymer coatings which employed counterions possessing similar properties.

Hence, to construct an odour map possessing optimised discriminating ability towards odourants, we need to choose sensor pairs of significantly different interacting characteristics. An easy way to do this is to employ counterions of significantly different physical and chemical properties, as in the above study.

An odour map can be constructed using  $S_{rf}$  values from more than two pairs of sensors for an even better discrimination of odorants located close with each other on two-dimensional odour maps. Figure 3.13 shows a polar type odour map using  $S_{rf}$  values from four different polymer coatings for several vapours. Each of the four direction represents a normalised  $S_{rf}$  value from one sensor pairs. Again, since  $S_{rf}$  is not greatly influenced by the concentration of vapour, the shapes of these polar type maps can represent particular vapours, and so can also be used for their identification.

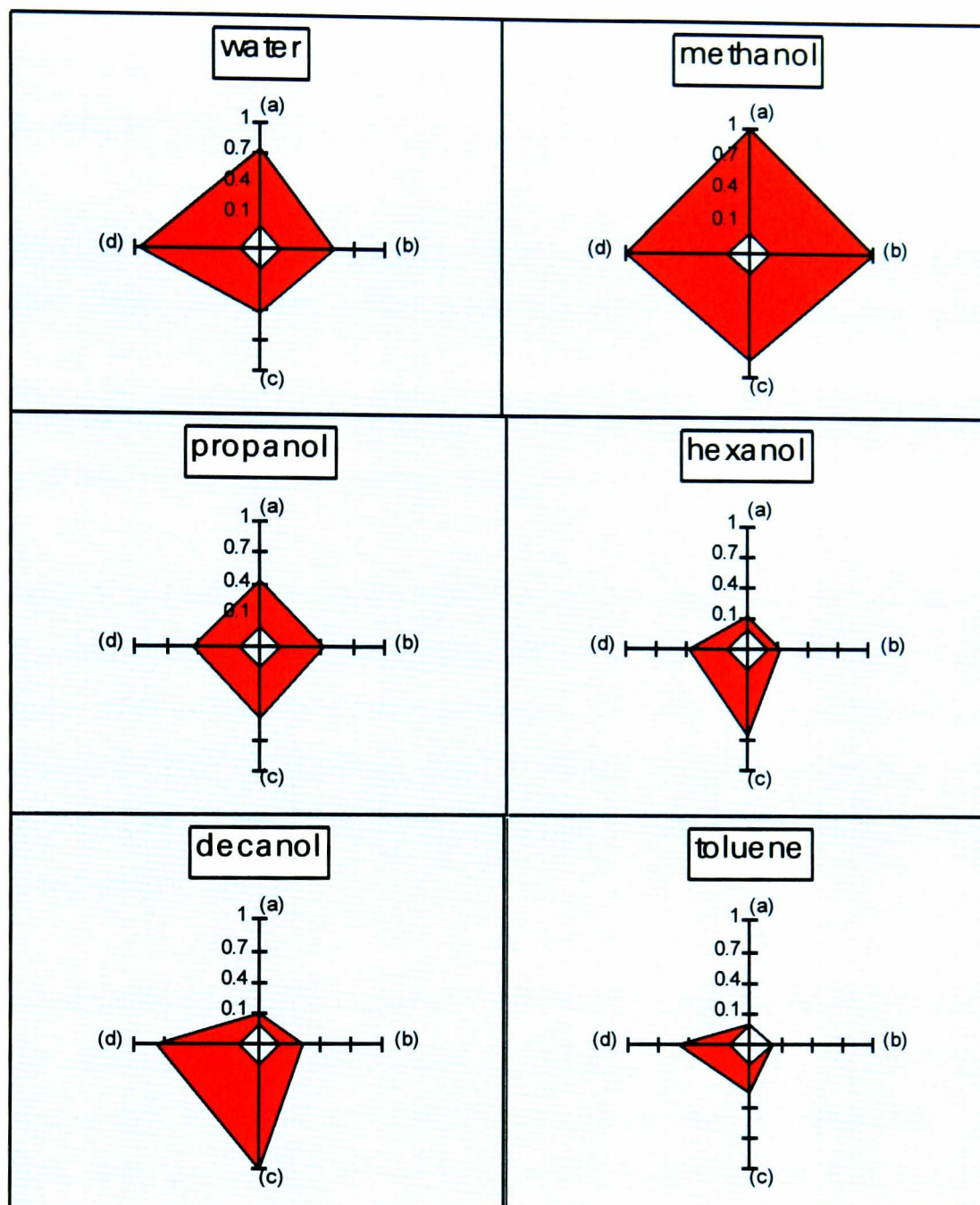


Figure 3.13 A group of polar odour maps showing a series odorants:

- (a) — Normalised  $S_{rf}$  value for DecSO<sub>3</sub><sup>-</sup>/ PPy film;
- (b) — Normalised  $S_{rf}$  value for SDSO<sub>4</sub><sup>-</sup>/ PPy film;
- (c) — Normalised  $S_{rf}$  value for CF<sub>3</sub>SO<sub>3</sub><sup>-</sup>/ PPy film;
- (d) — Normalised  $S_{rf}$  value for Tos<sup>-</sup>/ PPy film.

### 3.5 CONCLUSIONS

The results of this chapter can be summarised as the following conclusions:

The sensor response models for QCM, interdigitated electrodes and a hybrid system have been established. The vapour-polymer interactions and sensor pair's response have been linked by a sensitivity coefficient  $S$ , which can be obtained and evaluated by measurement and analysis of the particular value of  $S_{rf}$  (reflecting the selectivity of this sensor pair for a particular vapour).

A pair of sensors showing concentration independence can be formed on separate QCM and interdigitated electrodes polymerised under the same conditions, such that the concentration relationships (linearity) are the same. The film thickness is suggested thicker (around 10 kHz in frequency shift by coating material deposition) on QCM for good sensitivity, and is within an optimum range on interdigitated electrode for both good sensitivity and good stability.

$S_{rf}$  is determined by both the interaction between organic molecules and polymers ( $S$ ) and the characteristic of the vapour under detection ( $MW$ ).  $S_{rf}MW$  value can be introduced as a new parameter for studying the vapour-polymer interaction. Test results for a DecSO<sub>3</sub><sup>-</sup>/PPy sensor pair for methanol over a period of 45 days have shown an improved combined sensor response ( $S_{rf}$ ) stability of the hybrid measurement system.

Odour maps have shown the feasibility of distinguishing odourants using a significantly lower number of different types of sensor coatings incorporating counterions of significantly different physical and chemical properties. This has shown an improved selectivity of a hybrid compared with the single property measurement system.

In the next chapter, the nature of vapour-polymer interaction mechanism will be studied using the introduced parameter  $S_{rf}MW$ , coupled with linear solvation energy relationships to gain a better understanding of the nature of the interactions and the responses of the sensors.

## **Studies on the Mechanisms of Vapour-Polymer Interaction**

### **4.0 INTRODUCTION**

The essential strategy for the development of vapour sensors is to synthesise a sensing film which, due to its chemical interaction with a target analyte, generates the primary recognition signal. Regardless of the detection mechanisms involved, the response characteristics of the sensor should be a function of the nature of the interaction between the analyte and the sensor coating. This is of prime importance in *Electronic Nose* development, where a fundamental understanding of the mechanisms of interactions may be necessary to interpret sensor responses and to design useful sensor coatings for analytical applications [115].

As stated in Chapter 1, various mechanisms to describe the possible interactions between gases and conducting polymer coatings have been presented by Bartlett and Gardner in 1991 [103], which will be further discussed in Section 4.1 of this Chapter. There are other works devoted to the study of the sorption process during the vapour-polymer interaction [54, 84, 104] using a variety of methods, including a combination of mass and optical spectroscopy as well as work function measurements [105, 106]. The information collected has been used to examine the electronic structure in the inherent polymer bandgap as well as charge transfer into and out of the polymer backbone by monitoring the changes of charge concentration. Other methods such as an optical FT-iR spectroscopy [107, 108], cyclic voltammetry [107], Raman spectroscopy [109], ESR [107, 110], AFM [108] and UV-vis spectrometer [111] have also been used to study a range of parameters important in any measured responses, for example, the anion substitutes of the dopant counterions, hydrogen bonding interaction and other related properties of polypyrrole films such as the role of the counterions in the transport and

magnetic properties, substrate surface effect and the effect of oxygen. Theoretical approaches using molecular orbital computations have also been adapted to study hydrogen bonding mechanisms [112, 113]. In addition, a more comprehensive solubility model (linear solvation energy relationships, LSERs) has also been used successfully to characterise solubility properties in a number of diverse systems, where regression results have been compared with the experimental results for SAW sensors [41, 42, 44, 116]. This method uses selected representative molecular parameters to analyse particular interactions contributing to the overall sorption process, such as hydrogen bonding interactions and other processes such as polarity, polarizability and dispersion interactions.

In recent years, combined sensor pairs have also been employed to study the vapour sorption process due to their advantages of a multi-property measurement [80, 83, 85, 86]. In the study described here, hybrid sensor pairs of quartz crystal microbalance (QCM) and interdigitated electrode will be used in a similar fashion. The nature of vapour-polymer interaction mechanisms will be studied using the parameter  $S_{rf}MW$  (which has been introduced in Chapter 3 as a hybrid sensor pairs response  $S_{rf}$  multiplied by the vapour's molecular weight MW). Although  $S_{rf}MW$  is determined by the responses of sensors, it could still be considered as a “solubility property” of the vapour-polymer-sensor system since the sensor pair's response is directly proportional to the sorption process of vapours absorbed into the polymer. Linear solvation energy relationships (which employ five basic representative molecular interaction parameters) are also used for data regression and analysis to gain a better understanding of the nature of the response for a conducting polymer-based microresistor.

There are three main component parts involved in the vapour sensing process at a conducting polymer electrode — namely, vapour, polymer backbone and incorporated counterions. Hence, for a clearer understanding of each part's function, this study will be sub-divided accordingly. The strategy will be to change the property of one function part whilst keeping the other two constant. For example, methanol and deuterated methanol (partially and completely substituted) will be used as a set of vapour samples to study the influence of vapour hydrogen bonding activity. Alternatively, to study the effect of counterions, polypyrrole films incorporating different alkyl sulphonate and alkyl sulphate

counterions varying in size and acidity will be deposited at sensor surfaces, and each will be exposed to a set of chosen vapour samples which span a variety of analytes. Finally, co-polymer films of pyrrole and N-substituted pyrrole will be polymerised, and, the effect of polymer backbone hydrogen bonding activity will be studied.

As a result, this Chapter will reveal a fundamental understanding of a number of gas-polymer-sensor combinations and important contributing interactions to the overall response of a sensor. It will be demonstrated necessary and helpful to interpret and predict the sensors response and to assist sensor coatings design and choice. For example, once the solvent coefficients for dissolution of a gas into a polymer have been determined using LSERs analysis, then the hybrid responses  $S_{rf}MW$  can be evaluated for a given vapour, assuming its solvation parameters are known. Thus, this approach holds promise as a rapid means of predicting coating sensitivity and selectivity.

#### **4.1 Charge Transport in Polypyrrole and Possible Effects Contributing to the Gas Sensitivity**

As stated previously, for a wide range of materials, including ionic solutions, metal polymers and semiconductors, the electrical conductivity is proportional to the product of the concentration of charge carriers (electrons, holes, and ions) and their mobilities. In Chapter 1, the structure of polypyrrole, charge transport in polypyrrole, and possible interactions between gas and polymers were reviewed.

When a vapour molecule is absorbed into the polypyrrole film, it will change the conductivity of the film. The components of analyte-polymer interactions have been described by Bartlett et al. [103] as shown in Figure 4.1, including: the direct generation or removal of charge carriers within the film corresponding to oxidation or reduction of the polymer by the gas; the change in intrachain carrier mobility along the polymer chains due to the presence of gas molecules since it is sensitive to the level of structure order; the interaction of the vapour with counterions held within the film if the counterion motion is coupled to charge transfer along the polymer chains or if the interaction of the counterion

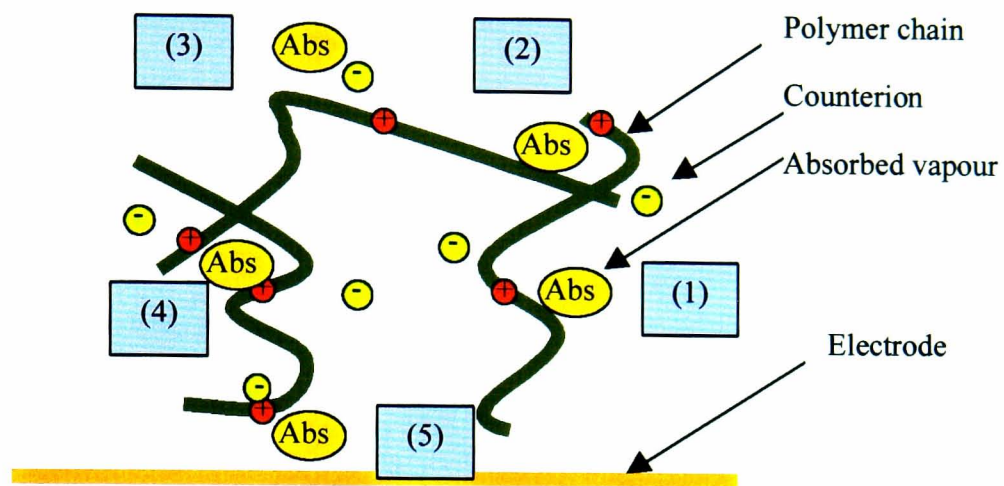


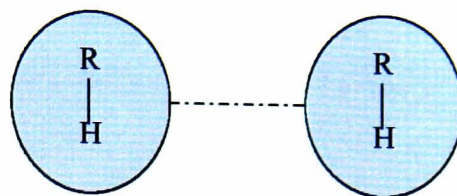
Figure 4.1 Illustration of possible mechanisms of the gas sensitivity of conducting polymer microresistors. (1) Carrier generation/removal by oxidation/reduction; (2) Change in intrachain carrier mobility; (3) Interaction with counterions; (4) Change in interchain hopping; and (5) Change in interfacial charge transfer.

with the vapour leads to a change in the structure of the polymer; the change in interchain hopping if the vapour absorption into the polymer alters the intrachain contacts; and the effect of the gas molecules on the rate of interfacial charge transfer between the metal contact and the polymer film. In addition, the response of the polymer film is also influenced by some physical effects such as polymer swelling for a certain kind of analyte, e.g. methanol at high concentration for a given polymer [54, 84, 104].

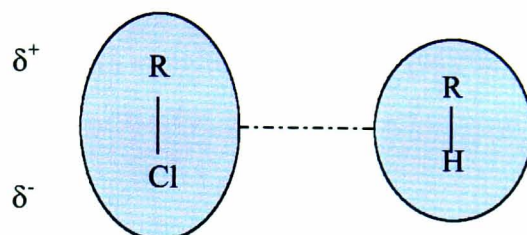
At present, the mechanism of the gas sensitivity is still poorly understood and it is not possible to distinguish between the variety of proposed mechanisms. Nevertheless, all of the possible mechanisms proposed are relative to the corresponding molecular interactions between vapours molecules and polymer matrix. For example, one possible reason for the direct generation or removal of charge carriers within the film could be related to the interaction between the vapour molecule and the polymer chain via hydrogen bonding. As a consequence, by understanding the relevant solubility interactions, the most important contributing parameters can be identified and further be used to optimise the polymers for practical applications. Various types of intermolecular solubility interactions relevant to the sorption of organic vapours by nonionic organic materials and the investigating methods will be introduced in the following sections.

## **4.2 Relevant Solubility Interactions to the Sorption of Vapours by Organic Materials**

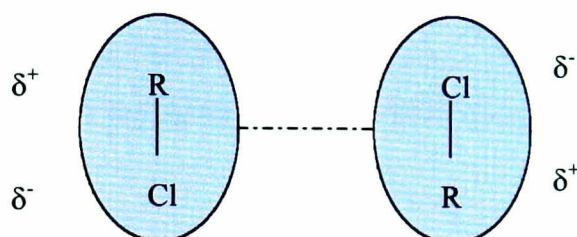
There are four intermolecular solubility interactions relevant to the sorption of organic vapours by nonionic organic materials [41,42,44,115,116,126], a classification based upon the component forces which give rise to the overall intermolecular attractions. The predominant forces include dispersion (called London or induced dipole-induced dipole) interactions, dipole-induced dipole (called Debye or induction) interactions, dipole-dipole (as known as Keesom or orientation) interactions, and hydrogen bonding interactions. The first three types of interactions are often grouped together as Van der Waals interactions [131-133]. The nature of all of these forces are illustrated in Figure 4.2, as (a) to (d) respectively.



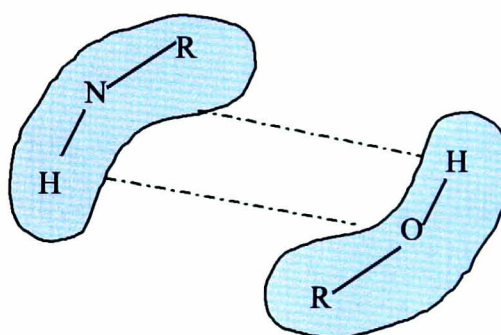
(a) Dispersion interaction



(b) Dipole-Induced dipole interaction



(c) Dipole-Dipole interaction



(d) Hydrogen-Bonding interaction

Figure 4.2 Graphic illustration of physisorption intermolecular interactions as described in the text: (a) dispersion interaction; (b) dipole-induced dipole interaction; (c) dipole-dipole interaction; and (d) hydrogen-bonding interaction.

Dispersion interactions occur between all molecules, and are produced from the transient creation of weak dipoles in a molecule as a result of the fluctuational polarisation of the electron cloud surrounding a molecular orbital. The transient dipole of a molecule induces a dipole in a second molecule when the two molecules are close enough to interact with each other. Since all substances engage in dispersive interactions to varying extents, this interaction is nonselective. For nonpolar materials, such as saturated hydrocarbons, dispersion interactions are the only significant intermolecular forces of attraction. Even for more polar molecules, this type of interactions can still be quite strong.

Interactions due to polarisability are referred to as the interactions of a dipole with an uncharged nondipolar polarisable species. The position of the electron cloud can be shifted and thus a dipole can be induced. The energy of the resulting interaction depends on the dipole moment of the permanent dipole and the polarisability of the adjacent molecule.

Dipole-dipole interactions are electrostatic interactions involving the attraction between the positively and negatively charged regions of dipolar species. These interactions are strongest for certain orientations of the dipoles. The attractive energy depends on the product of the magnitudes of the two dipole moments and a function related to probability that the dipoles are in an attractive orientation.

Hydrogen bonding can be considered as a special case of dipolar interactions. Such interactions are recognised to be important in many chemical and biochemical processes, e.g., DNA-DNA duplex recognition. Hydrogen bonding is an interaction between a covalently bound hydrogen atom, with some tendency to be donated (i.e. to serve as the acid), and a region of high electron density on an electronegative atom or group of atoms, which can accept the proton (i.e. to serve as the base). Typical proton donor groups include hydrogen bound covalently to electronegative atoms such as oxygen, nitrogen, sulphur, halogens, and in special cases, carbon and silicon [133]. The hydrogen atom acceptors are an unshared electron pair of an electronegative atom or the  $\pi$  electrons of a multiple bond system. Oxygen or nitrogen atoms are good acceptors whether they are attached to other atoms or groups [133].

The relative importance of each individual type of interaction described above depends on the particular structure of the species interacting. Hydrogen bonding is usually significant and sometimes dominant when hydrogen-bond acids and bases interact. Dipole-induced dipole interactions are generally weak, but dipole-dipole interactions can be dominant between strongly dipolar species. Dispersion interactions are the principle interactions between nonpolar species, and are generally a significant contributor to the sorption of all vapours by organic polymers [44]. In the case for polypyrrole, hydrogen bonding might be a significant interaction due to the existence of hydrogen and nitrogen atoms as well as the  $\pi$  electrons in the polymer chain.

### 4.3 Linear Solvation Energy Relationships (LSERs)

#### 4.3.1 Linear Solvation Energy Relationships (LSERs)

To study the contributions of particular interactions as stated above to the overall sorption process, linear solvation energy relationships (LSERs) have been successfully used in a number of diverse systems [116]. This model quantitatively represents the structure-activity for the process. The relationship takes a multivariate linear form which can therefore be determined using multi-linear regression. It can be constructed from the selected solute parameters [41, 42, 44, 116, 126], such as:

$$SP = SP_0 + r R_2 + s \pi_2^H + a \alpha_2^H + b \beta_2^H + l \log L^{16} \quad (4-1)$$

where SP is the solubility property under investigation,  $SP_0$  is a constant,  $R_2$ ,  $\pi_2^H$ ,  $\alpha_2^H$ ,  $\beta_2^H$  and  $\log L^{16}$  are solute parameters representing polarizability, dipolarity-polarizability, solute hydrogen-bond basicity, solute hydrogen-bond acidity and dispersion interaction, respectively. The coefficients r, s, a, b and l are solvent property constants which provide a measure of the respective solvent solubility interaction strengths. For example, l is an estimate of the dispersion interaction of the solvent, whereas a and b provide measures of the solvent's ability to act as a hydrogen-bond acid and a hydrogen-bond base. These parameters can be determined by multi-linear regression analysis. For a vapour-polymer-sensor sorption and response process, as stated in Chapter 3 and revised in this Chapter,

the parameter  $S_{rf}MW$  (which is a hybrid sensor pairs response  $S_{rf}$  multiplied by vapour's molecular weight  $MW$ , and is proportional to  $S$ ) will be used as the "solubility property" of study. The constant  $SP_0$  will be pre-set to zero in the regression because there is no response for the sensor pairs if there is no vapour-polymer interaction. The solute parameters  $R_2$ ,  $\pi_2^H$ ,  $\alpha_2^H$ ,  $\beta_2^H$  and  $\log L^{16}$  are those relative to the vapours (whilst the solvent property constants  $r$ ,  $s$ ,  $a$ ,  $b$  and  $l$  are those relative to the polymers).

Finally, the terms  $rR_2$ ,  $s\pi_2^H$ ,  $a\alpha_2^H$ ,  $b\beta_2^H$  and  $l \log L^{16}$  measure the contributions of particular interactions between vapour and polymer to the overall sorption process. In this case,  $rR_2$  is a polarizability term,  $s\pi_2^H$  is a polarity term,  $a\alpha_2^H$  is a hydrogen bonding term in which the vapour is the hydrogen-bond acid,  $b\beta_2^H$  is a hydrogen bonding term in which the vapour is the hydrogen-bond base, and  $l \log L^{16}$  is a dispersion term.

It is noted that the number of terms included in Equation 4-1 depends on the system under investigation. Other terms (e.g., molar refraction, dipole moments) may be included or substituted to provide a higher degree of correlation for different cases [126]. In this case, it is considered that the main contributions to the resistance changes in conducting polymer might be those related to the physisorption intermolecular interactions and hence, five terms covering all of the four types of intermolecular interactions are selected to study the sorption-response process of a vapour-polymer-sensor system.

After determining the solubility property (SP) for a representative set of solutes in the solvent system under study, using multivariate linear regression analysis, the coefficients  $r$ ,  $s$ ,  $a$ ,  $b$  and  $l$  in the LSERs (Equation 4-1) can be calculated. With a high degree of correlation, it could be expected that once the solvent coefficients have been obtained, the property under study, i.e.  $S_{rf}MW$ , can be determined for any solute, providing the required solvation parameters are known. In this respect, the LSERs have been considered as an empirical approach. Fortunately, the solvation parameters have been tabulated for a large number of vapour solutes and solvents which can be used in this study [116]. Thus, the empirical approach holds promise as a rapid means to predict the sensor's sensitivity and selectivity for a given conducting polymer. The regression

results of relative importance of each contributing terms can provide useful information to assist coating choice and design.

### 4.3.2 Sample Set Chosen

In order to obtain sufficient data to determine the dependant variable SP ( $S_{rr}MW$ ), a variety of vapours were selected to allow the interaction parameters to cover a property range as widely as possible and most importantly, not to be subjected to significant cross-correlation. A representative set of chosen organic vapours and their solvation parameters are listed in Table 4.1 [116].

<i>Solute</i>	<i>Polarizability</i> $R_2$	<i>Dipolarity/ Polarizability</i> $\pi_2^H$	<i>Acidity (H-bond)</i> $\alpha_2^H$	<i>Basicity (H-bond)</i> $\beta_2^H$	<i>Dispersion</i> $\text{Log } L^{16}$
<b>n-Hexane</b>	0.000	0.00	0.00	0.00	2.668
<b>Triethylamine</b>	0.101	0.15	0.00	0.79	3.040
<b>Methanol</b>	0.278	0.44	0.43	0.47	0.970
<b>Ethanol</b>	0.246	0.42	0.37	0.48	1.485
<b>1-propanol</b>	0.236	0.42	0.37	0.48	2.031
<b>1-butanol</b>	0.224	0.42	0.37	0.48	2.601
<b>Hexanol</b>	0.210	0.42	0.37	0.48	3.610
<b>Octanol</b>	0.199	0.42	0.37	0.48	4.619
<b>Decanol</b>	0.191	0.42	0.37	0.48	5.624
<b>Water</b>	0.000	0.45	0.82	0.35	0.260
<b>Trichloromethane</b>	0.425	0.49	0.15	0.02	2.480
<b>Toluene</b>	0.601	0.52	0.00	0.14	3.325
<b>Ethylacetate</b>	0.106	0.62	0.00	0.45	2.314
<b>Acetone</b>	0.179	0.70	0.04	0.49	1.696
<b>Acetonitrile</b>	0.237	0.90	0.07	0.32	1.739
<b>Pyrrole</b>	0.613	0.73	0.41	0.29	2.865

Table 4.1 Solvation parameters for selected organic vapours.

#### 4.4 $S_{rf}MW$ — AN INTRODUCED SOLUBILITY PROPERTY

As studied in Chapter 3, for a QCM-interdigitated conductimetric electrode sensor pair coated with polymer material of the same properties, the parameter  $S_{rf} = S_r/S_f$ , which represents the response of the hybrid sensor pair, can be expressed as:

$$S_{rf} = \frac{S}{(MW)u} m'_c = \frac{S}{(MW)u} k'' \rho \quad (4-2)$$

where  $\rho$  is the density of the polymer,  $k''$  is a geometric constant for the polymer coated on the interdigitated electrode, and  $u$  is atomic mass unit.

It has been shown that,  $S_{rf}$  is proportional to the vapour-polymer interaction sensitivity coefficient  $S$ , but inversely proportional to the vapour molecular weight ( $MW$ ).  $S_{rf}$  is also related to the sensor pair characteristic  $k''\rho$ . Assuming that the coatings on QCM and interdigitated electrode are made under the same polymerisation conditions and have the same absorption property, then if  $S$  is independent of the analyte concentration,  $S_{rf}$  will also be independent of the amount of the vapour absorbed, and hence also the vapour concentration. It has been verified experimentally in Chapter 3 that for an unknown vapour,  $S_{rf}$  represents a characteristic value which can be used to identify that vapour.

If  $S_{rf}$  is multiplied by the molecular weight  $MW$ , then as shown in Equation 3-15:

$$S_{rf}MW = Su^{-1}k'' \rho \quad (4-3)$$

In Chapter 3, it was shown that for a series of known vapours,  $S_{rf}MW$  is proportional to  $S$ , and hence will represent the magnitude of relative resistivity change caused by the absorption of a single vapour molecule for a given polymer. Different vapours give different values according to the intrinsic interactions with the polymer, and these can be used to constitute a set of unique variables based on the same criterion of comparison, i.e. all established by changes due to the unit molecule absorption. These variables can provide direct evidence of the strength of interactions with each

contributing term which is analysable using the LSERs method. In this way,  $S_{r^t}MW$  can be introduced as a new parameter to study the nature of vapour-polymer interactions and response mechanisms. As a result, an evaluation of the relative importance of the five interaction terms can be established.

## 4.5 RESULTS AND DISCUSSION

### 4.5.1 Experimental Strategy

Considering the three main factors involved in the vapour sensing process — namely, the vapour, the polymer backbone and the counterions incorporated, the study will also be divided into three main parts for an easier comparison and a clearer understanding of the importance and function of each factor. At the same time, the importance and usefulness of LSERs regression analysis will also be demonstrated.

In Section 4.5.2, the effect of a vapour's characters, such as the result of changing its hydrogen bonding activity, on the sensor response will be studied, with particular reference to the functional atom or group. In this case, methanol and deuterated methanol (partially and completely substituted) will be chosen as a set of examples to study and compare the responses using the same pair of sensors. The experimental hypothesis will be based on the fact that the acidity of methanol, and hence its ability in hydrogen bonding interaction, will be reduced to different extent by partial and complete deuteration.

In Section 4.5.3, the effects of counterions will be studied using the LSERs regression method. Polypyrrole coatings incorporated with different alkyl sulphonate and alkyl sulphate counterions, varying both in size and acidity will be chosen. It is already known that the structures of these polypyrrole polymers are consist of stacked polypyrrole chains separated by counterion aggregates [92, 93]. In this section, the sensor responses will be measured using a set of vapour samples which span a variety of solutes. Subsequently, LSERs will be adapted to analyse the data and to demonstrate the

usefulness of this empirical approach in predicting sensors responses and selectivity, as well as in understanding the interaction terms involved in the sorption process.

Finally, in Section 4.5.4, the effect of the polymer backbone will be studied. Polypyrrole films and co-polymer films composed of pyrrole and N-phenyl pyrrole will be polymerised with the same counterion  $\text{PF}_6^-$ . Since N-phenyl pyrrole possesses a reduced hydrogen bonding ability (it is less acidic than polypyrrole), the effects of polymer backbone hydrogen bonding activity can be obtained by comparing the experimental results for a set of vapours with the regression results.

#### **4.5.2 Effect of Vapour Characters on Vapour-Polymer Interactions**

The basis of a conducting polymer-based sensing system is the effect of the vapour properties on the sensor response, a fact which is important if one wants to improve a system's identification ability. This has already been demonstrated in the previous Chapters and is not the main concern of this section. Here, investigations were carried out using methanol and its derivatives as samples to try to identify which atom or group could influence the response, by their interaction with polymer coating. Particularly, the effects of vapour hydrogen bonding acidity on the vapour-polymer interaction were studied. Methanol ( $\text{CH}_3\text{OH}$ , or  $\text{MeOH}$ ), partially deuterated methanol ( $\text{CH}_3\text{OD}$ ) and completely deuterated methanol ( $\text{CD}_3\text{OD}$ ) were chosen as a set of sample vapours. The acidity of methanol molecule is reduced to a different extent by the process of deuteration. By comparing the difference of responses from the three vapour samples for the same polymer coating, the effect of vapour hydrogen bonding on the response was obtained.

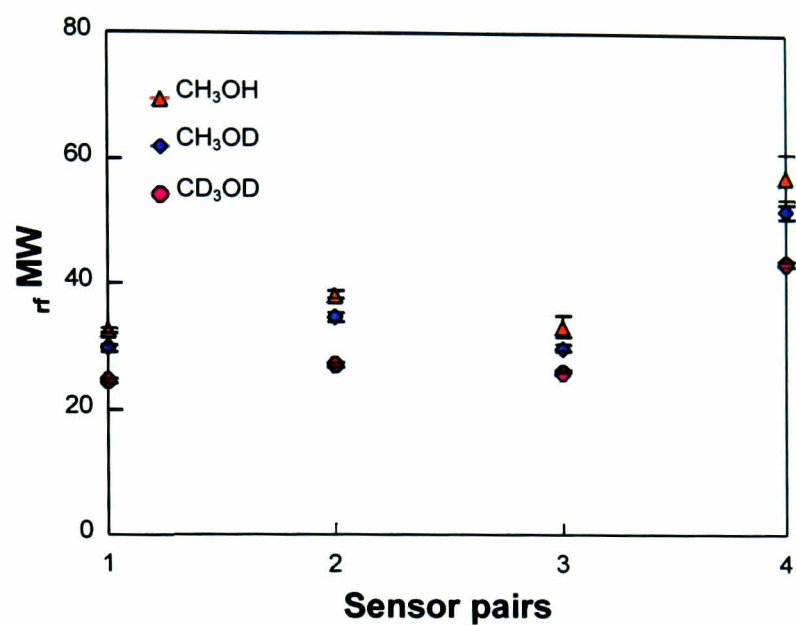
Two types of polymer films ( $\text{DecSO}_3^-/\text{PPy}$  and  $\text{SDSO}_4^-/\text{PPy}$ ) were polymerised on both QCMs and interdigitated electrodes to make sensor pairs as described in Chapter 2. Four microresistors for each type of polymer coating were prepared. Sensor pairs were exposed to the set of vapours, and both the resistance and frequency changes were measured. The values of  $S_{rf}$  were calculated and subsequently multiplied by the tested vapour molecular weight (MW).

Figure 4.3(a) shows the experimental results of  $S_{rf}MW$  for four sensor pairs coated with DecSO<sub>3</sub><sup>-</sup>/PPy polymer film, with error-bars representing standard deviation values of three parallel measurements. The baseline resistance of the four microresistors varied from 50 Ω to 156 Ω (from pair 1 to pair 4). Figure 4.3(b) shows the relative changes of  $S_{rf}MW$  from methanol (CH<sub>3</sub>OH) to methanol-d<sub>1</sub> (CH<sub>3</sub>OD) and methanol-d<sub>4</sub> (CD<sub>3</sub>OD) with respect to methanol as the base line, for comparison. The dash lines represent the average relative changes of  $S_{rf}MW$  for four pairs of sensors.  $S_{rf}MW$  decreased by 9.2% from methanol to methanol-d<sub>1</sub> and 24.6% from methanol to methanol-d<sub>4</sub> for this polymer. From methanol-d<sub>1</sub> to methanol-d<sub>4</sub> it decreased 15.4%. Assuming no synergistic effect, each deuterium atom on the alkyl chain contributes about 5.1% to the response.

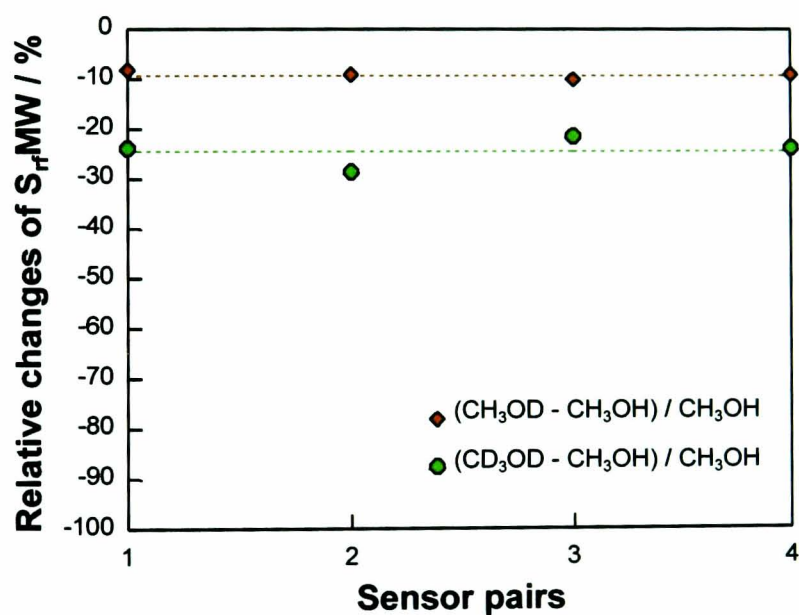
Similarly, Figure 4.4(a) shows the experimental results of  $S_{rf}MW$  for four sensor pairs coated with SDSO<sub>4</sub><sup>-</sup>/PPy polymer film, with error-bars representing standard deviation values of three parallel measurements. The baseline resistance of the four microresistors varied from 40 Ω to 77 Ω (from pair 1 to pair 4). Figure 4.4(b) shows the relative changes of  $S_{rf}MW$  from methanol to methanol-d<sub>1</sub> and methanol-d<sub>4</sub>. The dash lines represent the average of relative changes as above.  $S_{rf}MW$  dropped by 5.9% from methanol to methanol-d<sub>1</sub> and 34.8% from methanol to methanol-d<sub>4</sub> for this polymer. From methanol-d<sub>1</sub> to methanol-d<sub>4</sub>, this overall drop was 28.8%, such that each deuterated hydrogen atom on the alkyl chain would have about 9.6% contribution (given the same assumptions concerning synergistic effects).

It can be seen from Figures 4.3 and 4.4 that  $S_{rf}MW$  decreased according to the extent of the deuteration, which demonstrated the possible effects of hydrogen atoms either on the -OH group or on the -CH group.

It is well-known that hydrogen bonding is an interaction between a covalently bound hydrogen atom (for methanol molecule, it is on -OH or -CH; for pyrrole backbone, it is on -NH), and a region of high electron density on an electronegative atom or group of atoms (for methanol molecule, it is oxygen on -OH; for pyrrole backbone, these are the nitrogen on -NH or the π electron systems) [133]. The supposed interactions via hydrogen bonding could proceed in two ways. First, when the vapour is the acid,

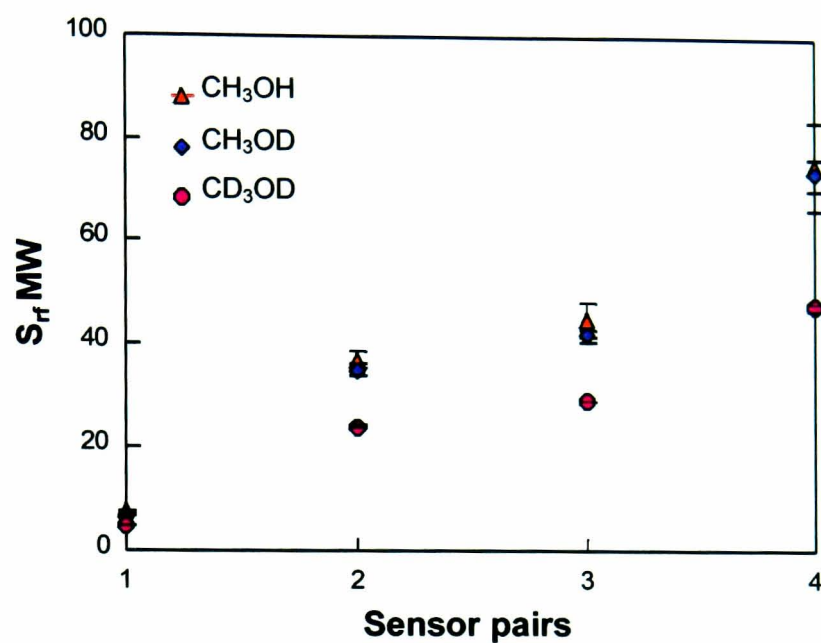


(a)

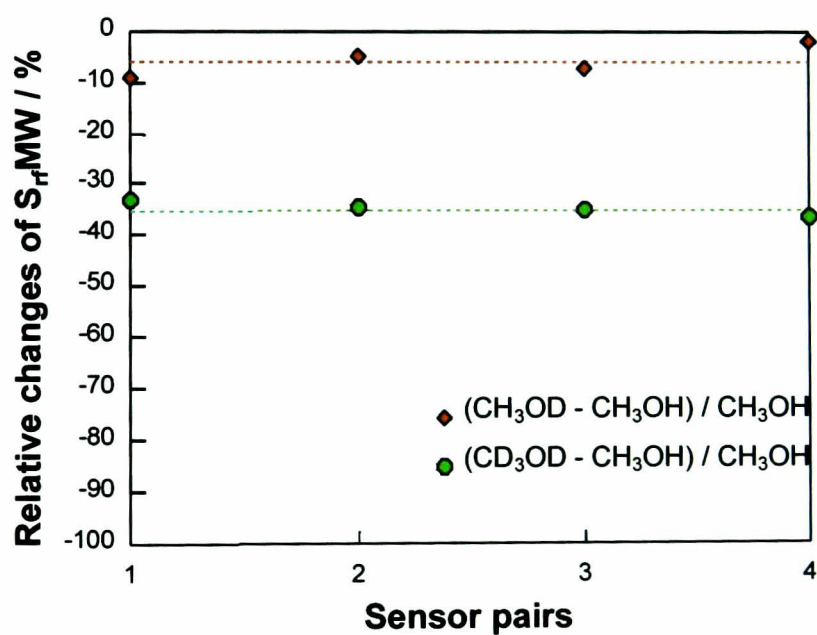


(b)

Figure 4.3 Plots showing (a)  $S_{rf} MW$  ; and (b) relative changes in responses of  $S_{rf} MW$  as a consequence of methanol ( $MeOH$ ) and deuterated methanols ( $CH_3OD$  and  $CD_3OD$ ) for  $DecSO_3^-/PPy$  sensor pairs. The base line resistances varied from 50 to 156  $\Omega$  from pair 1 to pair 4. The frequency change of corresponding QCM due to polymer coating was 12.8 kHz. The error-bars represent the variation in three measurements.



(a)



(b)

Figure 4.4 Plots showing (a)  $S_{rfMW}$  ; and (b) relative changes in responses of  $S_{rfMW}$  as a consequence of methanol (MeOH) and deuterated methanols ( $CH_3OD$  and  $CD_3OD$ ) for  $SDSO_4^-/PPy$  sensor pairs. The baseline resistances varied from 40 to 77  $\Omega$  from pair 1 to pair 4. The frequency change of corresponding QCM due to polymer coating was 16.8 kHz. The error-bars represent the variation in three measurements.

hydrogen atom on the –OH or –CH will interact with the polymer backbone base, namely nitrogen on –NH or  $\pi$  electron systems. Second, when vapour is the base, then oxygen on –OH will interact with the polymer backbone acid, namely hydrogen atom on –NH. The experimental results suggested the possible existence of a hydrogen bonding interaction between methanol hydrogen atom on both –OH and –CH with the nitrogen or  $\pi$  electron systems of pyrrole backbone.

It must be remarked that, considering all the possible interaction terms, as shown in Equation 4-1, from the changes observed in this experiment, it is still difficult to identify the “pure” contribution of the hydrogen bonding interactions. The observed changes may not be solely determined by the interaction contributed by the vapour’s acidity, because the deuteration may alter the other vapour solvation parameters (e.g. polarizability) at the same time. Thus, the observed changes in sensor’s response reflected an extensive change in vapour molecule properties, although the change of its acidity is the original and probably the most direct reason.

Obviously, an effective analytical method for further identifying the particular interactions is essential to complete the quantitative analysis. There are different ways to achieve this, such as an optical property measurements using FT-iR, as already introduced. In this study, the LSERs regression method will be used. This method will improve the basic understandings of sorption process, as will be shown in the next Section 4.5.3.

### **4.5.3 Effect of Incorporated Counterions on Vapour-Polymer Interactions**

Polypyrrole coatings incorporated with different alkyl sulphonate and alkyl sulphate counterions varying in size and acidity were polymerised as described in Chapter 2. Three sensor pairs with DecSO<sub>3</sub><sup>-</sup>/PPy, SDSO<sub>4</sub><sup>-</sup>/PPy and CF<sub>3</sub>SO<sub>3</sub><sup>-</sup>/PPy polymer coatings were exposed to a set of chosen organic vapours already listed in Table 4.1. The baseline resistance values for the corresponding interdigitated electrodes were 59 $\Omega$ , 56 $\Omega$  and 167 $\Omega$ , respectively. The frequency changes of QCMs due to the polymer coatings were 12.7 kHz for DecSO<sub>3</sub><sup>-</sup>/PPy, 16.8 kHz for SDSO<sub>4</sub><sup>-</sup>/PPy and 8.6 kHz for CF<sub>3</sub>SO<sub>3</sub><sup>-</sup>/PPy. Both

the resistance and frequency changes were measured at a QCM-conductimetric sensor pair. The average  $S_{rf}$  values of three parallel measurements were calculated and subsequently multiplied by the test vapour molecular weight (MW). The experimental set of data were then analysed with Equation 4-1 using the multi-linear regression method on the five solvation parameters of solute vapours listed in Table 4.1. Thus, the solvent coefficients  $r$ ,  $s$ ,  $a$ ,  $b$  and  $l$  for each polymer coating can be obtained. The LSERs regression  $S_{rf}MW$  values can be calculated by the sum of the five contributing terms, namely a polarizability term ( $rR_2$ ), a polarity term ( $s\pi_2^H$ ), a hydrogen bonding term in which the vapour is the hydrogen-bond acid ( $a\alpha_2^H$ ), and in which the vapour is the hydrogen-bond base ( $b\beta_2^H$ ), and a dispersion term ( $l \log L^{16}$ ).

For the DecSO<sub>3</sub><sup>-</sup>/PPy sensor pair, the regression gives

$$S_{rf}MW = 11.31 R_2 + 13.98 \pi_2^H - 10.70 \alpha_2^H + 68.20 \beta_2^H - 4.55 \log L^{16}$$

with a multi-linear regression correlation coefficient  $r_m = 0.93$ . For the SDSO<sub>4</sub><sup>-</sup>/PPy sensor pair, the regression gives

$$S_{rf}MW = 26.69 R_2 + 13.36 \pi_2^H - 29.76 \alpha_2^H + 125.64 \beta_2^H - 11.55 \log L^{16}$$

with a multi-linear regression correlation coefficient  $r_m = 0.95$ . Finally, for the CF<sub>3</sub>SO<sub>3</sub><sup>-</sup>/PPy sensor pair, we can get

$$S_{rf}MW = -240.87 R_2 + 23.42 \pi_2^H - 4.89 \alpha_2^H + 24.56 \beta_2^H + 71.14 \log L^{16}$$

with a multi-linear regression correlation coefficient  $r_m = 0.93$ .

The first purpose of this experiment is to show how this LSERs regression empirical approach promises a rapid means of predicting sensors sensitivity and selectivity towards vapours.

Figures 4.5(a) to (c) show both the experimental and LSERs regression results of  $S_{rf}MW$  versus molecular weights for the set of chosen vapours on the three individual

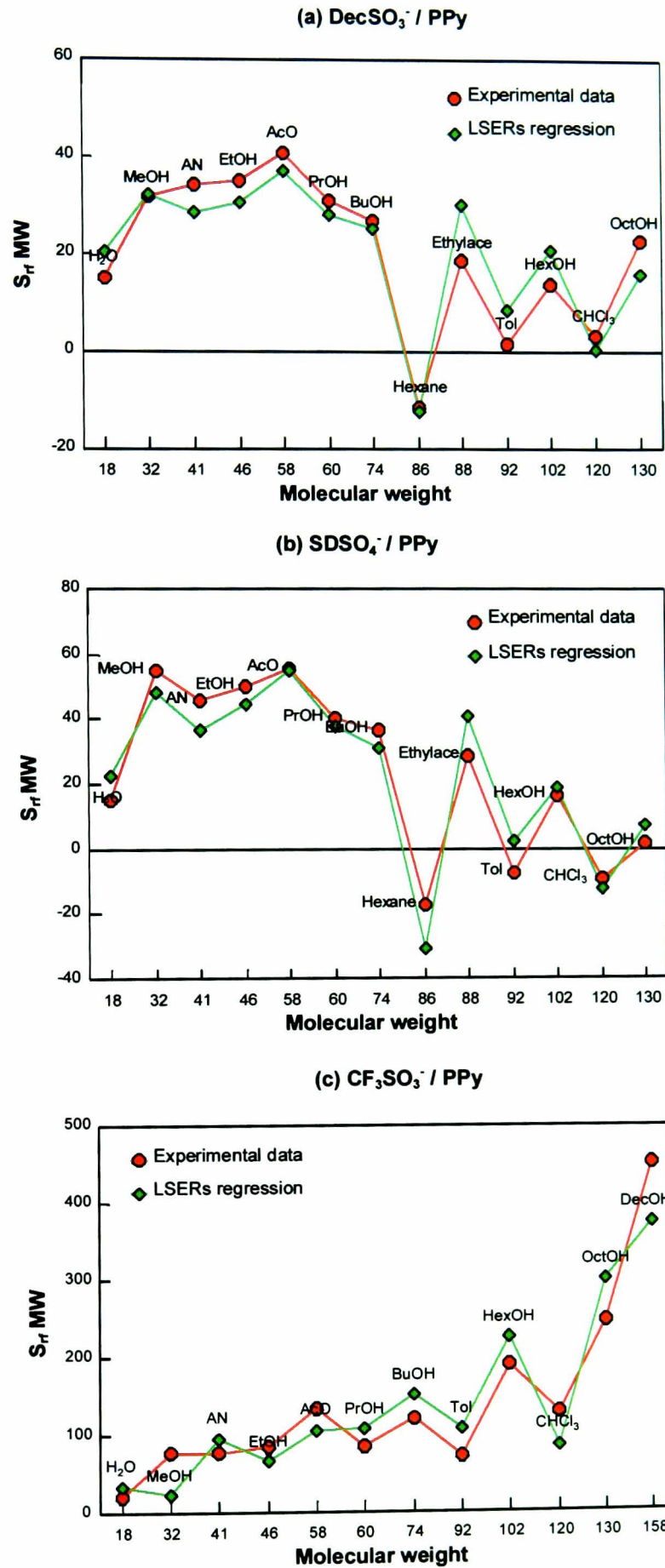


Figure 4.5 Experimental and linear solvation energy relationships (LSERs) regression results for sensor pairs: (a) DecSO<sub>3</sub><sup>-</sup>/PPy ( $f_c = 12.8$  kHz,  $R_0 = 59 \Omega$ ); (b) SDSO<sub>4</sub><sup>-</sup>/PPy ( $f_c = 16.8$  kHz,  $R_0 = 56 \Omega$ ); and (c) CF<sub>3</sub>SO<sub>3</sub><sup>-</sup>/PPy ( $f_c = 8.6$  kHz,  $R_0 = 167 \Omega$ ).

sensor pairs, respectively. It can be seen that the regression results mainly follow the experimental results for these tests. Figure 4.6 shows the regression  $S_{rf}MW$  values versus the experimental results for the three corresponding sensor pairs compared with a 45° line. It can be seen that the theoretical and experimental data were all located around this line, especially for the DecSO<sub>3</sub><sup>-</sup>/PPy and SDSO<sub>4</sub><sup>-</sup>/PPy sensor pairs, which means they are consistent with each other. In other words, for a given vapour which is not tested here, if its solvation parameters are known, then a predicted response for the DecSO<sub>3</sub><sup>-</sup>/PPy or SDSO<sub>4</sub><sup>-</sup>/PPy sensor pair can be calculated using the obtained corresponding regression results. Thus, in this way, this approach promises a rapid means of predicting sensors sensitivity and selectivity towards vapours. This prediction is of help in practice when we need to choose the correct polymer coating for a targeted vapour, whilst maintaining a small response for an interferential vapour.

A second purpose of this experiment is to study the effects of counterions on the sensitivity of response, and to show how the LSERs regression approach can assist in evaluation and understanding of the interaction terms involved in the sorption process.

Here, for a better understanding and simpler comparison of the essential roles of these three counterions, a series of alcohols were selected as solute samples. The five individual solute-solvent interaction contributing terms for the DecSO<sub>3</sub><sup>-</sup>/PPy, SDSO<sub>4</sub><sup>-</sup>/PPy and CF<sub>3</sub>SO<sub>3</sub><sup>-</sup>/PPy sensor pairs are shown in Figures 4.7(a) to (c). The intensity and the direction (with increasing or decreasing the resistivity) of each term can be seen. It is shown that for DecSO<sub>3</sub><sup>-</sup>/PPy and SDSO<sub>4</sub><sup>-</sup>/PPy sensor pairs, the hydrogen bonding interaction term  $b\beta_2^H$  is the dominant interaction; whilst for CF<sub>3</sub>SO<sub>3</sub><sup>-</sup>/PPy sensor pair, the dispersion interaction term is the most significant one.

The calculated regression results of the five individual interaction contribution terms for the three sensor pairs are listed in Table 4.2 with calculated  $S_{rf}MW$  values for each vapour. Alternatively, the importance of each of the five interaction terms can be evaluated by a normalised contribution of each term by the whole interaction contributions. Here, the normalisation was carried out by dividing the intensity of each term (represented by the absolute value) with the sum of all five intensities (all using absolute values). The calculation results are also listed in Table 4.2. The data listed in the last column is an evaluation of contribution of the two hydrogen bonding interaction

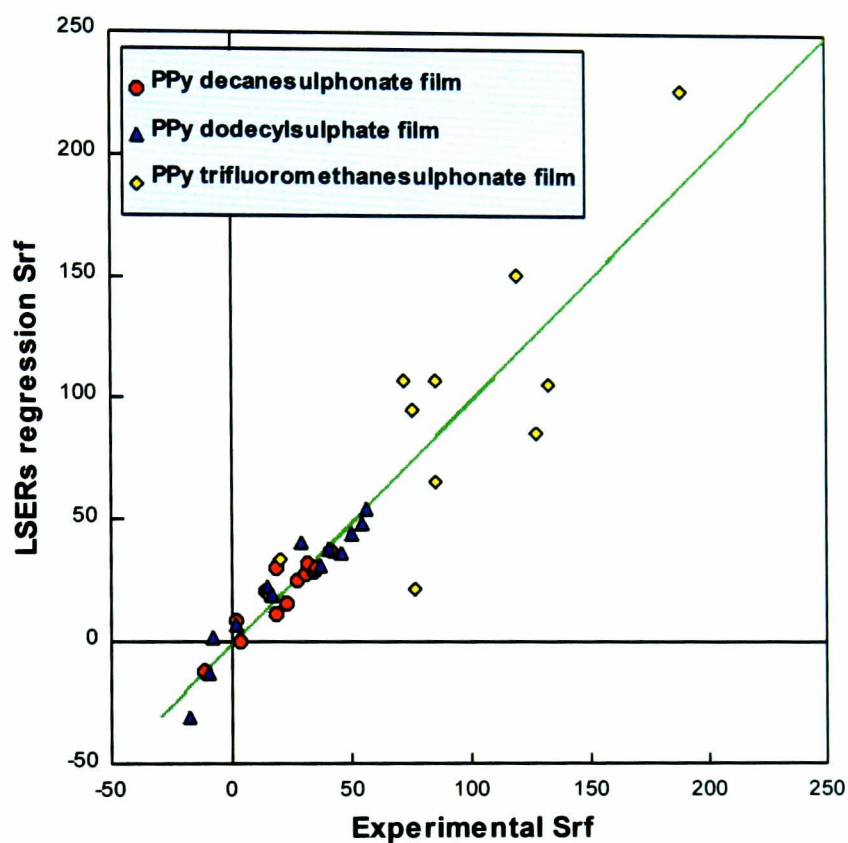


Figure 4.6 LSERs (linear solvation energy relationships) regression results versus experimental  $S_{rf}MW$  values for  $DecSO_3^-/PPy$  ( $f_c = 12.8$  kHz,  $R_0 = 59 \Omega$ ),  $SDSO_4^-/PPy$  ( $f_c = 16.8$  kHz,  $R_0 = 56 \Omega$ ) and  $CF_3SO_3^-/PPy$  ( $f_c = 8.6$  kHz,  $R_0 = 167 \Omega$ ) films.

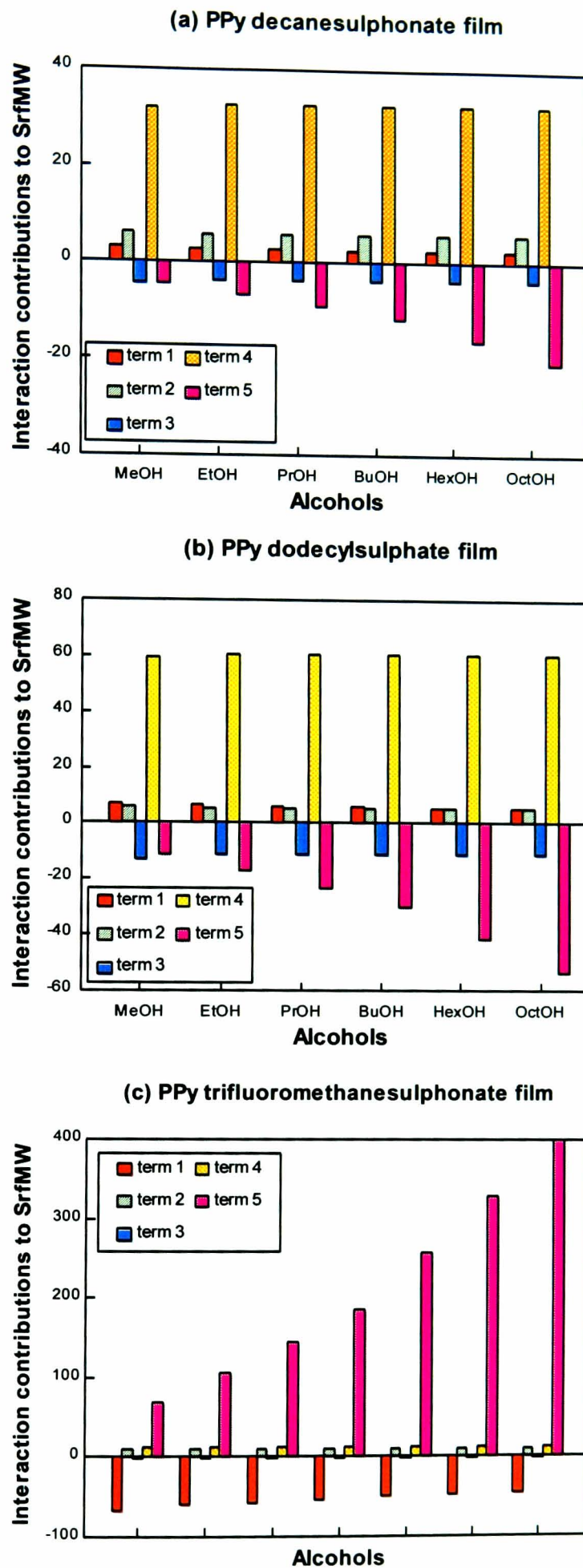


Figure 4.7 Interaction of contributing terms to the  $S_{rfMW}$  response for a family of alcohols for: (a)  $DecSO_3^-/PPy$ ; (b)  $SDSO_4^-/PPy$ ; and (c)  $CF_3SO_3^-/PPy$  films.

$$\text{term1} = rR_2, \text{ term2} = s\pi_2^H, \text{ term3} = a\alpha_2^H, \text{ term4} = b\beta_2^H, \text{ term5} = 1 \text{ LogL}^{16}$$

terms, which are the sum of the normalised contributions of terms  $a\alpha_2^H$  and  $b\beta_2^H$ . These data highlight the magnitude of the contributions of hydrogen bonding interactions to the total responses. It can be seen that for  $\text{DecSO}_3^-/\text{PPy}$  and  $\text{SDSO}_4^-/\text{PPy}$  polymer coatings, hydrogen bonding terms have significant effect (as high as 70%), whilst for the  $\text{CF}_3\text{SO}_3^-/\text{PPy}$  sensor pairs, they have much less influence (less than 10%).

Solute	Interaction terms					$S_{\text{rf}}\text{MW}$ (cal.)	Normalised contribution (in %)					Sum of H-bonding
	$rR_2$	$S\pi_2^H$	$A\alpha_2^H$	$b\beta_2^H$	$l\log L^{16}$		$rR_2$	$s\pi_2^H$	$a\alpha_2^H$	$b\beta_2^H$	$L\log L^{16}$	
<b><i>DecSO<sub>3</sub><sup>-</sup>/PPy Pair</i></b> : QCM $f_c = 12.8$ kHz, Interdigitated electrode $R_0 = 59 \Omega$												
MeOH	3.14	6.15	-4.60	32.06	-4.41	32.34	6.24	12.22	9.14	63.64	8.76	72.78
EtOH	2.78	5.87	-3.96	32.74	-6.75	30.68	5.34	11.27	7.60	62.83	12.96	70.43
PrOH	2.67	5.87	-3.96	32.74	-9.24	28.09	4.90	10.78	7.27	60.09	16.95	67.36
BuOH	2.53	5.87	-3.96	32.74	-11.83	25.36	4.45	10.32	6.96	57.50	20.78	64.46
HexOH	2.38	5.87	-3.96	32.74	-16.42	20.61	3.87	9.57	6.45	53.35	26.75	59.80
OctOH	2.25	5.87	-3.96	32.74	-21.00	15.90	3.42	8.92	6.02	49.73	31.91	55.75
DecOH	-----	-----	-----	-----	-----	-----	-----	-----	-----	-----	-----	-----
<b><i>SDSO<sub>4</sub><sup>-</sup>/PPy Pair</i></b> : QCM $f_c = 16.8$ kHz, Interdigitated electrode $R_0 = 56 \Omega$												
MeOH	7.42	5.88	-12.80	59.05	-11.20	48.35	7.70	6.10	13.28	61.29	11.63	74.57
EtOH	6.57	5.61	-11.01	60.31	-17.15	44.32	6.52	5.57	10.94	59.92	17.04	70.86
PrOH	6.30	5.61	-11.01	60.31	-23.45	37.75	5.91	5.26	10.32	56.53	21.98	66.85
BuOH	5.98	5.61	-11.01	60.31	-30.03	30.85	5.29	4.97	9.75	53.40	26.59	63.15
HexOH	5.61	5.61	-11.01	60.31	-41.68	18.82	4.51	4.52	8.87	48.55	33.56	57.41
OctOH	5.31	5.61	-11.01	60.31	-53.34	6.88	3.92	4.14	8.12	44.48	39.34	52.60
DecOH	-----	-----	-----	-----	-----	-----	-----	-----	-----	-----	-----	-----
<b><i>CF<sub>3</sub>SO<sub>3</sub><sup>-</sup>/PPy Pair</i></b> : QCM $f_c = 8.6$ kHz, Interdigitated electrode $R_0 = 167 \Omega$												
MeOH	-66.96	10.30	-2.11	11.55	69.00	21.78	41.87	6.44	1.32	7.22	43.15	8.54
EtOH	-59.25	9.83	-1.81	11.79	105.64	66.20	31.46	5.22	0.96	6.26	56.09	7.22
PrOH	-56.85	9.83	-1.81	11.79	144.48	107.44	25.29	4.38	0.81	5.25	64.28	6.05
BuOH	-53.96	9.83	-1.81	11.79	185.02	150.88	20.56	3.75	0.69	4.49	70.51	5.18
HexOH	-50.58	9.83	-1.81	11.79	256.80	226.03	15.29	2.97	0.55	3.56	77.63	4.11
OctOH	-47.93	9.83	-1.81	11.79	328.57	300.45	11.99	2.46	0.45	2.95	82.15	3.40
DecOH	-46.01	9.83	-1.81	11.79	400.35	374.16	9.79	2.09	0.39	2.51	85.22	2.90

Table 4.2 Regression results of the five individual interaction terms contributing to  $S_{\text{rf}}\text{MW}$  for different sensor pairs and the normalised contribution intensities to the sum of all intensities.

As stated previously, polypyrrole typically contains between 20 and 40 mol% (mole fraction) of counterions [91]. The counterion is known to affect the conductivity by changing the morphology of the polymer, the chemical defects, or the oxidation state of the polymer [97-99, 105]. In this study, the backbones of the films were made with the same monomer units, and were polymerised under the same conditions. Obviously, the sensors response differences observed have shown the influence of counterions. FT-iR measurements by Zotti [107] confirmed that the hydroxide anion from a solute can substitute the counterion in a reversible fashion in Tos<sup>-</sup>/PPy film. In the light of these results, it may be stated that, in general, the counterions incorporated during synthesis have a significant effect on the selectivities of conducting polymers to organic vapours.

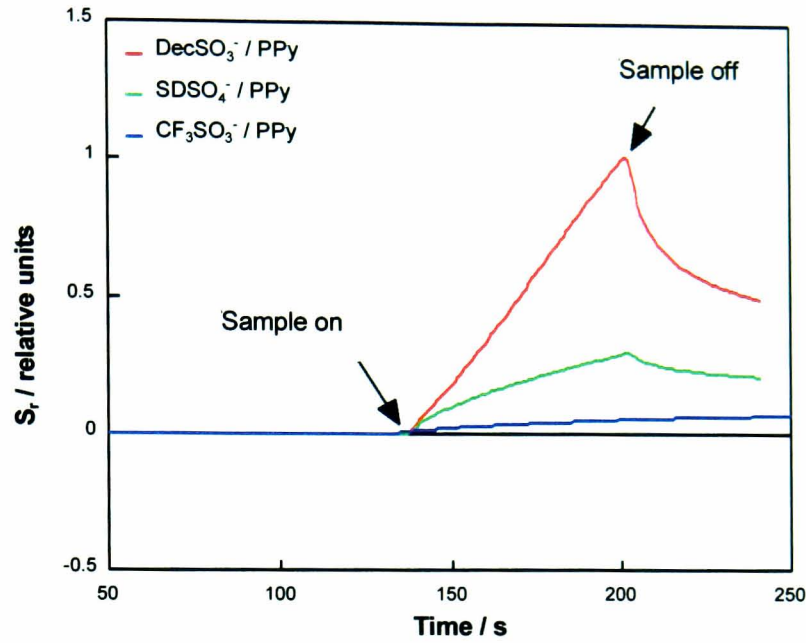
In addition, hydrogen bonding can be seen to play an important role in the extent of the interactions. The term for hydrogen bonding in which the vapour is an acid ( $a\alpha_2^H$ ) covers the interaction between vapour acidity (e.g. hydrogen on –OH group or the –CH group) and polymer basicity (e.g. nitrogen on –NH group or  $\pi$  electron systems of the backbone), whilst the  $b\beta_2^H$  term includes the interactions between vapour basicity (e.g. oxygen on the –OH group) and polymer acidity (e.g. hydrogen on –NH group of the backbone and maybe on the –CH group of the counterions). The interactions between vapour acidity and polymer basicity have also been confirmed by Blackwood and Topart [105, 106] using a combination of mass, optical spectroscopy, as well as work function measurements in the inherent polymer bandgap. They observed a charge transfer from the polymer to the dopant molecule, and the removal of electrons by the methanol dopant from BF<sub>4</sub><sup>-</sup>/PPy polymer film. The interactions between vapour basicity and polymer acidity have also been confirmed by Zotti et al. [107] using cyclic voltammetry measurement showing that there are interactions between oxidised polypyrrole with OH<sup>-</sup> (on methanol), which is most likely provided by the hydrogen on NH group of the polypyrrole backbone via hydrogen bonding.

It can be seen from the regression results in this work, as shown in Figure 4.7, that these two hydrogen bonding interactions ( $a\alpha_2^H$  and  $b\beta_2^H$ ) exist at the same time. For the DecSO<sub>3</sub><sup>-</sup>/PPy and SDSO<sub>4</sub><sup>-</sup>/PPy polymer films, the  $b\beta_2^H$  term was dominant and contributed to 64% of the sum of all five terms (see Table 4.2 “Normalised contribution” column), as shown by the normalised interaction strength. The other term  $a\alpha_2^H$  was

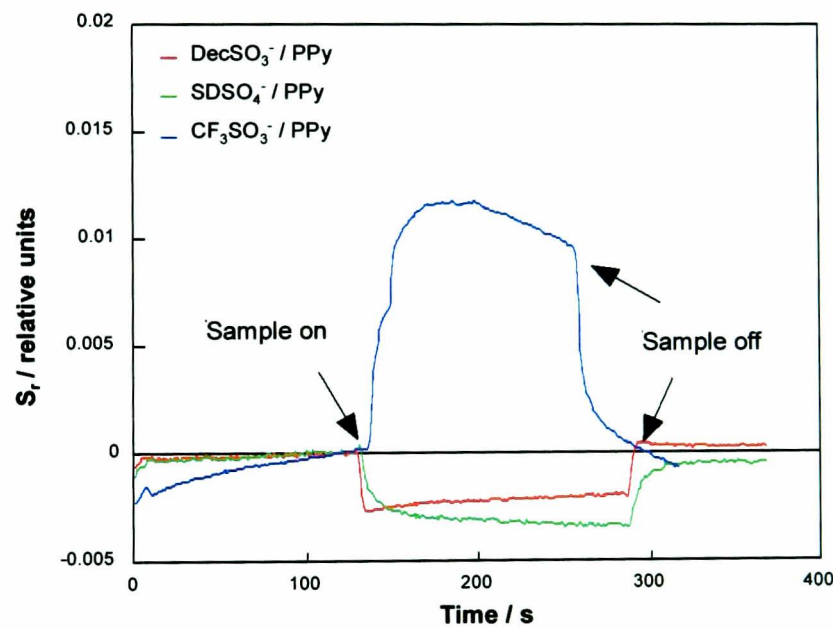
weaker and only made about 10% contributions. This shows that the oxygen on –OH group of alcohols have a strong hydrogen bonding interaction with the matrix, probably via the hydrogen on the –NH group of the pyrrole backbone, or the hydrogen on the –CH group in the counterion alkyl chain. Thus, it is reasonable to predict that for DecSO<sub>3</sub><sup>-</sup> and SDSO<sub>4</sub><sup>-</sup> counterions, alcohols (as odourants) act as electron donors, and both counterions and/or the polymer backbone accept electrons during the sorption interactions.

According to the regression results, DecSO<sub>3</sub><sup>-</sup>/PPy and SDSO<sub>4</sub><sup>-</sup>/PPy films are expected to be very sensitive to vapours with a high basicity. DecSO<sub>3</sub><sup>-</sup>/PPy is more sensitive to vapour basicity than SDSO<sub>4</sub><sup>-</sup>/PPy is. Further evidence for this hypothesis was given by the measurement of triethylamine, a solute sample possessing very high basicity. Measurements were carried out using the sensor pairs described above and, it was found that both DecSO<sub>3</sub><sup>-</sup>/PPy and SDSO<sub>4</sub><sup>-</sup>/PPy did give very large responses, as shown in Figure 4.8(a). The response of the interdigitated electrodes ( $S_r$ ) against time of measurement for the three polymers is shown, and  $S_{rf}MW$  values for DecSO<sub>3</sub><sup>-</sup>/PPy and SDSO<sub>4</sub><sup>-</sup>/PPy films were determined as 4183.1 and 618.8. Compared with the  $S_{rf}MW$  results for other vapours, shown in Figure 4.5(a) and (b), these responses were very large indeed.

With the CF<sub>3</sub>SO<sub>3</sub><sup>-</sup>/PPy polymer film, there was much less hydrogen bonding interaction contribution to  $S_{rf}MW$ , as shown by the LSERs regression results. The total normalised contributions varied from 2.9% to 8.5% for this set of samples, suggesting that CF<sub>3</sub>SO<sub>3</sub><sup>-</sup>/PPy polymer was not so sensitive to either the acidity or basicity of solutes as the other two polymers. Again, triethylamine was chosen to confirm this hypothesis. As expected, CF<sub>3</sub>SO<sub>3</sub><sup>-</sup>/PPy did not give so large a response as DecSO<sub>3</sub><sup>-</sup>/PPy and SDSO<sub>4</sub><sup>-</sup>/PPy films when compared with the other tested vapours. The value of  $S_{rf}$  is also shown in Figure 4.8(a).  $S_{rf}MW$  value was evaluated as 623.9 for this vapour which was the same magnitude as for other vapours, as shown in Figure 4.5(c). A possible reason for the relatively weak hydrogen bonding interaction between the alcohol and polymer matrix may due to the relatively low basicity of the counterion. It is also noticed that the polarizability term ( $rR_2$ ) for CF<sub>3</sub>SO<sub>3</sub><sup>-</sup>/PPy film was a negative value, which is consistent with the negative solvation polarizabilities of solutes with fluorinate group, as listed in Abraham's paper [116] (i.e. flurooctane (-0.02) and sulphur hexafluoride (-0.6) ).



(a)



(b)

Figure 4.8 Plots of  $S_r$  against time of measurement for  $\text{DecSO}_3^-/\text{PPy}$  ( $f_c = 12.8 \text{ kHz}$ ,  $R_0 = 59 \text{ }\Omega$ ),  $\text{SDSO}_4^-/\text{PPy}$  ( $f_c = 16.8 \text{ kHz}$ ,  $R_0 = 56 \text{ }\Omega$ ) and  $\text{CF}_3\text{SO}_3^-/\text{PPy}$  ( $f_c = 8.6 \text{ kHz}$ ,  $R_0 = 167 \text{ }\Omega$ ) polymers coatings for sample: (a) triethylamine (concentration 20% svp); and (b) n-hexane (concentration 50% svp).

Finally, the size of the counterions also has a large effect on the vapour-polymer interactions, which was mainly reflected by the magnitude of the dispersion term. Dispersion interactions occur when molecules are close enough to interact with each other, and the interaction energy is inversely proportional to the sixth power of distance ( $1/x^6$ ) between the two proximal atoms or groups [133]. From Figures 4.7(a) to (c) and Table 4.2, it can be seen that the dispersion term is much stronger for the  $\text{CF}_3\text{SO}_3^-/\text{PPy}$  polymer film than that for the  $\text{DecSO}_3^-/\text{PPy}$  and  $\text{SDSO}_4^-/\text{PPy}$  films. For the former pair, this interaction term is dominant, such that with lengthening chain of the alcohol, the  $\text{CF}_3\text{SO}_3^-/\text{PPy}$  sensor pair showed a rapid increase in dispersion interaction, resulting in a higher resistance of the polymer film. In contrast, for the  $\text{DecSO}_3^-/\text{PPy}$  and  $\text{SDSO}_4^-/\text{PPy}$  pairs, with an increase of alcohol's length, the dispersion term tended to imply a decrease in the resistance of the polymer film. The trend of this interaction was shown by the measurements for n-hexane, a vapour sample which only possesses dispersion interaction abilities, as listed in Table 4.1. The results of  $S_r$  against time of measurement is shown in Figure 4.8(b). For  $\text{CF}_3\text{SO}_3^-/\text{PPy}$  sensor pair, a positive change in resistance was detected, and for  $\text{DecSO}_3^-/\text{PPy}$  and  $\text{SDSO}_4^-/\text{PPy}$  pairs, a negative change in resistance was observed. By analysing the structure of the polymer films, reasonable explanations for the above results can be obtained.

As shown by Warren and Wernet [92, 93] in a study of the polymer morphology using X-ray diffraction, the structure of the polypyrrole containing counterions of alkyl sulphonates and alkyl sulphates consist of stacked polypyrrole chains separated by counterion aggregates. The spacing for these counterions obeys a linear relationship. The contour length of a single alkyl chain increases by 0.125 nm when each  $\text{CH}_2$  unit is added [93]. Hence,  $\text{SDSO}_4^-$  has larger layer distances than  $\text{DecSO}_3^-$ , and  $\text{CF}_3\text{SO}_3^-$  has the smallest layer distance. As stated in Section 4.1, a large counterion increased the separation of the polypyrrole chains, thereby presenting a greater obstacle to interchain charge transport [102]. The regression results suggest that the absorption of one large alcohol molecule into the counterion region may help to bridge the interchain charge transport for the  $\text{DecSO}_3^-/\text{PPy}$  and  $\text{SDSO}_4^-/\text{PPy}$  polymer films (thus, decreasing the resistivity of the film), as well as plasticize the film. For the  $\text{CF}_3\text{SO}_3^-/\text{PPy}$  polymer film, the spacing between polypyrrole chain layers is small, which introduces a large dispersion interaction effect on the resistance when vapour molecules are absorbed. As the size of

the absorbed molecule increases, this interaction will increase rapidly. The results suggested that for the  $\text{CF}_3\text{SO}_3^-/\text{PPy}$  polymer film, this interaction created an appreciable “obstacle” to charge transport, shown by a reduced conductivity of the polymer. Hence, the polymer will be expected to show higher sensitivities to larger odourant molecules than the other two pairs, which is confirmed by the trends of the dependence of  $S_{\text{rf}}\text{MW}$  on molecular weight, shown in Figures 4.5(a) to (c).

#### 4.5.4 Effect of Backbone Monomers on Vapour-Polymer Interactions

Polypyrrole film and co-polymer films composed of pyrrole and N-phenyl pyrrole were polymerised with the same counterion,  $\text{PF}_6^-$ , as described in Chapter 2. The monomer solution was prepared as a 0.1 M solution of N-phenyl pyrrole in acetonitrile, and then 20  $\mu\text{l}$  of pyrrole monomer (about 0.01 M) was added to make a monomer mixture. The baseline resistance values for the interdigitated electrodes were 2.18  $\text{k}\Omega$  for  $\text{PF}_6^-/\text{PPy}$  and 1.13  $\text{k}\Omega$  for  $\text{PF}_6^-/\text{P}(\phi\text{Py}+\text{Py})$ . The frequency changes of the corresponding QCMs due to the polymer coatings were 8.6 kHz for  $\text{PF}_6^-/\text{PPy}$  and 12.0 kHz for  $\text{PF}_6^-/\text{P}(\phi\text{Py}+\text{Py})$ . Our other studies on co-polymer compositions using XPS have shown that the composition of N-phenyl pyrrole and pyrrole in the film will be about 50% each [134]. Since the substitution of the hydrogen atom by a phenyl group on nitrogen of the pyrrole ring would decrease the hydrogen bonding acidity, then, the effects of polymer backbone hydrogen bonding acidity could be compared when the sensor pairs were exposed to the same set of vapour samples as in the last Section 4.5.3. Figures 4.9(a) to (b) show both the experimental data and the regression results for the  $\text{PF}_6^-/\text{PPy}$  and  $\text{PF}_6^-/\text{P}(\phi\text{Py}+\text{Py})$  sensor pairs using the average values of two parallel measurements.

For the  $\text{PF}_6^-/\text{PPy}$  sensor pair, the regression analysis gives

$$S_{\text{rf}}\text{MW} = 246.88 R_2 - 307.95 \pi_2^{\text{H}} - 185.81 \alpha_2^{\text{H}} + 684.26 \beta_2^{\text{H}} + 12.36 \log L^{16}$$

with a multi-linear regression correlation coefficient  $r_m = 0.81$ . For the  $\text{PF}_6^-/\text{P}(\phi\text{Py}+\text{Py})$  sensor pair, the regression analysis gives

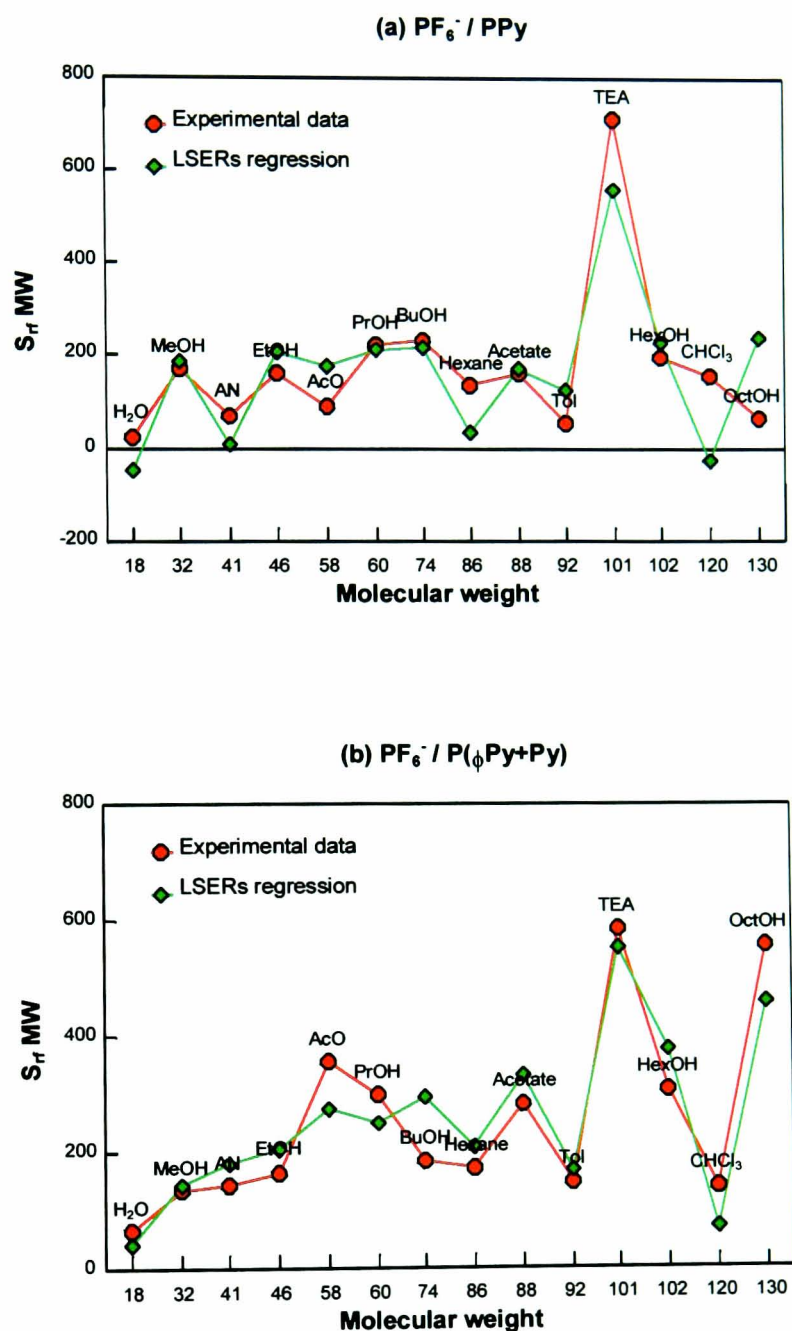


Figure 4.9 Experimental and LSERs (linear solvation energy relationships) regression results for polypyrrole and copolymer films. For  $PF_6^-/PPy$  sensor pair, the baseline resistance of the interdigitated electrode was 2.18 k $\Omega$ , and the frequency change of the corresponding QCM due to the polymer coating was 8.6 kHz; for  $PF_6^-/P(\phi Py+Py)$  sensor pair, the baseline resistance of the interdigitated electrode was 1.13 k $\Omega$ , and the frequency change of the corresponding QCM due to the polymer coating was 12.0 kHz.

$$S_{\text{rfMW}} = -220.69 R_2 - 38.22 \pi_2^{\text{H}} - 139.28 \alpha_2^{\text{H}} + 431.14 \beta_2^{\text{H}} + 78.35 \log L^{16}$$

with  $r_m = 0.92$ .

Figure 4.10 shows the regression  $S_{\text{rfMW}}$  values against experimental results for the two sensor pairs, with a 45° line of “perfect correlation” also shown. It can be seen that the theoretical and experimental data were more consistent for the  $\text{PF}_6^-/\text{P}(\phi\text{Py}+\text{Py})$  co-polymer film, than for the  $\text{PF}_6^-/\text{PPy}$  single monomer component film.

From the regression results, the polarizability term ( $rR_2$ ) is positive for the  $\text{PF}_6^-/\text{PPy}$  film and negative for the  $\text{PF}_6^-/\text{P}(\phi\text{Py}+\text{Py})$  film, possibly due to the effect of the toluene group on  $\phi\text{Py}$ . This hypothesis was confirmed by the regression results for the  $\text{Tos}^-/\text{PPy}$  film, where the polarizability term was also negative ( $-35.9R_2$ ). Secondly, the polarity terms  $s\pi_2^{\text{H}}$  are all negative for the two films, whilst they were positive for the  $\text{DecSO}_3^-/\text{PPy}$ ,  $\text{SDSO}_4^-/\text{PPy}$  and  $\text{CF}_3\text{SO}_3^-/\text{PPy}$  films. This may be related to the “round” structure of the  $\text{PF}_6^-$  counterion, which can not therefore be readily polarised. In addition, the doping level is lower than  $\text{DecSO}_3^-/\text{PPy}$ ,  $\text{SDSO}_4^-/\text{PPy}$  and  $\text{CF}_3\text{SO}_3^-/\text{PPy}$  films. Finally, the phenol group will reduce the acidity and the basicity of the PPy film because nitrogen has been substituted. Figure 4.11 shows the normalised contribution of the interaction term  $b\beta_2^{\text{H}}$  by the sum of the five contribution intensities for the two sensor pairs. The calculations were based on dividing the intensity of  $b\beta_2^{\text{H}}$  (represented by the absolute value of term) by the sum of all five terms (all using absolute values). It can be seen that, for most of the vapour samples, the co-polymer film tended to give a lower contribution than polypyrrole film did. The difference between the two may suggest the influence of the backbone polymer composition. As a result, the  $\text{PF}_6^-/\text{P}(\phi\text{Py}+\text{Py})$  co-polymer film would be expected to have relatively lower sensitivity to vapours with strong basicity, i.e. trimethylamine, than the  $\text{PF}_6^-/\text{PPy}$  single monomer film. This was verified by the experimental results shown in Figures 4.9(a) and (b). Finally, because the size of  $\text{PF}_6^-$  is small, the dispersion terms were similar with those of small counterions such as  $\text{CF}_3\text{SO}_3^-$ . They were all positive.

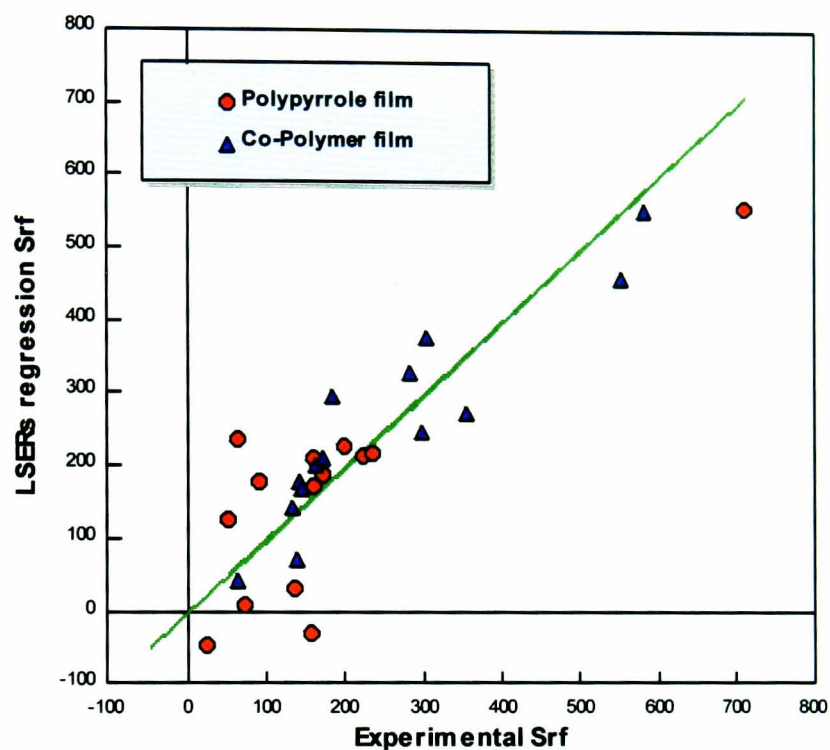


Figure 4.10 LSERSs (linear solvation energy relationships) regression results versus experimental  $S_{rf}MW$  values for  $PF_6^-/PPy$  film sensor pair ( $f_c = 8.6$  kHz,  $R_0 = 2.18$  k $\Omega$ ) and copolymer  $PF_6^-/P(\phi Py+Py)$  film sensor pair ( $f_c = 12.0$  kHz,  $R_0 = 1.13$  k $\Omega$ ).

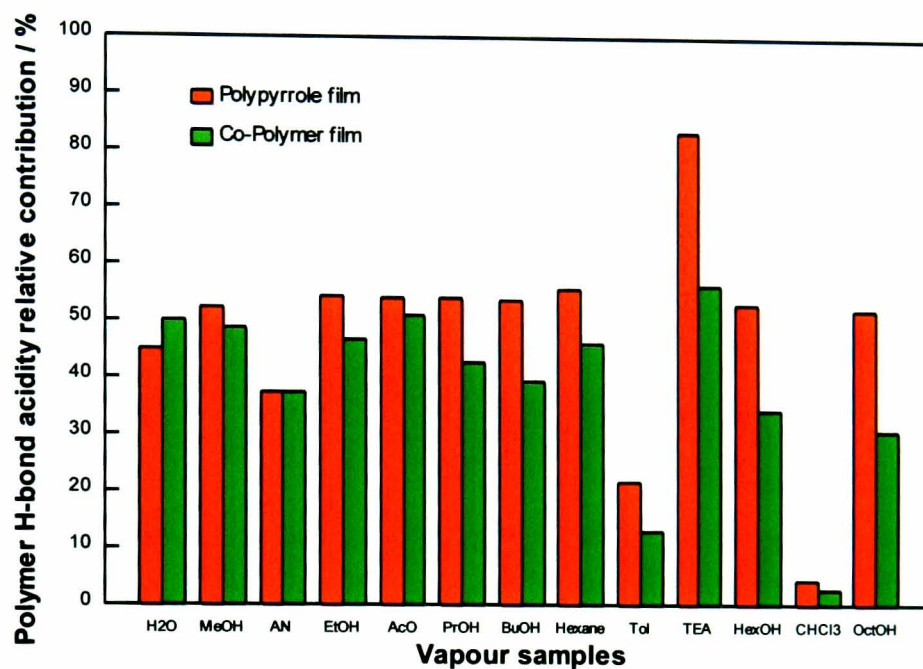


Figure 4.11 Polymer hydrogen-bonding acidity contribution to the overall response for  $S_{rf}MW$  against a set of vapour molecules for polypyrrole ( $PF_6^-/PPy$ ,  $f_c = 8.6$  kHz and  $R_0 = 2.18$  k $\Omega$ ) and copolymer ( $PF_6^-/P(\phi Py+Py)$ ,  $f_c = 12.0$  kHz and  $R_0 = 1.13$  k $\Omega$ ) films.

## 4.6 CONCLUSIONS

In this study,  $S_{rf}MW$  has been introduced as a solubility property to study the interactions between organic vapours and conducting polymers.  $S_{rf}MW$  is proportional to  $S$ , which is the relative resistivity change caused by a single molecule adsorbed into the polymer film. LSERs (linear solvation energy relationships) have been employed for the regression analysis of experimental results based on the five basic representative molecular interaction parameters to analyse particular interactions contributing to the overall sorption process. This empirical approach has shown that the predictions are consistent with the experimental results. Thus, the usefulness in predicting sensitivity and choosing conducting polymers for target odorants has been demonstrated.

The importance and usefulness of this method in analysing vapour-polymer interactions has also been demonstrated with the following major points of interest:

The selectivity of conducting polymer to organic vapours has been determined by use of all of the parameters involved in the sorption process, namely the vapour tested, the counterions incorporated during synthesis and the polymer backbone composition. All the polymer films studied have shown detectable changes to changes in vapour properties.

Among the five possible interaction terms considered in this study, in general, hydrogen bonding and dispersion interactions played the most important roles.  $DecSO_3^-$ /PPy and  $SDSO_4^-$ /PPy were very sensitive to vapours with a high basicity.  $CF_3SO_3^-$ /PPy was not highly sensitive to either the acidity or basicity of solutes. The changes of polymer backbone composition by using substituted pyrrole (N-phenyl pyrrole) have shown an altered hydrogen bonding interaction and a reduced sensitivity to the basicity of vapours.

The size of the counterions significantly influenced the gas-polymer interactions, as reflected by the dispersion term and the corresponding strength related with the structure of polymer film.  $CF_3SO_3^-$  has got a higher sensitivity to larger molecules than  $DecSO_3^-$  and  $SDSO_4^-$ . Larger counterions introduced negative interactions for the

dispersion term, with an increased conductivity, whilst smaller ones introduced positive interactions with a reduced conductivity.

Finally, polymers with fluorine containing and toluene groups, e.g.  $\text{CF}_3\text{SO}_3^-/\text{PPy}$ ,  $\text{Tos}^-/\text{PPy}$  and  $\text{PF}_6^-/\phi\text{Py}$  usually introduce a negative polarizability term, intending to increase the conductivity of the polymer film.

## **Multi-Component Analysis Using QCM-Interdigitated Electrode Hybrid Sensor Pairs**

### **5.0 INTRODUCTION**

Multi-component analysis of organic vapour mixtures is one of the most important tasks for an electronic nose to perform [32, 112, 135-137]. To date, single-property measurement systems have become the most commonly used methods, involving an array of non-specific sensors such as QCM [112, 135], field effect transistor (FET) [32] or ion-selective electrode (ISE) [136]. Detection and quantitation of analytes in multi-component samples using partially selective sensors requires the use of multivariate calibration methods such as multiple linear regression (MLR) [135, 138], partial least squares (PLS) [135, 136, 139], ordinary least squares (OLS), principle component analysis (PCA) or an artificial neural net method [140]. In such studies [135-140] the responses of the sensor array, when exposed to each analyte in the interfering presence of the second or third analyte, were interpreted by the multivariate calibration methods, which allowed the analysis of a mixture of analytes to be achieved as long as each corresponding analyte was known and calibrated (i.e. the sensor array was trained). To construct a single property sensor array, eight or nine QCMs with different polymer coatings [112, 135], or four to eight FETs with different catalytic and non-catalytic thin layers [32] were employed. Usually, for a mixture of two components, the response from each of the sensors constructs a three-dimensional calibration “surface”, determined by the sensitivity of the sensor to each of the analytes and varying with their concentrations [32]. For a sensor array comprising four to nine different sensors, the multivariate calibration is therefore very complicated. It is thus important to work out a convenient

method for the analysis of multi-component analytes, including methods employing fewer sensors and easier data calibrations.

Our previous work in Chapter 3 has demonstrated an improved selectivity, response stability and the appropriateness of a QCM-interdigitated electrode hybrid system for the discrimination of single component odours on an odour map. Importantly, the hybrid system showed vapour concentration independence over a wide concentration range. Each odourant has a relatively fixed location on the proposed two-dimensional odour map, corresponding to the characteristic of the vapour for a given polymer.

In this chapter, a novel method of multi-component analysis for organic vapour mixtures is introduced as an extended application of the proposed hybrid system and odour mapping technique. Combined QCM-interdigitated electrode sensor pairs will be fabricated to discriminate multi-component vapour analytes in two and three-component cases, allowing mixture vapour concentration independence to be studied. Mixtures of pure alcohols (methanol, ethanol and i-propanol) and their individual mixtures with water will be tested at different mixing ratios. This approach could significantly simplify multi-component analysis by reducing the number of sensors and hence the complexity of calibration when compared to a single property measurement system. Using only one polymer coating, the mixing ratio of any two components could be distinguished as long as each of them was known and calibrated. As to the three component mixture case, the composition could be addressed by introducing a second pair of sensors with a different coating, in order to construct a two-dimensional odour map. An appropriate data calibration is also needed. As the result, the enormous potential usefulness of a hybrid system to perform multi-component mixture analysis will be demonstrated.

## **5.1 QCM-INTERDIGITATED ELECTRODE HYBRID SYSTEM IN MULTI-COMPONENT ANALYSIS**

As stated in Chapter 3, for a QCM-interdigitated electrode sensor pair coated with the same polymer material, from Equation 3-14, the combined response  $S_{rf}$  can be:

$$S_{rf} = \left( \frac{\Delta R}{R_o} \right) / \left( \frac{\Delta f}{f_c} \right) = \frac{S}{(MW) u} k'' \rho \quad (5-1)$$

where the parameter  $S_{rf}$  represents the response of the combined sensor pair. It has been shown that within the range of vapour concentrations tested,  $S_{rf}$  is independent of the vapour concentration for a series of vapours [76, 77] and can be used to identify that vapour. Hence  $S_{rf}$  represents the sensor pairs selectivity to a particular vapour for a given polymer.

For a system consisting of mixtures, the composition can be more completely described in terms of the components that are present in it, different concentrations of which may be independently varied in the various phases [127]. The concept of the ideal gas has played an important role in discussion of the thermodynamics of such gases and vapours. Ideality in a gas implies a complete absence of cohesive forces, with an internal pressure of zero [127]. Many cases of practical interest are treated adequately by means of the ideal gas approximations, and even systems deviating from ideality are conveniently referred to the behaviour set by the ideal case in order to find some similar concept to act as a guide [127].

For a mixture of two components, we first assumed that the vapours behave as ideal gases, i.e. that there are no cohesive forces between analytes, for the levels of concentration used in the measurement. Under these circumstances, each of the analytes interacts with the polymer independently. Thus, the response for each component on both the QCM and the microchemo-resistor can be accumulative, i.e.:

$$\frac{\Delta f}{f_c} = \frac{\Delta f_1}{f_c} + \frac{\Delta f_2}{f_c} \quad \text{and} \quad \frac{\Delta R}{R_o} = \frac{\Delta R_1}{R_o} + \frac{\Delta R_2}{R_o} \quad (5-2)$$

where  $\Delta f$  and  $\Delta R$  are the overall changes in frequency and resistance,  $\Delta f_1$  and  $\Delta f_2$  are the frequency changes due to absorption of the first and second vapour components,  $\Delta R_1$  and  $\Delta R_2$  are the corresponding resistance changes,  $f_c$  is the frequency change by the coating deposition on QCM, and  $R_o$  is the baseline resistance of the interdigitated electrode.

For a given sensor pair, based on the concentration independence shown in Chapter 3, each vapour showed a particular  $S_{rf}$  value from that sensor pair. If the  $S_{rf}$  values for the first and second component pure vapours are defined as A and B, then:

$$A = \frac{\Delta R_1}{R_o} \bigg/ \frac{\Delta f_1}{f_c} \quad \text{and} \quad B = \frac{\Delta R_2}{R_o} \bigg/ \frac{\Delta f_2}{f_c} \quad (5-3)$$

Thus,  $S_{rf}$  for the mixture of two components can be written as:

$$S_{rf} = \frac{\Delta R}{R_o} \bigg/ \frac{\Delta f}{f_c} = \left( A \frac{\Delta f_1}{f_c} + B \frac{\Delta f_2}{f_c} \right) \bigg/ \left( \frac{\Delta f_1}{f_c} + \frac{\Delta f_2}{f_c} \right) \quad (5-4)$$

As indicated in Chapter 3, the general relationship between the relative frequency change due to the absorption of vapour and the vapour ambient concentration (in ppm) can be expressed using a Langmuir or Freundlich empirical isotherm. It has been shown in Section 3.3.1 that the Freundlich model provides a good fit for the polymer films used in our experiment. Hence we can use the Freundlich model to express the isotherm as:

$$\frac{\Delta f_1}{f_c} = k_1 C_1^{n_1} \quad \text{and} \quad \frac{\Delta f_2}{f_c} = k_2 C_2^{n_2} \quad (5-5)$$

where  $C_1$  and  $C_2$  are the ambient vapour concentrations in ppm for the two components, and  $k_1$ ,  $k_2$ ,  $n_1$  and  $n_2$  are all empirical constants for the QCM coating relative to the two components.

Therefore, in general, the combined output of a given sensor pair for a mixture of two components can be written as:

$$S_{rf} = \frac{Ak_1C_1^{n_1} + Bk_2C_2^{n_2}}{k_1C_1^{n_1} + k_2C_2^{n_2}} \quad (5-6)$$

To further simplify the system under investigation, it is now also assumed that the QCM sensor is linearly dependent on the vapour concentration within the tested

concentration range, i.e.  $n_1 = 1$  and  $n_2 = 1$ . We can also define a parameter  $\alpha = k_1/k_2$ , which is related to the ratio of partition coefficients  $K_1/K_2$  (the partition coefficient  $K$  is commonly used in the study of polymer absorption properties [41] which is linked with  $k$  via the density of polymer film and vapour molecular weight, determined by the vapour concentration unit used (by ppm or by mass), see later). Also, if the total vapour concentration is defined as  $C = C_1 + C_2$ , then:

$$S_{rf} = \frac{Ak_1C_1 + Bk_2C_2}{k_1C_1 + k_2C_2} = \frac{(A\alpha - B)\frac{C_1}{C} + B}{(\alpha - 1)\frac{C_1}{C} + 1} \quad (5-7)$$

To demonstrate the trends shown by Equation 5-7, a group of curves illustrating the relationships between the normalised  $S_{rf}$  and the mixing ratio of one component concentration over the total concentration (ppm/ppm) for varying  $\alpha$  values are simulated in Figure 5.1. Here, the  $S_{rf}$  values of A and B were normalised and hence, point (0, 0) corresponds to pure vapour 1 and point (1, 1) to pure vapour 2, respectively. The trends of the effect of  $\alpha$  on  $S_{rf}$  for a two-component mixture for a given polymer can be clearly demonstrated from these curves. In general, when two vapours have different absorption properties for the given polymer,  $\alpha \neq 1$ , there is a non-linear relationship between the response ( $S_{rf}$ ) and the vapour mixing ratio in composition ( $C_1/C$ ). Only when  $\alpha = 1$ , is there a linear relationship. Thus, it is reasonable to expect a curved response ( $S_{rf}$ ) - composition ( $C_1/C$ ) relationship for a mixture consisted of two different types of vapour molecules.

The relationships between  $k$  and  $K$ , ( $k_1/k_2$ ) and ( $K_1/K_2$ ) are now discussed. It is well-known that the distribution of a species between a sorption phase and an ambient medium (liquid or gas) can be described by a partition coefficient  $K$ , so that [126]:

$$K = \frac{C_s}{C_a} = \frac{(m_s/V_s)}{C_a} \quad (5-8)$$

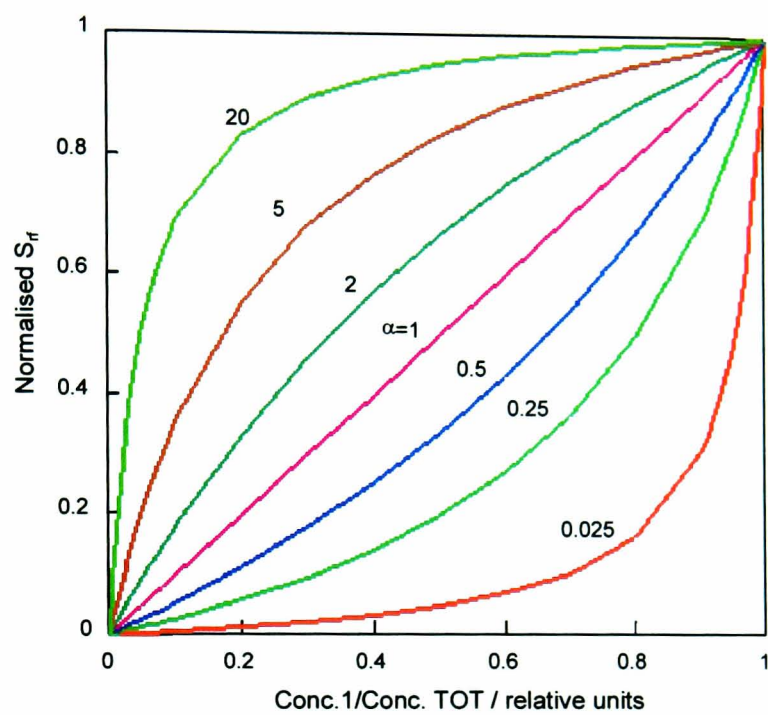


Figure 5.1 Illustration of normalised  $S_{rf}$  as a function of mixing ratio of two gaseous components, varying with different values of  $\alpha$  from 0.025 to 20.

where  $C_s$  is the concentration of analyte in the sorbate coating in equilibrium with  $C_a$  (the concentration in the ambient phase), and  $m_s$  is the mass of analyte sorbed into the coating of volume  $V_s$ . The value of the partition coefficient in this case will be expressed in a unit of mass of solute per unit volume [126]. From the following well-known equation [41, 141]

$$\frac{\Delta f}{f_c} = \frac{K}{\rho} C(w) \quad (5-9)$$

We can obtain

$$\frac{\Delta f_1}{f_c} = \frac{K_1}{\rho} C_1(w) \quad \text{and} \quad \frac{\Delta f_2}{f_c} = \frac{K_2}{\rho} C_2(w) \quad (5-10)$$

where  $K_1$  and  $K_2$  are the partition coefficients of the first and second vapours,  $C_1(w)$  and  $C_2(w)$  are the ambient concentrations of the two vapours in units of mass per unit volume,  $\rho$  is the density of the coating.

Comparing Equations 5-10 and 5-5, the relationship between  $K$  and  $k$  can be seen, which is related to the density of polymer film ( $\rho$ ) and vapour concentration unit used (in mass per unit volume or in ppm). Under the assumption that the QCM sensor is linearly dependent on the vapour concentration, if we use  $C(ppm)$  to represent vapour concentration with unit in ppm, then:

$$\frac{\Delta f_1}{\Delta f_2} = \frac{K_1 C_1(w)}{K_2 C_2(w)} = \frac{k_1 C_1(ppm)}{k_2 C_2(ppm)} \quad (5-11)$$

The relationship between  $C(ppm)$  and  $C(w)$  can be written as:

$$\frac{C_1(w)}{C_2(w)} = \frac{C_1(ppm) MW_1}{C_2(ppm) MW_2} \quad (5-12)$$

Thus, the relationship between  $\alpha$  and  $K_1/K_2$  can be expressed as:

$$\alpha = \frac{k_1}{k_2} = \frac{K_1}{K_2} \frac{MW_1}{MW_2} \quad (5-13)$$

Alternatively, Equation 5-13 can be rewritten as:

$$\frac{K_1}{K_2} = \alpha \frac{MW_2}{MW_1} \quad (5-14)$$

From Equation 5-10, it is known that the partition coefficient ratio of the two individual vapours can also be obtained experimentally using data for  $\Delta f_{1\text{pure}}$  and  $\Delta f_{2\text{pure}}$ , which are available from the resonant frequency changes caused by each pure vapour separately (here, the partition coefficient ratio is defined as  $(K_1/K_2)_{\text{pure}}$  meaning a ratio from two pure samples, when it is calculated in this way). If we use  $C(\%)$  to represent vapour concentration normalised by the saturated vapour pressure, when pure vapour samples are all saturated vapours or diluted to the same extent,  $C_1(\%) = C_2(\%)$ , we have:

$$\left( \frac{K_1}{K_2} \right)_{\text{pure}} = \frac{\Delta f_{1\text{pure}}}{\Delta f_{2\text{pure}}} \frac{C_2(w)}{C_1(w)} = \frac{\Delta f_{1\text{pure}}}{\Delta f_{2\text{pure}}} \frac{(MW)_2 (svp)_2}{(MW)_1 (svp)_1} \quad (5-15)$$

Clearly, Equations 5-14 and 5-15 can be used to compare the difference of absorption behaviour based on multi-component and single-component system, respectively. These can be used to examine the appropriateness of Equation 5-7 used to model the system as well as the validity of the ideality assumptions having been made to simplify the system under investigation.

We assumed that over a concentration range there is complete absence of cohesive forces in a gas and no analyte-analyte interactions between components. Each of the analytes interacts with polymer independently. Also, we assume that the QCM sensors are linearly dependent on the vapour concentration over certain concentration ranges. Then, if  $(K_1/K_2)_{\text{pure}}$  and  $K_1/K_2$  come to a similar value, Equation 5-7 can be considered as an appropriate description for a multi-component absorption process which follows the ideal case. If there are differences between  $(K_1/K_2)_{\text{pure}}$  and  $K_1/K_2$ , then Equation 5-7 will be

considered as a too simplistic solution for the absorption process for the given polymer and analytes. Such nonideal properties may be explained as the deviations from ideality, which are caused by the cohesive forces between unlike and like molecules [127]. Nevertheless, Equation 5-7 can still be used as a good calibration curve for data analysis in practice. This will be further discussed at the end of this chapter.

## **5.2 RESULTS AND DISCUSSION**

### **5.2.1 Sample Sets Chosen**

The sample sets which had been chosen for analysing the two-component gas systems were the mixtures of short chain alcohols, namely methanol with ethanol, and methanol, ethanol and iso-propanol in the presence of the most common environmental background gas, water vapour. The four sets of samples investigated were: methanol/ethanol, methanol/water, ethanol/water and propanol/water.

The sample set used in the three-component mixture analysis was composed of methanol, ethanol and water. Samples were prepared by mixing pure ethanol with water (1:1 in volume). Methanol was then added into the above solution at different ratios in volume to obtain a set of samples containing 10%, 25%, 50% and 70% methanol (v/v). Samples were selected to demonstrate the potential usefulness of the proposed method in monitoring some brewery distillation procedures.

### **5.2.2 Concentration Independence of Sensor Pair to Vapour Mixtures**

Mixtures of iso-propanol with water, varying in both mixing ratio (composition) and their concentration, were generated using the flow system described in Chapter 2. Each component of vapour was aspirated using pure nitrogen at different flow rates and mixed with the other. Table 5.1 gives the details of the composition of samples accordingly. The data listed in the first two columns were the flow meter's flow rate (in

cm<sup>3</sup> min<sup>-1</sup>) for bubbling the samples. The total flow rate was maintained at 205 cm<sup>3</sup> min<sup>-1</sup> ± 2% (using another stream of nitrogen for diluting). The mixing ratio of IPA to the mixture (listed in the third column in Table 5.1) was calculated by the method, described in Section 2.3.2, using both the calculated readings of the flow meters and the standard saturated vapour pressure data [123]. Here, the saturated vapour pressure was taken as 43.05 mm Hg for iso-propanol and 23.77 mm Hg for water vapour at 25°C, the molecular weights being 60 Daltons for iso-propanol and 18 Daltons for water. The last column listed the concentration ratio of each sample, representing the extent of dilution by pure nitrogen.

A (H <sub>2</sub> O) cm <sup>3</sup> min <sup>-1</sup>	B (IPA) cm <sup>3</sup> min <sup>-1</sup>	Mixing ratio B/(A+B) C <sub>1</sub> (ppm)/C(ppm)	Concentration ratio
25	0	0.00	0.13
90	0	0.00	0.45
140	0	0.00	0.70
0	30	1.00	0.15
0	80	1.00	0.40
0	140	1.00	0.70
30	30	0.64	0.30
60	60	0.64	0.60
100	100	0.64	1.00
60	30	0.48	0.45
90	30	0.40	0.60
125	30	0.33	0.78
140	30	0.31	0.85
180	30	0.28	1.00
90	60	0.56	0.75
125	95	0.59	1.00
30	60	0.78	0.45
30	90	0.83	0.60
60	90	0.72	0.75
30	115	0.86	0.73
85	115	0.70	1.00
30	180	0.90	1.00

Table 5.1 Mixtures of iso-propanol/water samples.

Each sample listed in Table 5.1 was measured and  $S_{rf}$  value was obtained. Figure 5.2 shows  $S_{rf}$  versus the concentration of iso-propanol to the total concentration of iso-propanol/water mixture (ppm/ppm) for a DecSO<sub>3</sub><sup>-</sup>/PPy sensor pair. It can be seen that for all the tested samples, the values of  $S_{rf}$  are all located close to the best fit calibration curve. The  $S_{rf}$  values standing for pure iso-propanol and pure water are at the ordinates of 0 and 1, respectively. The other  $S_{rf}$  values representing mixtures of iso-propanol/water are all located at the positions related to these two characteristic positions. Statistical regression gave the best fit value of  $\alpha$  to Equation 5-7 as 0.4. From Equation 5-14, the partition coefficient ( $K$ ) ratio between iso-propanol and water can be evaluated as 0.12, representing a lesser degree of absorption of iso-propanol into the polymer film relative to water. This also showed the strong influence of the common background water vapour for this sensor.

It can also be seen from Figure 5.2 that for the samples at the same mixing ratios (0, 0.64 and 1) but varying in concentrations (diluted from 13% to non-diluted vapour), the values of  $S_{rf}$  were all grouped. Hence,  $S_{rf}$  is independent of mixture sample's concentration over the tested range but only related with the mixing ratio of the two components. Hence  $S_{rf}$  can be used to identify a vapour mixture in the same way as was shown in Chapter 3 for the single component analysis cases. As long as the two compositions of the mixture are known and the individual  $S_{rf}$  value for each of the pure vapour is calibrated, the mixing ratio of the two vapours can be obtained from the calibration curve expressed by Equation 5-7. In this way, multi-component analysis of the composition of two individual vapours could be achieved. Meanwhile, using the value of  $\alpha$  obtained by regression, information about the partition coefficient ratio can be obtained via Equation 5-14.

### 5.2.3 Two-Component Vapour Mixtures

Two-component vapour mixtures of methanol/ethanol, methanol/water and ethanol/water were generated and measured. Table 5.2 gives the details of the composition of samples. The total flow rate was maintained at 200 cm<sup>3</sup> cm<sup>-1</sup> by additional pure nitrogen. Vapour concentrations were calibrated using the same method as

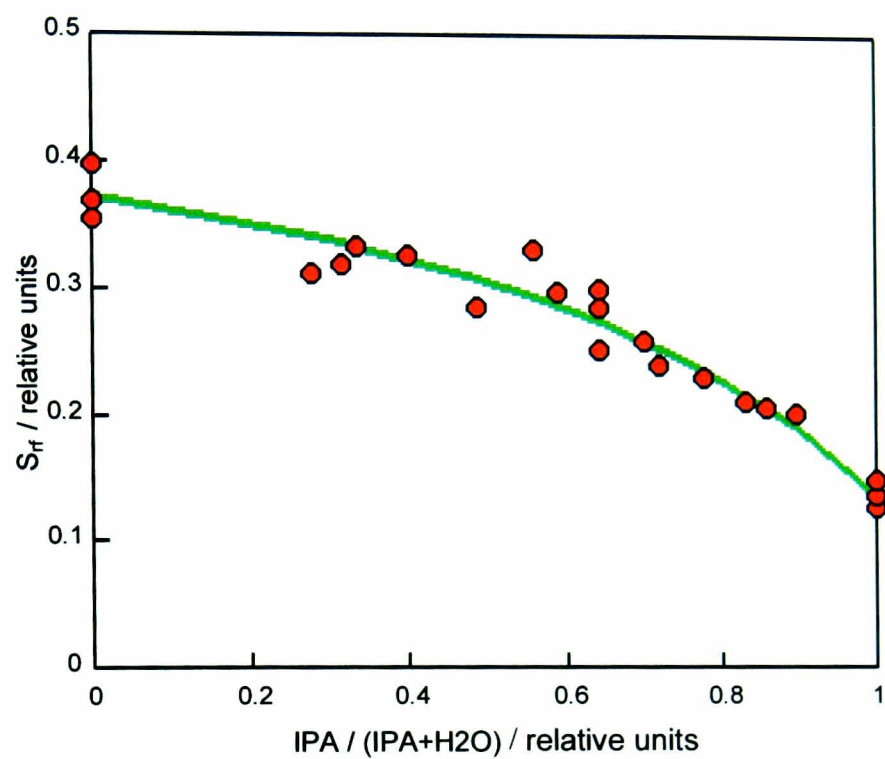


Figure 5.2 Plot of  $S_{rf}$  versus concentration ratio of IPA in IPA/H<sub>2</sub>O mixtures for a DecSO<sub>3</sub><sup>-</sup>/PPy sensor pair ( $\alpha = 0.40$ ), see text for details.

for iso-propanol/water mixtures and verified using FT-iR measurement (for methanol/ethanol), as shown in Chapter 2 [123, 125, 142, 143]. The saturated vapour pressure values for methanol, ethanol and water are 117.5, 57.5 and 23.77 mm Hg at 25°C, and the molecular weights are 32, 46 and 18 Daltons, respectively.

Mixture	Flow rate for bubblers ( $\text{cm}^3 \text{cm}^{-1}$ )			Mixing ratio of components $C_1/C_{\text{total}}$ (in ppm)
	MeOH	EtOH	H <sub>2</sub> O	
svp (mm Hg)	117.5	57.5	23.77	
MW	32	46	18	
<b>MeOH/EtOH</b> ( $C_{\text{MeOH}}/C_{\text{total}}$ )	100	0		1
	80	30		0.835
	50	50		0.672
	30	80		0.452
	0	100		0
<b>MeOH/H<sub>2</sub>O</b> ( $C_{\text{MeOH}}/C_{\text{total}}$ )	100		0	1
	70		30	0.916
	50		50	0.832
	30		70	0.692
	20		80	0.574
	0		100	0
<b>EtOH/H<sub>2</sub>O</b> ( $C_{\text{EtOH}}/C_{\text{total}}$ )		100	0	1
		80	20	0.899
		50	50	0.707
		30	70	0.523
		20	80	0.397
		0	100	0

Table 5.2 Two-component mixtures of methanol/ethanol, methanol/water and ethanol/water.

Figures 5.3 (a) to (c) show the  $S_{if}$  values for DecSO<sub>3</sub><sup>-</sup>/PPy, CF<sub>3</sub>SO<sub>3</sub><sup>-</sup>/PPy, and Tos<sup>-</sup>/PPy sensor pairs as a function of the mixing ratios of methanol in methanol/ethanol mixtures (ppm/ppm), the error bars showing average standard deviation values of between two to six measurements for each sample. The baseline resistance values for the DecSO<sub>3</sub><sup>-</sup>/PPy, CF<sub>3</sub>SO<sub>3</sub><sup>-</sup>/PPy, and Tos<sup>-</sup>/PPy interdigitated microresistors were 59 Ω, 53 Ω and 56 Ω, respectively. The frequency changes of corresponding QCMs due to the polymer coatings were 12.7 kHz, 8.6 kHz and 6.8 kHz, respectively. Calibration curves were obtained by best fitting the tested data to Equation 5-7 are also shown in the same figures. The best fit values of  $\alpha$  for these three pairs were 0.50, 0.95 and 0.80, respectively. The difference in the  $\alpha$  values is due to the difference in the vapour absorption properties for different polymers, varying with the counterions incorporated into the polymer film. Since in this experiment, methanol was chosen as the principle component and ethanol its diluent,  $\alpha$  actually reflects a coefficient ratio of methanol to ethanol according to Equation 5-13. Using Equation 5-14, the partition coefficient ( $K$ ) ratio of methanol to ethanol can be calculated as 0.72, 1.37 and 1.15 for the three different polymers, respectively. Thus, larger  $\alpha$  values (1.37 and 1.15 for CF<sub>3</sub>SO<sub>3</sub><sup>-</sup>/PPy and Tos<sup>-</sup>/PPy sensor pairs) represent a greater absorption of methanol into the polymer film relative to ethanol, whilst a smaller  $\alpha$  value (0.72 for DecSO<sub>3</sub><sup>-</sup>/PPy sensor pair) suggests lesser degree of absorption of methanol.

In a similar way, mixtures of methanol/water and ethanol/water were also measured using the same DecSO<sub>3</sub><sup>-</sup>/PPy, CF<sub>3</sub>SO<sub>3</sub><sup>-</sup>/PPy and Tos<sup>-</sup>/PPy sensor pairs. Figures 5.4 (a) to (c) and Figures 5.5 (a) to (c) present the corresponding results. The concentration ratio was calculated using the same method as stated. It is noted that for these mixtures, the DecSO<sub>3</sub><sup>-</sup>/PPy sensor pair showed different trends from those showed by the CF<sub>3</sub>SO<sub>3</sub><sup>-</sup>/PPy and Tos<sup>-</sup>/PPy sensor pairs, and the data did not fit to Equation 5-7 very well (no best fit  $\alpha$  values could be obtained for this sensor pair). For CF<sub>3</sub>SO<sub>3</sub><sup>-</sup>/PPy and Tos<sup>-</sup>/PPy sensor pairs, the best fit  $\alpha$  values for methanol/water mixtures were 0.05 and 0.35, for ethanol/water mixtures, they were 0.20 and 0.15, respectively. Using Equation 5-14, for CF<sub>3</sub>SO<sub>3</sub><sup>-</sup>/PPy and Tos<sup>-</sup>/PPy sensor pairs, the partition coefficient ratios of methanol to water were calculated as 0.03 and 0.20, the partition coefficient ratios of ethanol to water were calculated as 0.08 and 0.06, respectively.

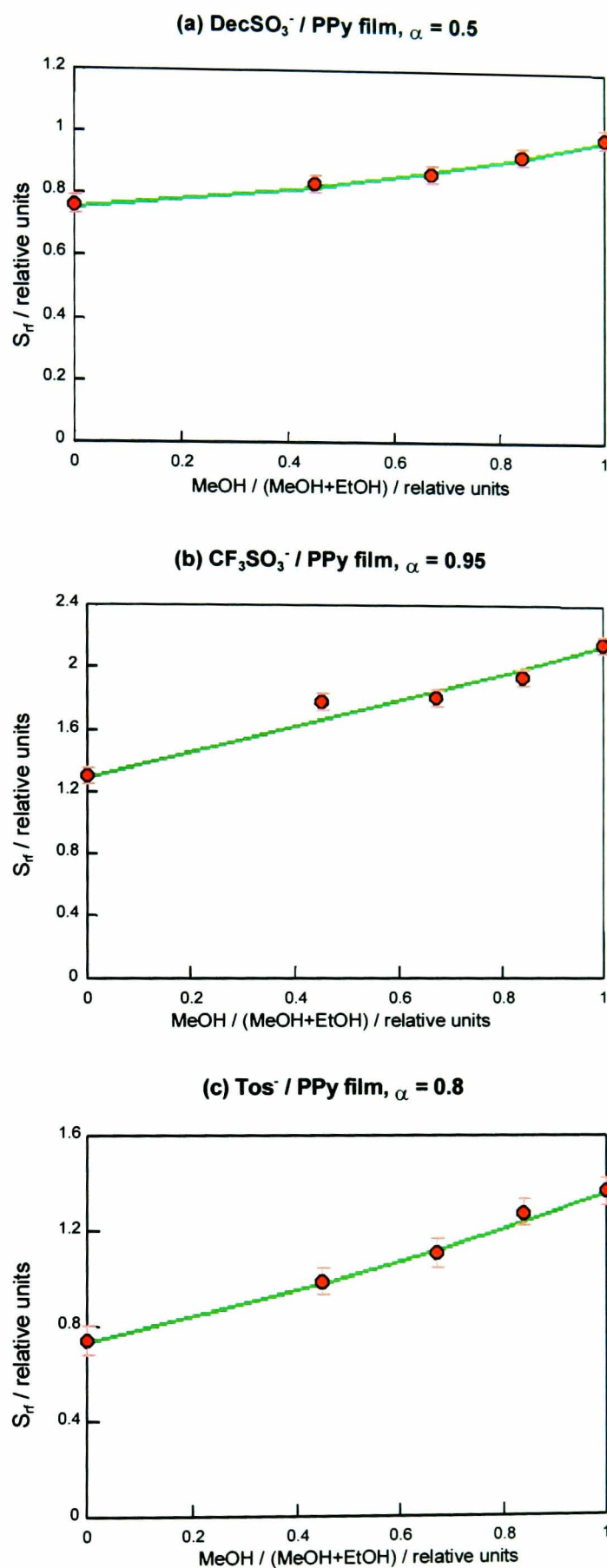


Figure 5.3 Plot of  $S_{rf}$  versus concentration ratio of methanol in methanol/ethanol mixtures for: (a) a DecSO<sub>3</sub><sup>-</sup>/PPy sensor pair ( $f_c = 12.7$  kHz,  $R_0 = 59 \Omega$ ); (b) a CF<sub>3</sub>SO<sub>3</sub><sup>-</sup>/PPy sensor pair ( $f_c = 8.6$  kHz,  $R_0 = 53 \Omega$ ); and (c) a Tos<sup>-</sup>/PPy sensor pair ( $f_c = 6.8$  kHz,  $R_0 = 56 \Omega$ ).

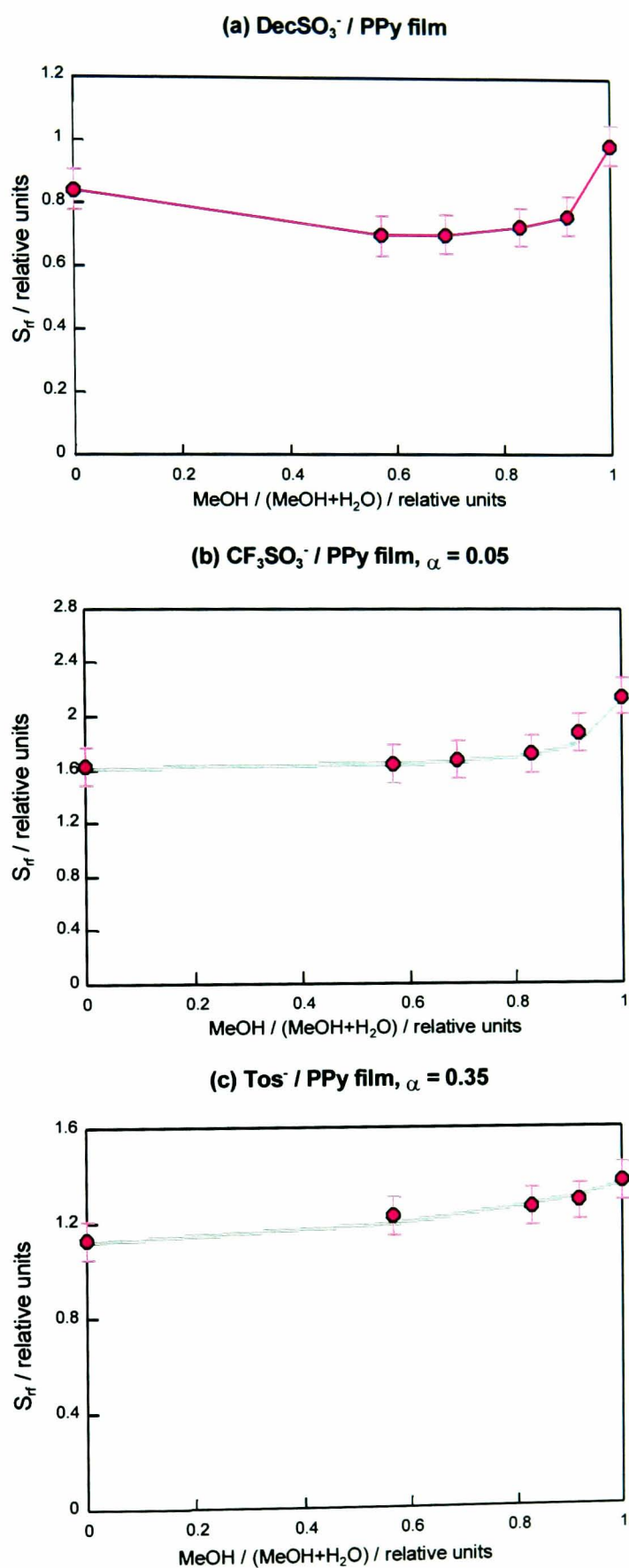


Figure 5.4 Plot of  $S_{rf}$  versus concentration ratio of methanol in methanol/water mixtures for: (a) a DecSO<sub>3</sub><sup>-</sup>/PPy sensor pair ( $f_c = 12.7$  kHz,  $R_0 = 59 \Omega$ ); (b) a CF<sub>3</sub>SO<sub>3</sub><sup>-</sup>/PPy sensor pair ( $f_c = 8.6$  kHz,  $R_0 = 53 \Omega$ ); and (c) a Tos<sup>-</sup>/PPy sensor pair ( $f_c = 6.8$  kHz,  $R_0 = 56 \Omega$ ).

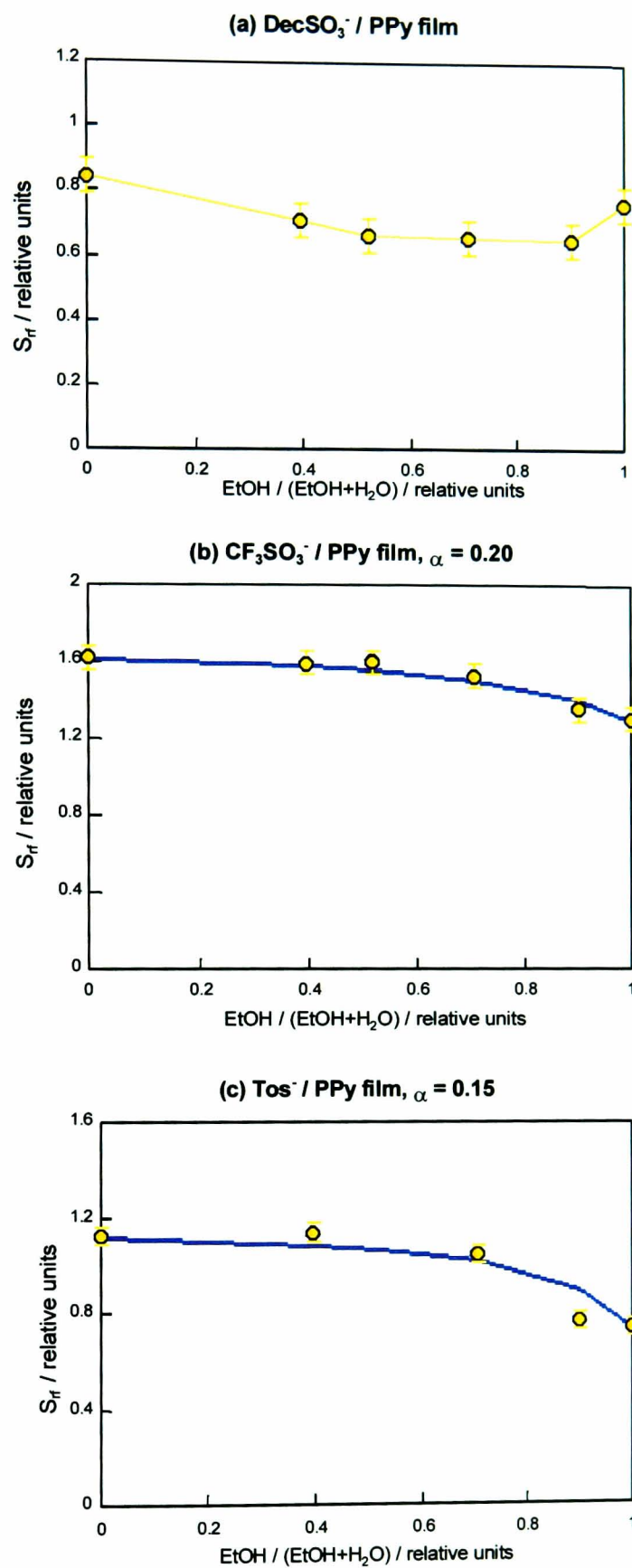


Figure 5.5 Plot of  $S_{rf}$  versus concentration ratio of ethanol in ethanol/water mixtures for: (a) a DecSO<sub>3</sub><sup>-</sup>/PPy sensor pair ( $f_c = 12.7$  kHz,  $R_0 = 59 \Omega$ ); (b) a CF<sub>3</sub>SO<sub>3</sub><sup>-</sup>/PPy sensor pair ( $f_c = 8.6$  kHz,  $R_0 = 53 \Omega$ ); and (c) a Tos<sup>-</sup>/PPy sensor pair ( $f_c = 6.8$  kHz,  $R_0 = 56 \Omega$ ).

Compared with the result for methanol/ethanol mixtures,  $\alpha$  values in these cases are relatively low, which suggests that less alcohol is absorbed into the polymer coatings compared with water vapour. It is also noted from these figures that the  $S_{rf}$  values remained at the levels similar to those for pure water until the alcohol concentration ratio reached 80%, suggesting a significant influence of the water content in the mixtures during the overall absorption.

In summary, Figures 5.3 to 5.5 show that the mixing ratios of two-component mixtures can be determined based on the values of  $S_{rf}$  from each sensor pair, as long as the two compositions are known and calibrated using Equation 5-7 ( $A$ ,  $B$  and  $\alpha$  can be determined). The linearity is greatly dependent on the absorption partition coefficients of the two vapours in the sensing polymer. For the  $CF_3SO_3^-/PPy$  and  $Tos^-/PPy$  sensor pairs, Equation 5-7 can be used to calibrate the experimental results for all the mixture cases. For the  $DecSO_3^-/PPy$  sensor pair, the results did not fit to this Equation for methanol/water and ethanol/water mixtures. Clearly some of the polymers behave “better” than others, depending on their counterions.

#### 5.2.4 Three-Component Vapour Mixtures

Three-component vapour mixtures were prepared by mixing ethanol and water at 1:1 in volume (v/v). Thereafter different amounts of methanol (in volume) were added to the solution to construct three-component mixture samples (10%, 25%, 50% and 70% by volume).

Figures 5.6 (a) to (c) show the  $S_{rf}$  values from the  $DecSO_3^-/PPy$ ,  $CF_3SO_3^-/PPy$  and  $Tos^-/PPy$  sensor pairs (same as before) versus the ratio of methanol (by volume) in methanol/ ethanol/water mixture solutions. Similar to the two-component cases, all the  $S_{rf}$  values for these different samples are located around a curve determined by the  $S_{rf}$  values of pure methanol and ethanol/water (1:1 v/v) vapour. The best fit curves were also shown.

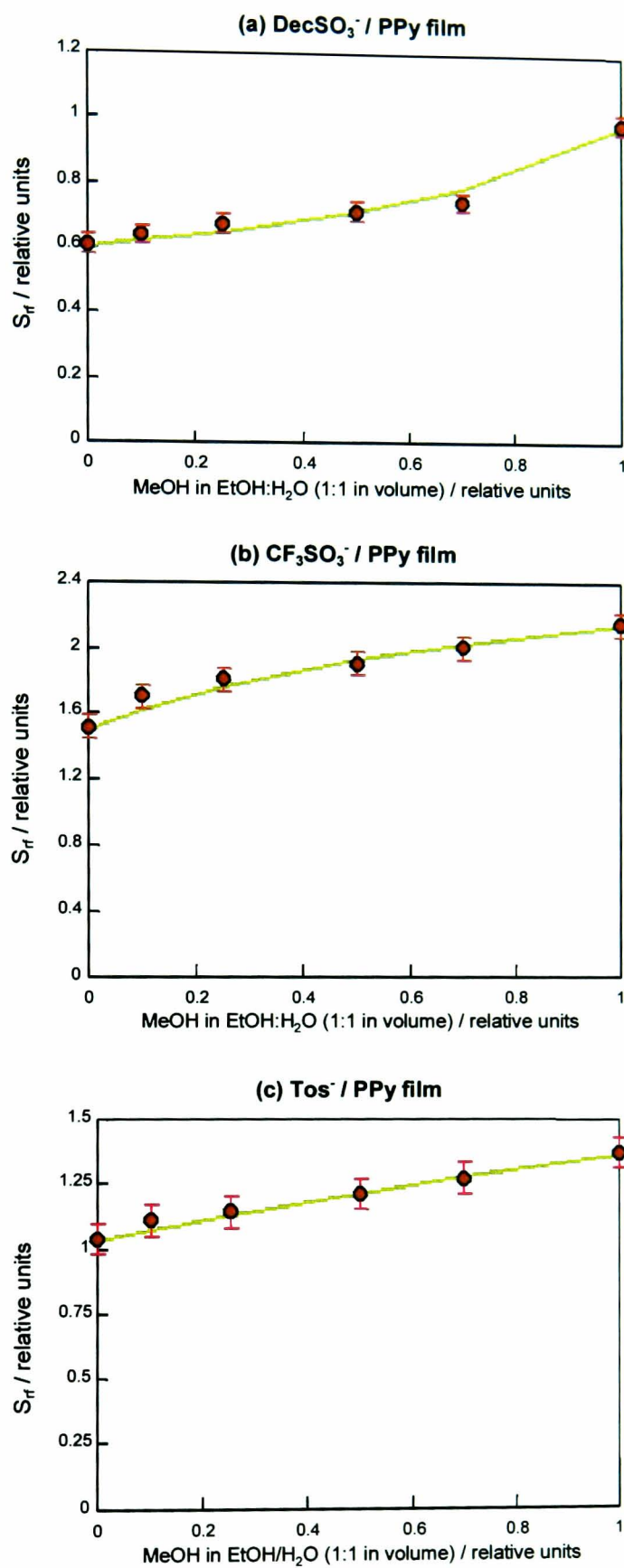


Figure 5.6 Plot of  $S_{rf}$  versus ratio of methanol (in volume) in ethanol/water (1:1 v/v) mixtures for: (a) a DecSO<sub>3</sub><sup>-</sup>/PPy sensor pair ( $f_c = 12.7$  kHz,  $R_0 = 59$   $\Omega$ ); (b) a CF<sub>3</sub>SO<sub>3</sub><sup>-</sup>/PPy sensor pair ( $f_c = 8.6$  kHz,  $R_0 = 53$   $\Omega$ ); and (c) a Tos<sup>-</sup>/PPy sensor pair ( $f_c = 6.8$  kHz,  $R_0 = 56$   $\Omega$ ).

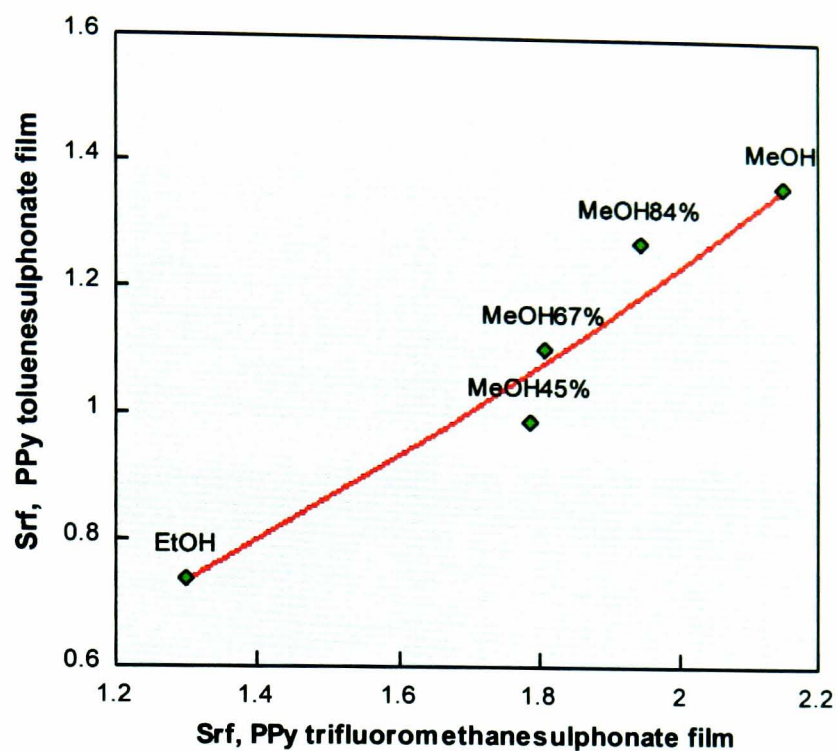
### 5.2.5 Odour Mapping in Multi-Component Vapour Analysis

To show the application of odour mapping technique, proposed in this study for multi-component analysis, a two-dimensional odour map was constructed using the  $S_{rf}$  values from the  $CF_3SO_3^-/PPy$  and  $Tos^-/PPy$  sensor pairs. The experimental data (see Section 5.2.3 and 5.2.4) and best fit curves for the two and three-component mixture cases are shown on the odour maps in Figures 5.7 (a) to (d) with the details of sample conditions. For example, the points labelled by 'MeOH', 'EtOH' and 'H<sub>2</sub>O' stand for pure methanol, ethanol and water, respectively. The data labelled by 'EtOH:H<sub>2</sub>O 1:1 (v/v)' stands for the mixture solution of ethanol and water. Points with percentage values such as 'MeOH45%' or 'EtOH71%' refer to the amounts of methanol or ethanol in the mixtures. Positions in (d) labelled by "percentage (v)" refer to the ratio in volume for the three-component mixtures. Figures 5.7 (a) to (d) clearly show the data locations on the odour map as a function of components type and their mixing ratios.

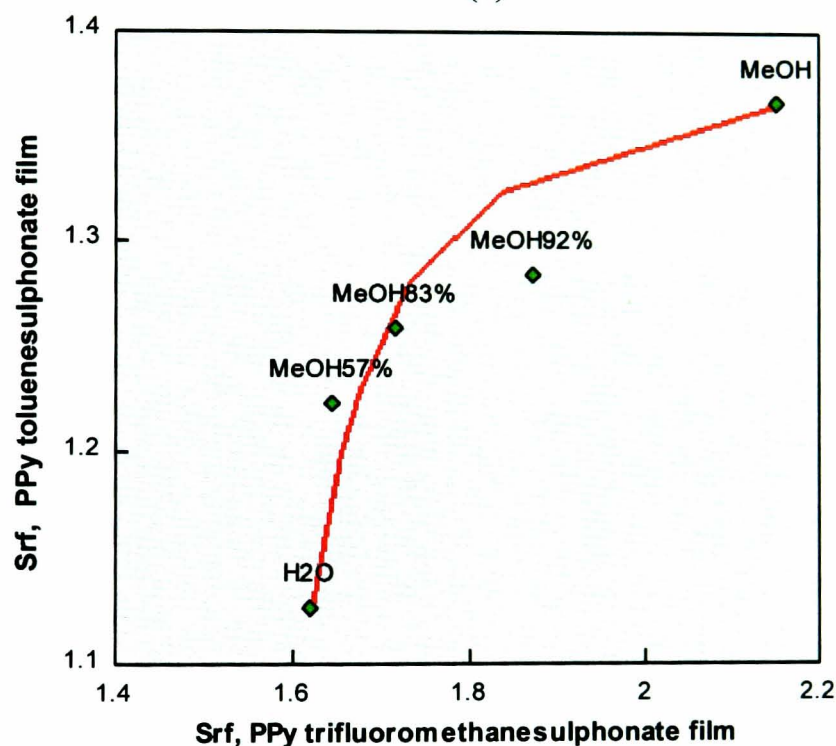
More comprehensively, Figure 5.8 is plotted, by combining the results shown in Figures 5.7 (a) to (d). It can be seen in Figure 5.8 that the measurement results for the mixtures from the two sensor pairs were located at places related to the results of each individual component methanol, ethanol and water. Here calibration curves are shown in Figure 5.8, representing several measured examples of two or three component mixtures.

Figure 5.8 has demonstrated the ability of this odour mapping method for the analysis of two and three-component mixtures in a simple way, by employing fewer sensor pairs and easier data calibration (using a two dimensional curve instead of a three dimensional surface). Importantly, this method can also be extensively used for the analysis of other mixtures, composed of analytes other than methanol, ethanol and water, as long as each component is known and calibration is made.

Finally based on Equations 5-14 and 5-15, the ratios  $K_1/K_2$  and  $(K_1/K_2)_{pure}$  can be compared to study the difference of absorption behaviour based on multi-component and single-component systems. These techniques will be used to evaluate the appropriateness of Equation 5-7 (which was used to model the system) as well as determine the validity of the ideality assumptions (which were used to simplify the study).

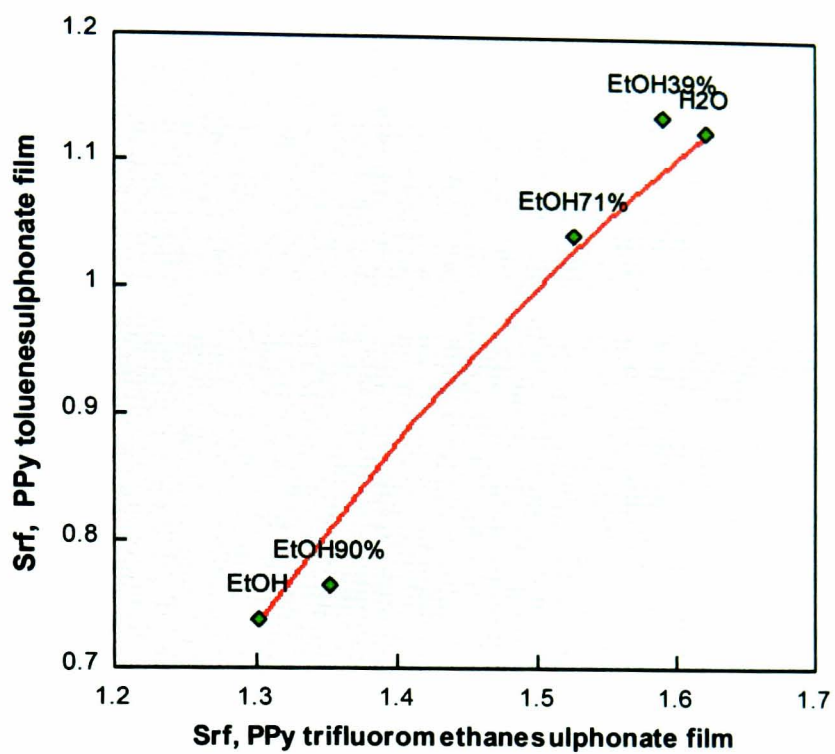


(a)

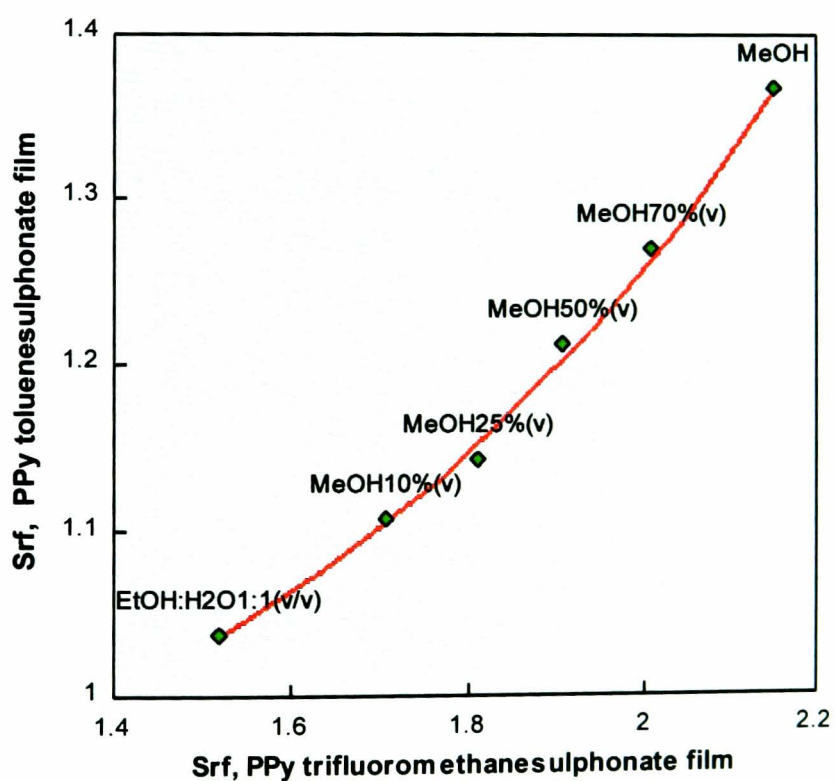


(b)

Figure 5.7 Plot showing a two-dimensional odour maps for a series of vapour mixtures based on  $S_{rf}$  values from a  $CF_3SO_3^-/PPy$  ( $f_c = 8.6$  kHz,  $R_0 = 53 \Omega$ ); and a  $Tos^-/PPy$  ( $f_c = 6.8$  kHz,  $R_0 = 56 \Omega$ ) sensor pair for: (a) methanol/ethanol mixtures; (b) methanol/water mixtures; (c) ethanol/water mixtures; and (d) methanol/ethanol/water mixtures. The data labelled by 'EtOH:H<sub>2</sub>O 1:1 (v/v)' stands for the mixture solution of ethanol and water, the position labelled by 'MeOH', 'EtOH' and 'H<sub>2</sub>O' stand for pure methanol, ethanol and water, respectively. Positions with percentage values refer to the ratio of methanol or ethanol in the mixtures in amount. Labels in (d) are all ratios in volume.



(c)



(d)

Figure 5.7 Continued.

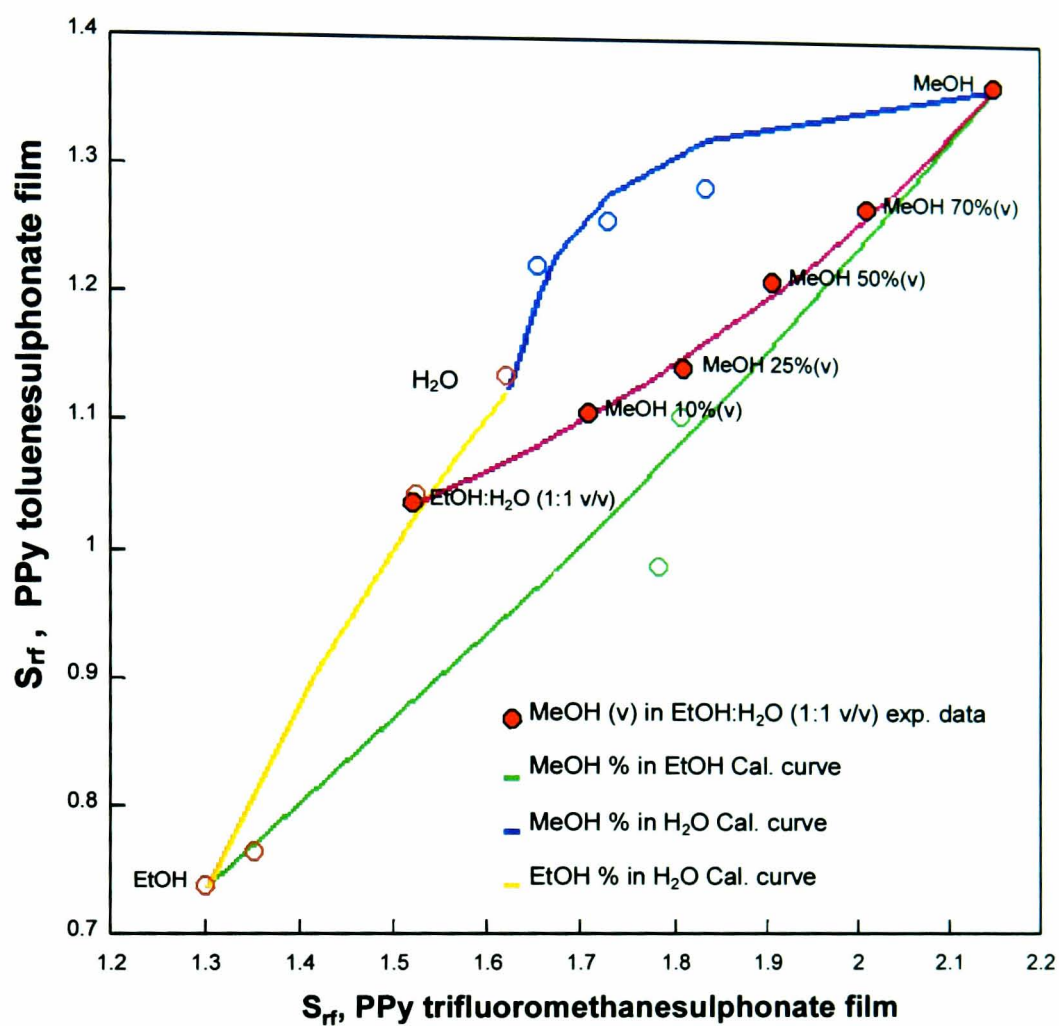


Figure 5.8 Plot showing a two-dimensional odour map for vapour mixtures of two and three components based on  $S_{rf}$  values from a  $CF_3SO_3^-/PPy$  sensor pair ( $f_c = 8.6$  kHz,  $R_0 = 53 \Omega$ ); and a  $Tos^-/PPy$  sensor pair ( $f_c = 6.8$  kHz,  $R_0 = 56 \Omega$ ).

The experimental data of  $\Delta f_{1\text{pure}}$  and  $\Delta f_{2\text{pure}}$  used to calculate the partition coefficient ratios  $(K_1/K_2)_{\text{pure}}$  are obtained from resonant frequency changes by the absorption of pure samples where the samples were all 50% diluted saturated vapours and are listed in Table 5.3. The saturated vapour pressure values at 25°C and molecular weights are also listed in this table.

Table 5.4 shows the calculated values of  $(K_1/K_2)_{\text{pure}}$  by Equation 5-15 and  $K_1/K_2$  values by Equation 5-14 using the regression  $\alpha$  value for each of these two-component mixtures, i.e. methanol/ethanol, methanol/water, ethanol/water and iso-propanol/water, for three polymers as studied in Section 5.2.3. The last two columns in Table 5.4 list the ratios of  $(K_1/K_2)_{\text{pure}}$  to  $K_1/K_2$  and the corresponding average values for each polymer.

It can be seen from data in Table 5-4 that, firstly, the values of  $(K_1/K_2)_{\text{pure}}$  and  $K_1/K_2$  for methanol/ethanol mixtures are much higher than those for mixtures with water as one component. This means that less alcohol molecules are absorbed when water vapour presented, compared with methanol/ethanol alcohol mixtures. It can also be seen that the values of  $(K_1/K_2)_{\text{pure}}$  are generally larger than  $K_1/K_2$ . The  $\text{CF}_3\text{SO}_3^-/\text{PPy}$  film showed a greater scatter with an average of 3.62. All the three films tested show deviations from ideality. One reason is the existence and effect of cohesive forces between different and the similar molecules when they were absorbed into the polymer film. The existence of cohesive forces can be confirmed by the fact that when ethanol is mixed with water, there is an evolution of heat on mixing, meaning the attractive forces between ethanol and water molecules in solution greater than those between the same molecules in the pure liquids [127]. As a result, it should be expected that the attraction of ethanol-water in the polymer may change the idealised response assumption of the system, such as the resistive sensors response properties. It can be seen that Equation 5-7 describes the methanol/ethanol alcohol mixture systems better than methanol/water and ethanol/water mixtures for all the three polymer coatings from the near 1  $(K_1/K_2)_{\text{pure}}$  to  $K_1/K_2$  ratio values (1.23, 0.73 and 1.12). This means that the two types of alcohol molecules are attracted less to each other and interacted with polymers more independently as assumed. Then, methanol/ethanol mixture system is more closer to ideality as described by Equation 5-7. For the methanol/water and ethanol/water cases, however, Equation 5-7 can still be used as a calibrating curve for experimental data.

although it is less appropriateness to model the mixture system because of the large deviation from ideality.

Film		H <sub>2</sub> O	MeOH	EtOH
svp (mm Hg)		23.77	117.5	57.5
MW		18	32	46
DecSO <sub>3</sub> <sup>-</sup> /PPy	Δf (Hz)	204.6	622.0	472.2
	STDS	15.86	47.06	53.84
	C <sub>v</sub> (%)	7.76	7.56	11.40
CF <sub>3</sub> SO <sub>3</sub> <sup>-</sup> /PPy	Δf (Hz)	232.8	464.9	299.3
	STDS	17.14	24.46	38.28
	C <sub>v</sub> (%)	7.36	5.48	12.79
Tos <sup>-</sup> /PPy	Δf (Hz)	256.9	485.6	253.6
	STDS	13.19	47.29	18.39
	C <sub>v</sub> (%)	5.14	9.74	7.26

Table 5.3 Resonant frequency changes by absorption of pure samples where the samples were all 50% diluted saturated vapours, for three polymer coatings.

Film	Mixtures	(K <sub>1</sub> /K <sub>2</sub> ) <sub>pure</sub>	K <sub>1</sub> /K <sub>2</sub>	(K <sub>1</sub> /K <sub>2</sub> ) <sub>pure</sub> / (K <sub>1</sub> /K <sub>2</sub> )	AVE
DecSO <sub>3</sub> <sup>-</sup> /PPy	MeOH/H <sub>2</sub> O	0.33	-	-	1.52
	EtOH/H <sub>2</sub> O	0.38	-	-	
	IPA/H <sub>2</sub> O	0.22	0.12	1.80	
	MeOH/EtOH	0.87	0.72	1.23	
CF <sub>3</sub> SO <sub>3</sub> <sup>-</sup> /PPy	MeOH/H <sub>2</sub> O	0.21	0.03	7.45	3.62
	EtOH/H <sub>2</sub> O	0.21	0.08	2.67	
	MeOH/EtOH	1.00	1.37	0.73	
Tos <sup>-</sup> /PPy	MeOH/H <sub>2</sub> O	0.21	0.20	1.05	1.64
	EtOH/H <sub>2</sub> O	0.16	0.06	2.73	
	MeOH/EtOH	1.29	1.15	1.12	

Table 5.4 Results of (K<sub>1</sub>/K<sub>2</sub>)<sub>pure</sub> calculated by Equation 5-14 and K<sub>1</sub>/K<sub>2</sub> value calculated by Equation 5-13 via regression result of α value for each of the two-component mixtures, for three polymer coatings.

From the above study, it can be seen that although there still exists a need to further improve the system modelling work, the basic concepts proposed in this study for mixture analysis, including the ideality assumptions we made to simplify this system are, in principle, workable for the alcohol mixtures and polymers such as Tos<sup>-</sup>/PPy. This work clearly shows that this simple method has made the analysis of multi-component vapour mixtures achievable using the proposed odour mapping technique by careful choice of counterions and data calibration. The main advantages are the employment of few polymer coatings, such as two, and convenient data calibration using a two-dimensional curve instead of a three-dimensional surface.

### 5.3 CONCLUSIONS

A simple and novel method of multi-component analysis for organic vapour mixtures has been introduced and demonstrated using hybrid sensor pairs and odour mapping technique. The relationship between the sensor pair's output and the mixing ratio of two-component mixtures has been studied theoretically and verified experimentally. Sensor pair's output with mixtures of two components was found to be closely related to the output of each component. A relationship largely determined by the partition coefficient ratio of each component into the polymer coating was found to exist. In general, the relationship departs from ideality especially when water was used as one of the solvent. Hence, calibration is always necessary. In this way, using only one polymer coating, mixtures of two components can be distinguished as long as each of them is known and calibrated. Mixtures of three components have also been investigated and the composition can be analysed on an odour map by introducing a second pair of sensors with a different polymer coating as well as appropriate calibration. The results have shown the feasibility of distinguishing the ratios of mixtures using a significantly simpler method, with a lower number of polymer coatings and easier data calibration, compared with the commonly used single property measurement systems. This approach has demonstrated the potential usefulness of a hybrid system to perform the analysis of multi-component vapour mixtures.

## **Conclusions and Future Work**

### **6.1 CONCLUSIONS**

This research has been concerned with the establishment and characterisation of a QCM-interdigitated electrode hybrid “second generation” *Electronic Nose* system. Research objectives covered a number of technical limitations and analytical difficulties that need to be solved in the “first generation” *Electronic Nose* system. To this end, work has been carried out, including the design and fabrication of the electronic nose system, optimisation of the sensors response, device modelling, vapour-polymer interaction mechanism studies, and the application of the nose in multi-component analysis. The conclusions from this study are summarised below.

A QCM–interdigitated electrode hybrid sensor odour measurement system has been established. Sensor fabrication techniques have been developed and the corresponding sensor characteristics have been discussed. During the sensor fabrication, the thickness of sensing film coatings was determined by varying the electrical charge passed during the polymerisation (by varying the length of time the step potential was applied). Electrical charge and polymer film thickness on gold electrode increased linearly with the increase of polymerisation time. Thinner films give a higher sensitivity but also faster baseline resistance drift with time. There is a balance between the two factors, which has to be resolved analytically. By testing the properties of 16 different coatings, “optimal” individual initial resistance ranges have been suggested, which enable lower baseline resistance drift with time, and with good sensitivity. A set of sensors can be made with initial resistance variation of less than 10  $\Omega$  for batch fabrication. Interdigitated electrodes with the same resistance value showed a similar sensitivity and

the same speed in response. Sensors detection limit depended on the type of coating and the thickness of the sensing film. Sample concentrations between 1.5 ppm and  $10^5$  ppm was found to be a reasonable dynamic range. Although the baseline resistance increased with time, the response of combined sensors ( $S_{rf}$ ) remained very stable during a test period of 45 days, which showed an improved stability using a hybrid system.

The sensor response models for QCM, interdigitated electrodes and hybrid system were then established. The vapour-polymer interactions and sensor pair's response were linked by a sensitivity coefficient  $S$ , which was obtained and evaluated by the measurement and analysis of the particular value of  $S_{rf}$  (reflecting the selectivity of this sensor pair for a particular vapour). A pair of sensor with concentration independence was formed on separate QCM and interdigitated electrodes, polymerised under the same conditions, such that the concentration relationships were the same. A thicker film was proposed for the QCM (over 10 kHz in frequency shift by coating material) and found to be within an optimum range on interdigitated electrode. The combined response ( $S_{rf}$ ) was determined by both the interaction between organic molecules and polymers ( $S$ ) and the characteristic of vapour under detection ( $MW$ ). The  $S_{rf}MW$  value was introduced as a new solubility property for vapour-polymer interaction study. Meanwhile, proposed "odour maps" have shown the feasibility of distinguishing odourants using a significantly lower number of different types of sensor coatings, incorporating counter-ions of significantly different physical and chemical properties. This has shown an improved selectivity of a hybrid system compared with the single property measurement system.

The nature of vapour-polymer interaction mechanisms was studied using the solubility property  $S_{rf}MW$  and linear solvation energy relationships, and thus a better understanding of the nature of the response was gained.  $S_{rf}MW$  was proportional to the relative resistivity change caused by a single molecule adsorbed into the polymer film. LSERs (linear solvation energy relationships) were employed for the regression of experimental results based on the five basic representative molecular interaction parameters in order to analyse particular interactions contributing to the overall sorption process. This empirical approach consistently predicted the experimental results. Thus, the usefulness in predicting sensitivity and choosing conducting polymers for target odorants was demonstrated.

The importance and usefulness of this method in analysing vapour-polymer interactions was also demonstrated with the following major points of interest:

The selectivity of conducting polymer to organic vapours was determined by the parameters involved in the sorption process, namely the vapour tested, the counterions incorporated during synthesis and the polymer backbone composition.

Among the five possible interaction terms considered in this study, in general, hydrogen bonding and dispersion interactions played more important roles. DecSO<sub>3</sub><sup>-</sup>/PPy and SDSO<sub>4</sub><sup>-</sup>/PPy were sensitive to vapours with a large basicity. CF<sub>3</sub>SO<sub>3</sub><sup>-</sup>/PPy was not highly sensitive to either acid or basic solutes, but to dispersion interactions. Changes of polymer backbone composition using substituted pyrrole (N-phenyl pyrrole) have shown an altered hydrogen bonding interaction and a reduced sensitivity to the basicity of testing vapours.

Also, the size of the counterions had significant effects on the interactions in some cases. This interaction was reflected by the dispersion term and the strength of this term was related with the structure of polymer film. CF<sub>3</sub>SO<sub>3</sub><sup>-</sup> was shown to have a greater sensitivity to larger molecules than DecSO<sub>3</sub><sup>-</sup> and SDSO<sub>4</sub><sup>-</sup>. Larger counterions bring in negative interactions of the dispersion term with an increased conductivity, while smaller ions result in positive interactions with a reduced conductivity. In addition, polymers containing fluoride and toluene groups like CF<sub>3</sub>SO<sub>3</sub><sup>-</sup>/PPy, Tos<sup>-</sup>/PPy and PF<sub>6</sub><sup>-</sup>/φPy usually introduce a negative polarizability term, intending to increase the conductivity of the polymer film.

Finally, a simple and novel method of multi-component analysis for organic vapour mixtures was introduced and demonstrated using hybrid sensor pairs and odour mapping technique. The relationship between the sensor pair's output and the mixing ratio of two-component mixtures has been studied theoretically and verified experimentally. A sensor pair's output with mixtures of two components were closely related to the output of each component. The relationship is largely determined by the partition coefficient ratio of each component into the polymer coating. Thus, using only one polymer coating, mixtures of two components can be distinguished as long as either

of them is known and calibrated. Mixtures of three components have also been investigated and the composition has been analysed on an odour map by introducing a second pair of sensors with a different polymer coating as well as appropriate calibration. The results have shown the feasibility of distinguishing the mixing ratios of mixtures using a significantly simpler method with two main advantages (the employment of lower number of polymer coatings such as two, and convenient data calibrations), compared with the commonly used single property measurement systems. This approach has demonstrated the potential usefulness of a hybrid system to perform the analysis of multi-component vapour mixtures.

## 6.2 FUTURE WORK

Despite progresses having been made in this work with new methods, materials being developed [144-148], much work is still required before artificial noses can reach their full potential in various applications [149].

To further develop this research, work needs to be carried out on two main aspects. First, the practical application of the developed *Electronic Nose* in this work needs to be extended. An important application is in agriculture where the Nose could be used to detect the oestrous of cows [150-157]. One of the approach to this is to select an array of sensors with the most difference in responses. For example, to construct an array of eight microresistors, four conducting polymer films could be chosen as DecSO<sub>3</sub><sup>-</sup>/PPy, CF<sub>3</sub>SO<sub>3</sub><sup>-</sup>/PPy, Tos<sup>-</sup>/PPy and PF<sub>6</sub><sup>-</sup>/P(Py+φPy). The other four films could consist of carbon-black polymer, which are also studied in this group [144].

Based on the successful demonstration of the analysis method in vapour-polymer interaction study, another focus of future work should be concentrated on the exploration of interaction mechanisms, e.g. to study more polymer coatings with varying compositions, or, alternatively, to investigate effects from more relevant parameters besides the five selected solute parameters. In the end, a full understanding of the vapour-polymer interaction mechanisms could be achieved.

## References

1. J. W. Gardner and P. N. Bartlett, "A brief history of electronic nose", *Sensors and Actuators B*, **18-19**, 211-220 (1994).
2. M. P. Byfield and I. P. May, Olfactory sensor array systems: the electronic nose, *GEC J. of Research*, **13**, 17-27 (1996).
3. J. W. Gardner, "Diagnosing illness with an electronic nose", *Proc. Of the 3<sup>rd</sup> East Asian Conf. on Chemical Sensors*, 24-31 (1997).
4. J. W. Gardner and W. E. Gardner, "The role of the electronic nose in condition monitoring", *Insight*, **39**, 865-869, (1997).
5. S. Baldacci, T. Matsuno, K. Toko, R. Stella and D. DeRossi, "Discrimination of wine using taste and smell sensors", *Sensors and Materials*, **10**, No.3, 185-200, (1998).
6. R. W. Moncrieff, "An instrument for measuring and classifying odours", *J. Appl. Physiol.*, **16**, 742 (1961).
7. T. M. Buck, F. G. Allen and M. Dalton, "Detection of chemical species by surface effects on metals and semiconductors", Surface Effects in Detection, Spartan Books Inc. USA, (1965).
8. A. Dravnieks and P. J. Trotter, "Polar vapour detection based on thermal modulation of contact potentials", *J. Sci. Instrum.*, **42**, 624 (1965).
9. K. Persaud and G. H. Dodd, "Analysis of discrimination mechanisms of the mammalian olfactory system using a model nose", *Nature*, **299**, 352-355 (1982).
10. I. Lundstrom, "Approach and mechanism to solid state based sensing", *Sensors and Actuators B*, **35-36**, 11-19 (1996).
11. J. R. Barker, "Prospects for molecular electronics", *Hybrid Circuits*, **14**. 19-24 (1987).
12. M. Schewizer-Berberich, J. Goppert, A. Hierlemann, J. Mitrovics, U. Weimar, W. Rosenstiel and W. Gopel, "Application of neural-network systems to the dynamic response of polymer-based sensor arrays", *Sensors and Actuators B*, **26-27**, 232-236 (1995).

13. G. Niebling and A. Schlachter, "Qualitative and quantitative gas analysis with non-linear interdigital sensor arrays and artificial neural networks", *Sensors and Actuators B*, **26-27**, 289-292 (1995).
14. S. Singh, E. L. Hines and J. W. Gardner, "Fuzzy neural computing of coffee and tainted-water data from an electronic nose", *Sensors and Actuators B*, **30**, 185-190 (1996).
15. P. Wang and J. Xie, "A novel recognition method for electronic nose using artificial neural network and fuzzy recognition", *Sensors and Actuators B*, **37**, 169-174 (1996).
16. J. W. Gardner, E. L. Hines and C. Pang, "Detection of vapours and odours from a multisensor array using pattern recognition: self-organising adaptive resonance techniques", *Measurement and Control*, **29**, 172-178 (1996).
17. E. L. Hines, J. W. Gardner and C. E. R. Potter, "Olfactory feature maps from an electronic nose", *Measurement and control*, **30**, 262-268 (1997).
18. D. Hodgins, "The development of an electronic nose for industrial and environmental applications", *Sensors and Actuators B*, **26-27**, 255-258 (1995).
19. J. V. Hatfield, P. Neaves, P. J. Hicks, K. Persaud and P. Travers, "Towards an integrated electronic nose using conducting polymer sensors", *Sensors and Actuators B*, **18-19**, 221-228 (1994).
20. F. R. Visser and M. Taylor, "Improved performance of the Aromascan A32S electronic nose and its potential for detecting aroma differences in dairy products", *J. Sensory Studies*, **13**, 95-120, (1998).
21. P. I. Neaves and J. V. Hatfield, "A new generation of intergrated electronic noses", *Sensors and Actuators B*, **26-27**, 223-231 (1995).
22. T. C. Pearce, J. W. Gardner, S. Friel, P. N. Bartlett and N. Blair, "Electronic nose for monitoring the flavour of beers", *Analyst*, **118**, 371-177 (1993).
23. B. Bourrounet, T. Talou and A. Gaset, "Application of a multi-gas-sensor device in the meat industry for boar-taint detection", *Sensors and Actuators B*, **26-27**, 250-254 (1995).
24. B. Hivert, "A fast and reproducible method for gas sensor screening to flavour compounds", *Sensors and Actuators B*, **26-27**, 242-245 (1995).

25. H. Holmberg, F. Winguist, I. Lundstrom, J. W. Gardner and E. L. Hines. "Identification of paper quality using a hybrid electronic nose", *Sensors and Actuators B*, **26-27**, 246-249 (1995).
26. M. Holmberg, F. Winquist, I. Lundstrom, J. W. Gardner and E. L. Hines, "Drift counteraction for an electronic nose", *Sensors and Actuators B*, **35-36**, 528-535 (1996).
27. H. K. Hong, H.W. Shin, D. H. Yun, S. R. Kim, C. H. Kwon, K. Lee and T. Moriizumi, "Electronic nose system with micro gas sensor array", *Sensors and Actuators B*, **35-36**, 338-341 (1996).
28. C. D. Natale, F. Davide, A D'Amico, P. Nelli, S. Groppelli and G. Sberveglieri, "An electronic nose for the recognition of the vineyard of a redwine", *Sensors and Actuators B*, **33**, 83-88 (1996).
29. H. V. Shurmer, J. W. Gardner and P. Corcoran, "Intelligent vapour discrimination using a composite 12-element sensor array", *Sensors and Actuators B*, **1**, 256-260 (1990).
30. F. Vianello, A. Stefani, M. L. Di Paolo, A. Rigo, A. Lui, B. Margesin, M. Zen, M. Scarpa and G. Soncini, "Potentiometric detection of formaldehyde in air by an aldehyde dehydrogenase FET", *Sensors and Actuators B*, **37**, 49-54 (1996).
31. X. Vilanova, E. Llobet, J. Brezmes, J. Calderer and X. Correig, "Numerical simulation of the electrode geometry and position effects on semiconductor gas sensor response", *Sensors and Actuators*, **48**, 425-431 (1998).
32. K. Domansky, D. L. Baldwin, J. W. Grate, T. B. Hall, J. Li, M. Josowicz and J. Janata, "Development and calibration of field-effect transistor-based sensor array for measurement of hydrogen and ammonia gas mixtures in humid air", *Anal. Chem.*, **70**, 473-481 (1998).
33. G. Sauerbrey, *Z. Physik*, **155**, 206-213 (1959).
34. W. H. King, "Piezoelectric sorption detector", *Anal. Chem.*, **36**, 1735-1739 (1964).
35. C. Di Natale, J. A. J. Branink, F. Bungaro, F. Davide, A. d'Amico, R. Paolesse, T. Boschi, M. Faccio and G. Ferri, "Recognition of fish storage time by a metalloporphyrines-coated QMB sensor array", *Meas. Sci. Technol.*, **7**, 1103-1114 (1996).
36. H. Nanto, K. Kondo, M. Habara, Y. Douguchi, R. I. Waite and H. Nakazumi. "Identification of aroma from alcohol using a Japanese-lacquer-film-coated quartz

- resonator gas sensor in conjunction with pattern recognition analysis”, *Sensors and Actuators B*, **35-36**, 183-186 (1996).
37. Z. Z. Ozturk, R. Zhou, V. Ahsen, O. Bekaroglu and W. Gopel, “Molecular recognition with metal containing supramolecular compounds”, *Sensors and Actuators*, **B35-36**, 404-408 (1996).
  38. M. Janghorbani and H. Freund, “Application of a piezoelectric quartz crystal as a partition detector”, *Anal. Chem.*, **45**, 325-332 (1973).
  39. J. D. Galipeau, L. J. LeGore, K. Snow, J. J. Caron, J. F. Vetelino and J. C. Andle, “The integration of a chemiresistive film overlay with a SAW microsensor”, *Sensors and Actuators B*, **35-36**, 158-163 (1996).
  40. A. Leidl, R. Hartinger, M. Roth and H. E. Endres, “A new SO<sub>2</sub> sensor system with SAW and IDC elements”, *Sensors and Actuators B*, **34**, 339-342 (1996).
  41. J. W. Grate, A. Snow, H. Wohltjen, M. H. Abraham, R. A. McGill and P. Sasson, “Determination of partition coefficients from surface acoustic wave vapour sensor responses and correlation with gas-liquid chromatographic partition coefficients”, *Anal. Chem.*, **60**, 869-875 (1988).
  42. J. W. Grate and M. H. Abraham, “Solubility interaction and the design of chemical selective sorbent coatings for chemical sensors and arrays”, *Sensors and Actuators B*, **3**, 85-111 (1991).
  43. R. A. McGill, M. H. Abraham and J. W. Grate, “Choosing polymer coatings for chemical sensors”, *Chemtech*, September, 27-37 (1994).
  44. J. W. Grate, M. H. Abraham and R. A. McGill, “Sorbent polymer materials for chemical sensors and arrays”, Handbook of Biosensors and Electronic Noses: Medicine, Food, and the Environment, E. Kress-Rogers, Eds., CRC Press, Inc. (1997).
  45. P. McAleron, J. M. Slater, P. Lowthian and M. Appleton, “Interpreting signals from an array of non-specific piezoelectric chemical sensors”, *Analyst*, **121**, 743-748 (1996).
  46. Z. P. Deng, D. C. Stone and M. Thompson, “Poly N-(2-cyanoethyl)pyrrol as a selective film for the thickness-shear-mode acoustic wave sensor”, *Can. J. Chem.*, **73**, 1427-1435 (1995).

47. Z. P. Deng, D. C. Stone and M. Thompson, "Selective detection of aroma components by acoustic wave sensors coated with conducting polymer films". *Analyst* **121**, 671-679 (1996).
48. Z. P. Deng, D. C. Stone and M. Thompson, "Effect of redox state on the response of poly-N-(2-cyanoethyl)pyrrol coated thickness-shear-mode acoustic wave sensors to organic vapours", *Analyst* **121**, 1341-1348 (1996).
49. S. B. Adeloju and G. G. Wallace, "Conducting polymers and the bioanalytical sciences: New tools for biomolecular communication", *Analyst*, **121**, 699-703 (1996).
50. J. N. Barisci, C. Conn and G. G. Wallace, "Conducting polymer sensors", *TRIP*, **4**, 307-311 (1996).
51. A. Deronzier and J. C. Moutet, "Polypyrrole film containing metal complexes: syntheses and applications", *Coordination Chemistry Reviews* **147**, 339-371 (1996).
52. J. W. Gardner and P. N. Bartlett, "Potential application of electropolymerized thin organic films in nanotechnology", *Nanotechnology* **2**, 19-32 (1991).
53. J. W. Gardner and P. N. Bartlett, "Application of conducting polymer technology in microsystems", *Sensors and Actuators*, **A51**, 57-66 (1995).
54. M. Josowicz, "Application of conducting polymers in potentiometric sensors", *Analyst*, **120**, 1019-1024 (1995).
55. A. G. MacDiarmid, "Polyaniline and polypyrrole: Where are we headed?" *Synthetic Metals*, **84**, 27-34 (1997).
56. S. S. Schiffman, B. G. Kermani and H. T. Nagle, "Analysis of medication off-odors using an electronic nose", *Chem. Senses*, **122**, 119-128 (1997).
57. K. C. Persaud, S. M. Khaffaf, J. S. Payne, A. M. Pisanelli, D. H. Lee and H. G. Byun, "Sensor array techniques for mimicking the mammalian olfactory system", *Sensors and Actuators B*, **35-36**, 267-273 (1996).
58. A. F. Diaz, K. K. Kanazawa and G. P. Gardini, "Electrochemical polymerization of pyrrole", *J.C.S. Chem. Comm.*, 635-636 (1979).
59. K. C. Persaud and P. Pelosi, "An approach to an artificial nose", *Trans. Am. Soc. Artif. Intern. Organs*, **31**, 297-300 (1985).
60. J. J. Miasik, A. Hooper and B. C. Tofield, "Conducting polymer gas sensors", *J. Chem. Soc. Faraday Trans.*, **82**, 1117-1126 (1986).

61. P. N. Bartlett, P. B. M. Archer and S. K. Ling-Chung, "Conducting polymer gas sensors part 1. Fabrication and characterization", *Sensors and Actuators* . **19**, 125-140 (1989).
62. P. N. Bartlett, P. B. M. Archer and S. K. Ling-Chung, "Conducting polymer gas sensors 2. Response of polypyrrole to methanol vapour", *Sensors and Actuators* . **19**, 141-150 (1989).
63. P. D. Harris, W. M. Arnold, M. K. Andrews and A. C. Partridge, "Resistance characteristics of conducting polymer films used in gas sensors", *Sensors and Actuators B-Chemical*, **42**, 177-184 (1997).
64. P. N. Bartlett, J. M. Elliott and J. W. Gardner, "Integrated sensor arrays for the dynamic measurement of food flavour release", *Measurement and control*, **30**, 273-279 (1997).
65. T. Nakamoto, H. Ishida and T. Moriizumi, "An odor compass for localising an odour source", *Sensors and Actuators B*, **35-36**, 32-36 (1996).
66. K. Yano, U. T. Bornscheuer, R. D. Schmid, H. Yoshitake, H. S. Ji, K. Ikebukuro, Y. Masuda and I. Karube, "Development of an odorant sensor using polymer-coated quartz crystals modified with unusual lipids", *Biosensors and Bioelectronics*, **13**, 397-405, (1998).
67. X. X. Cai, A. Sun, L. Cui and X. L. Hai, "A novel odor sensor coated with a lipid-membrane", *Sensors and Actuators B*, **12**, 15-18 (1993).
68. A. Sun, H. Y. Xu, Z. K. Chen, L. Cui and X. L. Hai, "Research on electrical-properties of amphiphilic lipid membranes by means of interdigitated electrodes", *Materials Science & Engineering C- Biomimetic Materials Sensors and Systems*, **2**, 159-163 (1995).
69. A. Sun, L. Cui, Z. K. Chen, H. Y. Xu and Q. Z. Zhou, "Lipid microresistor as mimicking olfactory sensor- the role of the response of lipids to C1 to C4 alcohols", *Sensors and Actuators B*, **20**, 151-158 (1994).
70. E. J. Severin, R. D. Sanner, B. J. Doleman and N. S. Lewis, "Differential detection of enantiomeric gaseous analytes using carbon black-chiral polymer composite, chemically sensitive resistors", *Anal. Chem.*, **70**, 1440-1443 (1998).
71. B. J. Doleman, M. C. Lonergan, E. J. Severin, T. P. Vaid and N. S. Lewis, "Quantitative study of the resolving power of arrays of carbon black-polymer composites in various vapor-sensing tasks", *Anal. Chem.*, **70**, 4177-4190 (1998).

72. I. Lundstrom, R. Erlandsson, U. Frykman, E. Hedborg, A. Spetz, H. Sundgren, S. Welin and F. Winqvist, "Artificial olfactory images from a chemical sensor using a light-pulse technique", *Nature*, **352**, 47-50 (1991).
73. F. Josse, R. Lukas, R. Zhou, S. Schneider and D. Everhart, "AC-impedance-based chemical sensors for organic solvent vapours", *Sensors and Actuators B*, **35-36**, 363-369 (1996).
74. M. C. Petty, "Gas sensing using thin organic films", *Biosensors and Bioelectronics*, **10**, 129-134 (1995).
75. K. Spaeth, G. Kraus and G. Gauglitz, "In-situ characterization of polymer films for application in chemical sensing of volatile organic compounds by spectroscopic ellipsometry", *Fresenius. J. Anal. Chem.*, **357**, 292-296 (1997).
76. L. Cui, M. Swann, A. Glidle, J. Barker and J. Cooper, "Odour mapping using microresistor and piezo-electronic sensor pairs", *Technical Digest of 7<sup>th</sup> International Meeting on Chemical Sensors*, Beijing, (1998).
77. L. Cui, M. Swann, A. Glidle, J. Barker and J. Cooper, "Odour mapping using microresistor and piezo-electric sensor pairs", *Sensors and Actuators-B*, May (1999). In print.
78. V. I. Anisimkin, E. Verona, V. E. Zemlyakov, R. G. Kryshthal and A. V. Medved, "Integrated sensor array for analysis of multicomponent gas mixtures", *Technical Phys. Letters*, **24**, 640-642, (1998).
79. J. W. Gardner, "Intelligent gas sensing using an integrated sensor pair", *Sensors and Actuators B*, **26-27**, 261-266 (1995).
80. J. M. Slater, J. Paynter and E. J. Watt, "Multi-layer conducting polymer gas sensor arrays for olfactory sensing", *Analyst*, **118**, 379-384 (1993).
81. J. F. Pearson and J. M. Slater, "Coated-wire and composition ion-selective electrodes based on doped poly(pyrrole)", *Analyst*, **117**, 1885-1890 (1992).
82. R. Zhou, M. Haimbodi, D. Everhart and F. Josse, "Polymer-coated QCR sensors for the detection of organic solvents in water", *Sensors and Actuators B*, **35-36**, 176-182 (1996).
83. J. M. Slater and E. J. Watt, "Examination of ammonia-poly(pyrrole) interactions by piezoelectric and conductivity measurements", *Analyst*, **116**, 1125-1130 (1991).
84. J. M. Slater and E. J. Watt, "Gas and vapour detection with poly(pyrrole) gas sensors", *Analyst*, **117**, 1265-1270 (1992).

85. Y. Kunugi, K. Nigorikawa, Y. Harima and K. Yamashita, "A selective organic vapour sensor based on simultaneous measurements of changes of mass and resistance of a poly(pyrrole) thin film", *J. Chem. Soc. Commun.*, 873-874 (1994).
86. K. Nigorikawa, Y. Kunugi, Y. Harima, and K. Yamashita, "A selective gas sensor using a polypyrrol thin film as a sensitive matrix on a piezoelectric crystal". *J. of Electroanalytical Chemistry*, **396**, 563-567 (1995).
87. D. C. Dyer and J. W. Gardner, "High-precision intelligent interface for a hybrid electronic nose", *Sensors and Actuators A*, **62**, 724-728 (1997).
88. K. K. Kanazawa, A. F. Diaz, M. T. Krounbi and G. B. Street, "Electrical properties of pyrrole and its copolymers", *Synthetic Metals*, **4**, 119-130 (1981).
89. T. K. Skotheim, *Handbook of Conducting Polymers*, New York: M. Dekker, (1986).
90. G. K Chandler and D. Pletcher, "The electrochemistry of conducting polymers", in *Electrochemistry*, 117-149, (1985).
91. B. R. Saunders, R. J. Fleming and K. S. Murray, "Recent advances in the physical and spectroscopic properties of polypyrrole films, particularly those containing transition-metal complexes as counterions", *Chem. Mater.*, **7**, 1082-1094 (1995).
92. L. F. Warren, J. A. Walker, D. P. Anderson, C. G. Rhodes and L. J. Buckley, "A study of conducting polymer morphology", *J. Electrochem. Soc.*, **136**, 2286-2295 (1989).
93. W. Wernet, M. Monkenbusch and G. Wegner, *Makromol.* "A new series of conducting polymers with layered structure: Polypyrrole n-alkylsulfates and n-alkylsulfonates", *Chem. Rapid Commun.*, **5**, 157-164 (1984).
94. N. S. Allen, K. S. Murray, R. J. Fleming and B. R. Saunders, "Physical properties of polypyrrole films containing trisoxalatometallate anions and prepared from aqueous solution", *Synthetic Metals*, **87**, 237-247 (1997).
95. A. M. Farrington and J. M. Slater, "Prediction and characterisation of the charge/size exclusion properties of over-oxidized poly(pyrrole) films". *Electroanalysis*, **9**, 843-847 (1997).
96. G. R. Mitchell, F. J. Davis and C. H. Legge, "The effect of dopant molecules on the molecular order of electrically-conducting films of polypyrrole", *Synthetic Metals*, **26**, 247-257 (1988).

97. D. Bloor, A. P. Monkman, G. C. Stevens, K. M. Cheung and S. Pugh, "Structure-property relationships in conductive polymers", *Mol. Cryst. Liq. Cryst.*, **187**, 231-239 (1990).
98. K. M. Cheung, D. Bloor and G. C. Stevens, "The influence of unusual counterions on the electrochemistry and physical properties of polypyrrole", *J. Materials Science*, **25**, 3814-3837 (1990).
99. K. M. Cheung, D. Bloor and G. C. Stevens, "Characterization of polypyrrole electropolymerized on different electrodes", *Polymer*, **29**, 1709-1717 (1988).
100. Z. P. Deng, D. C. Stone and M. Thompson, "Characterization of polymer films of polypyrrole derivatives for chemical sensing by cyclic voltammetry, X-ray photoelectron spectroscopy and vapour sorption studies", *Analyst*, **122**, 1129-1138 (1997).
101. A. Watanabe, M. Tanaka and J. Tanaka, "Electrical and optical properties of a stable synthetic metallic polymer-polypyrrole", *Bull. Chem. Soc. Jpn.*, **54**, 2278-2281 (1981).
102. M. Yamaura, T. Hagiwara and K. Iwata, "Enhancement of electrical-conductivity of polypyrrole film by stretching-counterion effect", *Synth. Metal*, **26**, 209-224 (1988).
103. P. N. Bartlett and J. W. Gardner, "Odour sensors for an electronic nose", in Sensors and Sensory systems for an Electronic Nose, J. W. Gardner, Eds., Kluwer Academic Publishers (1991).
104. M. Josowicz and P. Topart, "Studies of the Interactions between Organic Vapours and Organic Semiconductors. Application to Chemical Sensing", in Sensors and Sensory systems for an Electronic Nose, J. W. Gardner, Eds., Kluwer Academic Publishers (1991).
105. B. Blackwood and M. Josowicz, "Work function and spectroscopic studies of interactions between conducting polymers and organic vapours", *J. Phys. Chem.*, **95**, 493-502 (1991).
106. P. Topart and M. Josowicz, "Characterization of the interaction between poly(pyrrole) films and methanol vapour", *J. Phys. Chem.*, **96**, 7824-7830 (1992).
107. G. Zotti, G. Schiavon, S. Zecchin and G. D'Aprano, "The reversible hydroxide doping of polypyrrole. Delay of polaron and mobile bipolaron injection in polypyrrole by H bonding hydroxide anions", *Synthetic Metals*, **80**, 35-39 (1996).

108. J. K. Avlyanov, H. H. Kuhn, J. Y. Josefowicz and A. G. MacDiarmid, "In-situ deposited thin films of polypyrrole: Conformational changes induced by variation of dopant and substrate surface", *Synthetic Metals*, **84**, 153-154 (1997).
109. L. Zuppiroli, S. Paschen and M. N. Bussac, "Role of the dopant counterions in the transport and magnetic properties of disordered conducting polymers", *Synthetic Metals*, **69**, 621-624 (1995).
110. A. Adachi and J. Yamauchi, "Effect of oxygen polypyrrole as studied by conductivity and ESR measurements", *Bull. Chem. Soc. Jpn.*, **69**, 811-814 (1996).
111. D. Y. Kim, J. Y. Lee, D. K. Moon and C. Y. Kim, "Stability of reduced polypyrrole", *Synthetic Metals*, **69**, 471-474 (1995).
112. M. Thompson and D. C. Stone, "Molecular modeling and the selective sensor response", in *Sensors and Sensory systems for an Electronic Nose*, J.W. Gardner, Eds., Kluwer Academic Publishers (1991).
113. J. M. Slater and J. Paynter, "Prediction of Gas Sensor Response Using Basic Molecular Parameters", *Analyst*, **119**, 191-195 (1994).
114. D. Bolliet and C. F. Poole, "Mixture-design approach to retention prediction using the solvation parameter model and ternary solvent systems in reversed-phase liquid chromatography", *Analytical Commun.* **35**, 253-256, (1998).
115. K. T. Lau, J. Micklefield and J. M. Slater, "The optimisation of sorption sensor arrays for use in ambient conditions", *Sensors and Actuators-B*, **50**, 69-79, (1998).
116. M. H. Abraham, "Scales of solute hydrogen-bonding: Their construction and application to physicochemical and biochemical processes", *Chem. Soc. Rev.*, **22**, 73-83 (1993).
117. H. Beitnes and K. Schroder, "Detection of trace concentrations of gases with coated piezoelectric quartz crystals", *Anal. Chim. Acta.*, **158**, 57-65 (1984).
118. A. Kipling and M. Thompson, "Network analysis method applied to liquid-phase acoustic wave sensors", *Anal. Chem.*, **62**, 1514-1519 (1990).
119. J. W. Gardner, "Electrical conduction in solid-state gas sensors", *Sensors and Actuators*, **18**, 373-387 (1989).
120. J. W. Gardner, "A diffusion-reaction model of electrical conduction in the tin oxide gas sensors", *Semicond. Sci. Technol.*, **4**, 345-350 (1989).
121. J. W. Gardner and P. N. Bartlett, "Design of conducting polymer gas sensors: modelling and experiment", *Synthetic Metals*, 55-57 (1993).

122. J. W. Gardner, P. N. Bartlett and K. F. E. Pratt, "Modelling of gas-sensitive conducting polymer devices", *IEE Pro.-Circuits Devices Syst.*, **142**, 321-333 (1995).
123. D. R. Lide, CRC Handbook of Chemistry and Physics, 74<sup>th</sup> Edition 1993-1994, CRC Press, (1994).
124. A. J. Martin and W. B. Booth, "Indoor air quality sensors", BSRIA Technical Note TN 1/96, (1996).
125. G. Socrates, Infrared Characteristic Group Frequencies: Tables and Charts, John Wiley & Sons, (1994).
126. D. S. Ballantine, R. M. White, S. J. Martin, A. J. Ricco, E. T. Zellers, G. C. Frye and H. Wohltjen, Acoustic Wave Sensors: Theory, Design, and Physico-Chemical Applications, ACADEMIC PRESS, Chapter 5 (1997).
127. W. J. Moore, Physical Chemistry, 5<sup>th</sup> Edition, Longman Group Limited, 497-498 (1972).
128. H. T. Nagle and R. Gutierrez-Osuna, "The how and why of electronic noses", *IEEE Spectrum*, September, 22-34, (1998).
129. D. Machin and C. E. Rogers, Encyclopedia of Polymer Science and Technology, Vol. 12, 679-700, M. Herman, Eds., New York Chichester: Wiley (1985).
130. M. J. Hephher and D. Reilly, "Piezoelectric sensors", Sensors Systems for Environmental Monitoring Vol One: sensors Technologies, M. Campbell, Eds., Blackie Academic & Professional UK (1997).
131. M. J. Winter, Chemical Bonding, Oxford Science Publications, (1994).
132. J. N. Murrell, S. F. Kettle and J. M. Tedder, The Chemical Bond, John Wiley & Sons, (1985).
133. S. N. Vinogradov and R. H. Linnell, Hydrogen Bonding, Van Nostrand Reinhold Company, (1971).
134. M. Swann, A. Glidle, L. Cui, J. Barker and J. Cooper, paper in preparation.
135. W. P. Carey, K. R. Beebe and B. R. Kowalski, "Multicomponent analysis using an array of piezoelectric crystal sensors", *Anal. Chem.*, **59**, 1529-1534 (1987).
136. M. Otto and D. R. Thomas, "Model studies on multiple channel analysis of free magnesium, calcium, sodium and potassium at physiological concentration levels with ion-selective electrodes", *Anal. Chem.*, **57**, 2647-2651 (1985).

137. A. D. Brailsford, M. Yussouff and E. M. Logothetis, "Theory of gas sensors: response of an electrochemical sensor to multi-component gas mixtures", *Sensors and Actuators B*, **34**, 407-411 (1996).
138. N. R. Draper and R. Smith, Applied Regression Analysis, 2<sup>nd</sup> Edition, Wiley New York, (1981).
139. P. Geladi and B. R. Kowalski, "Partial least-squares regression – a tutorial", *Anal. Chim. Acta*, **185**, 1-17, (1986).
140. J. R. Stetter, P. C. Jurs and S. L. Rose, "Detection of hazardous gases and vapors: pattern recognition analysis of data from an electrochemical sensor array", *Anal. Chem.*, **58**, 860-866 (1986).
141. P. T. Moseley and A. J. Crocker, Sensor Materials, Institute of Physics Publishing, Bristol and Philadelphia, (1997).
142. J. M. Bates and M. Campbell, "Gas sensors and analysers", Sensor Systems for Environmental Monitoring, Vol 1. Sensor Technologies, M. Campbell, Eds., Blackie Academic & Professional, (1997).
143. R. J. Young and P. A. Lovell, Introduction to Polymers, Chapman & Hall, (1991).
144. M. J. Swann, A. Glidle, L. Cui, J. Barker and J. M. Cooper, "The determination of gaseous molecular density using a hybrid vapour sensor", *Chem. Commun.*, 2753-2754 (1998).
145. L. Torsi, M. Pezzuto, P. Siciliano, R. Rella, L. Sabbatini, L. Valli, P. G. Zambonin, "Conducting polymers doped with metallic inclusions: New materials for gas sensors", *Sensors and Actuators B*, **48**, 362-367 (1998).
146. W. Gopel, C. Ziegler, H. Breer, D. Schild, R. Apfelbach, J. Joerges and R. Malaka, "Bioelectronic noses: a status report; part 1", *Biosensors and Bioelectronics*, **13**, 479-493, (1998).
147. C. Ziegler, W. Gopel, H. Hammerle, H. Hatt, G. Jung, L. Laxhuber, H. L. Schmidt, S. Schutz, F. Vogtle and A. Zell, "Bioelectronic noses: a status report; part 2". *Biosensors and Bioelectronics*, **13**, 539-571 (1998).
148. W. Gopel, "Controlled signal transduction across interfaces of 'intelligent' molecular systems", *Biosensors and Bioelectronics*, **10**, 35-39 (1995).
149. E. Schaller, J. O. Bosset and F. Escher, "'Electronic noses' and their application to food", *Food Sci. Tech. -Lebensmittel-Wissenschaft & Tech.*, **31**, 305-316, (1998).

150. N. B. Blazquez and S. E. Long, "Rate of discharge and morphology of sweat glands in the perineal, lumbodorsal and scrotal skin of cattle", *Research in Veterinary Science*, **57**, 277-284 (1994).
151. W. R. Klemm, G. N. Hawkins and E. De Los Santos, "Identification of compounds in bovine cervico-vaginal mucus extracts that evoke male sexual behaviour". *Chemical Sensors*, **12**, 77-87 (1987).
152. W. R. Klemm, "Blood acetaldehyde fluctuates markedly during bovine estrous cycle", *Animal Reproduction Science*, **35**, 9-26 (1994).
153. A. Lane and D. C. Wathes, "An electronic nose to detect changes in perineal odors associated with estrus in the cow", *J. Dairy Science*, **81**, 2145-2150, (1998).
154. W. D. Ma, B. A. Clemment and W. R. Klwmm, "Cyclic changes in volatile constituents of bovine vaginal secretions", *J. Chemical Ecology*, **21**, 1895-1906 (1995).
155. T. H. Misselbrook, P. J. Hobbs and K. C. Persaud, "Use of an electronic nose to measure odour concentration following application of cattle slurry to grassland", *J. Agricultural Engineering Research*, **166**, 213-220 (1997).
156. D. H. O'Neill and V. R. Phillips, "A review of the control of odour nuisance from livestock buildings", *J. Agric. Engng. Res.*, **53**, 23-50 (1992).
157. V. M. Owen, "Sniffer technology becomes commercial reality", *Biosensors and Bioelectronics*, **10**(1/2) (1995).

## Appendix:

### Interdigitated Electrode Sensor Baseline Resistance Stability with Time

(a) PPy dodecylsulfate film

SDSO <sub>4</sub> <sup>-</sup> /PPy/H <sub>2</sub> O, pH 4.8, 0.8V vs. Ag/AgCl			
Sensor No	R <sub>0</sub> (initial)	R (90 days)	R (180 days)
d8	41.00	54.00	64.00
d12	52.00	122.00	184.00
d6	56.00	121.00	167.00
d11	82.00	291.00	447.00
d3	118.00	387.00	796.00
d9	148.00	510.00	1050.00
d5	193.00	607.00	1030.00
Proper initial R <sub>0</sub> : <100 Ω			

(b) PPy decanesulphonate film

DecSO <sub>3</sub> <sup>-</sup> /PPy/H <sub>2</sub> O, pH 4.8, 0.8V vs. Ag/AgCl			
Sensor No	R <sub>0</sub> (initial)	R (90 days)	R (180 days)
e11	49.00	77.00	113.00
e6	50.00	87.00	228.00
e5	51.00	77.00	145.00
e8	63.00	88.00	198.00
e3	143.00	339.00	676.00
e7	209.00	654.00	2140.00
e9	226.00	1500.00	5950.00
e10	250.00	2120.00	8170.00
Proper initial R <sub>0</sub> : 120-150 Ω			

(c) PPy hexanesulphonate film

<b>HexSO<sub>3</sub><sup>-</sup>/PPy/H<sub>2</sub>O, pH 4.8, 0.8V vs. Ag/AgCl</b>			
<b>Sensor No</b>	<b>R<sub>0</sub> (initial)</b>	<b>R (90 days)</b>	<b>R (210 days)</b>
14/7-4	63.00		83.00
14/7-3	73.00		197.00
14/7-1	92.00		248.00
14/7-2	154.00		540.00
<b>Proper initial Ro: 100-150 Ω</b>			

(d) PPy butanesulphonate film

<b>ButSO<sub>3</sub><sup>-</sup>/PPy/H<sub>2</sub>O, pH 4.8, 0.8V vs. Ag/AgCl</b>			
<b>Sensor No</b>	<b>R<sub>0</sub> (initial)</b>	<b>R (90 days)</b>	<b>R (270 days)</b>
15/5-14	38.00		146.00
15/5-10	60.00		350.00
15/5-11	61.00		363.00
15/5-9	88.00		734.00
15/5-12	138.00		1400.00
15/5-13	171.00		1900.00
<b>Proper initial Ro: 60-70 Ω</b>			

(e) PPy ethanesulphonate film

<b>EtSO<sub>3</sub><sup>-</sup>/PPy/H<sub>2</sub>O, pH 4.8, 0.9V vs. Ag/AgCl</b>			
<b>Sensor No</b>	<b>R<sub>0</sub> (initial)</b>	<b>R (90 days)</b>	<b>R (180 days)</b>
a5	40.50	145.00	392.00
a3	46.00	144.00	496.00
a2	47.00	206.00	482.00
a4	52.00	243.00	548.00
a8	52.30	197.00	592.00
a1	54.00	270.00	625.00
a7	57.50	341.00	816.00
<b>Proper initial Ro: 50-60 Ω</b>			

(f) PPy toluenesulphonate film

<b>TEATos/PPy/AN, 1.0V vs. Ag/AgCl</b>			
<b>Sensor No</b>	<b>R<sub>0</sub> (initial)</b>	<b>R (90 days)</b>	<b>R (180 days)</b>
f2	42.00	55.00	76.00
f6	53.00	79.00	118.00
f8	59.00	95.00	139.00
f5	77.00	141.00	232.00
f3	81.00	132.00	215.00
f7	90.00	167.00	256.00
f4	131.00	217.00	-----
<b>Proper initial R<sub>0</sub>: 100-200 Ω</b>			

(g) PPy hexafluorophosphate film

<b>TEAPF<sub>6</sub>/PPy/AN, 1.00V vs. Ag/AgCl</b>			
<b>Sensor No</b>	<b>R<sub>0</sub> (initial)</b>	<b>R (90 days)</b>	<b>R (180 days)</b>
h5	22.00	30.00	40.00
h6	23.00	30.00	46.00
h9	46.00	66.00	105.00
h7	104.00	379.00	836.00
h8	171.00	465.00	13.58K
h4	228.00	1550.00	4.7K
h3	345.00	15600.00	113.0K
<b>Proper initial R<sub>0</sub>: 60-100 Ω</b>			

(h) Phenyl Py hexafluorophosphate film

<b>TEAPF<sub>6</sub>/ØPPy+PPy/AN, 1.05V vs. Ag/AgCl</b>			
<b>Sensor No</b>	<b>R<sub>0</sub> (initial)</b>	<b>R (90 days)</b>	<b>R (180 days)</b>
i9	65.00	482.00	1.34K
i4	71.00	729.00	2.48K
i5	84.00	556.00	6.23K
i6	199.00	3300.00	11.5K
i2	421.00	3880.00	63.5K
i8	767.00	6170.00	76.2K
<b>Proper initial R<sub>0</sub>: 50-60 Ω</b>			

(i) PPy trifluoromethanesulphonate film

<b>CF<sub>3</sub>SO<sub>3</sub><sup>-</sup>/PPy/H<sub>2</sub>O, pH 4.5, 0.8V vs. Ag/AgCl</b>			
<b>Sensor No</b>	<b>R<sub>0</sub> (initial)</b>	<b>R (90 days)</b>	<b>R (180 days)</b>
b2	35.00	140.00	351.00
b5	43.00	310.00	1.04K
b8	63.00	1230.00	5.6K
b3	83.00	1796.00	8.18K
b4	117.00	1220.00	5.36K
b6	160.00	5630.00	39.0K
b7	229.00	7370.00	46.9K
<b>Proper initial R<sub>0</sub>: 30-40 Ω</b>			

(j) PPy perfluorooctanesulphonate film

<b>C<sub>8</sub>F<sub>17</sub>SO<sub>3</sub><sup>-</sup>/PPy/H<sub>2</sub>O, pH 4.5, 0.8V vs. Ag/AgCl</b>			
<b>Sensor No</b>	<b>R<sub>0</sub> (initial)</b>	<b>R (90 days)</b>	<b>R (180 days)</b>
c10	38.00	40.00	41.60
c3	56.00	105.00	229.00
c2	67.80	135.00	429.00
c1	74.80	138.00	411.00
c11	147.00	465.00	1690.00
c7	205.00	589.00	2100.00
c5	352.00	1222.00	4110.00
c8	577.00	1900.00	7100.00
<b>Proper initial R<sub>0</sub>: 70-100 Ω</b>			

The following films have shown much faster baseline resistance drift than film (a) to (j). They are not suitable to make sensors.

KCl/PPy/H <sub>2</sub> O, pH 4.8, 0.8V vs. Ag/AgCl			
Sensor No	R <sub>0</sub> (initial)	R (90 days)	R (180 days)
2/7-8	40.00	1.64K	
2/7-10	36.00	1.7K	
5/3-3	52.00	9.65K	
5/3-4	56.00	5.4K	
5/3-5	146.00	50K	

TEAP/PPy/AN, 1.10V vs. Ag/AgCl			
Sensor No	R <sub>0</sub> (initial)	R (90 days)	R (180 days)
g6	80.00	93K	
g5	99.00	>200K	
g2	124.00	92K	
g3	165.00	>200K	

TEAP/∅PPy+PPy/AN, 1.10V vs. Ag/AgCl			
Sensor No	R <sub>0</sub> (initial)	R (90 days)	R (180 days)
11/11 4-1	1000.00	168K	
11/11 4-2	329.00	122K	
12/9 1-1	410.00	>200K	
12/9 1-2	173.00	108K	

TEAP/CH <sub>3</sub> PPy+PPy/AN, 1.10V vs. Ag/AgCl			
Sensor No	R <sub>0</sub> (initial)	R (90 days)	R (180 days)
12/9 3-2	14.7K	>200K	
12/9 3-4	5.4K	>200K	

TEAPF <sub>6</sub> /CH <sub>3</sub> Py+PPy/AN, 1.15V vs. Ag/AgCl			
Sensor No	R <sub>0</sub> (initial)	R (90 days)	R (180 days)
12/9 4-2	16.3K	>200K	
12/9 4-3	21K	>200K	

TEAT/PPy/AN, 1.05V vs. Ag/AgCl			
Sensor No	R <sub>0</sub> (initial)	R (90 days)	R (180 days)
13/9 8-1	95.00	>200K	
13/9 8-2	94.00	>200K	
4/2 a	133.00	>200K	

